University of Alberta

The Characterization of Ion Emission from Plasmas Produced by ns and fs Laser Pulses

by

Rahim Janmohamed

A thesis submitted to the Faculty of Graduate Studies and Research in partial fulfillment of the requirements for the degree of Master of Science

Department of Electrical and Computer Engineering

Edmonton, Alberta

Fall 2005

Library and Archives Canada
Published Heritage Branch
395 Wellington Street
Ottawa ON K1A 0N4
Canada

Bibliothèque et Archives Canada
Direction du Patrimoine de l'édition
395, rue Wellington
Ottawa ON K1A 0N4
Canada

0-494-09196-7

Your file *Votre référence*
ISBN:
Our file *Notre référence*
ISBN:

NOTICE:
The author has granted a non-exclusive license allowing Library and Archives Canada to reproduce, publish, archive, preserve, conserve, communicate to the public by telecommunication or on the Internet, loan, distribute and sell theses worldwide, for commercial or non-commercial purposes, in microform, paper, electronic and/or any other formats.

The author retains copyright ownership and moral rights in this thesis. Neither the thesis nor substantial extracts from it may be printed or otherwise reproduced without the author's permission.

AVIS:
L'auteur a accordé une licence non exclusive permettant à la Bibliothèque et Archives Canada de reproduire, publier, archiver, sauvegarder, conserver, transmettre au public par télécommunication ou par l'Internet, prêter, distribuer et vendre des thèses partout dans le monde, à des fins commerciales ou autres, sur support microforme, papier, électronique et/ou autres formats.

L'auteur conserve la propriété du droit d'auteur et des droits moraux qui protège cette thèse. Ni la thèse ni des extraits substantiels de celle-ci ne doivent être imprimés ou autrement reproduits sans son autorisation.

In compliance with the Canadian Privacy Act some supporting forms may have been removed from this thesis.

While these forms may be included in the document page count, their removal does not represent any loss of content from the thesis.

Conformément à la loi canadienne sur la protection de la vie privée, quelques formulaires secondaires ont été enlevés de cette thèse.

Bien que ces formulaires aient inclus dans la pagination, il n'y aura aucun contenu manquant.

Canada

Abstract

Ions emitted from plasmas produced by nanosecond and femtosecond laser pulses are important for many applications. Faraday cup detectors are widely used to study ion emission, despite the limitations imposed by the space charge effect. Using particle-in-cell simulations, it is found that the current understanding of the space charge effect is incomplete. Using simulations incorporating both ions and electrons, excellent agreement with experiment has been achieved.

The ion emission from nanosecond laser-produced plasmas in the 10^8-10^{10} W/cm^2 intensity regime is important for applications such as pulsed laser deposition. The characteristics of both carbon and zinc oxide ultraviolet ablation plumes have been measured in this intensity regime.

The fast ion emission from femtosecond infrared laser-produced copper plasmas in the 10^{14}-10^{16} W/cm^2 intensity regime has also been characterized. The intensity scaling of the fast ion properties is investigated thoroughly. This emission is potentially useful for applications such as ion implantation.

Acknowledgements

In the name of Allah, the most beneficent, the most merciful.

I would like to express my sincere gratitude to my supervisors, Dr. Ying Tsui and Dr. Robert Fedosejevs, for their support and guidance over the course of this thesis. I would also like to express my heartfelt appreciation for their patience and kindness in allowing me time to pursue other avenues of study in the last two years. I am convinced that few others in their place would have been so supportive.

I would like to thank my colleagues in the Laser Plasma Group at the University of Alberta for their help. In particular, I would like to thank Cristina Serbanescu; without her assistance, this work would not have been possible. I would also like to thank Blair Harwood, Rick Conrad, Michael Argument, Michael Taschuk, Sean Kirkwood, Matt Reid, Hong Sang, Yang-Wen Sun, Chris Germain, Zahidur Chowdhury, Craig Unick, and Yogesh Godwal for their assistance in the course of my studies.

I would also like to thank John Steele and Geoff Redman, whose work in part provided the foundation of portions of my thesis.

I would like to acknowledge the financial support of the Natural Sciences and Engineering Research Council of Canada, Alberta Heritage Scholarship Trust, Alberta's Informatics Circle of Research Excellence, Alberta Ingenuity, and the University of Alberta.

Lastly, I would like to thank my friends and family for their support. From a very early age, my parents emphasized the importance of education, and they have not hesitated to make the sacrifices necessary to allow me to pursue a better life through education. This work is the fruit of their labor.

Table of Contents

Abstract.....i

Acknowledgements.....ii

Table of Contents.....iii

List of Tables.....vi

List of Figures.....viii

List of Symbols.....xvi

Chapter 1: Introduction.....1

Chapter 2: Ion Detection.....4

Background.....4

a) Langmuir Probes.....4

b) Faraday Cups.....9

Methods.....11

a) Analytical Model.....11

b) Simulation.....12

c) Experiment.....13

Results and Discussion.....16

a) Analytical Model and Simulation Results.....16

b) Experimental and Simulation Results.....24

c) Two-Particle Simulations.....30

d) Ion Detector Selection.....37

Conclusion.....38

Chapter 3: Ion Emission from Plasmas Produced by ns Laser Pulses.....39

Background.....39

a) Pulsed Laser Deposition.....39

b) Laser-Matter Interaction Theory.....42

c) Literature Survey.....48

Experiment.....49

Results and Discussion.....54

a) Angular Distribution Results.....54

b) Evaluation of Applicability of Theoretical Models.....63

c) Ion Energy Spectrum.....65

d) Estimation of Ion Charge State.....71

e) Electron Temperature.....74

Conclusion.....77

Chapter 4: Ion Emission from Plasmas Produced by fs Laser Pulses.....78

Introduction.....78

a) Chirped Pulse Amplification.....78

b) Applications of femtosecond Ion Emission.....78

Background.....81

a) Laser-Matter Interaction Theory.....81

b) Literature Survey.....83

Experiment.....85

Results and Discussion.....92

a) Identification of Ion Species.....92

b) Ion Energy Scaling.....102

c) Ion Energy Spectrum.....105

d) Ion Peak Current Density.....113

e) Assessing the Feasibility of Ion Implantation.....115

Conclusion.....117

Chapter 5: Conclusion.....119

Appendix.....121

Bibliography.....168

List of Tables

Table 3-1. Estimated total charge emitted in the plasma plume, for a carbon target, for three different laser intensities.....61

Table 3-2. Estimated total charge emitted in the plasma plume, for a ZnO target, for two different laser intensities.....61

Table 3-3. A comparison between the measured values of ion energy (taken here to be the peak ion energy) and the ion energy calculated from a simple gas expansion model (Equations 3-17 and 3-18).....64

Table 3-4. Total energy of the ZnO plasma plume, resulting from fitting the data in Figure 3-24 to a cosine distribution.....69

Table 3-5. Total energy of the C plasma plume, resulting from fitting the data in Figure 3-23 to a cosine distribution.....70

Table 3-6. Summary of the fraction of ionization values integrated over all space, for three different intensities.....73

Table 3-7. Electron temperature for three different intensities incident on a carbon target, measured at different angles with respect to the target normal.....76

Table 3-8. Electron temperature for two different intensities incident on a zinc oxide target, measured at different angles with respect to the target normal.....76

Table 4-1. Estimated deflection angles for various ion species with various velocities.....100

Table 4-2. The number of protons with energies in the given range, calculated from the energy spectrum in Figure 4-18.....109

Table 4-3. The estimated total energy carried by the fast proton flux, for different angular distribution characteristics.....110

List of Figures

Figure 2-1. A schematic of a Langmuir probe used for ion detection.....4

Figure 2-2. A schematic of the probe current I vs. the bias voltage V for a typical Langmuir probe.....5

Figure 2-3. A schematic of the collection of the ion flux using a Langmuir probe, and the resulting ion signal.....6

Figure 2-4. An example ion current temporal profile generated using Equations 2-10 and 2-11.....8

Figure 2-5. Schematic diagrams of two ion detectors.....10

Figure 2-6. A schematic 1D representation of the electrostatic potential within the Faraday cup.....10

Figure 2-7. The geometry of the Faraday cup employed in the one-dimensional analytic model.....11

Figure 2-8. A schematic of the experimental setup used to generate ion signals.....14

Figure 2-9. The biasing circuit used to bias the detectors.....16

Figure 2-10. The transmission fraction (F) for different ion charge states (Z), keeping Zen_{pk} fixed, for four different values of Zen_{pk}.....17

Figure 2-11. Distorted waveforms calculated using the steady-state analytic model using different densities.....18

Figure 2-12. Distorted waveforms resulting from the OOPIC simulations, with different ion densities.....19

Figure 2-13. The transmission fraction (F) as a function of the peak ion density (n_{pk}), for both the analytic model and the simulations.....20

Figure 2-14. The transmission fraction (F) as a function of the ion peak velocity (v_{pk}).....21

Figure 2-15. The transmission fraction (F) as a function of the length of the Faraday cup (z_f). 22

Figure 2-16. The transmission fraction (F) as a function of the collector biasing voltage (ϕ_f) 23

Figure 2-17. Some typical signals recorded from individual laser shots.....25

Figure 2-18. A typical output waveform from the OOPIC simulations, for comparison purposes.....26

Figure 2-19. A typical output waveform from the OOPIC simulations, for comparison purposes.....27

Figure 2-20. A comparison between the transmission fraction vs. velocity trends for experiment, simulation, and analytical calculations.....28

Figure 2-21. The electrostatic potential profile within the Faraday cup, calculated from an OOPIC simulation.....29

Figure 2-22. Schematics for electron repulsion in Faraday cups. 30

Figure 2-23. Image taken from the two-particle simulation showing the penetration of the electrons into the interior of the Faraday cup.....31

Figure 2-24. Image taken from the two-particle simulation showing the effect of the presence of the electrons within the Faraday cup on the electrostatic potential.....32

Figure 2-25. Image taken from the two-particle simulation showing the penetration of the electrons into the interior of the Faraday cup.....33

Figure 2-26. Image taken from the two-particle simulation showing the effect of the presence of the electrons within the Faraday cup on the electrostatic potential.....33

Figure 2-27. An output waveform from the two-particle OOPIC simulations.....34

Figure 2-28. A typical output waveform from the two-particle OOPIC simulations, for comparison purposes. 35

Figure 2-29. A comparison between the transmission fraction vs. velocity trends for experiment, simulation (both one-particle and two-particle), and analytical calculations.....36

Figure 3-1. A schematic of pulsed laser deposition (PLD), used to deposit a thin film of material on a substrate. 39

Figure 3-2. A schematic of the experimental setup used to produce DLC films via PLD..... 41

Figure 3-3. A scanning electron micrograph of a DLC film grown via PLD.....42

Figure 3-4. Laser-matter interaction theory.....43

Figure 3-5. A schematic of the laser-matter interaction described by the self-regulating model due to Mora.....45

Figure 3-6. A schematic of the experimental setup for the nanosecond low incident intensity experiments.....49

Figure 3-7. An example digitized image of the laser spot on target, obtained using a filtered CCD camera.....50

Figure 3-8. A one-dimensional cross-section through the focal spot image, along the horizontal axis. 51

Figure 3-9. A one-dimensional cross-section through the focal spot image, along the vertical axis.....51

Figure 3-10. The results of the focal spot size measurements for the KrF laser using a 70 cm lens, performed using a filtered CCD camera.....52

Figure 3-11. A schematic intensity (I) profile along a spatial coordinate (x)..... 53

Figure 3-12. A typical ion signal collected by a Langmuir probe.....54

Figure 3-13. The angular distribution of the peak ion energy, for three different laser intensities incident on a carbon target. 55

Figure 3-14. The angular distribution of the peak ion energy, for two different laser intensities incident on a zinc oxide target.....56

Figure 3-15. The scaling of the peak ion energy with intensity for both carbon and zinc oxide, using the detectors positioned closest to the target normal (θ_p=6-7°) 57

Figure 3-16. The angular distribution of the peak current density, for three different laser intensities incident on a carbon target.....59

Figure 3-17. The angular distribution of the peak current density, for two different laser intensities incident on a zinc oxide target.....59

Figure 3-18. The angular distribution of the charge collected by the probes, for three different laser intensities incident on a carbon target.....60

Figure 3-19. The angular distribution of the charge collected by the probes, for two different laser intensities incident on a zinc oxide target. 60

Figure 3-20. The ion energy spectrum, calculated from the time-of-flight spectrum.....66

Figure 3-21. The angular distribution of the average ion energy, for three different laser intensities incident on a carbon target.....67

Figure 3-22. The angular distribution of the average ion energy, for three different laser intensities incident on a zinc oxide target.....67

Figure 3-23. The angular distribution of the total energy of the ions incident on the Langmuir probes.....68

Figure 3-24. The angular distribution of the total energy of the ions incident on the Langmuir probes.....69

Figure 3-25. A comparison of the conversion efficiencies observed in this experiment, and values reported by Y. Y. Tsui [Tsu92].....70

Figure 3-26. The angular distribution of the fraction of ionization of the total ablation plume, for three different laser intensities on a carbon target.....72

Figure 3-27. An example of the bias curve from a Langmuir probe used to extract T_e for a carbon plasma.....75

Figure 4-1. A schematic of the technique of chirped pulse amplification, used to achieve high laser intensities without causing damage to the laser amplifier.....78

Figure 4-2. A schematic of one proposal for the fast ignitor scheme for inertial confinement fusion.....79

Figure 4-3. A schematic of the preplasma plume.....81

Figure 4-4. Summary of the currently available data for fast ion scaling with laser irradiance.....85

Figure 4-5. A schematic of the experimental setup for plasma generation and fast ion detection in the femtosecond regime. 86

Figure 4-6. An image of the prepulse train which precedes the main pulse in the laser system. 87

Figure 4-7. The focused beam profile at low laser energy as measured using an infrared CCD camera (Ultrak K-500) with Spiricon LBA-400PC software.....88

Figure 4-8. Side view of the experimental geometry.....90

Figure 4-9. A schematic of the use of the PIN diode to capture the hot electron jet signal to ensure optimum focus of the laser beam on the target.....90

Figure 4-10. A typical focal scan using the PIN diode detector to monitor the hot electron signal.....91

Figure 4-11. Example Langmuir probe signals. 93

Figure 4-12. Example Langmuir probe signals, with (a) and without (b) target pre-cleaning.....95

Figure 4-13. Example Langmuir probe signals, with (a) and without (b) target pre-cleaning.....96

Figure 4-14. A schematic of the crude ion spectrometer used in the attempt to identify the various ion species present in the fast ion flux.....98

Figure 4-15. The magnetic field between the two bar magnets, measured along the ion trajectory.....98

Figure 4-16. The Langmuir probe signals exhibiting the deflected ion signals.....101

Figure 4-17. The Langmuir probe signals exhibiting the deflected ion signals.....102

Figure 4-18. Intensity scaling of the velocity corresponding to the peak of the fast proton signal. 103

Figure 4-19. Intensity scaling results for the ion energy (Equation 2-6) corresponding to the fast proton peak, from several different investigations under varying conditions.....104

Figure 4-20. Fitting the peak profile described by Equations 2-10 and 2-11 to the proton signal from a single laser shot.....106

Figure 4-21. The energy spectrum *N(E)* corresponding to the fitted temporal profile of Figure 4-20, for the fast protons.....108

Figure 4-22. A hypothesized angular distribution of energy carried by the proton flux.....110

Figure 4-23. The estimated average proton energy as a function of intensity, for both s- and p-polarized radiation.....111

Figure 4-24. The estimated total number of protons (N_p) striking the detector, as a function of intensity, for both s- and p-polarized radiation. 112

Figure 4-25. The estimated total energy carried by the fast protons striking the detector, as a function of the incident laser intensity, for both s- and p-polarized radiation.....113

Figure 4-26. The peak current density incident on the detector as a function of the laser intensity.. 114

Figure 4-27. The doping profile of energetic boron ions implanted into a silicon wafer.....116

Additional figures are included in the Appendix.

List of Symbols

A_{90} - focal spot area calculated according to the 90% contour method

A_{det} - probe area

a_h – hot electron scaling parameter

$\vec{B}$ - magnetic field

B_h – hot electron scaling parameter

c - speed of light

c_p - specific heat at constant pressure

c_s - ion acoustic velocity

D – thermal diffusivity

d_B - length of the particle trajectory within the magnetic field

d_L - lens-to-target distance

dm/dt- mass ablation rate

d_p – probe distance from laser focal spot

e - electron charge

E – ion kinetic energy

$\overline{E}$ - ion average energy

$\vec{E}$ - electric field

E_F - electric field of the laser pulse

E_{osc} – electron oscillation energy in optical field

E_L - laser energy on target

f – focal length of a lens

F – transmission fraction

$\bar{F}$ - Lorentz force

I - probe current

I_A - absorbed laser energy

I_{det} – detector current

I_e, I_i – electron and ion current

I_{e0} - electron current at the plasma potential V_p

$I_{incident}$ - ion current incident on the grid of a Faraday cup

I_L - laser intensity on target

I_{pk} - amplitude of the ion signal peak

I_r – radiation intensity

I_{se} - electron saturation current

I_{si} - ion saturation current

I_{tot} – inflated ion current, due to secondary electron emission

$\bar{J}$ - current density

J_i – ion current density

k_B - Boltzmann's constant

$\ln \Lambda$ – Coulomb logarithm

L_{pre} - plasma scale length due to prepulse

m – general particle mass

m_e - electron mass

m_i – ion mass

n – the value of the exponent in a cos^n distribution

$N(E)$ – ion energy spectrum

n_0 - particle density at the entrance of the Faraday cup

n_c - critical density of a plasma

n_e, n_i – electron and ion density

N_i – total number of ions

N_p - number of protons

p – pressure

p_1, p_2 - temporal fitting parameters in the modified Gaussian function

p_A - ablation pressure

q – general particle charge

Q - heat source

r – radial coordinate, in cylindrical coordinate system

t - time

T – temperature

T_e - electron temperature

T_{grid} - transmission of the grid of a Faraday cup

T_h - hot electron temperature

t_{pk} - temporal location of the ion signal peak

U_i - ionization energies

V - bias voltage

$v_\perp$ - perpendicular velocity component

v_∞ - ion terminal velocity

v_0 - particle velocity at the entrance of the Faraday cup

v_e, v_i - electron and ion velocity

v_f - fluid velocity

v_{osc} – detector voltage, as measured on an oscilloscope

V_p - the plasma potential

v_{pk} - velocity of the ions arriving at the peak of signal

x – distance coordinate

x_0 - the point at which the laser radiation has been attenuated by a factor exp(-2)

$\overline{Z}$ - average charge state of the ions

z - longitudinal dimension

z_0 - Rayleigh range

z_f – grid to collector spacing in a Faraday cup

α_{IB} - absorption coefficient for inverse Bremmstrahlung absorption

γ - effective heat capacity ratio

$\gamma_{eff}(v)$ - effective secondary electron emission coefficient

ΔH_{fus} - energy required to change states, from solid to liquid

ΔT – change in temperature of a target due to heating by the laser pulse

ε_0 - permittivity of free space

ϕ - electrostatic potential

ϕ_f - collector biasing voltage

κ - thermal conductivity

λ_D - Debye shielding length

λ_L – laser radiation wavelength

μ_0 - permeability of free space

θ_{def} – angle of deflection

θ_{inc} - laser angle of incidence on target (measured with respect to the target normal)

θ_p – probe angle (measured with respect to the target normal)

ρ - mass density

ρ_q - charge density

σ_1. σ_2 – temporal fitting parameters in the modified Gaussian function

$\tau_{e\text{-}e}$ - electron-electron collision time constant

$\tau_{e\text{-}ph}$ - electron-phonon collision time constant

τ_L – laser pulse duration

ω - beam waist; the diameter at which the beam intensity drops to exp(-2) of its peak value)

ω_0 - beam waist at the position of best focus

Note: SI units are used throughout, unless otherwise noted.

Chapter 1
Introduction

Laser-produced plasmas have been a rich area of experimental physics for several decades. Despite years of effort, investigators delving into the physical laws governing laser-matter interactions still have much to learn. Part of the complexity can be attributed to the diversity of laser systems, capable of producing a wide range of pulse energies and pulse durations, and therefore, a wide range of laser intensities. Researchers have come to understand that the behavior of laser-produced plasmas can vary dramatically depending on these laser parameters. One of the most important parameters is the laser intensity.

At low incident laser intensities (roughly $<10^6$ W/cm^2, depending on the target and the laser parameters [Bau00]), the laser essentially acts as a heat source. The absorbed laser energy causes an increase in the local temperature of the target. As the laser intensity increases ($\sim10^7$ W/cm^2), the absorbed energy is sufficient to cause a change of state in the target material, from a solid to a liquid. As the intensity increases further ($\sim10^8$ W/cm^2), the target material is vaporized. This hot gas will expand, producing an outward flux of neutral target particles and clusters of particles. A small number of the target particles may become ionized via collisions or other causes. The vaporized target material thus consists of a mixture of neutral particles, ions and electrons. As the incident laser intensity increases further ($\sim10^8$-10^9 W/cm^2), an increasing number of particles in the plume of target material will become ionized. Eventually, when the laser intensity is sufficient, the plasma plume is fully ionized (roughly $>10^9$ W/cm^2, depending on the pulse length). The charged particles present in the plasma plume may reach fairly high energies (several hundred electron-Volts or more). The characteristics of plasmas produced in the 10^{11}-10^{14} W/cm^2 intensity regime are fairly well-understood; theoretical models developed to describe the laser-matter interaction have been well-supported by experiments in this intensity regime (see Chapter 3). Since the advent of ultrashort laser pulses and the chirped pulse amplification compression scheme (see Chapter 4), laser intensities have increased significantly. As the laser intensity increases beyond 10^{14} W/cm^2, the temperature of the laser-produced plasma will further increase, and the ions will be emitted with increasing energy. Eventually, at intensities above 10^{18} W/cm^2, electrons will emerge from the coronal plasma with relativistic velocities. Experiments at these intensities have allowed researchers to access new areas of physics.

Although interesting from a physics perspective, research in the field of laser-produced plasmas is largely driven by the diverse array of potential applications. In particular, the energetic charged particles emitted from laser-produced plasmas can be utilized in various contexts. This ion emission can be used to create thin films (Chapter 3), ignite a fusion pellet, kill cancerous cells, or dope a semiconductor (Chapter 4). Important to all of these applications is a proper understanding and characterization of the ion emission.

The purpose of this work is to measure and characterize the ion emission from nanosecond and femtosecond laser-produced plasmas. It is expected that

these results will facilitate the use of this ion emission for specific applications such as pulsed laser deposition and ion implantation. More generally, it is hoped that this contribution to the body of knowledge of ion emission from laser-produced plasmas will enable a better understanding of the physical laws underlying laser-matter interactions.

In Chapter 2, the issue of ion detectors is discussed. In particular, the space charge effect of the Faraday cup ion detector is investigated and characterized. Although the space charge effect has been recognized and characterized since 1970, it is discovered that the analytical model developed in 1970 is actually insufficient to describe the physical situation. In this chapter, a more accurate physical picture of the operation of a Faraday cup is elucidated. The selection of an appropriate detector to characterize the ion emission of nanosecond and femtosecond laser-produced plasmas is also discussed.

In Chapter 3, the nanosecond regime is investigated, using laser intensities in the range 10^8-10^{10} W/cm^2. In these experiments, the laser intensity profile varies over the laser focal spot area on target, as well as over the temporal duration of the pulse, so that while the peak intensity on target may be sufficient to create a fully ionized plasma plume, the lower intensity portions of the intensity profile create a neutral particle-dominated vapor plume. In addition, the shock wave driven into the target melts and vaporizes the target, and results in the emission of neutral particles, clusters of neutral particles, and nanoparticles. The total ablation plume thus consists of these two components. In terms of the observed behavior of the ablation plume, this work occupies a position between the neutral particle-dominated vapor plumes produced at ~10^8 W/cm^2, and the fully ionized plasma plumes produced above ~10^9 W/cm^2. Thus, the ablation plume which is investigated is a complex mix of neutral particles, ions, and electrons. In an effort to understand the ion component of the plume, the energy of the ion emission and the emitted charge are measured at various intensities with different targets. Additionally, the angular distribution of these quantities is characterized. Furthermore, the electron temperature of the laser-produced plasma at various incident intensities is measured. Theoretical models exist which successfully describe the laser-matter interaction at intensities in the range 10^{11}-10^{14} W/cm^2. The applicability of these models to the 10^8-10^{10} W/cm^2 intensity regime is also evaluated. This investigation is pertinent to the technique of pulsed laser deposition, in which the characteristics of the deposited film depend heavily on the characteristics of the particles emitted from the laser-produced plasma.

In Chapter 4, the femtosecond regime is investigated, using laser intensities in the range 10^{14}-10^{16} W/cm^2. In terms of intensity, this work occupies a position between the relatively well-understood 10^{12}-10^{14} W/cm^2 range, and the recently heavily studied relativistic regime (>10^{18} W/cm^2). In this transition regime, the observation of the emission of especially energetic ions has motivated an attempt to characterize this emission. In particular, the scaling of the ion energy with incident laser intensity is investigated. The total emitted charge and the proportion of the laser energy carried by these energetic ions are both

estimated. Finally, the feasibility of the application of the ion emission for ion implantation is discussed.

Chapter 2
Ion Detection

Background

Before the characterization of ion emission from laser-produced plasmas is attempted, the issue of ion detection must be addressed. For decades, investigators have studied particle fluxes in various experimental contexts using a variety of detectors, such as the microchannel plate [Dec02, Pan76, Str99], the Langmuir probe [Amo04, Cla02, Cla03, Che65, Hav03, Hut02, Las03, Nov99], and the Faraday cup [Amo97, Cla01, Cla03, Gup87, Koi99, Las03, Mis99, Pea77, Pel76, Qia95]. The simplest of these is the Langmuir probe.

a) Langmuir Probes

The Langmuir probe is a biased conductor used to intercept the ion flux emitted from the laser-produced plasma. A schematic of the detector is given in the figure below.

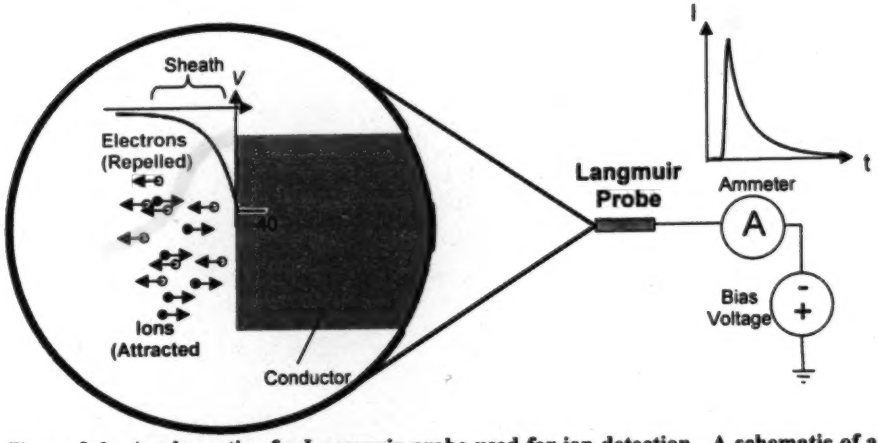

Figure 2-1. A schematic of a Langmuir probe used for ion detection. A schematic of a typical ion current signal from a laser-produced plasma is also depicted.

The theory of the Langmuir probe is now described in some detail. The existence of a sheath region (depicted in the figure above) is a consequence of the general plasma property that the plasma constituents will behave in such a way as to shield electrostatic disturbances and maintain a quasineutral, field-free configuration in the bulk of the plasma. This behavior is reminiscent of the behavior of conductors in external electric fields. The plasma shielding phenomenon is described by a characteristic length over which the disturbance in the electrostatic potential decays, called the Debye shielding length λ_D [Che74]:

$$\lambda_D = \sqrt{\frac{\varepsilon_0 k_B T_e}{n_e e^2}}, \qquad \text{(2-1)}$$

where ε_0 is the permittivity of free space, k_B is Boltzmann's constant, T_e is the electron temperature, n_e is the electron density, and e is the electron charge. This decay is depicted schematically in the figure above: outside of the sheath region, the electric field is zero and the plasma is quasineutral.

Now, the current measured by the probe consists of two components: the electron current I_e and the ion current I_i. The electron current is given by

$$I_e = -eA_{det}n_e v_e \qquad \text{(2-2)}$$

and the ion current is given by

$$I_i = \overline{Z}eA_{det}n_i v_i, \qquad \text{(2-3)}$$

where $\overline{Z}$ is the average charge state of the ions, A_{det} is the probe area, n_i is the ion density, and v_e and v_i are the particle speeds. Because of the discrepancy in the ion and electron masses, for identical ion and electron temperatures, the electron speed is much higher than the ion speed, and thus the electron component of the current usually dominates. Now, by manipulating the bias voltage of the probe, either the electron current or the ion current can be selectively excluded (Figure 2-2).

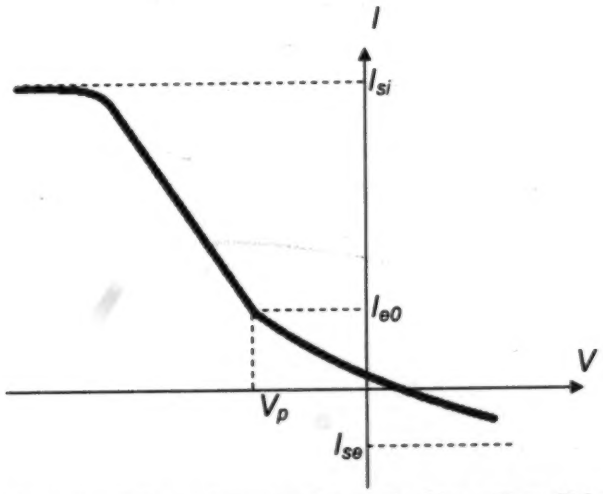

Figure 2-2. A schematic of the probe current I vs. the bias voltage V for a typical Langmuir probe. I_{se} is the electron saturation current, I_{si} is the ion saturation current, and I_{e0} is the electron current at the plasma potential V_p.

If the probe voltage is equal to the (unknown) plasma potential, both the electron current and the ion current are approximately unperturbed, so that the probe records both current contributions. If the probe voltage is lower than the plasma potential, the electron current is partially repelled. If the probe voltage is lowered further, only the ion current is collected. This is referred to as the ion saturation region. On the other hand, if the probe voltage is higher than the plasma potential, the relatively small ion current is repelled by the probe, and the probe measures only the electron current. This regime is called the electron saturation region. Detailed considerations based on the continuity equation and Laplace's

equation result in the following equation which governs part of the I-V characteristic:

$$I_e = I_{e0} \exp\left(\frac{e(V - V_p)}{k_B T_e}\right) \quad V < V_p \,, \quad \text{(2-4)}$$

where I_e is the electron current, T_e is the electron temperature of the plasma flux incident on the probe, and I_{e0} is the electron current at the plasma potential V_p. Note that the electron temperature in the plasma plume evolves as the plasma expands and cools, and thus, the measurement of T_e depends on the position of the detector. Assuming the plasma is reproducible on a pulse-to-pulse basis, the I-V characteristic can be built up point-by-point by performing a bias voltage scan. By plotting the I-V data on a semi-logarithmic graph, the data can be fitted to the above equation and the electron temperature of the plasma at a particular point in space can be obtained [Hut02, Koo71]. This procedure is carried out for the nanosecond laser-produced plasma investigated in Chapter 3.

Now, if the probe is biased such that it collects only the ion saturation current, the probe signal will resemble the schematic given in the figure below. For the majority of the experiments described in Chapters 3 and 4, detectors biased at -40 V were used, which was found to be sufficiently negative to ensure that only the ion current is collected.

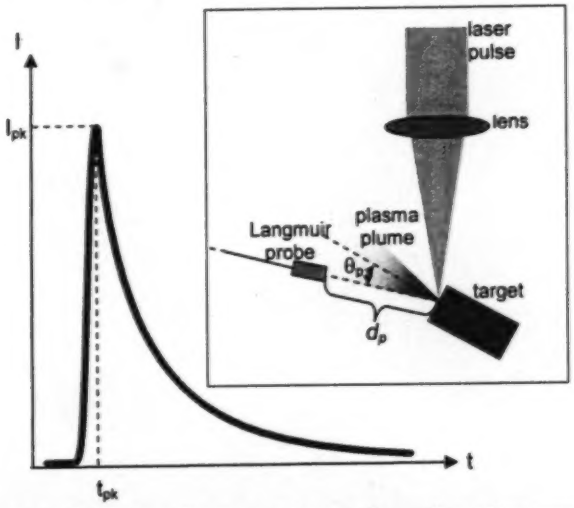

Figure 2-3. A schematic of the collection of the ion flux using a Langmuir probe, and the resulting ion signal. The probe is positioned at an angle θ_p (measured with respect to the target normal) and located a distance d_p from the laser focal spot.

Based on the time of flight of the ions, the velocity corresponding to a specific group of coincident ions in the signal can be calculated. The temporal velocity distribution of the ions within this signal is given by

$$v(t) = \frac{d_p}{t} = \frac{v_{pk} t_{pk}}{t}, \quad \text{(2-5)}$$

where v_{pk} represents the velocity of the ions arriving at the peak of signal. The velocity of an ion arriving at the detector is related to its kinetic energy (E) as follows: for an ion of mass m_i,

$$E = \frac{1}{2} m_i v^2 . \quad \text{(2-6)}$$

Using these equations, the ion energy spectrum can be calculated from the ion time-of-flight spectrum. Additionally, because the probes are typically terminated using a 50 Ω resistor (see Figure 2-9), the probe voltage (V) can be related directly to the ion current (I_i) incident on the probe:

$$I_i(t) = \frac{V(t)}{50\Omega} . \quad \text{(2-7)}$$

Integration of $I_i(t)$ yields the total charge collected by the detector. Of course, the current density $J_i(t)$ follows immediately:

$$J_i(t) = \frac{I_i(t)}{A_{det}} , \quad \text{(2-8)}$$

where A_{det} is the area of the detector. The above equations are used extensively in Chapters 3 and 4.

Additionally, the current amplitude is related to the peak velocity and peak density by (Equation 2-3)

$$I_{pk} = ZeA_{det} n_{pk} v_{pk} , \quad \text{(2-9)}$$

where Ze is the ion charge, and A_{det} is the area of the detector. This equation is used extensively in the analysis of the experimental results in this chapter.

Lastly, it is noted that in several instances (in Chapters 2 and 4), it will be necessary to model a typical Langmuir probe signal. The typical ion signal $I_i(t)$ is well-approximated by a two-piece modified Gaussian function, as follows:

$$I(t) = I_{pk} \exp\left[-\left| \frac{t - t_{pk}}{\sigma} \right|^p \right], \quad \text{(2-10)}$$

where

$$\sigma = \begin{cases} \sigma_1 & t < t_{pk} \\ \sigma_2 & t \geq t_{pk} \end{cases} \text{ and } p = \begin{cases} p_1 & t < t_{pk} \\ p_2 & t \geq t_{pk} \end{cases} , \quad \text{(2-11)}$$

are temporal fitting parameters, t_{pk} is the temporal location of the signal peak, and I_{pk} is the amplitude of this peak. An example of this temporal profile is given in the figure below.

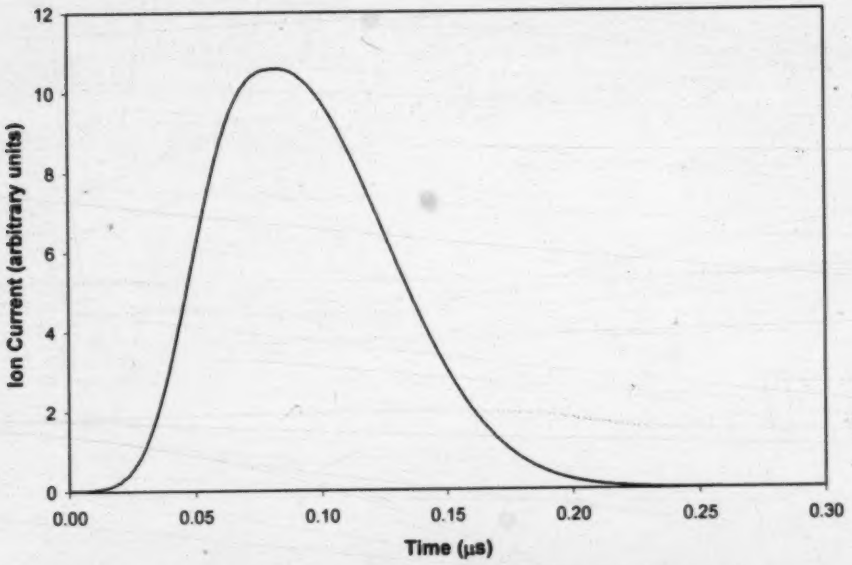

Figure 2-4. An example ion current temporal profile generated using Equations 2-10 and 2-11. The temporal parameters are as follows: σ_1=40 ns, σ_2=60 ns, p_1=3, p_2=2, and t_{pk}=82.8 ns.

Although the Langmuir probe is a versatile and useful tool in plasma diagnostics, it does have its limitations. The most significant drawback to the use of a Langmuir probe for detection of ion emission from laser-produced plasmas is its susceptibility to signal distortion due to secondary electron emission [Ben95, Sch80]. Secondary electron emission arises when energetic particles strike a metal surface and impart energy (via collisions) to electrons in the metal. Given sufficient energy, these secondary electrons may escape the metal surface. The Langmuir probes used in the present work are made of copper, and are used to detect energetic ions. Incident ions striking the copper surface may cause the emission of secondary electrons. This emission of negatively charged particles away from the copper face of a Langmuir probe registers as a positive current, and thus represents a distortion of the true signal. Fortunately, several previous studies have characterized and quantified the secondary electron emission under conditions which are similar to the experimental conditions of the present work. It was found that the total current $I_{tot}(t)$ registered by the detector is inflated by secondary electron emission according to the equation

$$I_i(t) = \frac{I_{tot}(t)}{1+\gamma_{eff}(v)}, \qquad \textbf{(2-12)}$$

where $I_i(t)$ is the true ion current, and $\gamma_{eff}(v)$ is the effective secondary electron emission coefficient, which generally varies with the incident ion velocity [Bad01].

The nanosecond experiments described in this chapter and the next took place at low laser intensities. For these low laser intensities, the ions emitted from

the laser-produced plasmas are of modest energy; the average ion velocities are always less than $5x10^4$ m/s or 13 eV/A.M.U. (see Chapter 2 and Chapter 3 results below). For this range of relatively small velocities, it is generally assumed that secondary electron emission is small; that is, $\gamma_{eff}(v)<<1$. This assumption has probably been implicitly made by all of the other groups who have reported results in the nanosecond low intensity (10^8-10^{10} W/cm^2) regime. Thus, in the results presented in Chapters 2 and 3, no corrections for secondary electron emission have been made.

On the other hand, for the femtosecond regime (Chapter 4), the ions emitted from the laser-produced plasmas are of considerable energy; peak ion velocities can range from ~0.2-1.2x10^6 m/s (0.2-7.5 keV/A.M.U., see Chapter 4 results below). At these energies, secondary electron emission cannot be neglected. Fortunately, a previous study can be used to quantify the secondary electron emission under these conditions. In 1976, R.R. Goforth performed a study of secondary electron emission due to energetic protons incident on a brass target and found that $\gamma_{eff}(v)$~3 for protons with velocity ranging from 0.25-1.4x10^6 m/s (0.3-10.2 keV/A.M.U.) [Gof76]. This value for the secondary electron emission coefficient is independent of velocity, within the 20% measurement uncertainty of Goforth's experiment. The Langmuir probes used in this work are composed of copper, and it is noted that brass is mostly composed of copper (typically ~60-90%). Furthermore, the range of velocities used in the secondary electron experiment nearly overlaps the range of proton velocities observed in the experiments of the present work. For these reasons, the value $\gamma_{eff}(v)$~3 is used in the analysis for protons. For heavier ions, $\gamma_{eff}(v)$~0.9 is a more appropriate value [Gof76]. All of the results in Chapter 4 have been corrected for secondary electron emission. At the same time, the reader must bear in mind the uncertainty inherent in this correction; previous studies have indicated that secondary electron emission is dependent on the precise surface condition [Ben95].

It must be noted that the validity of the assumption $\gamma_{eff}(v)<<1$ for the nanosecond regime is unknown. If true, it would seem that the secondary electron emission coefficient for heavier ions increases from nearly 0 at ion velocities near $5x10^4$ m/s to 0.9 at ion velocities of $2x10^5$ m/s or greater. This may be possible, but the increase seems abrupt. Thus, it is possible that secondary electron emission has some influence on the results of the experiments in this chapter and the next. In any case, it is clear that this issue requires further investigation.

b) Faraday Cups

The problem of the uncertainty in correcting for secondary electron emission in Langmuir probe signals can be solved by using deep-cup detectors [Pea77, Pel76]. These so-called Faraday cup ion detectors dramatically reduce secondary electron emission using a deep cup geometry (Figure 2-5b).

Figure 2-5. Schematic diagrams of two ion detectors. a) A schematic of a simple Langmuir probe, which consists of a conducting tip, usually made of copper. b) A schematic of a Faraday cup detector, in which the recession of the conducting face of the probe (henceforth referred to as the collector) allows the recapture of emitted secondary electrons.

The Faraday cup consists of a grounded grid at the entrance of the detector, and a collector at the end of the detector. The grid serves as a reference potential, provided that the grid spacing is less than the Debye shielding length (Equation 2-1). The collector is normally biased at a negative voltage, and serves to collect the ion signal.

These detectors continue to be widely used in the investigation of laser-produced plasmas [Amo97, Cla01, Cla03, Koi99, Las03, Mis99, Qia95]. The generally accepted model of Faraday cup operation is now described. Consider a plasma flux, consisting of ions and electrons, incident on the Faraday cup. It is believed that if the collector is biased sufficiently negatively, the electron flux is repelled at the grounded grid. The ions enter the cup, and reach the collector, generating a current signal. Any secondary electron emission from the collector surface is likely to be recaptured by the walls of the cup. Thus, the influence of secondary electron emission is reduced to negligible levels by the deep-cup geometry. The limitation of the cup was recognized and characterized in 1970, by T. S. Green [Gre70]. Due to the presence of a significant number of ions, a very large positive space charge accumulates inside the cup. If the space charge is sufficiently strong, additional arriving ions will be repelled and the cup signal is said to be distorted by space charge effects. Green constructed an analytic model describing the behavior of the ions inside the cup, and derived a condition to ensure that space charge distortion is avoided. In the present investigation, it has been found that the generally accepted model of Faraday cup operation is inadequate.

A proper physical understanding of the space charge distortion phenomenon is crucial. The most important physical quantity to consider is the electric potential ϕ (Figure 2-6).

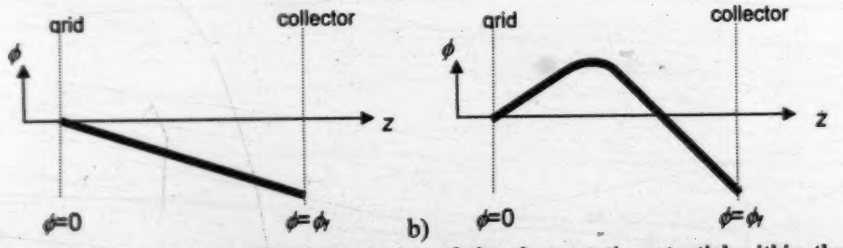

Figure 2-6. A schematic 1D representation of the electrostatic potential within the Faraday cup: a) in the absence of ions; b) in the presence of a significant number of ions.

In the absence of ions, the potential is a solution of Laplace's equation, and is a straight line joining the boundary conditions. When small numbers of ions are present, the potential is perturbed from its original state. As the space charge within the cup increases, a potential barrier forms and subsequently prevents the transmission of ion flux through to the collector. This barrier gives rise to the distortion of the observed signals.

In work performed by D. G. Redman [Red02], a 1D analytical model of a pulse of ions incident on a Faraday cup detector was developed. This model duplicates and expands upon the earlier work of T. S. Green [Gre70]. Using this model, the relationship between the parameters of the ion pulse and the resultant distortion of the observed signal can be described. Two-dimensional simulations of a pulse of ions incident on a Faraday cup detector were also performed. Finally, experiments using a Faraday cup to detect the ion flux from a laser-produced plasma were performed. The comparison of these three approaches yields useful insights into the important parameters governing this phenomenon. It is found that the generally accepted model of Faraday cup operation is inadequate to describe the space charge distortion phenomenon.

Methods

a) Analytical Model

The one-dimensional analytic model of the Faraday cup is depicted in the figure below.

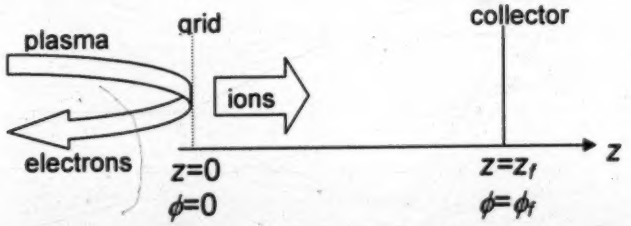

Figure 2-7. The geometry of the Faraday cup employed in the one-dimensional analytic model. Note the (negative) biasing of the collector, resulting in the repulsion of incident electrons and the attraction of incident ions.

The model assumes that the electron flux is repelled at the grid, so the only species present within the cup is the ions. The model was developed using Gauss' Law, the conservation of energy, and the continuity equation:

$$\frac{d^2\phi}{dz^2} = -\frac{Ze}{\varepsilon_0} n, \quad \textbf{(2-13)}$$

$$v^2 = v_0^2 - \frac{2Ze}{m_i}\phi, \quad \textbf{(2-14)}$$

$$\frac{d}{dz}(n,v) = 0, \quad \textbf{(2-15)}$$

where z is the longitudinal dimension, ϕ is the potential, and v_0 is the particle velocity at the entrance of the detector. The ion mass used is that of carbon.

It was assumed that the distribution of ions within the detector was at steady state. This steady-state assumption is valid as long as the ion temporal profile varies slowly over the ion transit time; that is,

$$\frac{z_f}{v_{pk}} << \sigma_1 \quad and \quad \frac{z_f}{v_{pk}} << \sigma_2 , \qquad \textbf{(2-16)}$$

where z_f is the length of the detector in Figure 2-7. The distortion of the ion flux due to space charge effects is characterized by the deviation of the ion flux reaching the detector (I_i) from the ion flux incident on the grid ($I_{incident}$). The effect of the grid transmission (T_{grid}) is also accounted for. The ratio of the two quantities (integrated over time) is referred to as the transmission fraction F:

$$F = \frac{\int I_i(t)dt}{T_{grid}\int I_{incident}(t)dt} . \qquad \textbf{(2-17)}$$

b) Simulation

The simulations were performed using a commercially available object-oriented particle-in-cell code called OOPIC Pro [Bru01, Ver95]. Previously, researchers relied upon hydrodynamic codes to describe the plasma as a fluid, using the fluid equations [Che74]. This fluid treatment was considered adequate for lower laser intensities. As the laser intensity increases, individual particles in the plasma reach higher velocities, and the approximations inherent in the fluid approach break down. In this intensity regime, plasma modeling requires a kinetic approach, in which the particle distribution function is used to describe the plasma [Che74]. Particle-in-cell (PIC) codes model the plasma as a collection of charged particles, and the particle distribution function contains all relevant information about the plasma. Due to computational constraints, the ratio of physical particles to numerical particles is large (typically 10^4-10^6), but generally, the number of numerical particles is still sufficient to model the statistical behavior of the physical particles. In OOPIC, the fields are calculated on a fixed mesh by applying Maxwell's equations [Bra04],

$$\bar{\nabla}\cdot\bar{E} = \frac{\rho_q}{\varepsilon_0}, \qquad \textbf{(2-18)}$$

$$\bar{\nabla}\cdot\bar{B} = 0, \qquad \textbf{(2-19)}$$

$$\bar{\nabla}\times\bar{E} = -\frac{\partial\bar{B}}{\partial t}, \qquad \textbf{(2-20)}$$

$$\bar{\nabla}\times\bar{B} = \frac{\bar{J}}{\mu_0} + \mu_0\varepsilon_0\frac{\partial\bar{E}}{\partial t}, \qquad \textbf{(2-21)}$$

where $\bar{E}$ is the electric field, $\bar{B}$ is the magnetic field, ρ_q is the charge density, $\bar{J}$ is the current density, μ_0 is the permeability of free space, and ε_0 is the permittivity of free space. The position and velocity distribution of the numerical particles is used to calculate the charge and current distributions. The fields are then applied

to the numerical particles using the Lorentz force equation and Newton's second law,

$$m\frac{d\vec{v}}{dt} = q\left(\vec{E} + \vec{v} \times \vec{B}\right), \quad \textbf{(2-22)}$$

where q is the particle charge, m is the particle mass, and v is the particle velocity. The particles are then moved to their new positions, the charge and current distributions are recalculated, the fields are computed once more, and the simulation advances. OOPIC Pro is a two dimensional PIC code which can employ a variety of time-dependent methods for generating particles, and can handle a variety of time-dependent boundary conditions. Additionally, a variety of diagnostics are available to the user, including phase space plots for each species of particle.

In this investigation, electrostatic simulations were used, since the relevant phenomena were adequately described without resorting to solving the full set of Maxwell's equations. A cylindrical geometry was used, with 100 cells in the longitudinal (z) direction and 5-6 cells in the radial (r) direction. These computational parameters were tested, and it was found that the number of cells in the radial dimension was not a critical factor. Thus, for the purposes of computational efficiency, only 5-6 cells were used in the radial direction. In order to accurately produce the desired temporal profile of the ion signal, the ion signal is discretized into 200-400 individual ion pulses, each with a single amplitude and velocity. Combined, these individual pulses adequately represented the amplitude and velocity distribution of the desired ion signal. For simplicity, the particle temperature was assumed to be zero. The ion mass used was that of carbon. The ion charge state is another important parameter. However, the relevant phenomena are described adequately by Gauss' Law, which is sensitive only to the combined variables Zen_{pk}. In the experiments, analytical calculations, and simulations, a value of Z=1 was used, with the assumption that the truly relevant quantity is the combined variable Zen_{pk}. The validity of this assumption will be discussed in the next section. The input files for the OOPIC Pro simulations are included in the Appendix.

By performing a series of simulations with varying computational parameters (chiefly, varying the timestep of the simulation and the ratio of numerical particles to physical particles), the numerical error in the simulation results was estimated to be ± 2%. This estimate is assumed to apply to all the simulation results in this chapter, although error bars are not included in any of the graphs for the purposes of clarity.

c) Experiment

Experimentally, the operation of the Faraday cup detector can be tested using the ion flux emitted from a laser-produced plasma. For an extensive description of the theory underlying the emission of charged particles from laser-produced plasmas, see Chapter 3. A schematic of the experimental setup is given in the figure below. The experiments were performed using a Lumonics Excimer-500 KrF laser, which provided a laser energy of E_L=70-80 mJ on target, with a pulse duration of τ_L=15 ns, at a laser wavelength of λ_L=248 nm.

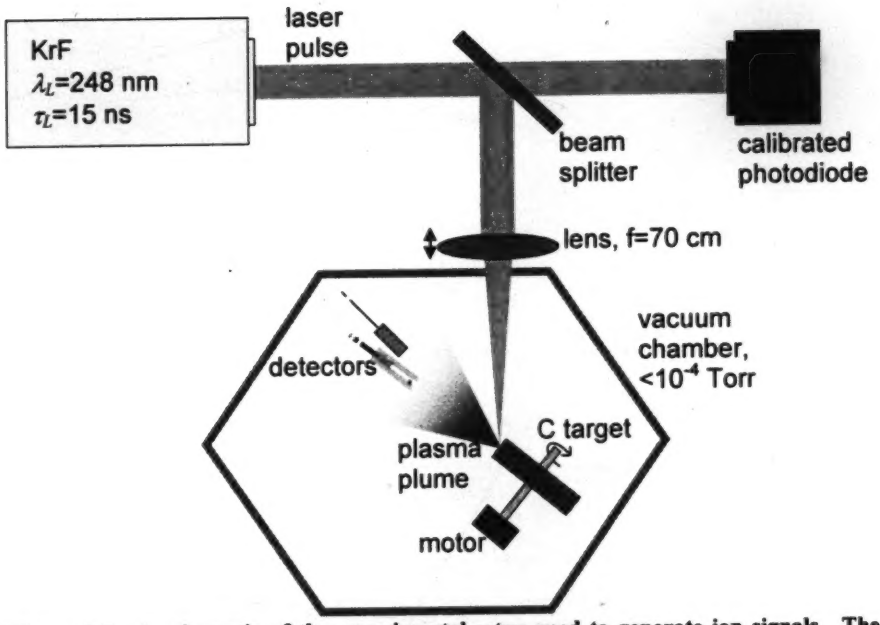

Figure 2-8. A schematic of the experimental setup used to generate ion signals. The Faraday cup and Langmuir probe are positioned symmetrically with respect to the target normal, located at identical distances and identical angles. The quoted distance values from the Faraday cup to the target are measured from the collector of the cup.

The laser was operating in the unstable resonator configuration, producing an unpolarized multimode rectangular beam [Sal91]. The laser pulses were focused onto the target using a planoconvex lens with a 70 cm focal length, located 3 m away from the laser output. The lens-to-target distance (d_L) was variable, and this provided a means to control the laser spot size (and thus the laser intensity) on target. By manipulating the laser intensity, the velocity of the particles arriving at the detector could be controlled [Git86]. Since the ion velocity is the main parameter of interest, the measurement or calculation of the laser intensity is not discussed here. For a complete discussion of the laser intensity on target, see Chapter 3.

The target was a solid graphite disk, which was rotated using a DC motor in order to provide a fresh target area for each laser pulse. The angle of incidence of the laser pulses on target was approximately 40° (with respect to the target normal). The vacuum chamber pressure was typically less than 1×10^{-4} Torr (measured using an Edwards Active Magnetron Gauge, AIM-S-NW25), which is sufficiently low to ensure that the target particle flux reaches the ion detectors.

For ion detectors, a Langmuir probe (consisting of a bare copper surface, with diameter 6.35 mm) and a Faraday cup were used. The Faraday cup contains a 400 mesh (37 μm grid spacing, transmission 0.27 ± 0.03) serving as the grid. The grid transmission was calculated from its geometry (measured using an

optical microscope), and also measured directly (by passing a laser beam through the grid). The average of the two results was taken as the grid transmission value. The grid must be chosen such that the plasma electrons incident on the detector cannot shield out the grid potential. To estimate the Debye shielding length at the grid for the experimental conditions, the results of this chapter and Chapter 3 are used. According to the results of the next section, the electron density incident on the grid is n_e=1.4x10^{17} m^{-3} (which corresponds to 3.7x10^{16} m^{-3} inside the cup, when accounting for the grid transmission). According to the results of Chapter 3 (Table 3-7), the electron temperature of a carbon plasma produced by a laser intensity of 1.9x10^{10} W/cm^2 measured at a distance of 18 cm from the target and an angle of 17° (measured with respect to the target normal) is 8 ± 4 eV. Keep in mind that the detector distance in the present experiment is 22 cm, so that the electron temperature of the plasma incident on the grid is likely lower (see Chapter 3). On the other hand, the detectors are positioned closer to the target normal in the present experiment (5°), and according to the trend of Table 3-7, the electron temperature may be higher as a result (see Chapter 3). Thus, using Equation 2-1, assuming an electron density of n_e=1.4x10^{17} m^{-3} and assuming the electron temperature to be T_e=4 eV, the Debye shielding length is 39.8 μm. In other words, the grid potential is shielded out at distances greater than 39.8 μm away from the grid wires. Since the grid wires are spaced 37 μm apart, all particles passing through the grid will pass within 18.5 μm of a grid wire, which is shorter than the Debye shielding length. Thus, it appears that the incident electrons are unable to shield the grid potential. This estimate is based on the characteristics of the electrons at the signal peak. It is noted that the electron temperature is likely to be smaller at later times in the ion signal, so that the electrons may be able to shield out the grid potential at these later times. Thus, some proportion of the electrons may be able to enter the cup during the tail end of the ion signal. This possibility is discussed further in the next section.

The Faraday cup also contains a copper conductor serving as the collector, separated from the grid by z_f=1.75 mm. The diameter of the aperture at the entrance of the Faraday cup was 3.18 mm. The dimensions of the Faraday cup were chosen to ensure that the behavior of the ion beam within the cup was approximately one-dimensional, as estimated by simple calculations supported by the simulation results. This design was intended to enable comparison of the experimental results with the analytical model, which is one-dimensional.

The detectors were located 22 cm from the target, in the plane of the incident laser pulse, at identical angles of 5° (with respect to target normal). The detectors were biased at -40 V, using the biasing circuit depicted in the figure below. The detectors were terminated with 50 Ω resistors, and the ion signals were displayed using Tektronix TDS 210/220 oscilloscopes.

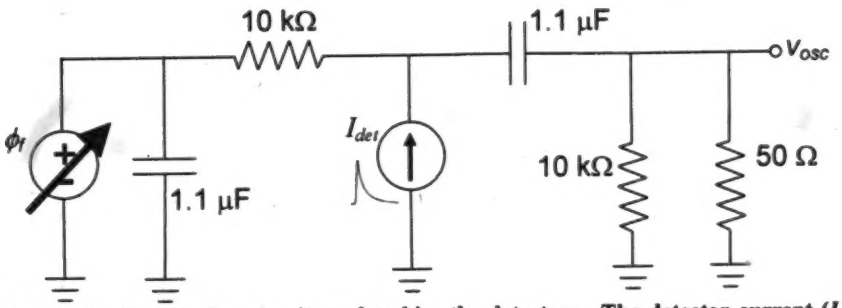

Figure 2-9. The biasing circuit used to bias the detectors. The detector current (I_{det}) passed through a 50 Ω resistor, and the corresponding voltage (v_{osc}) was measured using an oscilloscope. The biasing voltage (ϕ_f) was set to -40 V for the duration of the experiment.

The symmetrical positioning of the two detectors facilitates the comparison of their signals. The Langmuir probe is assumed to capture the undistorted ion signal. In order to analyze the experimental results, Equations 2-7 and 2-17 above were used to calculate the transmission fraction corresponding to a given laser shot. Additionally, Equations 2-5, 2-7, and 2-9 were used, with Z=1, to calculate the peak velocity and peak density of the ion flux incident on the detectors. These values were then employed in simulations performed in an attempt to reproduce the experimental results.

Results and Discussion

a) Analytical Model and Simulation Results

The central result of the analytical model developed by D. G. Redman [Red02] is the emergence of a criterion which is useful in determining whether or not space charge distortion will occur in a given situation. The criterion is as follows: if

$$\frac{2}{3}\left[\frac{\varepsilon_0 m v_0^2}{2Z^2 e^2 n_0}\right]^{1/2} > z_f \text{ , (2-23)}$$

where n_0 and v_0 represent the ion density and velocity at the grid, then the current signal will remain undistorted. This criterion is exactly equivalent to the condition first derived by T. S. Green in 1970 [Gre70]. Recall that the analytical model rests on the assumption of steady state, so if the condition above is satisfied for all times during the ion current profile $I(t)$, then the ion current will remain undistorted. In practice, this criterion is more useful as a guideline, and the user can replace $n_0 \sim n_{pk}$ and $v_0 \sim v_{pk}$.

Qualitatively, this criterion is consistent with the physical interpretation of the space charge phenomenon. As the kinetic energy of the individual ions increases, the numerator also increases, indicating less space charge distortion, as expected. On the other hand, as the density (or charge state) increases, the denominator increases, indicating stronger space charge distortion, as expected. The length of the gap between the grid and the collector (z_f, see Figure 2-7) is also

an important parameter, and its effect can be understood by realizing that the total charge within the cup at a given time increases with z_f, increasing the space charge field. Note that in the analytic model due to Green, it is assumed that $\phi_f \sim 0$ [Gre70], since this value is usually small compared to the ion kinetic energy (e.g. E~150 eV for carbon ions with $v_{pk}=5\text{x}10^4$ m/s) and the space charge potential barrier amplitude. Thus, this quantity does not enter into Equation 2-23. This issue is discussed further below.

It is also interesting to note that the parameters n_{pk} and Z appear in the criterion, but not in the expected combination Zen_{pk}, as discussed in the previous section. The combination Zen_{pk} affects the electrostatic potential, but it is evident that only Ze affects the height of the potential barrier seen by each individual particle. To confirm this, several simulations were performed, changing the value of Z but keeping Zen_{pk} fixed. The results are summarized in the figure below.

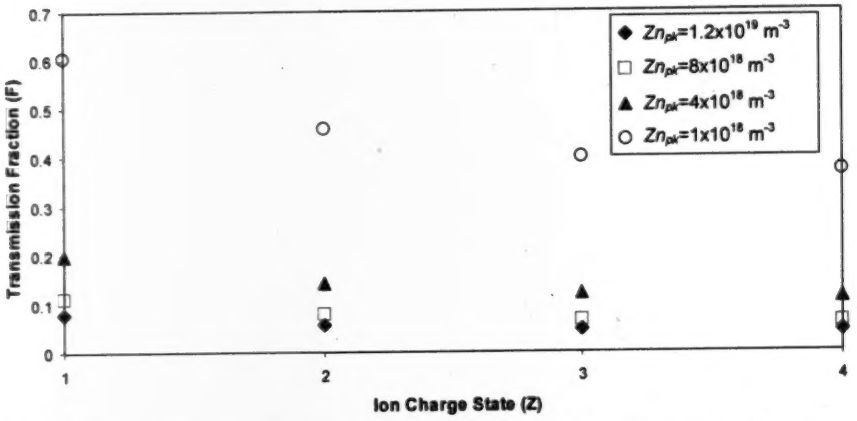

Figure 2-10. The transmission fraction (F) for different ion charge states (Z), keeping Zen_{pk} fixed, for four different values of Zen_{pk}.

As Z is increased, the fraction of the ion flux which reaches the collector drops by as much as 40%. This is in qualitative agreement with the analytic criterion described above. Keeping Zn_{pk} fixed while increasing Z will increase the size of the denominator of the criterion, indicating an increase in space charge distortion. Thus, it appears that Z is an important parameter in its own right. This will be discussed further in the description of the experimental results.

The steady-state analytic model was also used to calculate distorted waveforms, for a range of peak densities. The calculations were performed numerically using a computer code developed by D. G. Redman [Red02].

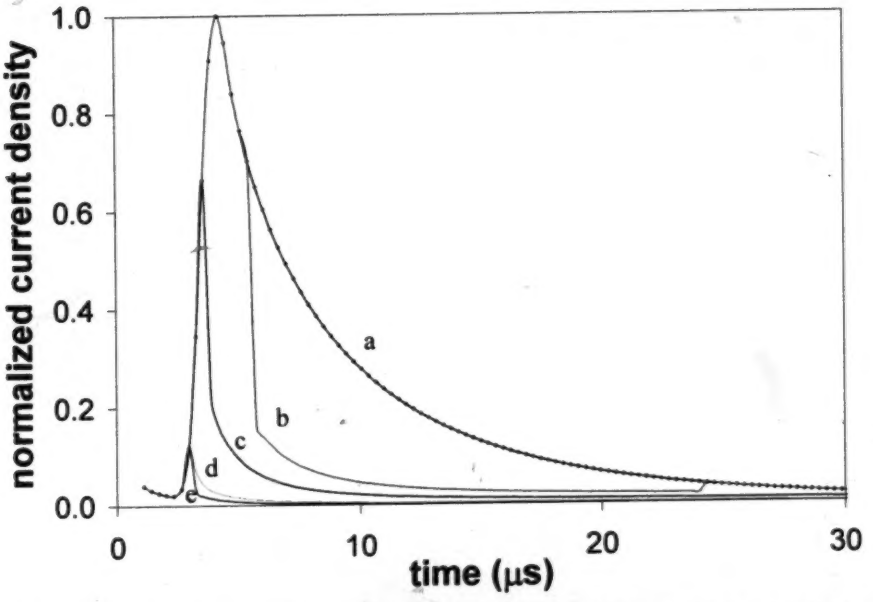

Figure 2-11. Distorted waveforms calculated using the steady-state analytic model using different densities. The density values are as follows: a- $2.5\text{x}10^{17}$ m^{-3}; b- $1.3\text{x}10^{18}$ m^{-3}; c- $2.5\text{x}10^{18}$ m^{-3}; d- $1.3\text{x}10^{19}$ m^{-3}; e- $2.5\text{x}10^{19}$ m^{-3}. Each calculation employed z_f=150 μm and ϕ_f=-30 V, and $v_{pk}=5\text{x}10^4$ m/s. The parameters of the temporal profile are as follows: σ_1=1.1 μs, σ_2=4 μs, p_1=3, p_2=0.75, and t_{pk}=4.4 μs.

These waveforms represent the normalized current which reaches the collector (Figure 2-7), calculated for different ion peak densities. The smallest density ($n_{pk}=2.5\text{x}10^{17}$ m^{-3}) results in an undistorted signal, identical to the incident ion flux. It is clear that as the ion density increases, the degree of distortion and the importance of the space charge effect both increase. Immediately, the reader will note that the distorted waveforms, considered independently, do not actually appear to be distorted in any way. While the peak amplitude, peak time, and integrated ion flux are all affected to varying degrees, the general shape of the distorted signal is similar to that of the true (incident) ion signal. An unsuspecting investigator would be unaware that the observed ion signal is in fact a poor representation of the true ion signal. Another important point to note is that the early region of each waveform is undistorted. This is due to the fact that the early arriving ions have higher velocities than the late arriving ions (Equation 2-5), and are thus able to surmount the potential barrier which is rapidly forming within the Faraday cup. Note that the z_f values used here and in subsequent calculations are relatively small in comparison with a typical experimental implementation of a Faraday cup. This value was chosen to ensure that the behavior of the ions within the cup could be treated as one-dimensional, and also to provide reasonable values for the ion peak density and velocity.

The results of the OOPIC simulation of the exact same situation are given in the figure below. Additional waveforms for different parameter values are included in the Appendix.

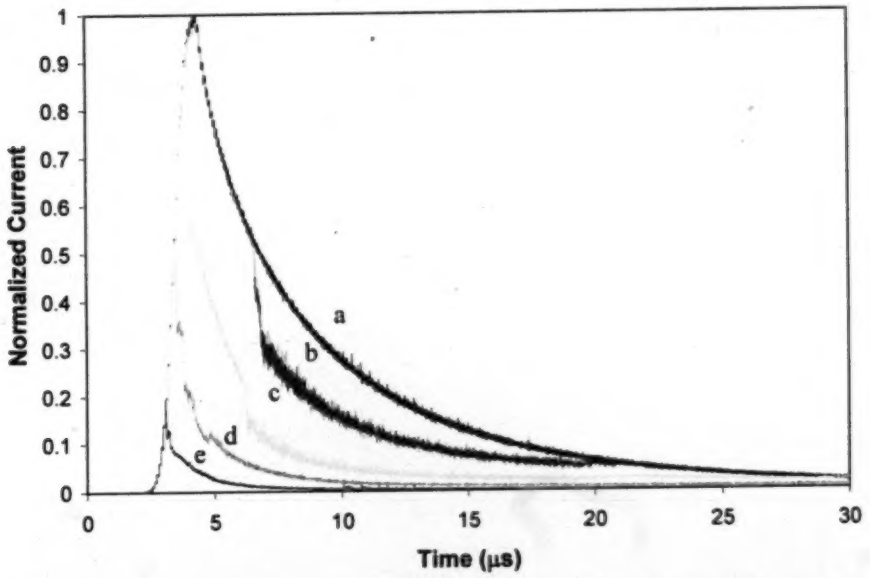

Figure 2-12. Distorted waveforms resulting from the OOPIC simulations, with different ion densities. The ion density values are as follows: a- 5×10^{17} m^{-3}; b- 1×10^{18} m^{-3}; c- 2×10^{18} m^{-3}; d- 5×10^{18} m^{-3}; e- 2×10^{19} m^{-3}. This group of simulations employed z_f=150 μm and ϕ_f=-30 V, and $v_{pk}=5\times10^4$ m/s, in order to facilitate comparison with the results of the steady-state analytic calculation in the preceding figure. The parameters of the temporal profile are also identical: σ_1=1.1 μs, σ_2=4 μs, p_1=3, p_2=0.75, and t_{pk}=4.4 μs.

Again, the smallest peak density ($n_{pk}=5\times10^{17}$ m^{-3}) results in an undistorted signal. There are a few qualitative differences between the simulation results and the analytic results. The main difference is that the onset of space charge distortion in the simulations is a relatively violent process, when the simulation waveforms are compared to the analytically calculated waveforms. This results in a more dramatic drop in the transmitted current at the onset of space charge distortion. Additionally, in the simulations, the potential barrier which purportedly prevents ion transmission actually oscillates in amplitude, periodically allowing some of the ion flux to pass through. In fact, the temporal resolution of the simulation was adjusted in order to adequately capture this phenomenon. The oscillations occur with a period of several tens of nanoseconds. The oscillations in current are visible in the waveforms, appearing as high-frequency noise in the tail region.

In order to quantitatively compare the analytic model with the simulations, a series of analytic calculations were performed, determining the variation of the transmission fraction (F, defined by Equation 2-17) with various key parameters in the model. A series of simulations were also performed using identical

parameters, again computing the transmission fraction for each simulation. Selected simulation waveforms from these series are included in the Appendix. The figures below summarize the results of the transmission fraction calculations. The first of these summarizes the variation of transmission fraction (F) with peak ion density (n_{pk}).

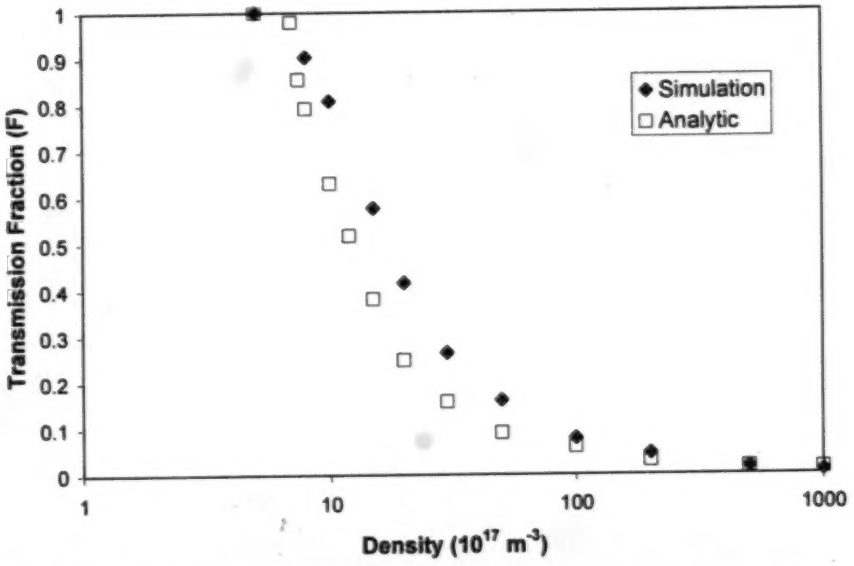

Figure 2-13. The transmission fraction (F) as a function of the peak ion density (n_{pk}), for both the analytic model and the simulations. Both the analytic calculations and the simulations employed z_f=150 μm, ϕ_f=-30 V, and v_{pk}=5x10^4 m/s, with σ_1=1.1 μs, σ_2=4 μs, p_1=3, p_2=0.75, and t_{pk}=4.4 μs.

Qualitatively, the two results agree, both demonstrating the same trend. Both exhibit a smooth decline over a relatively narrow density range, as space charge distortion begins to take effect around n_{pk}=5x10^{17} m^{-3} and virtually eliminates the ion signal around n_{pk}=1x10^{19} m^{-3}. Quantitatively, the agreement is relatively good, with some minor differences. These differences will be discussed further later in this section. Additionally, the observed trend is consistent with the physical picture of the phenomenon. As the ion density increases, the space charge within the Faraday cup increases, resulting in a larger potential barrier and thus a decrease in the ion flux reaching the collector.

Next, the variation of the transmission fraction with the ion peak velocity was considered.

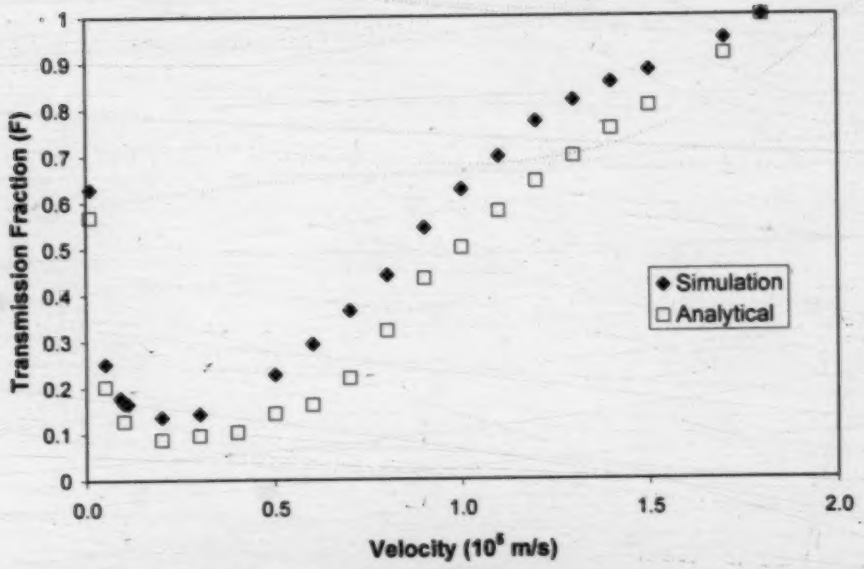

Figure 2-14. The transmission fraction (F) as a function of the ion peak velocity (v_{pk}). Both the analytic calculations and the simulations employed z_f=150 μm, ϕ_f=-30 V, and n_{pk}=3.5x10^{18} m^{-3}, with σ_1=1.1 μs, σ_2=4 μs, p_1=3, p_2=0.75, and t_{pk}=4.4 μs.

Again, qualitatively, the agreement is good, with both results demonstrating similar behavior: a precipitous drop in transmission fraction, followed by a smooth increase with increasing velocity. Both curves reach a minimum at a velocity of 2x10^4 m/s. Quantitatively, the disagreement is modest. Possible reasons for the disagreement will be discussed later in this section. Above 2x10^4 m/s, the increase in transmission fraction with increasing velocity is consistent with the physical understanding of the situation. As the ion velocity increases, the individual particles have sufficient kinetic energy to overcome the potential barrier due to the excessive space charge within the Faraday cup, and thus an increasing fraction of the ion flux reaches the collector. However, the observed trend does exhibit one unexpected feature. As the velocity decreases below 2x10^4 m/s, the transmission fraction increases, and thus seemingly contradicts Equation 2-23. The source of this behavior is not clear. One possible explanation is that the slower-moving ions constitute a smaller current density, which may reduce the buildup of space charge within the cup.

Next, the variation of the transmission fraction with the length of the Faraday cup (i.e. the grid to collector distance, z_f in Figure 2-7) was considered.

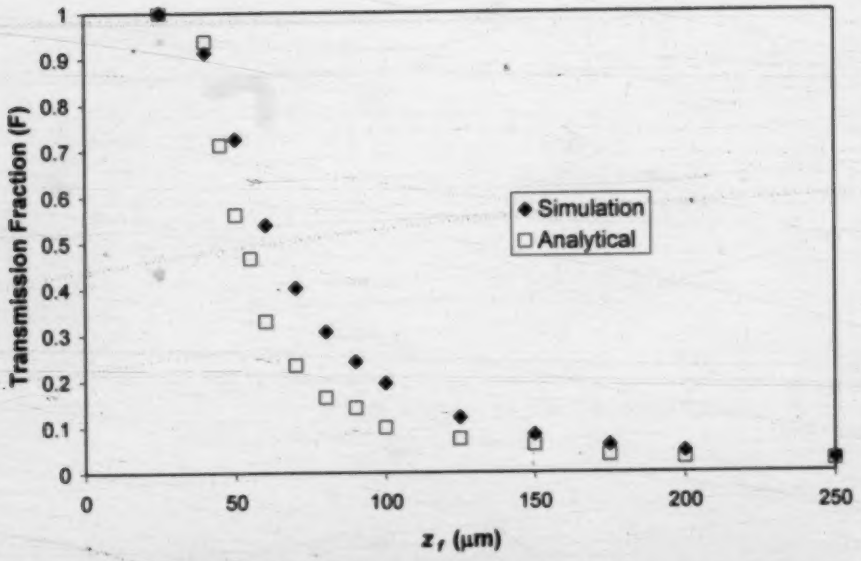

Figure 2-15. The transmission fraction (F) as a function of the length of the Faraday cup (z_f). Both the analytic calculations and the simulations employed v_{pA}=5x10^4 m/s, ϕ_f=-30 V, and n_{pA}=1x10^{19} m^{-3}, with σ_1=1.1 μs, σ_2=4 μs, p_1=3, p_2=0.75, and t_{pA}=4.4 μs.

Both sets of data exhibit a similar trend: a smooth decline in transmission fraction with increasing Faraday cup length. Once again, there is some quantitative disagreement between the two results. The observed trend can be explained by noting that the total charge within the cup at a given time increases with z_f, increasing the space charge field.

The final parameter of interest is the collector biasing voltage.

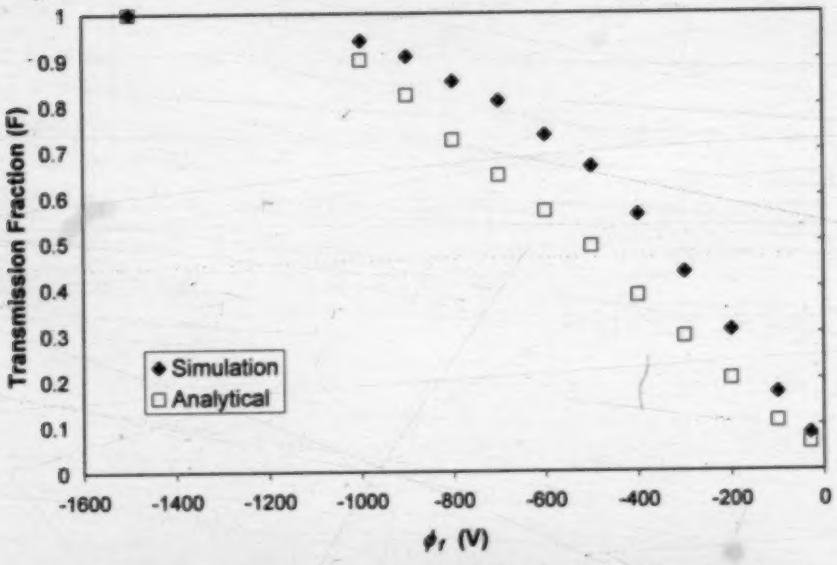

Figure 2-16. The transmission fraction (F) as a function of the collector biasing voltage (ϕ_f). Both the analytic calculations and the simulations employed z_f=150 μm, v_{pk}=5x10^4 m/s, and n_{pk}=1x10^{19} m^{-3}, with σ_1=1.1 μs, σ_2=4 μs, p_1=3, p_2=0.75, and t_{pk}=4.4 μs.

Once again, qualitatively, the two results are in agreement. Both exhibit a smooth decline in transmission fraction as the biasing voltage becomes more positive. However, there is some quantitative disagreement between the two data sets. This disagreement will be discussed later in this section. Again, the observed trend is readily explained by the physical understanding of the situation. As the biasing voltage becomes more positive, the potential barrier amplitude increases, and the transmission fraction decreases. The collector biasing voltage does not enter into the analytical criterion in Equation 2-23, since it is assumed that the collector voltage is negligible compared to the ion energy (e.g. E~150 eV for carbon ions with v_{pk}=5x10^4 m/s) and the space charge potential barrier. From the above graph, when this assumption breaks down, the collector voltage becomes an important parameter.

Overall, it is apparent that the analytical and simulation results are in qualitative agreement, exhibiting similar trends and behavior. Quantitatively, the disagreement between the simulations and the analytical results is minimal. In all cases, the simulation results exhibit higher transmission fraction values compared to the analytical results. The differences between the analytic results and the simulation results may be explained by key differences in the two methods. The analytical model is a one-dimensional model. On the other hand, the simulations are conducted in a cylindrical geometry, which is obviously more appropriate to the physical situation. Although the length of the Faraday cup detectors was fairly small, radial spreading of the ion current was observed in the simulations, which indicates the limitations of the analytic model. More importantly, the

analytic model is based on the steady-state assumption. It is clear from the simulations that the amplitude of the potential barrier oscillates in time, again indicating the limitations of the analytic model. These differences lead to smaller transmission fraction values in the analytical calculations. By ignoring the radial spreading of the ions, the analytical model maintains higher ion densities, which consequently reduces the calculated transmission fraction. Also, the oscillatory behavior of the potential barrier observed in the simulations seems to allow greater ion flux transmission; by ignoring this time-dependent behavior, the analytical model predicts smaller transmission fraction values compared to those predicted by the simulations.

b) Experimental and Simulation Results

The results of the experimental investigations will now be presented. The figure below represents two individual laser shots, each depicting the undistorted current (as captured by the Langmuir probe) as well as the distorted current (captured by the Faraday cup). Additional examples of experimentally observed detector signals are included in the Appendix. The signals were corrected to eliminate the difference between the detector areas, as well as to account for the transmission factor of the grid. The error in the measurement of this last parameter was the dominant source of error in this experiment.

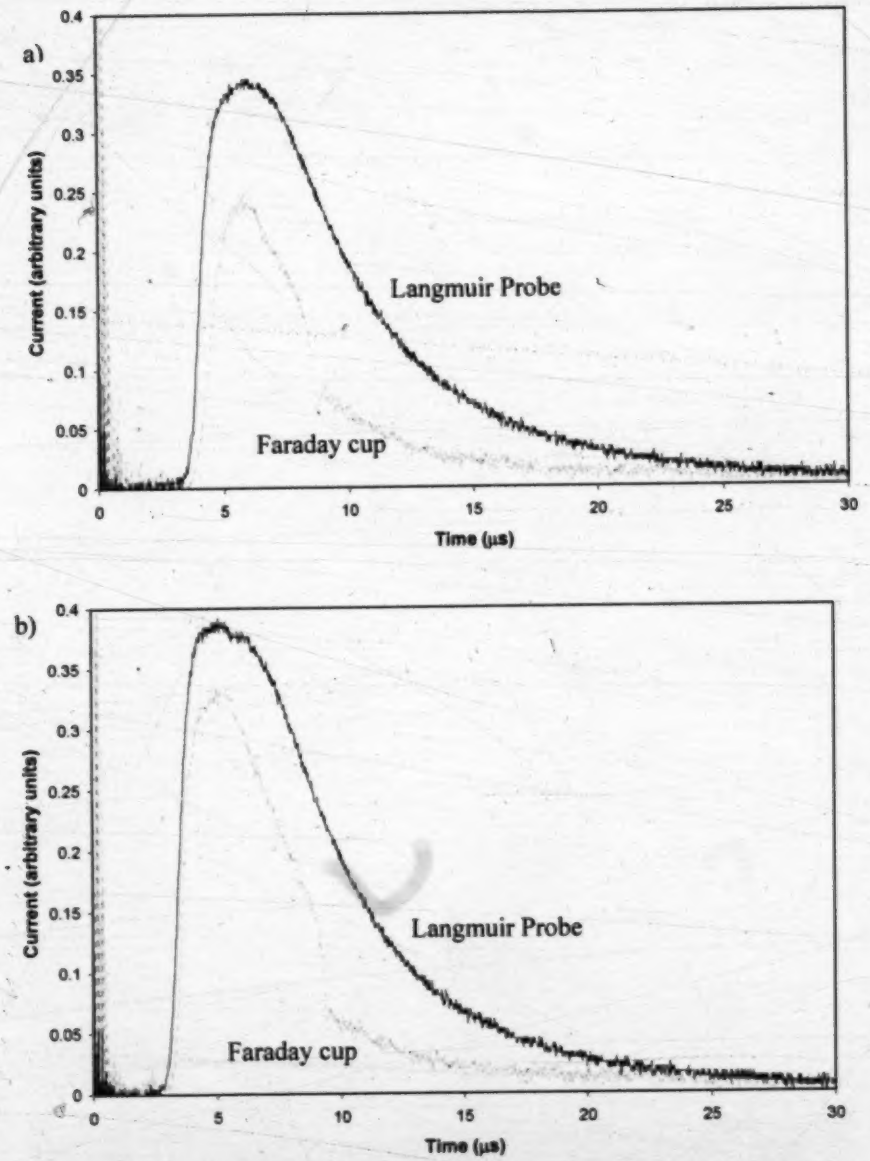

Figure 2-17. Some typical signals recorded from individual laser shots. The signals in a) correspond to a laser intensity of I_L=1.4x10^{10} W/cm^2 (laser energy E_L=72.3 mJ, lens-to-target distance d_L=51.1 cm) with F=0.48, whereas the signals in b) correspond to a laser intensity of 1.7x10^{10} W/cm^2 (E_L=73.0 mJ, d_L=51.4 cm) with F=0.62. The signals were corrected for factors such as the grid transmission and the detector aperture diameters.

The noise near time zero is photoelectric emission occurring when energetic photons emitted by the hot plasma strike the detector surfaces and eject electrons.

The Faraday cup parameters were as follows: z_f=1.75 mm, 400 mesh (37 μm grid spacing, and transmission 0.27 ± 0.03), 3.18 mm aperture diameter. The Langmuir probe diameter was 6.35 mm. Both the Langmuir probe and the collector of the Faraday cup were located 22 cm from the target, at angles of 5° (with respect to target normal).

Applying Equations 2-5, 2-7 and 2-9 to the above Langmuir probe signals, values for the peak ion density and velocity can be calculated, with the assumption Z=1. As discussed earlier in this section, the selection of an accurate value for this parameter is important. Under the conditions of this experiment, there is some evidence (see Chapter 3) to indicate that this assumption may be inaccurate. This issue will be addressed further later in this section. According to Equations 2-5, 2-7 and 2-9, for the signal in a), n_{pk}=3.6x10^{16} m^{-3}, and v_{pk}=3.7x10^4 m/s. For the signal in b), n_{pk}=3.6x10^{16} m^{-3}, and v_{pk}=4.2x10^4 m/s. By fitting several experimental Langmuir probe signals, the following average temporal profile parameters were obtained using Equations 2-10 and 2-11: σ_1=1.7 μs, σ_2=7.2 μs, p_1=3, p_2=1.2, and t_{pk}=5.5 μs.

The figure below gives a typical waveform produced in simulations attempting to reproduce the experimental conditions.

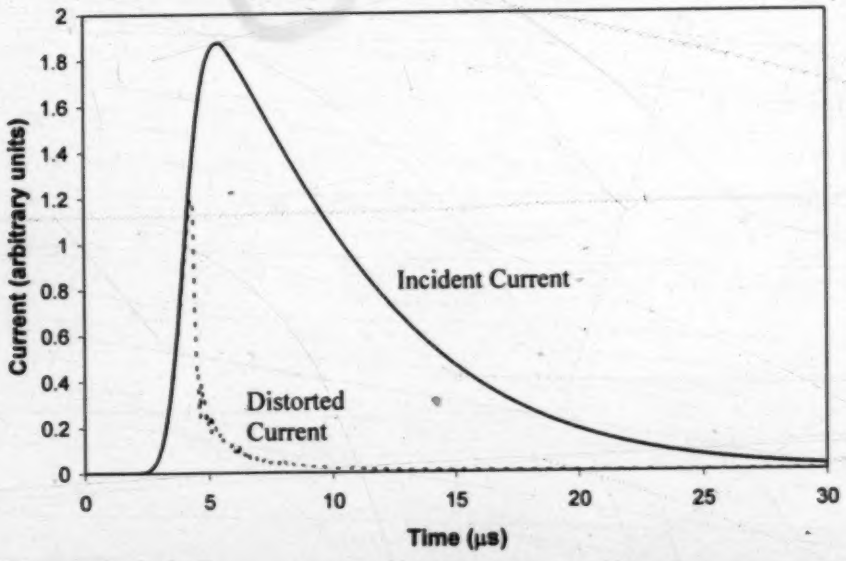

Figure 2-18. A typical output waveform from the OOPIC simulations, for comparison purposes. This particular simulation was performed using z_f=1.75 mm, v_{pk}=4x10^4 m/s, ϕ_f=-40 V, and n_{pk}=3.7x10^{16} m^{-3}, with σ_1=1.7 μs, σ_2=7.2 μs, p_1=3, p_2=1.2, and t_{pk}=5.5 μs. These parameters were carefully chosen to match the experimental conditions, averaged over several laser shots.

Although the simulation parameters closely matched the experimental parameters, the result is quite different: the calculated transmission fraction was F=0.14. The simulation signal exhibits much stronger space charge distortion than the experimental signal. To achieve a comparable level of space charge distortion, the ion velocity in the simulation had to be increased. The resulting simulation output is given in the figure below.

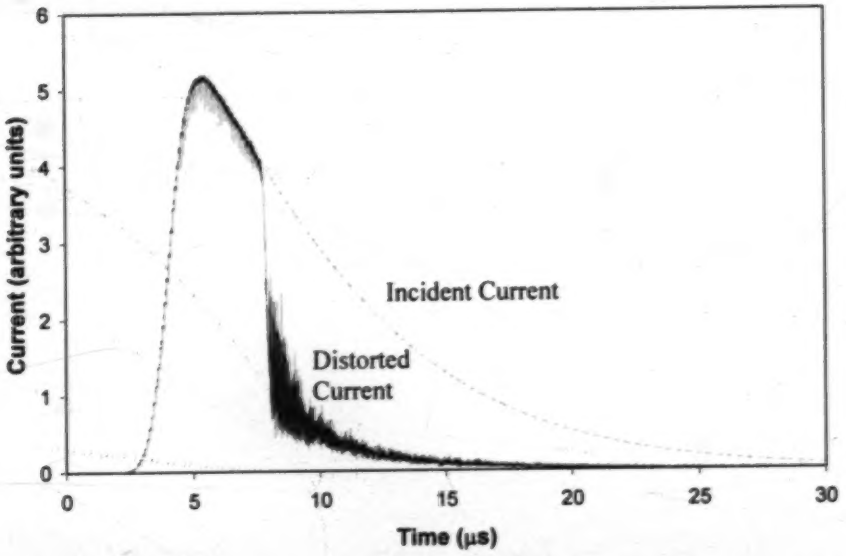

Figure 2-19. A typical output waveform from the OOPIC simulations, for comparison purposes. This particular simulation was performed using z_f=1.75 mm, v_{pk}=1.1x10^5 m/s, ϕ_f=-40 V, and n_{pk}=3.7x10^{16} m^{-3}, with σ_1=1.7 μs, σ_2=7.2 μs, p_1=3, p_2=1.2, and t_{pk}=5.5 μs. These parameters were carefully chosen to match the experimental situation, with the exception of the ion peak velocity, which was chosen to provide a transmission fraction (F~0.5) similar to that observed in the laser shots above.

Immediately, the reader will notice the similarity between the distorted waveforms in Figures 2-17 and 2-19. All three waveforms are fairly similar in shape to the undistorted (i.e. input) current waveform. All three of the above waveforms exhibit a region of sharp change where the signal drops suddenly, which, in the simulation, corresponds to the onset of space charge distortion. A significant difference is that the simulation waveform adheres closely to the undistorted waveform in the early non-space charge limited region, whereas the experimental waveforms depart from what is assumed to be the undistorted waveform. This may represent some kind of pre-threshold space charge distortion, in which the ion flux is only partially repelled by the buildup of space charge within the Faraday cup, resulting in a smaller amplitude ion signal. Alternatively, the difference may be explained by secondary electron emission. It has been assumed that the Langmuir probe signal is a flawless record of the true ion current. This is not necessarily the case, as secondary electron emission may

artificially inflate the signal amplitude recorded by the probe. A smaller amplitude Langmuir probe signal would more closely match the Faraday cup signal in the early region of the waveform, where the signal is expected to be undistorted, due to the higher particle velocity (Equation 2-5). However, as discussed previously, most groups studying ion emission in this intensity regime assume that secondary electron emission is small under these conditions.

In order to ascertain the level of quantitative agreement between the experiments and the simulations, a series of simulations which closely reproduce the experimental conditions were performed. The figure below summarizes the results.

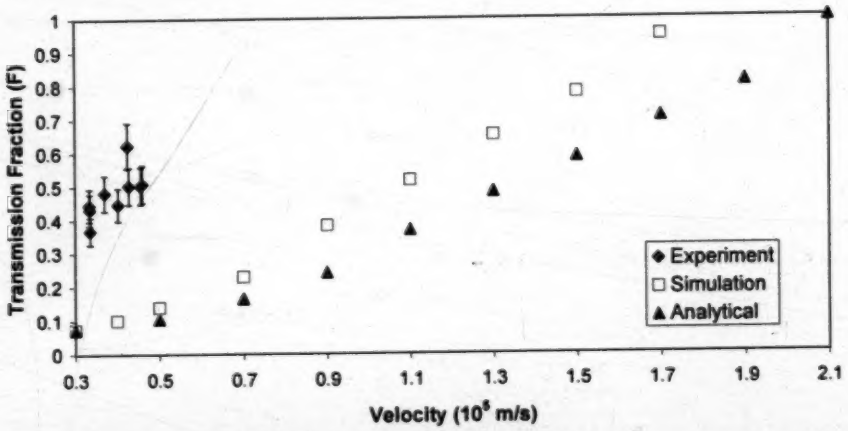

Figure 2-20. A comparison between the transmission fraction vs. velocity trends for experiment, simulation, and analytical calculations. The parameters for these results were closely matched, with n_{pk}=3.7x10^{16} m^{-3}, z_f=1.75 mm, and ϕ_f=-40 V, with σ_1=1.7 μs, σ_2=7.2 μs, p_1=3, p_2=1.2, and t_{pk}=5.5 μs. Care was also taken to ensure that the radial geometry of the Faraday cup used in the experiment was reproduced in the simulation, even though the simulations indicated that the ion motion is largely confined to the longitudinal dimension. The (averaged) laser parameters for the experimental results were E_L=73 mJ, d_L=51.2 cm, I_L=1.6x10^{10} W/cm^2.

The error bars are based on the variation in the transmission fraction values due to the error in measurement of the transmission of the grid at the entrance of the Faraday cup. It is difficult to draw definitive conclusions from the limited experimental data available. As described earlier, by controlling the laser intensity, the ion peak velocity could be controlled. However, in order to produce the above graph, all other variables (in particular, peak ion density) must be kept constant. Being unable to independently control the velocity and density, the stochastic nature of laser matter interactions and accumulated data from many laser shots were both employed in order to produce the above graph. Although there is a significant scatter in the experimental data, a positive correlation between transmission fraction and velocity is evident. Thus, qualitatively, the experimental data agree with the simulation results. Quantitatively, there is a significant disagreement between the experiments and simulations.

The chief difference between the experiments and the simulations is that the simulations involve an ion flux incident on the detector, whereas in the experiments, a plasma flux, consisting of ions and electrons, is incident on the detector. According to the generally accepted model of Faraday cup operation, the electron flux is repelled at the grid of the Faraday cup. This is true under normal (distortionless) operation of the Faraday cup, since the electron flux is repelled by the electrostatic potential profile established by the grid and the biasing plane (Figure 2-22a). However, when a sufficient number of ions enter the cup, the potential profile is distorted (see figure below), and the electrons may no longer be repelled effectively.

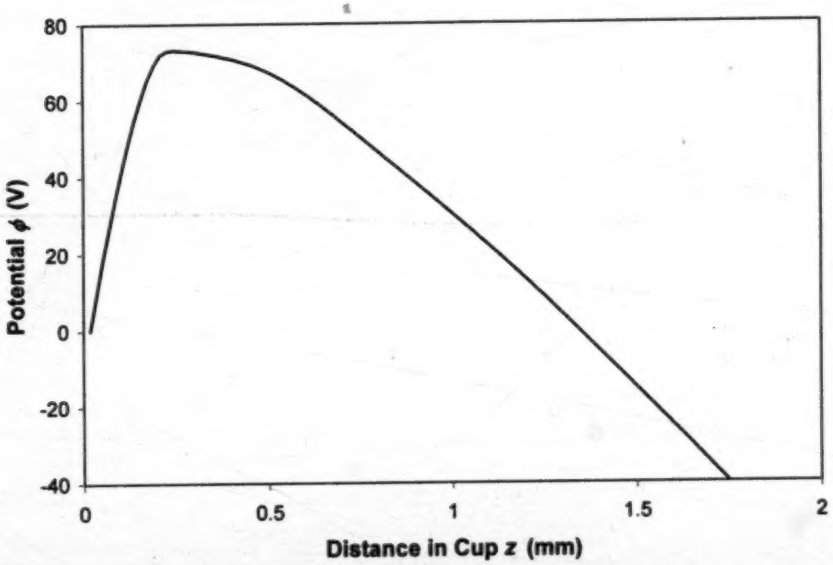

Figure 2-21. The electrostatic potential profile within the Faraday cup, calculated from an OOPIC simulation. This particular simulation employed z_f=1.75 mm, v_{pk}=4x10^4 m/s, ϕ_f=-40 V, and n_{pk}=3.7x10^{16} m^{-3}, with σ_1=1.7 μs, σ_2=7.2 μs, p_1=3, p_2=1.2, and t_{pk}=5.5 μs, and the resulting value of F was 0.1.

This potential profile appears as a valley to the electrons incident on the cup, and they may enter the cup (see figure below).

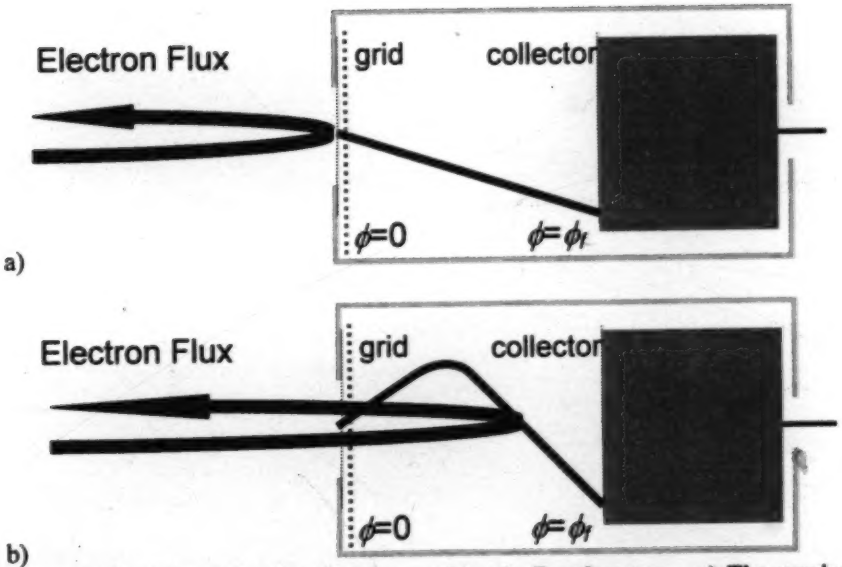

Figure 2-22. Schematics for electron repulsion in Faraday cups. a) The previously accepted model of electron repulsion at the entrance of the Faraday cup. b) The current study indicates that the electron flux penetrates deep into the cup when the potential profile (ϕ) is distorted.

The presence of electrons within the cup will subsequently affect the potential profile, alleviating the effect of the ion buildup on the potential profile.

c) Two-Particle Simulations

In order to assess the hypothesized role of electrons in the space charge effect, several two-particle simulations were performed, which included both electrons and ions. The electron flux and the ion flux both had identical density and velocity profiles. All other conditions were identical to those used in the simulations of Figure 2-19, such that the simulation conditions closely matched the experimental conditions. Note that recombination was not calculated in the simulation, although with both ions and electrons present within the cup, there is some finite probability of ion and electron recombination.

As expected, the inclusion of electrons in the simulation results in an alleviation of the space charge distortion of the ion current. During the simulation, when the positive charge starts to build up inside the cup, the potential profile begins to curve upward, forming a small barrier to the ion flux. The electrons are no longer repelled by this distorted potential profile (see figure below).

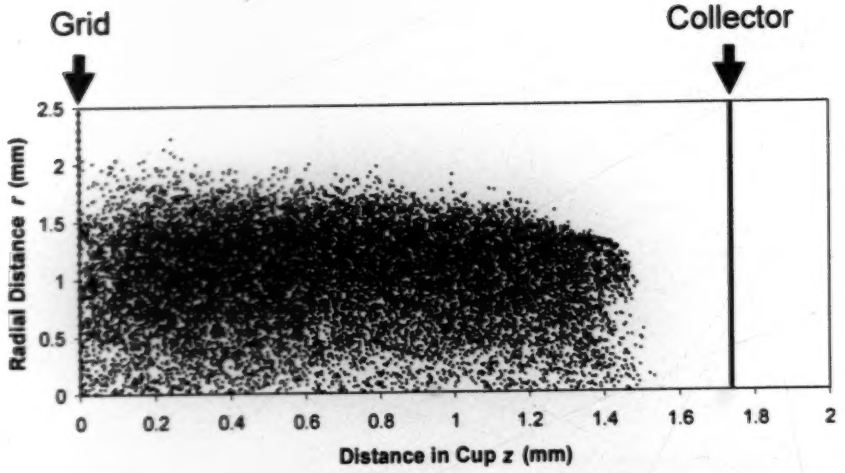

Figure 2-23. Image taken from the two-particle simulation showing the penetration of the electrons into the interior of the Faraday cup. This image is taken at t=8.6 μs, for the simulation with z_f=1.75 mm, v_{pi}=7x10^4 m/s, ϕ_f=-40 V, and n_{pi}=3.7x10^{16} m^{-3}, and σ_1=1.7 μs, σ_2=7.2 μs, p_1=3, p_2=1.2, and t_{pi}=5.5 μs, resulting in F=0.87. Recall that the simulations employ cylindrical coordinates. The circular aperture at the entrance of the cup has a radius of 1.6 mm.

The electrons readily penetrate the cup, and are repelled only when the electrostatic potential becomes sufficiently negative. The negative space charge of the electrons counteracts the positive space charge of the ions, reducing the potential barrier which the incident ions face when entering the cup (see figure below).

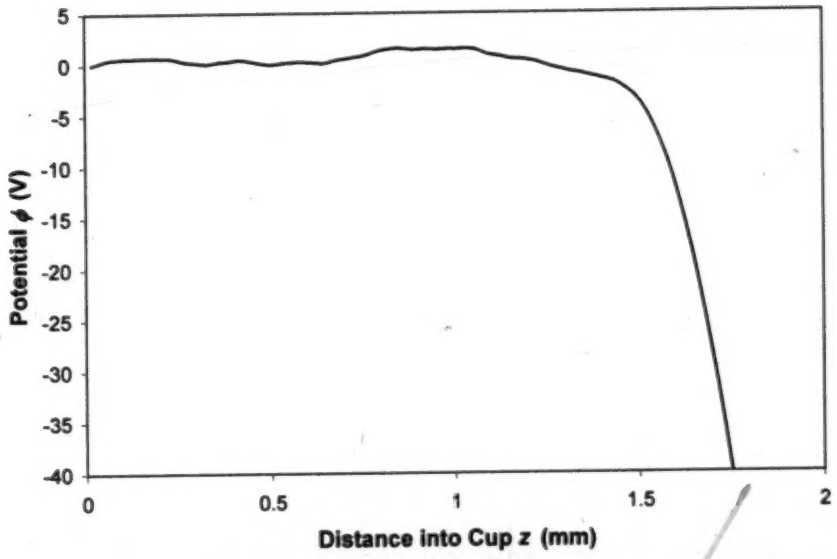

Figure 2-24. Image taken from the two-particle simulation showing the effect of the presence of the electrons within the Faraday cup on the electrostatic potential. This image is taken at t=8.6 μs, for the simulation with z_f=1.75 mm, v_{pk}=7x10^4 m/s, ϕ_f=-40 V, and n_{pk}=3.7x10^{16} m^{-3}, and σ_1=1.7 μs, σ_2=7.2 μs, p_1=3, p_2=1.2, and t_{pk}=5.5 μs, resulting in F=0.87.

Compare the potential in this figure to the potential from the one particle simulations in Figure 2-21 above. The potential barrier in the two-particle case is greatly reduced by the presence of the electrons, delaying the onset of space charge distortion. Since the later-arriving electrons have smaller velocities (and therefore energies), they are unable to penetrate the cup as deeply, and a potential barrier is eventually able to form (see figures below).

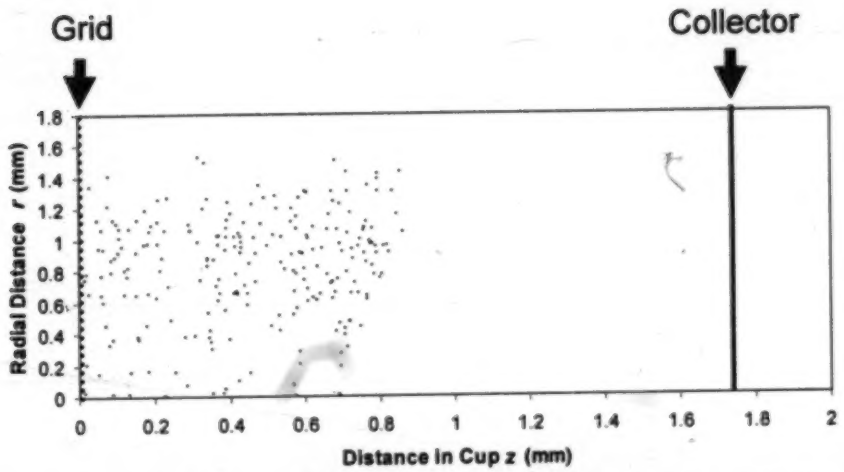

Figure 2-25. Image taken from the two-particle simulation showing the penetration of the electrons into the interior of the Faraday cup. This image is taken at t=29 μs, for the simulation with z_f=1.75 mm, v_{pk}=7x10^4 m/s, ϕ_f=-40 V, and n_{pk}=3.7x10^{16} m^{-3}, with σ_1=1.7 μs, σ_2=7.2 μs, p_1=3, p_2=1.2, and t_{pk}=5.5 μs, resulting in F=0.87. Recall that the simulations employ cylindrical coordinates. The circular aperture at the entrance of the cup has a radius of 1.6 mm.

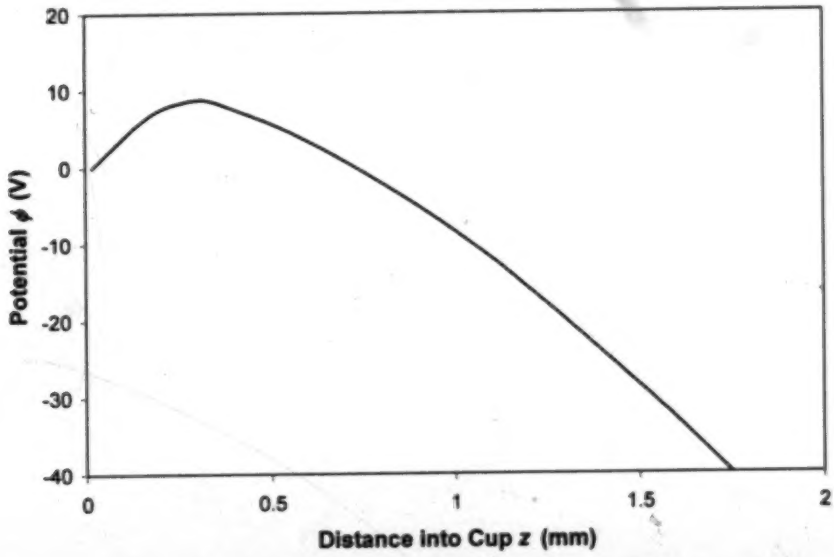

Figure 2-26. Image taken from the two-particle simulation showing the effect of the presence of the electrons within the Faraday cup on the electrostatic potential. This image is taken at t=29 μs, for the simulation with z_f=1.75 mm, v_{pk}=7x10^4 m/s, ϕ_f=-40 V, and n_{pk}=3.7x10^{16} m^{-3}, with σ_1=1.7 μs, σ_2=7.2 μs, p_1=3, p_2=1.2, and t_{pk}=5.5 μs, resulting in F=0.87.

Note that the figures above (Figures 2-23, 2-24, 2-25, and 2-26) correspond to the same simulation. The figure below indicates the temporal profile of the ion current incident on the collector from this same simulation. As indicated from the figures above, no potential barrier exists at early times, so the current remains undistorted. The potential barrier forms at later times, distorting the ion current after ~15 μs.

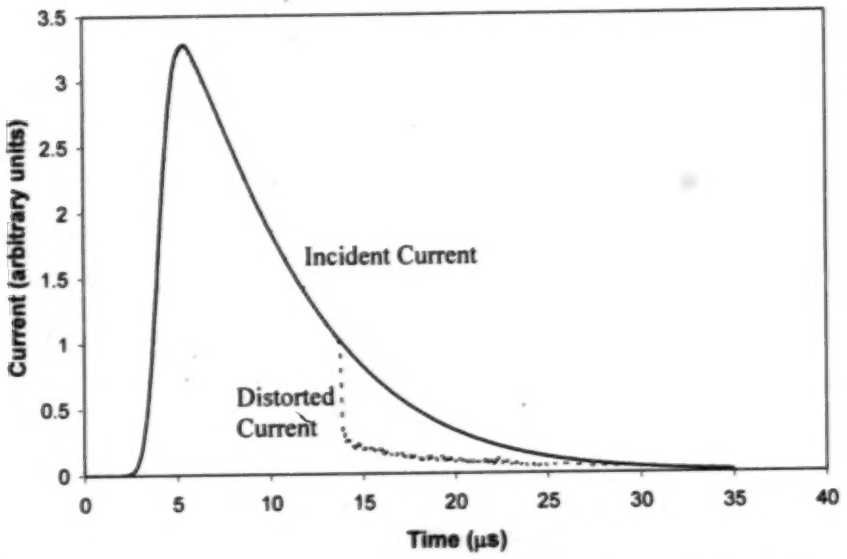

Figure 2-27. An output waveform from the two-particle OOPIC simulations. This particular simulation was performed using z_f=1.75 mm, v_{pk}=7x10^4 m/s, ϕ_f=-40 V, and n_{pk}=3.7x10^{16} m^{-3}, with σ_1=1.7 μs, σ_2=7.2 μs, p_1=3, p_2=1.2, and t_{pk}=5.5 μs resulting in F=0.87.

Using a velocity which more closely approximates that seen in experiment (v_{pk}=4x10^4 m/s), the following current profile is obtained. Additional examples of current waveforms from the two-particle simulations are included in the Appendix.

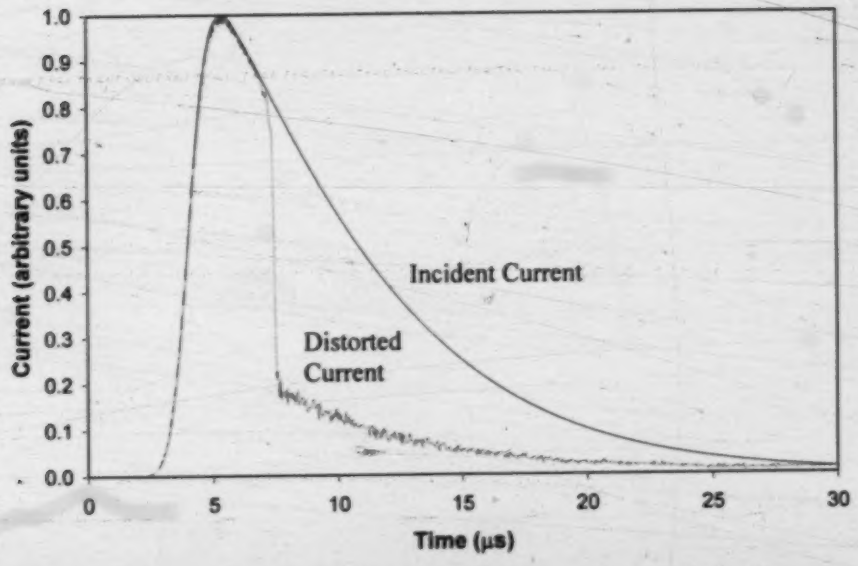

Figure 2-28. A typical output waveform from the two-particle OOPIC simulations, for comparison purposes. This particular simulation was performed using z_f=1.75 mm, v_{p1}=4x10^4 m/s, ϕ_f=-40 V, and n_{p1}=3.7x10^{16} m^{-3}, with σ_1=1.7 μs, σ_2=7.2 μs, p_1=3, p_2=1.2, and t_{p1}=5.5 μs. These parameters were carefully chosen to match the experimental situation.

A qualitative comparison between Figure 2-28 and Figure 2-17 indicates that the above waveform closely matches the experimental waveforms. Both the simulation and the experimental waveforms exhibit a sharp drop in the ion current, indicating the onset of space charge distortion. One significant difference, also seen in the previous comparison between the single-particle simulation and the experiment, is that the early region of the distorted simulation waveform closely follows the input waveform, whereas the early region of the distorted experimental waveform does not. Overall, the two-particle simulation produces a waveform which is fairly similar to that produced by the single-particle simulation (Figure 2-19), with one important difference: the one-particle simulation uses a velocity of 1.1x10^5 m/s to produce a transmission fraction of ~0.5, whereas the two-particle simulation gives a similar transmission fraction at a much lower velocity (4x10^4 m/s).

The following graph provides an indication of the level of quantitative agreement between the two-particle simulations and the experiment.

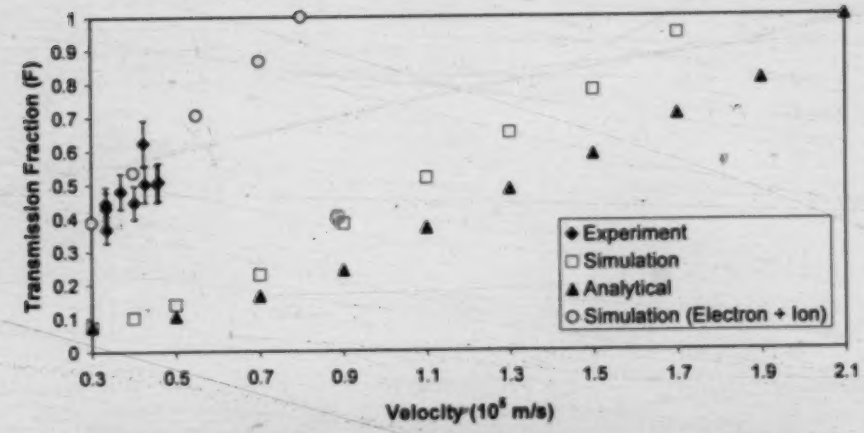

Figure 2-29. A comparison between the transmission fraction vs. velocity trends for experiment, simulation (both one-particle and two-particle), and analytical calculations. The parameters for these results were closely matched, with n_{pk}=3.7x10^{16} m^{-3}, z_f=1.75 mm, and ϕ_f=-40 V, with σ_1=1.7 μs, σ_2=7.2 μs, p_1=3, p_2=1.2, and t_{pk}=5.5 μs.

The agreement between the experimental results and the two-particle simulation results is remarkable. Qualitatively, the trend which is implied by the limited experimental data is matched by the two-particle simulation trend. As expected, the transmission fraction exhibits a smooth (almost linear) increase with increasing velocity.

Quantitatively, the transmission fraction values of the two-particle simulations and the experiment are in excellent agreement. The two-particle simulation results do appear to be slightly larger than the experimental results. To explain this, consider the issue of the average charge state (Z) of the ions in the experiment. Throughout this chapter, a charge state of 1 has been assumed. A more reasonable estimate for a carbon plasma at a laser intensity of I_L~1-2x10^{11} W/cm^2 would be Z~1.3 [Tsu93]. For more discussion of this estimate, see Chapter 3. From the graph in Figure 2-10, it would seem that if Z=1.3 was used for the two-particle simulations, the transmission fraction values would decrease slightly, improving the agreement with the experimental results.

The results of this graph appear to confirm the presence of electrons within the Faraday cup for the above experiments. Thus, it is possible that the previously accepted model of the operation of a Faraday cup is incomplete. The assumed rejection of the electron flux at the grid of the Faraday cup appears to break down under the conditions of space charge distortion.. If this is the case, then it appears that the analytical model describing the space charge effect overestimates the importance of the phenomenon, by a factor of ~4-5 (Figure 2-29). A more complex analytical model, involving both electrons and ions, would be required.

However, an alternative explanation of the experimental results exists. If the electron flux incident on the cup is sufficiently dense or sufficiently cold (Equation 2-1), the Debye shielding length of the electrons becomes smaller than

the grid wire spacing. Thus, the electrons could shield the grid potential, allowing some proportion of the electrons to enter the cup. Additionally, although secondary electron emission is neglected in this chapter, there may in fact be some secondary emission which would also result in some accumulation of electrons within the cup. The presence of electrons in the cup due to the two above-mentioned effects would counteract the positive space charge due to the ions, reducing the distortion of the Faraday cup ion signal, exactly as observed.

In any case, whether the presence of electrons within the cup is attributed to the distorted potential profile or to the Debye shielding of the grid potential and secondary electron emission from the collector, it is clear from the excellent agreement between the experiment and the two-particle simulations that electrons play an important role in the non-ideal operation of a Faraday cup ion detector. Thus, the operation of the Faraday cup is more complex than previously anticipated. Further experiment and simulation are required to explore this complexity. An analytic model incorporating both ions and electrons could also be developed.

d) Ion Detector Selection

Lastly, the selection of ion detectors for the nanosecond and femtosecond experiments is discussed. In this discussion, the condition of Equation 2-23 is employed, keeping in mind that the analytical model may overestimate the effect of space charge distortion (Figure 2-29). For the nanosecond regime, the average ion velocities are always less than $5\text{x}10^4$ m/s, the ion densities typically fall in the range $1\text{-}5\text{x}10^{16}$ m^{-3}, with the assumption of carbon and oxygen ions with Z=1 (see results of Chapter 3). According to the condition of Equation 2-23, the required value of z_f is less than ~0.3 mm. This is obviously a very small value, and while a larger value of z_f would probably suffice (Figure 2-29), multiplying this value by a factor of 4 or 5 still gives z_f~1-2 mm. Fabrication of such a Faraday cup detector might be problematic. In any case, the extra effort would be unnecessary; as discussed earlier, secondary electron emission under these plasma conditions is small. Thus, for the nanosecond ion emission investigation, the simpler Langmuir probe is selected.

For the femtosecond regime, the characteristics of the ion flux are markedly different. The average ion velocities range from $0.2\text{-}1.3\text{x}10^6$ m/s, the ion densities are typically in the range $1\text{-}3\text{x}10^{14}$ m^{-3}, and hydrogen ions (i.e. protons) with Z=1 are assumed to be present (see Chapter 4). According to the condition of Equation 2-23, the required value of z_f is less than 7 mm. This is a more reasonable value, especially considering the possibility that the analytical model overestimates the effect of space charge distortion. Fabrication of such a Faraday cup is not difficult. However, space charge distortion of the low energy tail of the ion signal is still a possibility. At the same time, if Langmuir probe detectors were chosen, secondary electron emission can be corrected for using the results of R. R. Goforth [Gof76] as discussed previously. For these reasons, simple Langmuir probe detectors were chosen for the femtosecond ion emission studies.

As a further demonstration of the importance of proper detector selection, the experimental configuration of P. D. Gupta *et al.* is examined [Gup87]. This group used a Faraday cup detector (z_f=35.4 mm, A_{det}=1.1x10^{-5} m^2) to study the ion emission from an aluminum target (m_i=26.98 A.M.U., assume Z=4.5) ablated with a Raman-compressed KrF laser system (λ_L=268 nm, τ_L=2 ns, E_L<1 J, I_L=7x10^{11} W/cm^2). In their study, it was found that the ion peak velocity was approximately 2x10^5 m/s at this intensity. The ion current amplitude is not given, but if the criterion of Equation 2-23 is inverted, the maximum permissible ion density incident on the detector can be calculated. Doing so, it is found that the ion density must be less than 5.5x10^{12} m^{-3} in order to avoid space charge distortion. This is a very low density. According to Equations 2-7 and 2-9 (assuming 50 Ω termination is used), this density corresponds to an ion signal level of 0.45 mV, which is very low. For comparison, the signal levels achieved in the present work typically range from several tens of millivolts to several volts. Now, keep in mind that the criterion of Equation 2-23 may overestimate the effect of space charge distortion, by a factor of ~4-5 (Figure 2-29). Additionally, given the cup dimensions used by Gupta *et al.*, the radial spreading of the ion beam within the cup is likely to be significant, reducing the ion density and therefore, reducing the likelihood of space charge distortion. In any case, it is possible that the signals observed by Gupta *et al.* were distorted by the space charge effect.

Conclusion

Although there are a few outstanding questions, the understanding of the physical situation of space charge distortion of Faraday cup ion signals has been greatly enhanced. From the results of Figure 2-29, it appears that the single-particle analytical model may be insufficient to describe the physical situation. The analytical results appear to overestimate the distortion caused by space charge effects (by a factor of ~4-5). The excellent agreement between the experimental results and the two-particle simulations indicates that electrons play an important role in the non-ideal operation of a Faraday cup detector. This role can be further investigated using a combination of experiment, simulation, and analytical modeling. Also in the future, the issue of secondary electron emission and its role in the present experimental configuration should be addressed.

Finally, ion detectors have been selected to be used in the nanosecond and femtosecond ion emission studies. Langmuir probes have been chosen because of their simplicity, and because the use of Faraday cup detectors is not practical for the experimental conditions of the present work. Although these detectors are susceptible to secondary electron emission, this emission is either small or can be corrected for under the experimental conditions.

Chapter 3:
Ion Emission from Plasmas Produced by ns Laser Pulses

Background

a) Pulsed Laser Deposition

Having addressed the issue of ion detectors, the characterization of the ion emission produced in the nanosecond regime will now be discussed. Low intensity (10^8-10^{10} W/cm^2) nanosecond laser-produced plasmas occur in a variety of contexts. Many industrial applications of lasers, such as laser machining, involve the generation of such plasmas. Additionally, techniques such as laser induced breakdown spectroscopy (LIBS) and micromachining involve laser-matter interactions in this intensity regime.

One of the most important uses of ion emission from laser-produced plasmas is the process of pulsed laser deposition (PLD). PLD is a particularly versatile technique used to produce a thin film of material on a substrate (Figure 3-1). A laser pulse incident on a target creates a flux of target material referred to as the ablation plume. This plume, consisting of ions, electrons, and neutral particles, is then deposited on a nearby substrate (Figure 3-1).

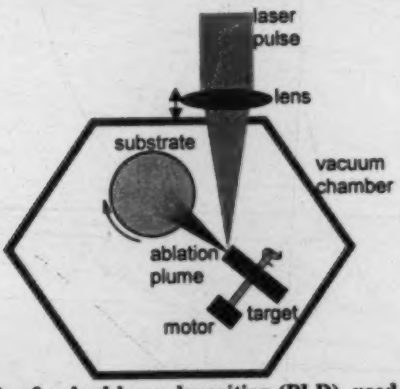

Figure 3-1. A schematic of pulsed laser deposition (PLD), used to deposit a thin film of material on a substrate.

PLD can be used with a variety of materials. Zinc oxide, a semiconductor, has attracted interest due to its broad optical transparency and its conductive properties (when sufficiently doped). Such properties make it ideal for its use in transparent electrodes for flat-panel displays or solar cells [Cla02]. Zinc oxide is also an ultraviolet wavelength emitter; researchers are seeking to exploit this property to create ultraviolet lasers or ultraviolet light-emitting diodes [Yan03].

Recent interest in PLD has focused on carbon, and in particular, the production of diamond-like carbon films via the ablation of graphite targets. Diamond-like carbon (DLC) is a form of amorphous carbon which contains sp^3 hybridized bonds normally found in diamond. DLC films have a number of interesting properties, including high mechanical hardness, optical transparency,

chemical stability, and high thermal conductivity. Potential applications of DLC films include protective coatings [Col92] and high temperature capacitors [Rob02].

Various groups have attempted to produce DLC films under a variety of experimental conditions, ranging from nanosecond low intensity (10^8-10^{10} W/cm^2) lasers at ultraviolet and infrared wavelengths [Cla01 and references within, Vic99] to femtosecond high intensity (10^{14}-10^{17} W/cm^2) lasers at infrared wavelengths [Qia95, Van98b]. These groups have achieved mixed results, with varying degrees of film quality (measured in terms of the fraction of sp^3 hybridized bonds contained in the film). To date, some of the highest quality films (85% sp^3 hybridized bonds) have been produced using ultraviolet radiation (248 nm) at a laser intensity of $1x10^9$ W/cm^2 [Wei04]. Similar results (>90% sp^3 hybridized bonds) have been produced using ultraviolet radiation (193 nm) at a similar intensity ($5x10^8$ W/cm^2) [Cla01]. While the understanding of the physical processes involved in PLD is far from complete, it is clear that the ion energy plays an important role. It is believed that ion energies in the range of 90-140 eV enhance the likelihood of sp^3 bond formation [Hav03, Rob94]. Energies substantially below [Wei04] or above [Van98b] this range result in lower-quality films, although this claim is disputed by C. B. Collins *et al.*, who reported very high quality DLC films using higher ion energies (~2 keV) [Col92]. Other film properties, such as conductivity, have also been shown to vary with the ion energy [Pap92]. Some investigators have claimed that the charge state Z of the ions is important [Col92]. For DLC film production via plasma chemical vapor deposition, the electron temperature is an important factor [Ike05]; presumably, the same can be said of the electron temperature in the PLD technique. Clearly, characterization and control of the ion emission from nanosecond laser-produced plasmas is important in predicting and improving the quality of deposited films.

Of course, PLD can employ a wide variety of target materials, and this versatility is one of the chief advantages of the technique. The films that are produced vary widely in quality, in terms of film-substrate adhesion and quality of the crystal (orderliness of the growth, i.e. epitaxy). Film quality depends chiefly on the characteristics of the ion flux, such as ion energy and angular distribution, as well as other deposition parameters such as substrate to target distance. Excessive ion energies can be detrimental, causing substrate damage or sputtering of the deposited film. An enhanced understanding of the characteristics of ion emission from laser-produced plasmas would allow better control of the ion flux, enabling users to produce higher quality films. Additionally, monitoring of ion characteristics during a deposition can be used to ensure the reproducibility of the plasma plume characteristics, and thereby the characteristics of the deposited films.

Lastly, an experiment intended to demonstrate the utility of the ion flux emitted from the nanosecond laser-produced plasma is described. The production of a porous diamond-like carbon (DLC) film was attempted, using the pulsed laser deposition (PLD) technique. To obtain a porous film, the glancing angle deposition (GLAD) geometry was employed [Vic99]. A schematic of the experimental setup is given in the figure below.

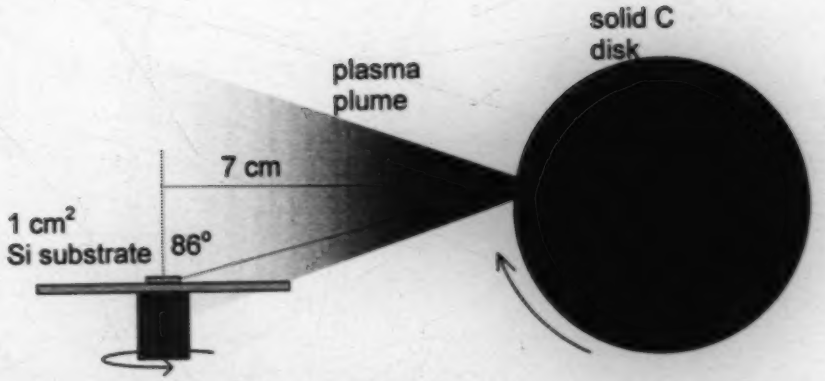

Figure 3-2. A schematic of the experimental setup used to produce DLC films via PLD. The incident laser pulses which generate the plasma plume are not shown.

To perform the deposition, the KrF laser system (described extensively in the next section) was operated at a repetition rate of 20 Hz. A 70 cm lens focused the 248 nm 15 ns pulses on the graphite target. The deposition lasted ~90 minutes, corresponding to ~1.1×10^5 laser pulses. The average pulse energy on target was measured to be 68 mJ, and the lens-to-target distance was 50.8 cm, corresponding to an intensity of 1.1×10^{10} W/cm^2. The 1 cm^2 silicon substrate was positioned 7 cm away from the target, at a GLAD deposition angle of 86°. A scanning electron micrograph of the resultant film is given in the figure below. The image was produced using the JEOL 6301F field emission scanning electron microscope in the University of Alberta's Department of Earth and Atmospheric Sciences.

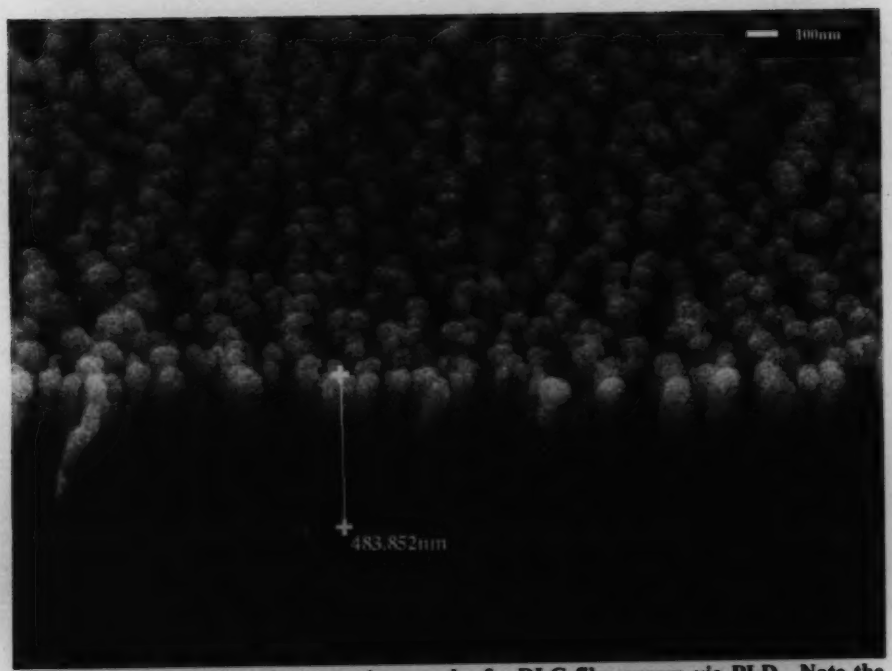

Figure 3-3. A scanning electron micrograph of a DLC film grown via PLD. Note the nano-column structure of the film which is typical of the GLAD technique. Note that the film is viewed from an angle of elevation of 56°, so that the true thickness of the film is 584 nm.

Notice the interesting nano-column structure of the film, which is a hallmark of the GLAD technique. The nanostructures range from 70-110 nm in width. The overall film thickness is 584 nm, corresponding to a deposition rate of 0.054 Å/pulse. Due to the nanostructures, the film is quite porous. Based on scanning electron micrographs of the top of the film, it is estimated that 46% (by volume) of this film is empty space.

Now, since it is well-established that the film properties vary with the characteristics of the ion flux, it would be interesting to perform a systematic study of the variation of the film characteristics with the variation in the characteristics of the ion emission. The purpose of this chapter is to enable this or similar investigations by studying the ion emission from laser produced plasmas in the nanosecond low intensity (10^8-10^{10} W/cm^2) regime. In particular, the energy distribution and the angular distribution of the ion flux are measured, and the intensity dependence of these distributions is investigated. This information can be used to enhance the understanding of the important role of ions in applications such as PLD.

b) Laser-Matter Interaction Theory

The basic theory underlying laser-matter interactions will now be described. When a laser pulse is incident on matter, some of the laser energy is absorbed, and some is reflected. The absorbed energy can give rise to a

tremendous variety of physical phenomena. The importance of these various effects depends on the conditions under which the laser-matter interaction takes place. One of the most important parameters is the incident laser intensity, which can range over many orders of magnitude. At very low intensities, the absorbed laser energy simply heats the target material. This absorption of the laser energy can be described according to the Drude model [Kit95]. In this model, the target material, usually a metal such as copper or aluminum, consists of a sea of free electrons within an ion lattice. The electric field of the laser pulse accelerates the electrons, causing them to oscillate at the optical frequency. As the electrons move, they collide with other electrons, with an associated electron-electron collision time constant $\tau_{e\text{-}e}$, which is typically of the order of 10^{-14} to 10^{-12} s [Bau00]. The absorption of the laser energy occurs when these oscillating electrons collide with ions in the lattice, transferring energy to the lattice in the form of phonons (quantized lattice vibrations). This process has an associated electron-phonon collision time constant $\tau_{e\text{-}ph}$, which is typically of the order of 10^{-12} to 10^{-10} s [Bau00]. The large difference between $\tau_{e\text{-}e}$ and $\tau_{e\text{-}ph}$ is due to the large difference in mass between the electrons and the lattice ions. Thus, via collisions, the laser energy thermally heats a small area of the target material, and the laser can simply be treated as a heat source.

The deposited laser energy results in a moderate increase in temperature at the laser spot described by the heat diffusion equation

$$\rho c_p \frac{\partial T(\bar{x},t)}{\partial t} - \nabla[\kappa \nabla T(\bar{x},t)] = Q(\bar{x},t), \qquad \text{(3-1)}$$

where ρ is the mass density, c_p is the specific heat at constant pressure, κ is the thermal conductivity, T is the temperature distribution in the target, and Q is the heat source (in this case, the laser energy) [Bau00]. In general, the solution of the heat equation must take into account the temperature dependence of the material parameters, and therefore numerical methods of solution are usually employed. A schematic of the temperature distribution in the material is given in Figure 3-4a.

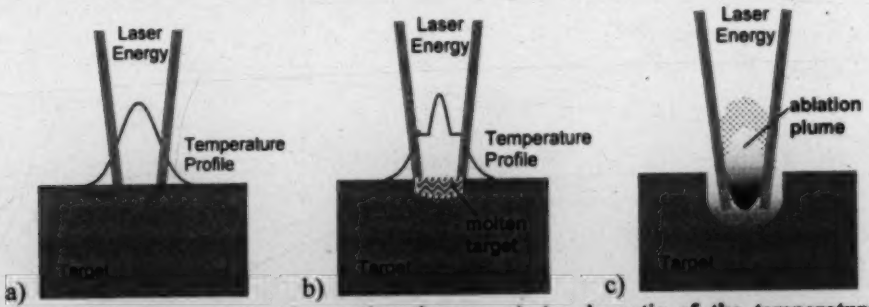

Figure 3-4. Laser-matter interaction theory. a) A schematic of the temperature distribution in a material which results from a deposition of laser energy at low intensity. b) As the incident laser intensity increases, a phase change can occur. The plateau in the temperature profile is caused by the energy required to change states (ΔH_{fus}). c) If the laser intensity reaches the plasma threshold, the target material is vaporized and ionized.

The heat equation must be employed with due caution. For instance, the magnitudes of the collision times compared to the laser pulse length must be considered. If the pulse length is long compared to both collision times, the laser energy is thermalized rapidly, such that a one-temperature model encompassing both ions and electrons will suffice. If, however, the pulse length is comparable to or shorter than the electron-phonon collision time, a two-temperature model distinguishing between electrons and ions must be employed.

Examining Figure 3-4a, a low incident laser intensity (roughly $<10^6$ W/cm^2, depending on the target material and the laser parameters) results in a moderate increase in the temperature of the target material. As the incident intensity increases (~10^7 W/cm^2), a larger amount of energy is deposited into a smaller area of material in a shorter period of time, and if the threshold temperature is reached, a phase change will occur in the material (Figure 3-4b). Increasing the laser intensity further will result in the vaporization (~10^8 W/cm^2) and subsequent ionization (~10^8-10^9 W/cm^2) of the target material (Figure 3-4c). The chief mechanisms of plasma formation are photoionization, in which a target atom is ionized by a sufficiently energetic photon (or by the nonlinear interaction of several photons), and collisional ionization, in which a target atom is ionized by a collision with a sufficiently energetic free electron. As the intensity is further increased (>10^9 W/cm^2), the particles in the plasma become fully ionized.

The intensity regime studied in this chapter is the range ~10^8-10^{10} W/cm^2. Due to the intensity profile of the laser radiation on the target surface, the ablation plume is a complex mix of ions and electrons originating from the peak of the intensity profile and neutral particles originating from the lower intensity region of the profile. The total ablation plume thus consists of two components: a higher energy plasma plume and a lower energy vapor plume. In this transition region between a vapor and a fully ionized plasma, the average charge state $\bar{Z}$ of the ions is an important parameter. This parameter will be discussed further later in this chapter. The behavior of a fully ionized laser-produced plasma has been studied extensively. There exist several theoretical models to describe the behavior of this plasma in the 10^{11}-10^{14} W/cm^2 intensity range. These models have been quite successful in describing the laser-matter interaction in this intensity regime [Git86, Gup86, Gup87, Ng84, Tsu92]. One of the aims of the present work is to evaluate the possibility of extending the applicability of these theoretical models to lower intensities.

The theoretical models will now be described in some detail. The first is a comprehensive self-regulating model due to P. Mora which describes the interaction [Mor82]. The leading edge of the laser pulse creates a coronal plasma, which then interacts with the remainder of the laser pulse. In the self-regulating model, the laser pulse is sufficiently long that a steady state heat flow between the various target regions is reached. A schematic of the laser-matter interaction described by the self-regulating model is given in Figure 3-5.

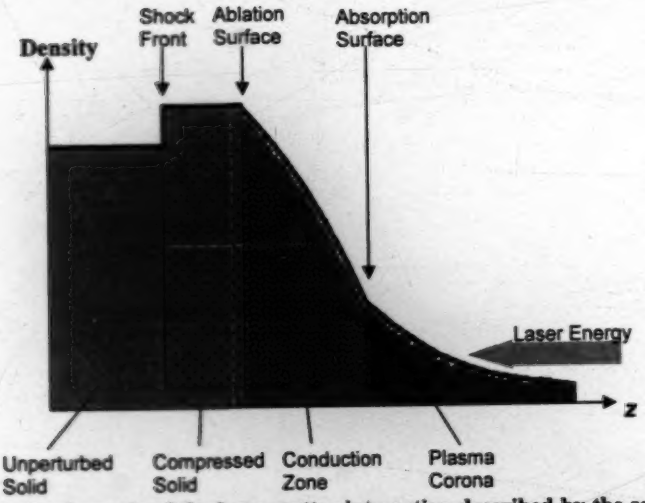

Figure 3-5. A schematic of the laser-matter interaction described by the self-regulating model due to Mora. The vertical axis represents the particle density, and the horizontal axis represents the distance *z* along the laser propagation axis.

At steady state, the incident laser energy is absorbed by an expanding plasma corona, and the energy is transferred through the conduction zone to the ablation surface, where the target material is vaporized. The large inward pressures generated during the ablation process result in the formation of a compression wave which propagates into the material.

The use of the term "self-regulating" is due to the fact that the generation of the coronal plasma regulates itself. The coronal plasma absorbs most of the laser energy, shielding the solid target, resulting in a slower rate of plasma generation. As this plasma expands, more laser energy reaches the target, allowing a greater ablation rate, and so on.

The self-regulating model rests on several assumptions. The most important, of course, is that the laser pulse is of sufficient duration to establish a steady state heat flow. Additionally, the laser intensity is assumed to be constant for the duration of the pulse; however, this is usually not the case.

The self-regulating model employs the fluid equations to describe the density profile of the expanding isothermal coronal plasma. Specifically, the continuity equation

$$\frac{\partial \rho}{\partial t} + \frac{\partial \rho v_f}{\partial x} = 0, \qquad (3\text{-}2)$$

and the momentum transfer equation

$$\frac{\partial \rho v_f}{\partial t} + v_f \frac{\partial \rho v_f}{\partial x} + \frac{\partial p}{\partial x} = 0, \qquad (3\text{-}3)$$

are used in a one dimensional planar geometry, where p is the pressure, v_f is the fluid velocity, and ρ is the mass density. Additionally, the expanding plasma is treated like an ideal gas, using

$$p = n_e k_B T_e \quad \text{(3-4)}$$

as the equation of state, where k_B is Boltzmann's constant, T_e is the electron temperature, and n_e is the electron density. Note that the assumption of an isothermal coronal plasma is reasonable, since the Spitzer-Harm equation for the thermal conductivity of a plasma

$$\kappa \propto T_e^{5/2} \quad \text{(3-5)}$$

demonstrates that the thermal conductivity of a plasma is strongly temperature dependent, so that at high temperatures, the thermal conductivity is relatively high [Spi62].

The solution to the fluid equations is an exponentially decaying density profile:

$$\rho = \begin{cases} \rho_0 & x \le -c_s t \\ \rho_0 \exp\left[-\left(1+\dfrac{x}{c_s t}\right)\right] & x > -c_s t \end{cases} \quad \text{(3-6)}$$

where c_s is the ion acoustic velocity, given by

$$c_s = \sqrt{\frac{\bar{Z} k_B T_e}{m_i}}, \quad \text{(3-7)}$$

with m_i as the ion mass and $\bar{Z}$ as the average charge state of the plasma ions. The exponentially decaying density profile is depicted schematically in Figure 3-5.

The absorption of the laser energy by the coronal plasma is described by the inverse bremsstrahlung absorption mechanism. The process of absorption in a plasma is similar to the process of absorption in a metal discussed earlier; the only difference is that the ions are free to move rather than being confined to a lattice. In this case, electron-ion collisions result in the transfer of energy from the optical fields to the plasma. Thus, the radiation intensity I_r is exponentially damped as it propagates through the coronal plasma:

$$I_r = I_0 \exp(-\alpha x). \quad \text{(3-8)}$$

The absorption coefficient for the inverse bremmstrahlung process is

$$\alpha_{IB} = \frac{e^4}{3(2\pi)^{3/2}(m_e c^2)^{1/2}\varepsilon_0^2 k_B^{3/2}} \bar{Z} \ln\Lambda T_e^{-3/2} n_c \left[\frac{n_e}{n_c}\right]\left[1-\frac{n_e}{n_c}\right]^{-1/2} \quad \text{(3-9)}$$

where

$$\ln\Lambda = \ln\left[\frac{3}{2}\frac{(4\pi\varepsilon_0)^{3/2}}{\bar{Z}e^3}\left(\frac{k_B^3 T_e^3}{\pi m_e}\right)^{1/2}\right] \quad \text{(3-10)}$$

is the Coulomb logarithm and

$$n_c = \frac{4\pi^2 m_e \varepsilon_0 c^2}{e^2 \lambda_L^2} \quad \text{(3-11)}$$

is the critical density of a plasma, and e is the elementary charge, ε_0 is the permittivity of free space, m_e is the electron mass, c is the speed of light, and λ_L is the laser wavelength [Bau00]. The absorption coefficient depends on the plasma density, charge state, and temperature, all of which are unknown *a priori*. Thus,

the calculations involved in the self-regulating model must often be performed iteratively, depending on the desired level of accuracy. Now, by convention, the absorption surface (Figure 3-5) is defined as the point x_0 at which the laser radiation has been attenuated by a factor exp(-2). For convenience, the model assumes that all of the absorption occurs at this point. Then, based on energy considerations,

$$\frac{\partial}{\partial t}\left[\frac{3}{2}n_e k_B T_e + \frac{1}{2}\rho v^2\right] + \frac{\partial}{\partial x}\left[\frac{3}{2}n_e v k_B T_e + \frac{1}{2}\rho v^3\right] + \frac{\partial Q}{\partial x} + \frac{\partial pv}{\partial x} = I_A \delta(x - x_0) \quad \textbf{(3-12)}$$

where Q is the heat flux and I_A is the absorbed laser energy. The model requires one final assumption: the conduction zone is assumed to have reached steady state; that is, both the thickness of the conduction zone and the heat flux into the zone are constant. Using the above equations and assumptions, the electron temperature, mass ablation rate and ablation pressure can be calculated for given experimental conditions. The electron temperature is given by

$$\frac{k_B T_e}{e} = \left[\frac{e^2 m_i^{1/2}}{192(2\pi)^{7/2} m_e^{3/2} c^3 \varepsilon_0^3}\right]^{1/4} \bar{Z}^{1/8} \lambda_L^{1/2} (\ln \Lambda \tau_L)^{1/4} I_A^{1/2} \quad \textbf{(3-13)}$$

where τ_L is the laser pulse duration. Recall that the electron temperature evolves in time, as the plasma plume expands and cools. This temperature represents the maximum temperature attained by the plasma, before any significant expansion and cooling take place. The mass ablation rate is given by

$$\frac{dm}{dt} = \left[\frac{3}{4}\frac{(2\pi)^{7/2} m_e^{3/2} m_i^{7/2} c^3 \varepsilon_0^3}{e^6}\right]^{1/4} \bar{Z}^{-9/8} \lambda_L^{-1/2} (\ln \Lambda \tau_L)^{-1/4} I_A^{1/2}. \quad \textbf{(3-14)}$$

The ablation pressure is given by

$$p_A = \left[\frac{3}{4}\frac{(2\pi)^{7/2} m_e^{3/2} m_i^{7/2} c^3 \varepsilon_0^3}{e^6}\right]^{1/8} \bar{Z}^{-9/16} \lambda_L^{-1/4} (\ln \Lambda \tau_L)^{-1/8} I_A^{3/4}. \quad \textbf{(3-15)}$$

Note that these equations apply to a one dimensional planar expansion.

The self-regulating model is complemented by a simple gas expansion model which describes the expansion of the hot plasma plume. Specifically, this model provides a method of estimating the final or terminal ion velocity after the expansion of the hot plasma converts the internal energy of the plasma into the kinetic energy of its constituents. The total energy per unit volume of the plasma consists of the thermal energy of the plasma, the ionization energies of the individual ions, the energy stored in the pressure gradient of the plasma, and the kinetic energy of the plasma:

$$E = \frac{3}{2}\left(1 + \bar{Z}\right) n_i k_B T_e + n_i \sum_{i=1}^{\bar{Z}} U_i + p + \frac{1}{2}\rho v^2, \quad \textbf{(3-16)}$$

where U_i represent the ionization energies, and n_i is the ion density [Tsu92]. Recall that the characteristics (e.g. particle density, temperature) of the plasma plume evolve as the plume expands and cools. After the plasma has expanded and cooled, the pressure and temperature are assumed to be negligible, as the thermal and pressure gradient energy are converted into kinetic energy. The ionization energy may also be converted into kinetic energy via recombination,

but the importance of this process is indeterminate. Consequently, two extreme cases can be considered: no recombination, so that the ionization energy remains stored in the plasma, and full recombination, so that most of the ionization energy is converted into kinetic energy. For the case of no recombination, the terminal velocity (v_∞) is given by

$$v_\infty = \sqrt{\frac{(\bar{Z}+1)}{m_i}\left(\gamma^{*}+5\right)k_B T_e} \qquad \text{(3-17)}$$

and for the case of full recombination, the terminal velocity is given by

$$v_\infty = \sqrt{\frac{(\bar{Z}+1)}{m_i}\frac{\gamma^{*}+1}{\gamma^{*}-1}\gamma^{*}k_B T_e}\,, \qquad \text{(3-18)}$$

where γ^{*} is the effective heat capacity ratio (analogous to the ratio of heat capacities at constant volume and constant pressure $\gamma=c_v/c_p$ for ideal gases) given by

$$\gamma^{*} = 1+\frac{(1+\bar{Z})k_B T_e}{\frac{3}{2}(1+\bar{Z})k_B T_e+\sum_{i=1}^{\bar{Z}}U_i}. \qquad \text{(3-19)}$$

In the present work, the estimate $\gamma^{*}\sim 1.3$ is used. Another model for the plume expansion is also used in the literature [Amo97, Cla01, Koi99], but it is not discussed here.

To reiterate, these theoretical models have been very successful in describing nanosecond laser-matter interactions in the 10^{11}-10^{14} W/cm^2 intensity regime. The intensity scaling laws for the electron temperature [Git86, Gup86], mass ablation rate [Gup87, Ng84], ablation pressure [Gup87, Ng84], and the predicted ion velocities [Git86, Tsu92] have all been found to agree with experiment. This success is largely due to fact that in this intensity regime, laser-produced plasmas are fully ionized. An important question which will be addressed in this chapter is the applicability of these models to lower laser intensities (10^8-10^{10} W/cm^2). At these lower intensities, the plume of ablated target material is more complex, consisting of neutral particles and clusters, in addition to ions and electrons. Note that the ions are more energetic than the neutral particles, so that for the most part, the plasma plume will lead the vapor plume as the ablation plume expands.

c) Literature Survey

Due to the importance of laser-produced plasmas for applications such as pulsed laser deposition, a number of groups have conducted experimental investigations into the characteristics of the plasma plume produced by laser-matter interactions in the nanosecond 10^8-10^{10} W/cm^2 intensity regime. Using a variety of laser systems (XeCl, KrF, Nd:YAG) and targets (C, Al, Ta, etc.), groups have investigated the kinetic energy, angular distribution, and total number of ions emitted by laser-produced plasmas [Amo97, Cla01, Din80, Gup87, Koi99, Las03, Mis99, Nov99, Rup91, Rup95, Thu00a, Thu00b, Zha02]. For instance, using a XeCl laser with a 20 ns pulse duration incident on a graphite target, K. J. Koivusaari *et al.* measured a peak ion energy ranging from 50eV to 450 eV for

intensities in the range 0.5-2x10^9 W/cm^2 [Koi99]. On the other hand, using the 3rd harmonic of an Nd:YAG laser (τ_L=6 ns) incident on an aluminum target, S. Amoruso *et al.* observed slightly less energetic ions (10-100 eV) for intensities in the range 1-5x10^9 W/cm^2 [Amo97]. Regarding the angular distribution of the ion emission, using an Nd:YAG laser (τ_L=9 ns, I_L=1.6x10^{10} W/cm^2), L. Laska *et al.* fitted the peak ion current density values with a $\cos^n$ distribution, and found that the value of n ranges from 4 for an aluminum target to 33 for a tungsten target [Las03]. These results will be discussed further in the Results and Discussion section.

Experiment

A schematic of the experimental setup is given in Figure 3-6. The experimental configuration is similar to that described in the previous chapter, and is repeated here. For the experiments, a Lumonics Excimer-500 KrF 248 nm laser was employed. This laser provided ~40-130 mJ pulses on target, with 15 ns duration. The laser energy actually varied during an experiment, depending on the state of the gases in the laser cavity. The laser energy was highest after a refill of gas, and it gradually decreased over time as the laser was used.

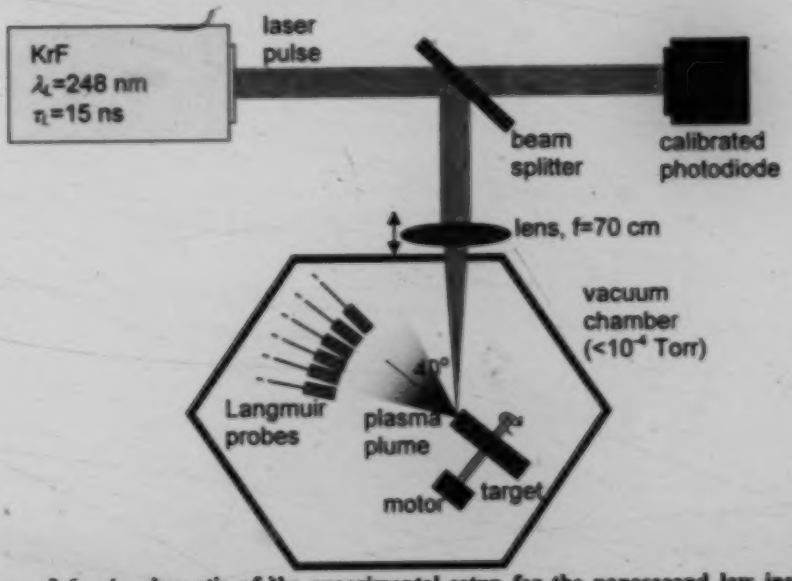

Figure 3-6. A schematic of the experimental setup for the nanosecond low incident intensity experiments.

The laser was operating in the unstable resonator configuration, producing a multimode rectangular beam [Sal91]. The laser pulses were focused onto the target using a planoconvex lens with a 70 cm focal length, located 3 m away from the laser output. The longitudinal position of the lens was variable, and this provided a means to control the laser spot size (and thus the laser intensity) on

target. In a separate measurement, the laser spot size on target was determined, using a filtered CCD camera (COHU 6612D), with image capturing software (Spiricon LBA-400PC). An example image is provided in the figure below.

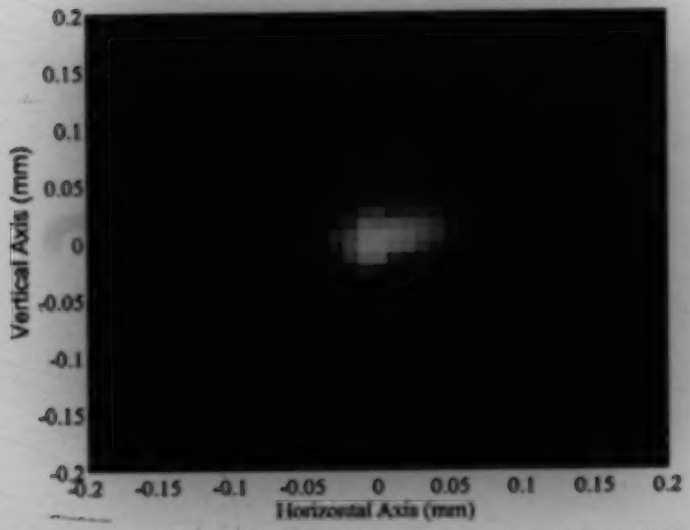

Figure 3-7. An example digitized image of the laser spot on target, obtained using a filtered CCD camera. This particular image was taken at a lens-to-target distance of 52.8 cm, which is close to the best focus.

It is clear from the figure above that the focal spot is asymmetric. The asymmetry worsens for larger focal spots (at smaller lens-to-target distances). This is largely due to the multimode quality of the laser beam itself. The asymmetry is revealed more readily by one-dimensional cross-sections through the peak intensity point of the focal spot (see figures below).

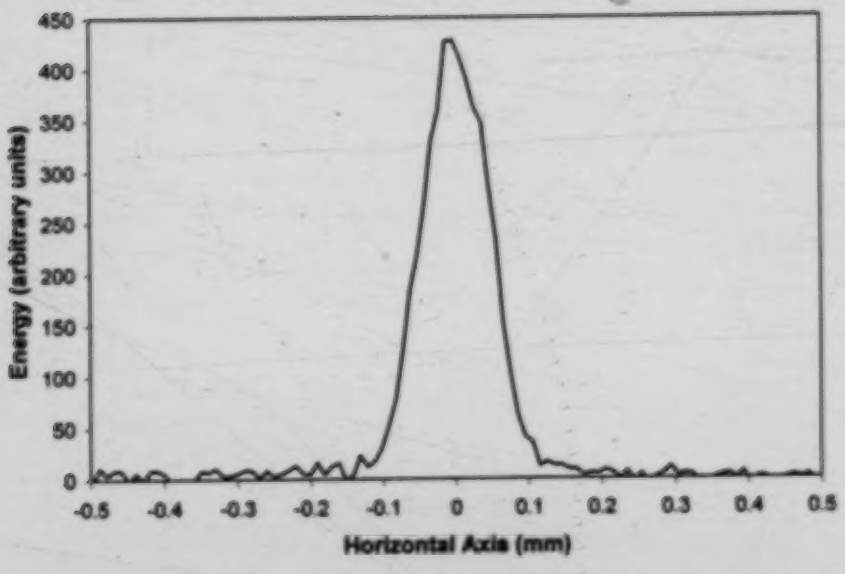

Figure 3-8. A one-dimensional cross-section through the focal spot image, along the horizontal axis.

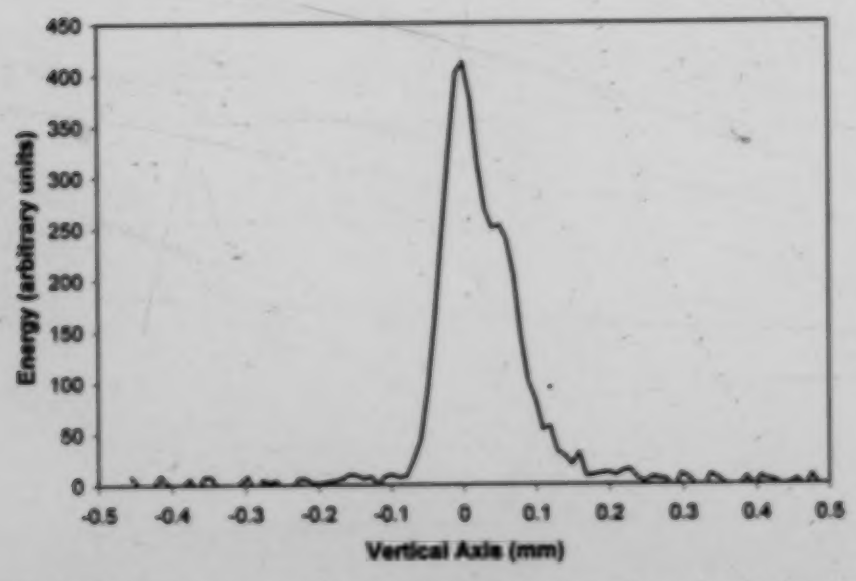

Figure 3-9. A one-dimensional cross-section through the focal spot image, along the vertical axis.

Although not quite Gaussian, the beam profile along the horizontal axis looks reasonable. The beam profile along the vertical axis, however, exhibits a secondary lobe. This asymmetry has implications for the behavior of the laser-matter interaction. The peak of the energy profile in the figure above corresponds to the peak of the intensity profile, which generates the plasma present in the ablation plume. The lower energy regions of the profile, and in particular, the secondary lobe, correspond to lower intensity regions of the intensity profile. These lower intensity regions still contain sufficient energy to ablate the target material, producing a slower-moving vapor plume which may interact with the plasma portion of the ablation plume in a complex fashion. This issue will be discussed further in the next section.

Assuming the digitized pixel values from the camera are proportional to the energy of the laser beam incident on a pixel, the area which contains 90% of the laser energy was calculated. This area can be considered to be the size of the focal spot, and the method is referred to as the 90% contour method [Gup87]. For the figure above, the focal spot area was calculated to be 2.2×10^{-4} cm^2. Three shots at each lens-to-target distance were taken, and the results were averaged. The resulting averages for various lens-to-target distances are given in the figure below.

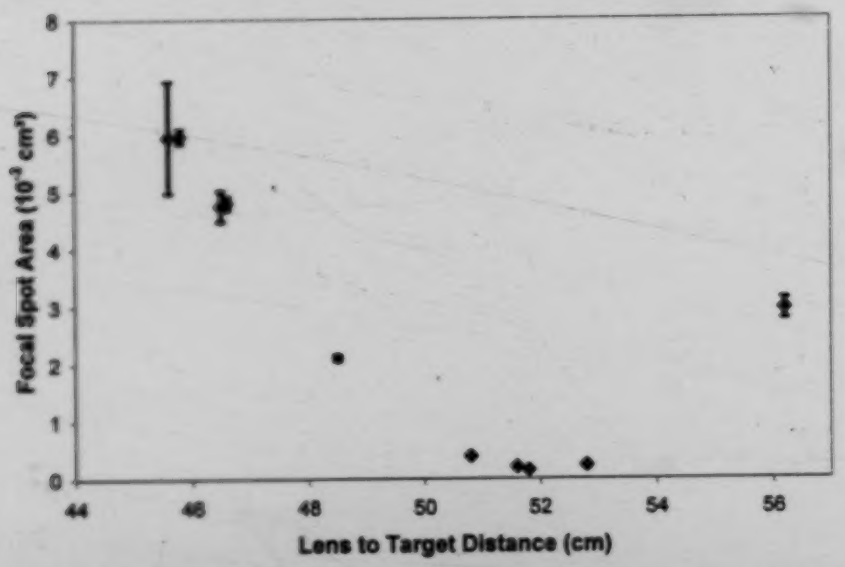

Figure 3-10. The results of the focal spot size measurements for the KrF laser using a 70 cm lens, performed using a filtered CCD camera. The focal spot area is calculated using the 90% contour method.

The error bars represent the difference between the largest and smallest calculated areas in each set of three laser shots. For the lens-to-target distances between 48 and 54 cm, the error ranges from 8-16%.

The photodiode, positioned before the lens as in Figure 3-6, was calibrated using a calorimeter (painted pyroelectric crystal) with a sensitivity of 2.67 V/J. The laser energy on target (E_L) could thus be calculated (assuming 92% transmission through the lens, and 92% transmission through the vacuum chamber window) for each pulse. The laser intensity (I_L) was calculated according to

$$I_L = \frac{0.90 E_L}{A_{90} \tau_L} \quad \text{(3-20)}$$

where τ_L is the nominal pulse duration (15 ns), and A_{90} is the focal spot area calculated according to the 90% contour method. Throughout this chapter, the intensity on target is varied by adjusting the lens-to-target distance d_L, which varies the focal spot area. The dominant source of error in the intensity calculation is the uncertainty in the focal spot area.

This intensity calculation is not uniformly employed in the literature. Some authors report the value for the peak of the intensity profile on target. Equation 3-20 above represents an intensity value which is averaged over the intensity profile on target (see figure below).

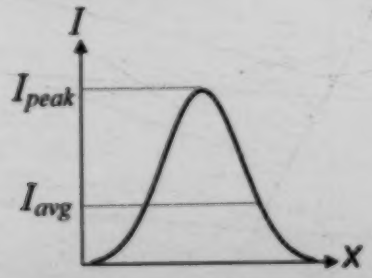

Figure 3-11. A schematic intensity profile along a spatial coordinate. Some authors report the peak intensity value, whereas Equation 3-20 represents an intensity value which is averaged over the area of the 90% contour (A_{90}).

In the present work, it was found that the average intensity (calculated according to Equation 3-20 above) was generally smaller than the peak intensity by a factor of ~2.

The target was either a solid graphite disk, or a solid zinc oxide disk. These targets were rotated using a DC motor in order to provide a fresh target area for each laser pulse. The angle of incidence of the laser pulses on target was approximately 40° (with respect to the target normal).

The vacuum chamber pressure was 2×10^{-4} Torr (as measured with an Edwards Active Magnetron Gauge, AIM-S-NW25). This pressure is not sufficiently low to rule out the possibility of charge exchange between the ions of the plasma plume and the background gas. Thus, the presence of the background gas may influence the results described in the next section, and in particular, may increase the fraction of neutral particles present in the ablation plume.

The Langmuir probes used to detect the ion component of the plasma plume were located at distances of 17-18 cm from the carbon target, and 16-18 cm

from the zinc oxide target, in the plane of the incident laser pulse, at angles ranging from 6° to 60° (with respect to target normal). The detector angles were measured with a precision of ± 0.5°. The probes were biased with a variable voltage supply. The probes were terminated with 50 Ω resistors (Figure 2-9), and the ion signals were displayed using Tektronix TDS210/220 oscilloscopes.

Results and Discussion

a) Angular Distribution Results

A typical Langmuir probe signal is given in the figure below. More examples of Langmuir probe data are included in the Appendix.

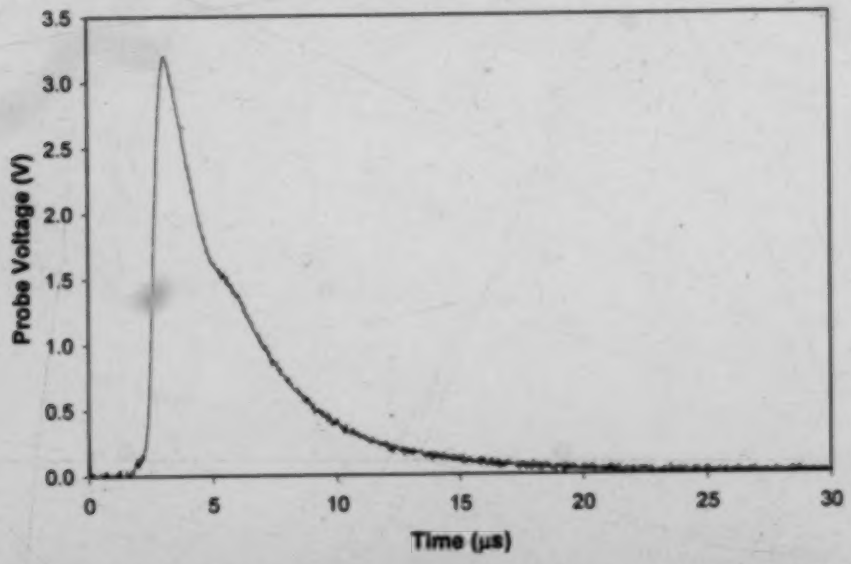

Figure 3-12. A typical ion signal collected by a Langmuir probe. This particular signal was produced at a laser intensity of ~2.1x10^{10}W/cm^2 (E_L=79.3 mJ, d_L=52.8 cm) incident on a carbon target, for a probe positioned 18 cm from the target, at an angle of 6°, biased at -40 V. Time zero represents the instant when the laser pulse strikes the target.

For the majority of the laser shots, the signals typically consisted of a single peak. This single peak is composed of so-called thermal ions, which have been heated by the laser energy at the peak of the intensity profile and subsequently expand into the vacuum. This group of ions can be further subdivided into ions with different charge states (Z); for the figure above, the signal probably consists of some combination of C^+, C^{2+}, and C^{3+} ions. The issue of the ion charge state remains an open question, since the Langmuir probe detectors cannot distinguish between ions of different charge states. The detectors are sensitive only to charge; to obtain a value for the absolute number of ions incident on the detector, the charge must be divided by an estimated average value for the charge state $\overline{Z}$.

In the results below, the assumption $\overline{Z}$ =+1 is made, with the understanding that any given value for an absolute number of ions should be divided by the true average charge state $\overline{Z}$. The issue of charge state will be discussed further below.

For the ZnO laser shots, depending on the applied bias voltage and the detector angle, the Langmuir probe signals were more complex, at times consisting of two or more peaks, indicating the presence of multiple groups of ions. This observation has been corroborated elsewhere. F. Claeyssens *et al.* [Cla02] have reported their observations of the plasma plume arising from a ZnO target (193 nm ArF laser, τ_L~20 ns, I_L=0.25-1x10^9 W/cm^2). This group attributed the multiple peaks to groups of Zn^{2+}, Zn^+, and O^+ ions. The bulk of the ion signal (i.e. the dominant peak) was attributed to a group of thermal Zn^+ and O^+ ions based on optical emission spectroscopy data. On this basis, it is assumed that the dominant species in the plasma plume are Zn^+ and O^+. Where necessary (such as for ion energy calculations), for consistency, it is arbitrarily assumed that the mass of the ions is that of oxygen.

Now, the aim of this chapter is to characterize the group of thermal ions which are emitted from the laser-produced plasma. To this end, the peak energy, peak current density, and angular distribution of the ion emission were all investigated. The electron temperature of the laser-produced plasma was also investigated. Furthermore, the energy spectrum of the ion emission was calculated.

The two figures below summarize the angular distribution of the peak ion energy for different laser intensities for two different target materials. The peak ion energy was defined by the time-of-flight of the ions arriving at the peak of the ion signal (Equations 2-5 and 2-6), in accordance with the literature.

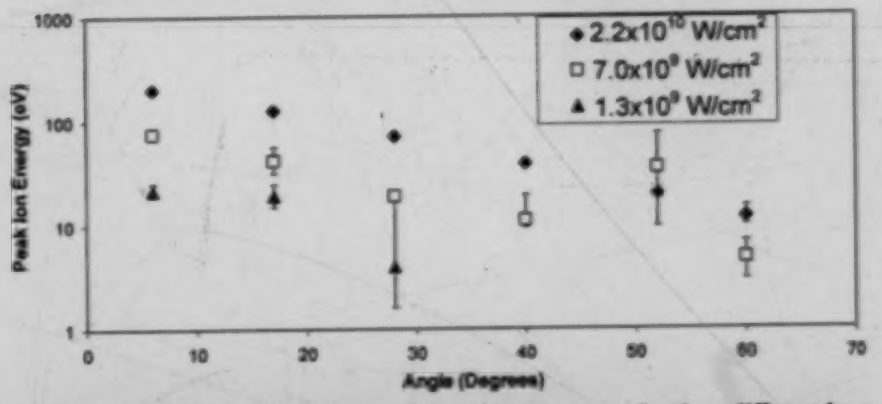

Figure 3-13. The angular distribution of the peak ion energy, for three different laser intensities incident on a carbon target. The (averaged) laser parameters were as follows: I_L=2.2x10^{10} W/cm^2, E_L=83.2 mJ, d_L=52.8 cm; I_L=7.0x10^9 W/cm^2, E_L=45.3 mJ, d_L=50.8 cm; I_L=1.3x10^9 W/cm^2, E_L=126.5 mJ, d_L=45.8 cm. Each data point represents the average of at least 7 laser shots.

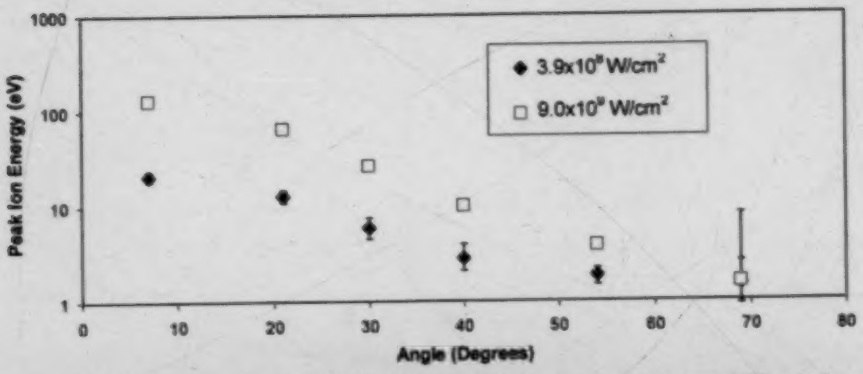

Figure 3-14. The angular distribution of the peak ion energy, for two different laser intensities incident on a zinc oxide target. The (averaged) laser parameters were as follows: I_L=9.0x10^9 W/cm^2, E_L=77.1 mJ, d_L=53.4 cm; I_L=3.9x10^8 W/cm^2, E_L=62.5 mJ, d_L=59.9 cm. Each data point represents the average of at least 7 laser shots. In the calculation of the ion energy, it was assumed that the ion species is oxygen.

Each data point in the above graphs represents the average of at least 7 laser shots. The shot-to-shot variation (usually 5-10%) in the peak ion energy was the dominant source of error in this measurement. The error bars represent the difference between the maximum and minimum measured peak ion energies, for each set of at least 7 laser shots.

It is clear that the most energetic ions are directed toward the target normal. This observation is supported by the results of F. Claeyssens *et al.* [Cla01]. Claeyssens *et al.* used a 193 nm ArF laser (τ_L~20 ns, I_L=1x10^9 W/cm^2) to ablate a graphite target, and observed a peak ion energy of ~110 eV at a detector angle (θ_p) of 0° (measured with respect to the target normal) fall off to ~85 eV at 25°. However, their experiment involved the rotation of the entire target while keeping the laser and the detector fixed, so that the angle of incidence of the laser on the target was changed in addition to the detector angle.

To determine the relationship between the peak ion energy and the incident laser intensity, the results for both targets are plotted in the figure below. These results are taken from the detector positioned at the angle closest to the target normal. Additionally, for the purposes of comparison, data from several other groups has been included. Using a XeCl laser with a 20 ns pulse duration incident on a graphite target, K. J. Koivusaari *et al.* measured a peak ion energy ranging from 50eV to 450 eV for intensities in the range 0.5-2x10^9 W/cm^2 [Koi99]. Using the 3rd harmonic of an Nd:YAG laser (τ_L=6 ns) incident on an aluminum target, S. Amoruso *et al.* observed slightly less energetic ions (10-100 eV) for intensities in the range 1-5x10^9 W/cm^2 [Amo97]. F. Claeyssens *et al.* [Cla01] used an ArF laser system (λ_L=193 nm, τ_L~20 ns, E_L=10-110 mJ, I_L=0.1-1.3x10^8 W/cm^2) to ablate a graphite target, producing ions ranging in peak energy from 70-140 eV. Y. Y. Tsui [Tsu92] used a KrF laser system (λ_L=248 nm, τ_L=2 ns, I_L=0.02-1x10^{13} W/cm^2) and found excellent agreement between the intensity scaling predictions of the self-regulating model and the observed ion energies.

The line in the figure below represents the best fit to this data set. Additionally, Tsui also used a ruby laser (λ_L=694 nm, τ_L~25 ns, I_L=1x10^{11} W/cm^2) to produce 640 eV carbon ions, and a separate KrF laser (λ_L=248 nm, τ_L~20 ns, I_L=2x10^{11} W/cm^2) to produce 1000 eV carbon ions [Tsu92]. All of this data is included in the figure below.

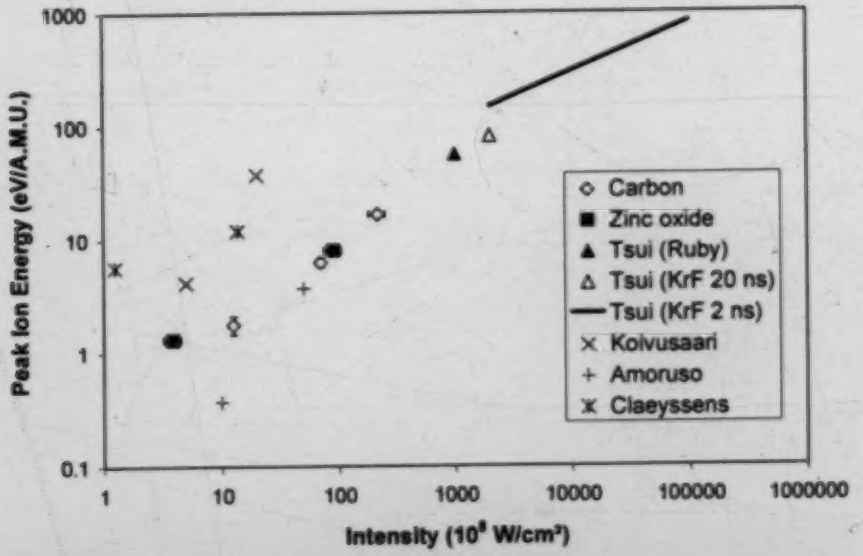

Figure 3-15. The scaling of the peak ion energy with intensity for both carbon and zinc oxide, using the detectors positioned closest to the target normal (θ_p=6-7°). The ion energies have been scaled to the ion mass measured in atomic mass units (A.M.U.), in order to facilitate comparison between results using different targets. The data from other groups is obtained from the following sources: Tsui (Ruby) [Tsu92], Tsui (KrF 20 ns) [Tsu92], Tsui (KrF 2 ns) [Tsu92], Koivusaari [Koi99], Amoruso [Amo97], and Claeyssens [Cla01].

In the present work, the intensity was varied by adjusting the lens-to-target distance to change the focal spot area. Here, the error in intensity due to the error in the focal spot area is included in the graph. Again, the error in the peak ion energy represents the shot-to-shot variation in this measurement.

The peak ion energies observed in the present work and those of Y. Y. Tsui [Tsu92] appear to follow a consistent trend, rising rapidly between 10^9 and 10^{11} W/cm^2 before assuming the $I^{0.44\text{-}0.50}$ scaling consistent with the predictions of the self-regulating model and the simple gas dynamic model. To some extent, the results of the other groups (Amoruso, Claeyssens, and Koivusaari) also follow this trend, exhibiting an increase with intensity towards the predictions of the theoretical models. However, the data of Claeyssens and Koivusaari are separated from the other data on the above graph by a significant gap. The most likely reason for the discrepancy is the calculation of the laser intensity. Claeyssens *et al.* measure the focal spot area using the ablation crater size [Cla01], which is

larger than the true focal spot size, due to the rapid diffusion of heat and energy out of the focal spot area. Thus, the actual intensity of their experiment is likely larger than the quoted 0.1-1.3x10^8 W/cm^2 range. This would shift their data to the right, improving agreement with the general trend. Although Koivusaari *et al.* do not describe their method of calculation of the laser intensity, it is possible that they use the same method. If that were the case, the agreement between their data and the overall trend would also improve. The overall trend is a reflection of the complex nature of the ablation plume in the transitional intensity regime. At the higher intensities (>10^{11} W/cm^2), the data appear to be described well by the self-regulating model, indicating that the plasma is fully ionized. In the transitional intensity regime (10^8-10^{10} W/cm^2), the ablation plume contains a significant fraction of neutral particles in addition to ions and electrons. This issue is discussed further later in this section.

Recall the production of the porous carbon film via PLD described in the first section of this chapter. Now, according to the results of the figure above, the peak ion energy during this deposition can be estimated to be ~110 eV (at an intensity of 1.1x10^{10} W/cm^2). This is comparable to the ~90 eV value quoted by J. Haverkamp *et al.* [Hav03] which would optimize the fraction of sp^3 hybridized bonds in a DLC film. It would be interesting to measure the fraction of sp^3 hybridized bonds in the film, and compare it to some of the values in the literature. Additionally, given the characterization of the ion emission at different laser intensities, it would be interesting to perform depositions over a range of intensities, and observe how the film properties change with the changing ion flux. However, note that in this intensity regime, the fraction of neutral particles present in the plasma is substantial, and the properties of the neutral particles is also likely to play a major role in the characteristics of deposited films.

Returning to the determination of the angular distribution of the ion flux, the peak current density (Equation 2-8) incident on the detector was investigated, as well as the charge collected by the detector. This data is summarized in the figures below.

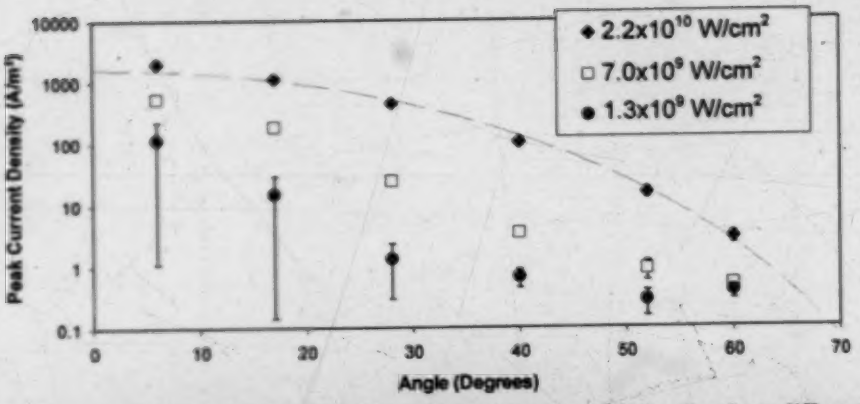

Figure 3-16. The angular distribution of the peak current density, for three different laser intensities incident on a carbon target. The laser parameters were as follows: I_L=2.2x10^{10} W/cm^2, E_L=83.2 mJ, d_L=52.8 cm; I_L=7.0x10^9 W/cm^2, E_L=45.3 mJ, d_L=50.8 cm; I_L=1.3x10^9 W/cm^2, E_L=126.5 mJ, d_L=45.8 cm. Each data point represents an average of at least 7 shots. When performing a fit to a cos^n distribution, the following values were obtained: n=9.4 ± 0.4 (2.2x10^{10} W/cm^2), n=10 ± 2 (7.0x10^9 W/cm^2) , n=7 ± 3 (1.3x10^9 W/cm^2), where the error is the standard error. The dashed line represents the cosine distribution fit to the highest intensity data. The accuracy of the fit at the lower intensities is considerably worse.

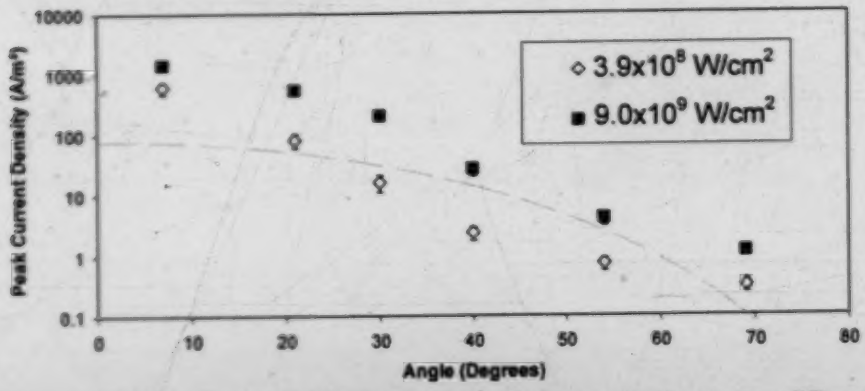

Figure 3-17. The angular distribution of the peak current density, for two different laser intensities incident on a zinc oxide target. The laser parameters were as follows: I_L=9.0x10^9 W/cm^2, E_L=77.1 mJ, d_L=53.4 cm; I_L=3.9x10^8 W/cm^2, E_L=62.5 mJ, d_L=59.9 cm. Each data point represents an average of at least 7 shots. When performing a fit to a cos^n distribution, the following values were obtained: n=7 ± 1 (9.0x10^9 W/cm^2), n=6 ± 2 (3.9x10^8 W/cm^2), where the error is the standard error. The dashed line represents the cosine distribution fit to the lowest intensity data. The accuracy of the fit at the higher intensity is slightly better.

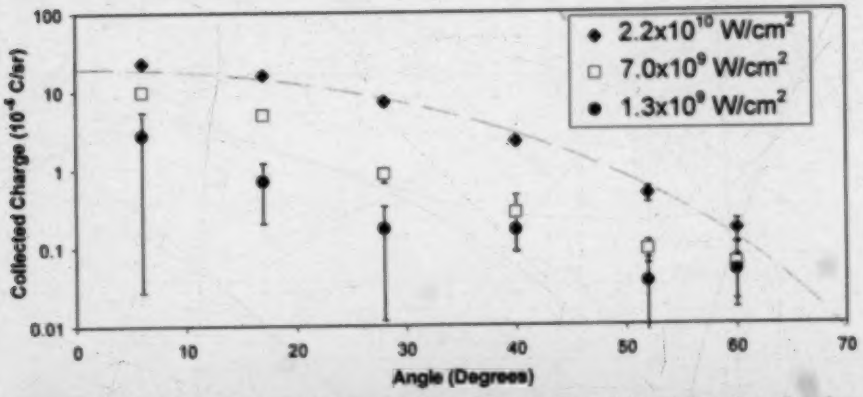

Figure 3-18. The angular distribution of the charge collected by the probes, for three different laser intensities incident on a carbon target. The laser parameters were as follows: I_L=2.2x10^{10} W/cm^2, E_L=83.2 mJ, d_L=52.8 cm; I_L=7.0x10^9 W/cm^2, E_L=45.3 mJ, d_L=50.8 cm; I_L=1.3x10^9 W/cm^2, E_L=126.5 mJ, d_L=45.8 cm. Each data point represents the average of at least 7 laser shots. The dashed line represents a cosine distribution fit to the highest intensity data. The accuracy of the fit at the lower intensities is considerably worse.

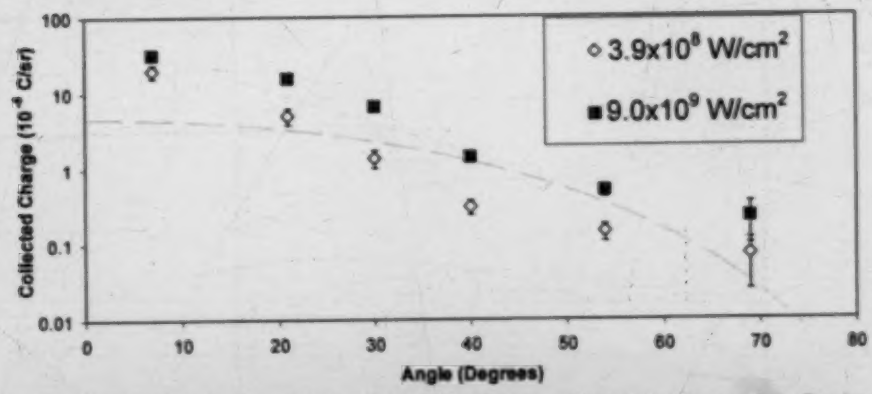

Figure 3-19. The angular distribution of the charge collected by the probes, for two different laser intensities incident on a zinc oxide target. The laser parameters were as follows: I_L=9.0x10^9 W/cm^2, E_L=77.1 mJ, d_L=53.4 cm; I_L=3.9x10^8 W/cm^2, E_L=62.5 mJ, d_L=59.9 cm. Each data point represents the average of at least 7 laser shots. The dashed line represents a cosine distribution fit to the lowest intensity data. The accuracy of the fit at the higher intensity is slightly better.

Each data point in the above four graphs represents the average of at least 7 laser shots. The shot-to-shot variation in the signal amplitude was the dominant source of error in all of the above four graphs. The error bars represent the difference between the maximum and minimum values for each data point. Note that the shot-to-shot variations increased for smaller amplitude signals, as the intensity is decreased or the detection angle (θ_p) is increased.

It is clear from the above figures that the bulk of the charge in the plasma plume is directed towards the target normal. This is one of the reasons why pulsed laser deposition is feasible as a thin film deposition technique. A more isotropic plasma expansion would undoubtedly result in a dramatically lower cost efficiency, since it would require more laser shots to produce the same film thickness.

The values of the collected charge at different angles have been fitted to a $\cos^n$ distribution. This distribution is commonly used in the literature [Cla01, Koi99, Las03]. The error in the value of n represents the standard error. This fitted distribution was then integrated to calculate the total charge emitted from the laser-produced plasma. The results of this analysis are summarized in the tables below. Note that the agreement between the data and the fitted distributions was generally poor (see Figures 3-18 and 3-19), except at the highest laser intensities.

Intensity	n	Total Charge (μC)
1.3×10^{9} W/cm^2	5 ± 2	9 ± 7
7.0×10^{9} W/cm^2	7 ± 1	33 ± 2
2.2×10^{10} W/cm^2	7.3 ± 0.4	150 ± 30

Table 3-1. Estimated total charge emitted in the plasma plume, for a carbon target, for three different laser intensities. The laser parameters were as follows: I_L=2.2×10^{10} W/cm^2, E_L=83.2 mJ, d_L=52.8 cm; I_L=7.0×10^{9} W/cm^2, E_L=45.3 mJ, d_L=50.8 cm; I_L=1.3×10^{9} W/cm^2, E_L=126.5 mJ, d_L=45.8 cm.

Intensity	n	Total Charge (μC)
3.9×10^{8} W/cm^2	5 ± 1	50 ± 50
9.0×10^{9} W/cm^2	5 ± 1	200 ± 100

Table 3-2. Estimated total charge emitted in the plasma plume, for a ZnO target, for two different laser intensities. The laser parameters were as follows: I_L=9.0×10^{9} W/cm^2, E_L=77.1 mJ, d_L=53.4 cm; I_L=3.9×10^{8} W/cm^2, E_L=62.5 mJ, d_L=59.9 cm.

From the figures above, it is clear that the plasma plume is significantly forward-directed. The forward-directed ions are more numerous and more energetic than ions emitted at wider angles (measured with respect to the target normal). This obviously has implications for pulsed laser deposition; a more strongly forward-directed ablation plume would be more efficient for the production of thin films, although the quality of the film would depend on the ion energy. It is interesting to note that in a typical PLD configuration, the substrate actually subtends some finite solid angle of the ion emission. Thus, the characteristics of the deposited film actually depend on the ion emission properties averaged over the finite solid angle. The present measurement enables

such an analysis. Additionally, the angular distribution of the ion energy (Figures 3-13 and 3-14) allows the possibility of selecting the ion energy by positioning the substrate at a particular angle. Some kind of deposition mask could be employed to select only a narrow range of angles, corresponding to a narrow range of ion energies. The decrease in ion current at wider angles could be compensated for by using a greater number of laser pulses during a film deposition, as required. However, it is still probably more practical to adjust the laser intensity to achieve the desired ion energy.

Qualitatively, the angular distribution results can be compared with a hydrodynamic model of the plasma expansion, which describes a forward-directed plume which can be roughly approximated by a cos^n distribution at small angles [Koo92]. In fact, the agreement between the angular distribution data and the fitted cosine distributions is generally poor, with the exception of the data at the highest intensities. The poor quality of the fitted distributions is reflected in the sizeable error bars in the above tables. Quantitatively, the fitted distributions for the peak current density (Figures 3-16 and 3-17) can be compared with those of L. Laska *et al.*. As mentioned previously, using an Nd:YAG laser (τ_L=9 ns, focal spot area $4x10^{-5}$ cm^2, I_L=$1.6x10^{10}$ W/cm^2), Laska *et al.* fitted the peak ion current density values with a cos^n distribution, and found that n=4 for an aluminum target, with higher n values for heavier elements [Las03]. Aluminum's atomic mass (~27 atomic mass units, i.e. 27 A. M.U.) is substantially larger than those of carbon (~12 A.M.U.) and oxygen (~16 A.M.U.), so that it might be expected that n<4 would be observed, rather than n=6-10. However, an important factor determining the angular distribution of the ion flux is the focal spot size. In the present work, the focal spot area used ranges from 0.2-$6x10^{-3}$ cm^2. These values are significantly larger than the focal spot size used by Laska *et al.*. For a smaller focal spot size, the plasma expansion is more spherical. For larger focal spot sizes, the plasma expansion is more planar, and more strongly forward-directed [Gup87]. A more suitable comparison might be the results published by F. Claeyssens *et al.* [Cla01]. As discussed previously, this group focused 193 nm ArF laser pulses (τ_L~20 ns) onto a $4x10^{-3}$ cm^2 spot on a graphite target, and observed n~5 for the total collected charge in the intensity range 0.25-$1x10^9$ W/cm^2. This value is in good agreement with the measured values for both C and ZnO targets, although, as noted previously, this group's method of acquiring the angular distribution of the ion emission is less than ideal, since the laser angle of incidence was also changed.

The signal amplitudes (in terms of the peak current density and the collected charge) observed here are somewhat consistent with values obtained elsewhere. Laska *et al.* (Nd:YAG laser, τ_L=9 ns, E_L~280 mJ, I_L=$1.6x10^{10}$ W/cm^2) observed a peak current density of 300 A/m^2 at a distance of 44 cm from the target, for an aluminum plasma [Las03]. This is larger than the range 100-2000 A/m^2 observed in the present study, measured using the detector closest to the target normal, taking into account the fact that the detectors were placed much closer to the plasma source (~17-18 cm away). Assuming isotropic expansion, Laska's value would scale to ~4800 A/m^2 at a similar detector distance. Presumably, the larger energy used by Laska *et al.* (~3-4 times that used in the

present work) is responsible for the higher observed peak current density. The present values for the collected charge are somewhat consistent with previously published values. R. Dinger *et al.* (Nd:YAG laser, τ_L=18 ns, E_L=15 mJ, I_L=7x10^9 W/cm^2) have reported observing ~2x10^{13} ions/sr emitted from a tantalum target [Din80]. Assuming a value of Z=+1, the collected charge values observed in the present work range from ~0.2-2x10^{15} ions/sr. This is roughly one order of magnitude larger than the value of Dinger *et al.*. However, the pulse energy used by Dinger is significantly smaller than those used in the present work (45-130 mJ). A smaller laser energy would produce fewer ions. Additionally, the detector distance used by Dinger is 25 cm, which is larger than those used in the present work (16-18 cm). As the plasma plume expands and cools, some of the plasma ions and electrons will recombine. Although the relative importance of this process is unknown, it could account for the smaller number of ions observed by Dinger. Of course, recombination is likely to affect the results of the present investigation as well. Additionally, A. Rupp and K. Rohr (Nd:YAG laser, τ_L=20 ns, E_L=210 mJ, I_L=1x10^{11} W/cm^2) have reported observing ~3x10^{14} ions/sr emitted from a tantalum target [Rup95]. This falls within the range observed in the present work, but the laser energy and intensity are higher in Rupp's experiment, so it might be expected that Rupp would observe a larger number of ions. On the other hand, in Rupp's experiment, the number of ions is measured 60 cm from the target. Again, recombination could be an issue, reducing the number of ions which reach the detector.

There is some additional uncertainty in the calculation of the collected charge (Tables 3-1 and 3-2). The asymmetry of the laser focal spot size on target limits the accuracy of the values. The horizontal dimensions of the focal spot are larger than the vertical dimensions, particularly at lower laser intensities. Since the focal spot dimensions are smaller vertically, the plasma plume is likely to be more spherical and less forward-directed in the vertical plane, compared to the horizontal plane. However, the integration of the angular distribution of the collected charge assumes that the angular distribution of the ion emission in the vertical plane matches the horizontal angular distribution measured by the Langmuir probes. Thus, the integrated collected charge values are likely to be inaccurate. In the future, the angular distribution in the vertical plane should also be measured, in order to obtain a more complete characterization of the plasma plume.

b) Evaluation of Applicability of Theoretical Models

The validity of the simple gas expansion model summarized in Equations 3-17 and 3-18 was also evaluated, using the self-regulating model to calculate the plasma temperature (Equation 3-13). In the calculations, the effective heat capacity ratio was assumed to be γ=1.3, the Coulomb logarithm was assumed to have the value ln Λ=13, the average charge state was assumed to be $\bar{Z}$=1, and for the zinc oxide target, the ion mass used was that of oxygen. Recall that the amount of kinetic energy gained due to ion and electron recombination is indeterminate in the present work. In practice, the energies calculated assuming full recombination and no recombination serve as upper and lower estimates,

respectively, for the ion energy. The calculated results are given in the table below. Again, the error in the measured ion energy values represents the shot-to-shot variations in the signal.

Target	Intensity (W/cm^2)	Ion Energy (Measured, eV)	T_e (Calculated, eV)	Ion Energy (No R., eV)	Ion Energy (Full R., eV)
ZnO	2.7×10^8	21 ± 2	3.7	23	37
	7.7×10^9	129 ± 9	19.7	124	197
C	1.1×10^9	21 ± 4	7.1	45	71
	7.9×10^9	76 ± 8	19.4	122	193
	1.9×10^{10}	200 ± 10	29.9	188	298

Table 3-3. A comparison between the measured values of ion energy (taken here to be the peak ion energy) and the ion energy calculated from a simple gas expansion model (Equations 3-17 and 3-18). The fourth column represents the electron temperature calculated using the self-regulating model. The fifth column represents the ion energy calculated using the theoretical models, assuming no recombination. The sixth column represents the ion energy calculated using the theoretical models, assuming full recombination. In the calculations, the effective heat capacity ratio was assumed to be γ=1.3, the Coulomb logarithm was assumed to have the value ln Λ=13, the average charge state was assumed to be $\bar{Z}$ =1, and for the zinc oxide target, the ion mass used was that of oxygen.

Overall, the measured ion energy values are somewhat inconsistent with the calculated values. Of course, the experimental ion emission exhibits a wide range of energies, and so it is possible that the choice to use the peak ion energy to represent the measured ion energy was inappropriate. However, when comparing the measured average ion energy (see below) to the calculated energy values, the agreement does not improve. The likely reason for this disagreement is that the theoretical models describe a fully ionized plasma. In the transition regime described in the present work, the plasma plume is more complex, consisting of neutral particles as well as ions and electrons. The emission of neutral particles is caused by a number of factors. The non-uniform intensity profile incident on the target means that lower intensity regions of the target will produce neutral particle-dominated plumes, rather than fully ionized plasma plumes. Additionally, lower intensities on target exist during the rising and falling portions of the temporal profile of the laser pulse. Considering the temporal profile of the intensity on target, at the lower intensities, the time it takes to reach the plasma threshold intensity may become a significant fraction of the laser pulse. This factor will increase the fraction of neutral particles in the ablation plume. Furthermore, the laser-matter interaction at low intensities may result in shock expulsion of liquid, vapor, and solid material from the target. A simple estimate

of the average temperature change of the target ΔT due to the laser pulse heating based on the energy balance [Bau00] gives

$$\Delta T = \frac{I_A}{2c_p\rho}\sqrt{\frac{\tau_L}{D}} \qquad (3\text{-}21)$$

where I_A is the absorbed laser energy, c_p is the specific heat capacity at constant pressure, ρ is the mass density, τ_L is the laser pulse duration, and D is the thermal diffusivity. According to this estimate, the temperature rise in a carbon target (graphite, with c_p=0.71 J/gK, D=12.58 cm^2/s, ρ=2.24 g/cm^3) ranges from ~1000 K to ~10 000 K for incident laser intensities ranging from 1x10^8 to 1x10^9 W/cm^2. Comparing these values to the melting and boiling points of carbon (~3900 K and ~4600 K, respectively), it appears that the ablation plumes produced in the intensity regime investigated in the present work represent a transition between a vapor plume and fully ionized plasma plume. Note that the estimated temperature values are very rough, and should only be used as a guideline. In particular, the reader should keep in mind that the estimated 1000 K temperature produced at 1x10^8 W/cm^2 does not imply that no plasma should be formed at this intensity; the peak of the intensity profile on target (both in the spatial and temporal domains) will be capable of producing some plasma. In any case, from this simple calculation, it seems reasonable that neutral particles would compose a significant portion of the ablation plume, especially considering that if the peak intensity is 1x10^9 or 1x10^{10} W/cm^2, some of the lower intensity regions of the laser intensity profile (in both the spatial and temporal domains) would fall in the 1x10^8 to 1x10^9 W/cm^2 range.

Note that the ions are more energetic than the neutral particles, so that for the most part, the plasma plume will lead the vapor plume as the ablation plume expands. Note also that the higher intensity ion energy values for both the carbon and zinc oxide targets fall within the range of the calculated values, within error. This is expected, since for increasing intensities, the plasma plume should consist of an increasing fraction of ions, thus more closely approximating the behavior of a fully ionized plasma.

c) Ion Energy Spectrum

Another important consideration when investigating the plasma plume characteristics is the ion energy spectrum. Based on the time-of-flight spectrum of the ions, this energy spectrum can be calculated. The spectrum $N(E)$ is defined such that the total number of ions (N_i) is given by

$$N_i = \int N(E)dE. \qquad (3\text{-}22)$$

In calculating the total number of ions, the charge state $\overline{Z}$ is assumed to be 1. To consider another charge state, simply divide the number of ions by $\overline{Z}$. To calculate the average energy $\overline{E}$ of the ions, the energy can be integrated over this spectrum:

$$\overline{E} = \frac{\int EN(E)dE}{N_i}. \qquad (3\text{-}23)$$

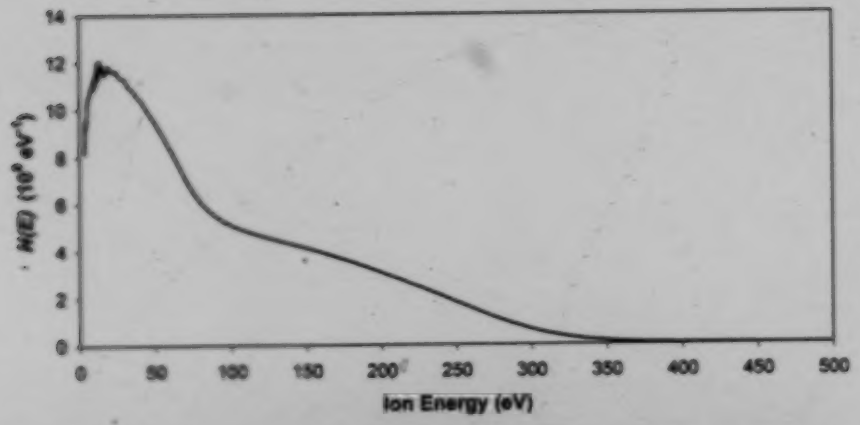

Figure 3-20. The ion energy spectrum, calculated from the time-of-flight spectrum. The intensity of this particular laser shot was 2.1×10^{10} W/cm^2 (E_L=84.3 mJ, d_L=52.8 cm), incident on a carbon target. The detector was positioned 18 cm away from the target, at an angle of 6° with respect to the target normal. This spectrum is based on the smoothed data. Assume Z=1.

Based on the known shot-to-shot variation in the signal amplitude the error in the spectral amplitude is estimated to be ± 6%.

This spectrum has an average energy of 101.6 eV. Compare this value to the value of the peak ion energy, which was 203 eV for this particular laser shot. The peak ion energy is commonly used in the literature as a measure of the average or most probable ion velocity, but it is apparent from the energy spectrum above that this identification is not necessarily accurate. A detailed analysis of the spectrum reveals that 1% of the ions have a kinetic energy greater than 319.8 eV, and 10% of the ions have an energy greater than 222.7 eV. The total energy carried by the ions incident on the detector is 23.9 μJ. Note the interesting shape of the high-energy portion of the spectrum. There appears to be two groups of thermal ions: a higher temperature group, and a lower temperature group. The dominant peak is the hotter, higher energy group. This higher energy group may consist of C^{2+} ions, which would be accelerated more readily owing to their higher charge-to-mass ratio. The ion energy spectra at lower laser intensities appear to consist of only one group of ions, indicating that the number of C^{2+} ions is negligible. The issue of the ion charge state is discussed further below.

Based on the equation for the average ion energy above, the angular distribution of the average ion energy can be computed, for the different target materials and different laser intensities.

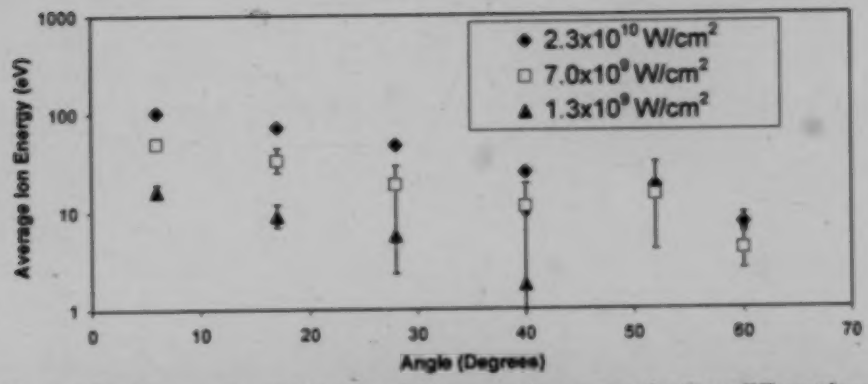

Figure 3-21. The angular distribution of the average ion energy, for three different laser intensities incident on a carbon target. The average ion energy $\overline{E}$ was calculated according to equation 3-23. The laser parameters were as follows: I_L=2.3x10^{10} W/cm^2, E_L=84.3 mJ, d_L=52.8 cm; I_L=7.0x10^9 W/cm^2, E_L=45.5 mJ, d_L=50.8 cm; I_L=1.3x10^9 W/cm^2, E_L=125.3 mJ, d_L=45.8 cm. Each data set represents the results of a single laser shot.

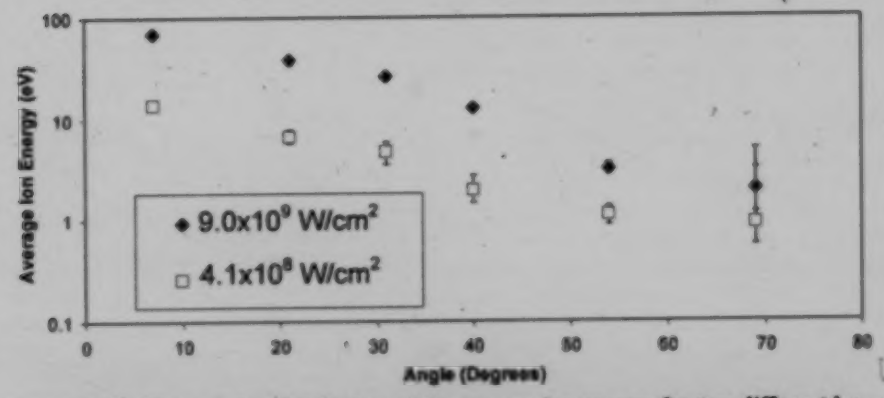

Figure 3-22. The angular distribution of the average ion energy, for two different laser intensities incident on a zinc oxide target. The average ion energy $\overline{E}$ was calculated according to equation 3-23. The laser parameters were as follows: I_L=9.0x10^9 W/cm^2, E_L=76.3 mJ, d_L=53.4 cm; I_L=4.1x10^8 W/cm^2, E_L=64.9 mJ, d_L=59.9 cm. Each data set represents the results of a single laser shot. In the calculation of the energy, it was assumed that the ion species is oxygen.

Each data set (corresponding to the given intensity) in the above two figures represents the results of a single laser shot. As mentioned previously, the shot-to-shot variation is the dominant source of error in the ion energy measurements. The error bars are estimated based on this known shot-to-shot variation.

The angular distribution of the average ion energy is similar to that of the peak ion energy, discussed above. Notice that the average ion energy for the carbon target ranges from 16 eV to 102 eV. By adjusting the incident laser

intensity, the ion energy can be tuned to achieve the ~90 eV optimum value quoted by [Hav03]. This would presumably provide the optimum probability of sp^3 bond formation in the production of diamond-like carbon films using pulsed laser deposition. However, recall that the ions are only one component of the plasma plume. The energy of the neutral particles is unknown, and will most likely affect the sp^3 bonding fraction in a deposited film.

In order to compare the values obtained for the average ion energy, consider the results of F. Claeyssens *et al.*. For the ZnO target, Claeyssens *et al.* (193 nm ArF laser, τ_L~20 ns) reported observing ion average energies in the range 14-27 eV (based on the mass of oxygen ions) for laser intensities in the range 0.25-1x10^9 W/cm^2 [Cla02]. The value of 13.7 eV at I_L=4.1x10^8 W/cm^2 obtained in the present work is close to this range.

The angular distribution of the total energy carried by the ions incident on the detector is summarized in the figures below.

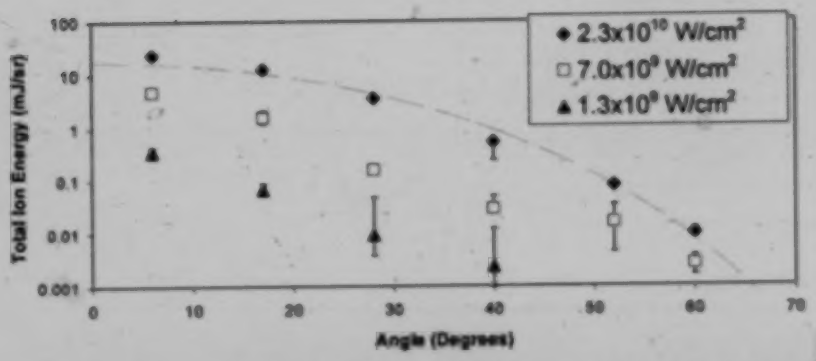

Figure 3-23. The angular distribution of the total energy of the ions incident on the Langmuir probes. The laser parameters were as follows: I_L=2.3x10^{10} W/cm^2, E_L=84.3 mJ, d_L=52.8 cm; I_L=7.0x10^9 W/cm^2, E_L=45.5 mJ, d_L=50.8 cm; I_L=1.3x10^9 W/cm^2, E_L=125.3 mJ, d_L=45.8 cm. Each data set represents a single laser shot, incident on a carbon target. Assume Z=1. The dashed line represents a cosine distribution fit to the highest intensity data. The accuracy of the fit at the lower intensities is considerably worse.

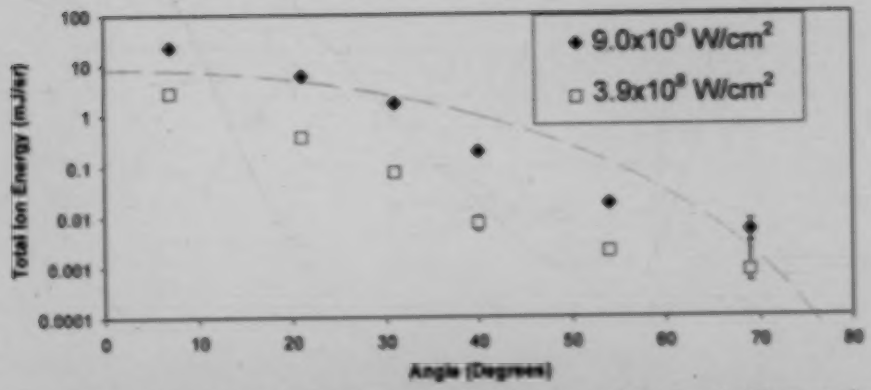

Figure 3-24. The angular distribution of the total energy of the ions incident on the Langmuir probes. The laser parameters were as follows: I_L=9.0x10^9 W/cm^2, E_L=76.3 mJ, d_L=53.4 cm; I_L=4.1x10^8 W/cm^2, E_L=64.9 mJ, d_L=59.9 cm. Each data set represents the results of a single laser shot, incident on a zinc oxide target. In the calculation of the energy, it was assumed that the ion species is oxygen, with Z=1. The dashed line represents a cosine distribution fit to the highest intensity data. The accuracy of the fit at the lower intensity is considerably worse.

Again, each data set (corresponding to the given intensity) in the above two figures represents the results of a single laser shot. Once again, the error bars are estimated based on the known shot-to-shot variation in ion energy.

Integrating the total energy carried by the ions over the angular distribution, the total energy carried by the ions in all directions can be calculated.

Intensity	n	Total Energy (mJ)	Conversion Efficiency
3.9x10^8 W/cm^2	7 ± 2	0.3 ± 0.4	0.004 ± 0.004
9.0x10^9 W/cm^2	8 ± 2	4 ± 4	0.06 ± 0.06

Table 3-4. Total energy of the ZnO plasma plume, resulting from fitting the data in Figure 3-24 to a cosine distribution. The power n of the fit is given, as is the result of the integration of the energy over the distribution. The conversion efficiency of the laser energy into the ion energy is also provided. In the calculation of the energy, it was assumed that the ion species is oxygen, with Z=1.

Intensity	n	Total Energy (mJ)	Conversion Efficiency
1.3×10^9 W/cm^2	18 ± 4	0.07 ± 0.05	0.0005 ± 0.0004
7.0×10^9 W/cm^2	10 ± 2	0.9 ± 0.7	0.02 ± 0.02
2.3×10^{10} W/cm^2	11.1 ± 0.6	9 ± 2	0.11 ± 0.03

Table 3-5. Total energy of the C plasma plume, resulting from fitting the data in Figure 3-23 to a cosine distribution. The power n of the fit is given, as is the result of the integration of the energy over the distribution. The conversion efficiency of the laser energy into the ion energy is also provided. Assume Z=1.

The errors in the values of n represent the standard error of the data with respect to the fit. The error in the total energy (and hence that of the conversion efficiency) is based on the error in the fitted value of n and the error in the amplitude of the fitted distribution. The agreement of the fitted distributions with the data was generally poor, except at the highest laser intensities (see Figure 3-24). As discussed previously, since the total energy is calculated by integrating the angular distribution of the total ion energy over all space, the asymmetry of the focal spot also introduces some unknown error in this calculation.

It is clear that the ion flux contains a significant fraction of the incident laser energy, particularly at high laser intensities. At slightly higher intensities (2×10^{11} W/cm^2), significantly higher conversion efficiencies (~0.8) have been observed, using 20 ns KrF laser pulses incident on a graphite target (see figure below) [Tsu92].

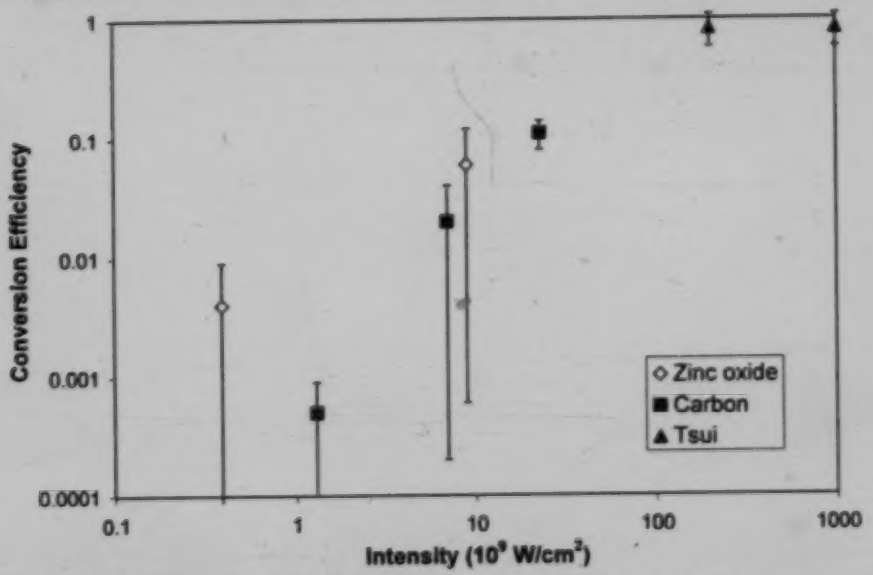

Figure 3-25. A comparison of the conversion efficiencies observed in this experiment, and values reported by Y. Y. Tsui [Tsu92].

For the lower intensities of the present work, the plasma consists of a mixture of ions and neutrals. The relatively small conversion efficiencies reported here indicate that the bulk of the remainder of the input energy is carried by the neutral particles, with some unknown proportion of the energy lost as radiation or as heat remaining in the target. The above conversion efficiency values indicate that the neutral particles constitute a substantial fraction of the ablation plume in the intensity range 10^8-10^{10} W/cm^2. As discussed previously, due to various factors, this intensity regime represents a transition region between the hot dense vapors produced at lower intensities and the fully ionized plasmas produced at higher intensities. The conversion efficiencies reported here reflect this. On the other hand, the higher values reported by Y. Y. Tsui [Tsu92] indicate that the ablation plumes produced at higher intensities are more fully ionized. Nonetheless, an outline of the trend in the transition region studied here is evident. It appears that the conversion efficiency values should rise rapidly in the 10^{10}-10^{11} W/cm^2 intensity range. In the future, this expected behavior can be verified experimentally.

d) Estimation of Ion Charge State

An experiment to determine the total particle flux emitted from the laser-produced plasma was performed. The flux includes ions, electrons, and neutral particles. Once the total particle flux was determined, the fraction of ionization of the total ablation plume, defined as the ratio of the number of ions in the plume to the number of particles in the plume, could be calculated. Note that this quantity differs from the average charge state, which is defined as the average charge of the ions. The fraction of ionization essentially represents the average charge of all the particles (assuming $\overline{Z}$ =1), including the neutral particles.

The number of ions was estimated using the calculated values of the collected charge (Figures 3-18 and 3-19), with the assumption $\overline{Z}$ =1.

A deposition of the particle flux on silicon substrates was conducted, and based on the thickness of the deposited film, the total number of carbon particles present in the ablation plume was estimated.

The experimental setup is similar to that used for ion measurements, with some differences. In place of the ion detectors, 1 cm^2 silicon substrates were substituted. The substrates were placed at identical angles (6°-60°) as the probes. However, in order to obtain a reasonable deposited film thickness on the substrates in a reasonable deposition time, the substrates were positioned substantially closer to the target: 5-7 cm, as opposed to 17-18 cm for the detectors. In the calculation of the fraction of ionization, this difference in distances was corrected for by assuming an isotropic plasma expansion. Of course, this assumption introduces some error into the calculation; the issue of error is discussed further below. Additionally, the KrF laser system was operated at a 20 Hz repetition rate. The laser parameters for the three separate depositions were as follows: at the highest intensity, the average laser energy was E_L=73.5 mJ, the lens-to-target distance was d_L=52.8 cm, the deposition time was 57 minutes (6.8×10^4 laser pulses), and the average intensity was I_L=1.9×10^{10} W/cm^2; at the

medium intensity, the average laser energy was E_L=48.2 mJ, the lens-to-target distance was d_L=50.8 cm, the deposition time was 57 minutes (6.8×10^4 laser pulses), and the average intensity was I_L=7.5×10^9 W/cm^2; at the lowest intensity, the average laser energy was E_L=73.0 mJ, the lens-to-target distance was d_L=45.8 cm, the deposition time was 65 minutes (7.8×10^4 laser pulses), and the average intensity was I_L=7.3×10^8 W/cm^2. Note that the intensity values quoted in the figure legend below correspond to the intensity of the collected charge measurements, which are taken from Figure 3-18.

The silicon substrates captured the deposited particle flux generated by the laser pulses incident on the graphite target, and the deposited film thickness was used to calculate the total particle flux.

The deposited film thickness was measured as follows. Before the experiment, a thin strip of tape was placed down the middle of the substrates. After the deposition, this strip was removed, leaving a gap in the deposited film. The depth of the gap corresponded to the film thickness. This depth was measured using a contact profilometer (Tencor Alphastep 200, from the University of Alberta's Micromachining and Nanofabrication Facility), in which a diamond-tipped stylus is scanned across the surface of the film. It was found that the thickness of the deposited film often varied (by 15-20% or more) within a given substrate.

The results are summarized in the figure below.

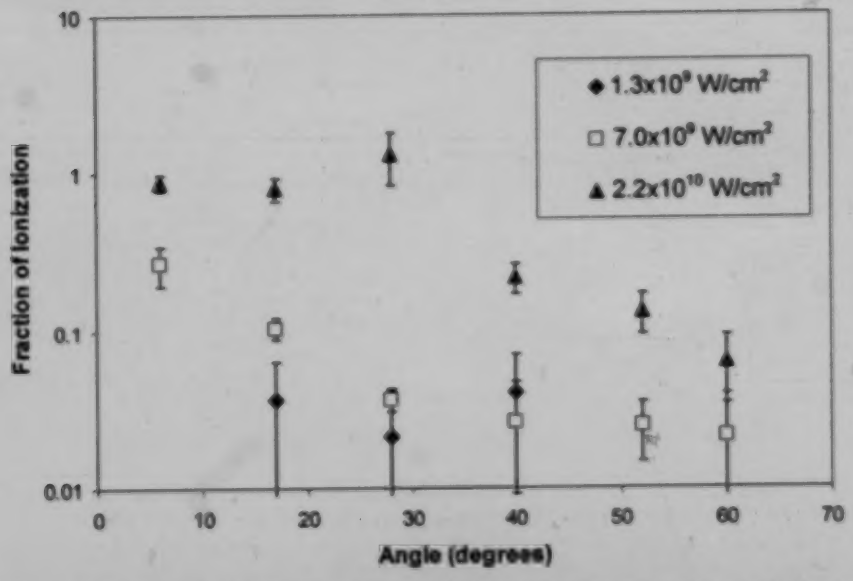

Figure 3-26. The angular distribution of the fraction of ionization of the total ablation plume, for three different laser intensities on a carbon target. The fraction of ionization is defined as the ratio of the number of ions to the total number of carbon particles in the total ablation plume. The large error bars are due to the significant error inherent in the technique used to measure the total particle flux.

The two dominant sources of error in the calculation of the fraction of ionization are the error in the film thickness as measured by the contact profilometer (which affects the calculation of the total particle flux) and the shot-to-shot variation in the collected charge (which affects the calculation of the ion flux). The fraction of ionization values in the above figure were calculated using the average values of the collected charge and the film thickness. The error bars represent the difference between the maximum and minimum calculated values, based on the maximum and minimum values for the collected charge and the film thickness. Notice that the value of the ionization fraction for the highest intensity at 28° is larger than 1, which would mean that there are more ions than particles, which is not possible. This is an indication of the level of error in this measurement. Another factor which contributes to the error is the assumption $\bar{Z}=1$ employed in the calculation of the number of ions. If the value $\bar{Z}=1.3$ were assumed (see below), the fraction of ionization values would decrease by 23%. Additionally, in the calculation, the density of graphite is used, whereas the true density of the carbon film has not been determined.

By integrating the angular distribution of the total particle flux over all space, and using the previously calculated values for the total emitted charge (Table 3-1), fraction of ionization values for the entire plume could be calculated. These values are summarized in the table below, again, quoting the intensity values from the collected charge experiments.

Intensity (W/cm^2)	Fraction of Ionization
1.3×10^9	0.05 ± 0.05
7.0×10^9	0.07 ± 0.02
2.2×10^{10}	0.5 ± 0.4

Table 3-6. Summary of the fraction of ionization values integrated over all space, for three different intensities.

The error bounds are based on the standard error of the fit for both the collected charge calculations and the total number of particles calculations.

For the two lower laser intensities, the ionization fraction is significantly smaller than 1, indicating that the ablation plume is primarily composed of neutrals, with a limited number of C^+ ions, and very few C^{2+} or C^{3+} ions present. Thus, the assumption of $\bar{Z}=1$ in many of the preceding calculations is probably accurate. On the other hand, for the higher laser intensity, the ionization fraction is close to 1, indicating that the ablation plume probably contains, in addition to neutrals and C^+ ions, a significant number of C^{2+} or C^{3+} ions. Thus, the assumption of $\bar{Z}=1$ used in many of the preceding calculations is probably inaccurate for the higher laser intensity values. This finding is consistent with other experiments performed in this intensity regime. Y. Y. Tsui *et al.*, using a KrF laser with a pulse duration of 20 ns and an intensity of 1.6×10^{11} W/cm^2

incident on a graphite target measured an average charge state which ranged from 1.1 to 1.5 [Tsu93]. A. Rupp and K. Rohr have reported observing carbon ions with Z=+1 to Z=+3 when a graphite target is irradiated with 14 ns pulses from an Nd:YAG laser at intensities in the range 0.1-7x10^{10} W/cm^2 [Rup91]. A. Thum-Jaeger *et al.* (Nd:YAG laser, τ_L=5 ns, I_L=5x10^{10} W/cm^2, carbon target) reported an average charge state of 2.3 [Thu00b]. Of these results, the values reported by Y. Y. Tsui *et al.* are probably most applicable, since the conditions under which those values were measured most closely approximate the experimental conditions of the present work. Nonetheless, the exact value of the average charge state for these experimental conditions remains an open question. Furthermore, due to the relatively high background pressure (2x10^{-4} Torr) present in the experimental chamber, the possibility of charge exchange between the ions of the plasma plume and the particles of the background gas must be acknowledged. This possibility is likely to increase the fraction of neutral particles present in the ablation plume, to an unknown degree.

e) Electron Temperature

The electron temperature is an important parameter describing the plasma plume. The electron temperature evolves in time, as the plasma expands and cools. The electron temperature of the plasma plume reaching the detectors can be measured, as discussed in Chapter 2. The electron temperature has been shown to be an important factor in the growth of diamond-like carbon films via plasma chemical vapor deposition [Ike05]. One would assume that this parameter is also relevant in the pulsed laser deposition technique. Additionally, measurement of the electron temperature may be particularly important in the application of the ion flux for chemical processing, since the rates of chemical reactions depend on the temperature.

The procedure for the measurement of the electron temperature is outlined in Chapter 2 (Equation 2-4), according to the method of D. W. Koopman [Koo71] and B. Toftmann *et al.* [Tof00]. A typical I-V curve is given in the figure below. Additional I-V curves are given in the Appendix.

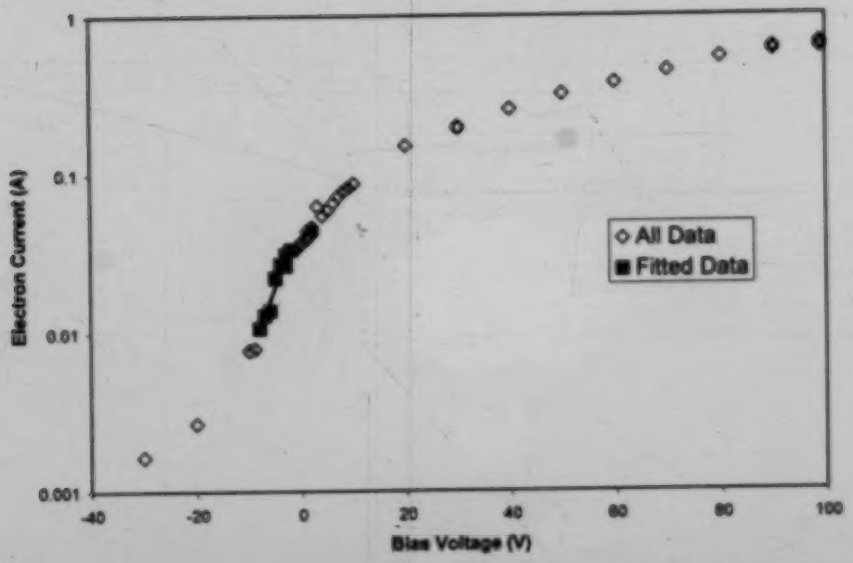

Figure 3-27. An example of the bias curve from a Langmuir probe used to extract T_e for a carbon plasma. This particular probe was located a distance 17.9 cm away from the target, at an angle of 17° with respect to the target normal. The average laser parameters were: I_L=1.9x10^{10} W/cm^2, E_L=72.0 mJ, d_L=52.8 cm. The slope of the fit allows the calculation of T_e=4.9 ± 0.4 eV, using Equation 2-4.

In the above graph, each data point represents a single laser shot. The dominant source of error in the calculation of the electron current is the uncertainty in the calculation of the ion current. The error in the electron current values can be up to 14%. Error bars are not shown for the purposes of clarity. The error in the quoted value of T_e corresponds to the standard error of the fit.

There is an additional uncertainty in the resulting T_e value due to the uncertainty in choosing the portion of the curve to fit. In this choice, the detailed descriptions of the method provided by both D. W. Koopman [Koo71] and B. Toftmann *et al.* [Tof00] were invaluable. Both these reports indicate that the most accurate fit is obtained when the portion of the curve near bias voltages of zero is fitted. The biasing curve should be fitted in the region of maximum slope, between both the electron and ion saturation regions, where the current rolls off.

Using the fitting procedure for each detector, at each intensity, values for the electron temperature were obtained. These values are summarized in the tables below. The laser parameters, averaged over the course of the biasing scan, are as follows: at the highest intensity for the carbon target, the average laser energy was E_L=72.0 mJ, the lens-to-target distance was d_L=52.8 cm, and the average intensity was I_L=1.9x10^{10} W/cm^2; at the medium intensity for the carbon target, the average laser energy was E_L=50.8 mJ, the lens-to-target distance was d_L=50.8 cm, and the average intensity was I_L=7.9x10^9 W/cm^2; at the lowest intensity for the carbon target, the average laser energy was E_L=108.1 mJ, the lens-to-target distance was d_L=45.8 cm, and the average intensity was I_L=1.1x10^9

W/cm^2; at the highest intensity for the zinc oxide target, the average laser energy was E_L=65.3 mJ, the lens-to-target distance was d_L=53.4 cm, and the average intensity was I_L=7.7x10^9 W/cm^2; at the lowest intensity for the zinc oxide target, the average laser energy was E_L=44.0 mJ, the lens-to-target distance was d_L=59.9 cm, and the average intensity was I_L=2.7x10^8 W/cm^2.

The error in the tables below represents the uncertainty in choosing the portion of the curve to fit, as well as the standard error of the fit. The error in choosing the portion of the curve to fit was estimated by fitting the data twice, using different regions of the I-V curve. The variation in the resulting value of T_e was used as the error estimate.

	T_e (eV)				
Intensity\Angle	**17°**	**28°**	**40°**	**52°**	**60°**
1.1x10^9 W/cm^2	5 ± 2	2 ± 1	2 ± 1	2 ± 1	2 ± 1
7.9x10^9 W/cm^2	3 ± 2	1 ± 1	1 ± 1	1 ± 1	2 ± 1
1.9 x10^{10} W/cm^2	8 ± 4	4 ± 1	2 ± 1	2 ± 1	2 ± 1

Table 3-7. Electron temperature for three different intensities incident on a carbon target, measured at different angles with respect to the target normal. These values were obtained using the procedure outlined in [Koo71].

	T_e (eV)					
Intensity\Angle	**7°**	**21°**	**30°**	**40°**	**54°**	**69°**
2.7x10^8 W/cm^2	8 ± 5	3 ± 1	2 ± 1	2 ± 1	2 ± 1	2 ± 1
7.7x10^9 W/cm^2	16 ± 6	4 ± 3	3 ± 1	1 ± 1	1 ± 1	2 ± 2

Table 3-8. Electron temperature for two different intensities incident on a zinc oxide target, measured at different angles with respect to the target normal. These values were obtained using the procedure outlined in [Koo71].

It is clear that the electron temperature is highest in the forward (i.e. target-normal) direction, and it generally increases with increasing intensity. The angular variation of the electron temperature is somewhat unexpected; the electron component of the plasma plume is generally thought to be well-thermalized, and a uniform electron temperature (at all measurement angles) should be observed. The higher T_e values measured at angles close to the target normal may be an indication of the presence of secondary electron emission. The higher energy ions emitted in the target-normal direction result in increased secondary electron emission, which would affect the electron current measurements, skewing the T_e values. The values measured at wider angles would be comparatively free of this effect, and may thus provide a more accurate picture of the temperature of the plume.

This measurement is particularly relevant to the production of diamond-like carbon films. N. Ikenaga *et al.* [Ike05] have reported that the dynamic hardness of DLC films created by plasma chemical vapor deposition depends on the electron temperature of the plasma. As the electron temperature increases from 1 to 5 eV, the dynamic hardness of the film decreases by a factor of 3-4. From the data in Table 3-7, it would appear that lower intensities and wider angles would be better for producing films with high dynamic hardness.

Conclusion

The ion emission from laser-produced plasmas for two different targets at several different laser intensities has been successfully characterized. Nearly all of the relevant characteristics of the ion flux have been measured, including the emitted charge, the ion peak and average energies, and the angular distribution of each of these quantities. The predictions of the self-regulating model, as well as a simple gas expansion model were also tested. Although successful at higher intensities, the validity of these models in this intensity regime (10^8-10^{10} W/cm^2) is in doubt, as the results did not agree with the predictions of these models. A more complex model, incorporating ions, electrons, and neutrals, would be more appropriate in this intensity regime. One outstanding issue is the question of the average charge state of the ions present in the ablation plume. Some attempt has been made to estimate this quantity, but the exact value of the average charge state remains an open question. Additionally, the question of secondary electron emission remains outstanding. In the future, a proper measurement of the emission in this regime would be invaluable. The measurements made in the present work enable further applications of the ion emission from nanosecond laser-produced plasmas.

Chapter 4
Ion Emission from Plasmas Produced by fs Laser Pulses

Introduction

a) Chirped Pulse Amplification

Having characterized the ion emission at lower laser intensities, the study of ion emission at higher laser intensities in the femtosecond regime will now be addressed. These higher intensities have been made possible by the advent of ultrashort laser pulses and chirped pulse amplification (CPA) [Str85]. The technique of CPA achieves higher laser powers by avoiding the limitations of traditional laser amplifiers [Str85]. A schematic of the CPA technique is shown in Figure 4-1.

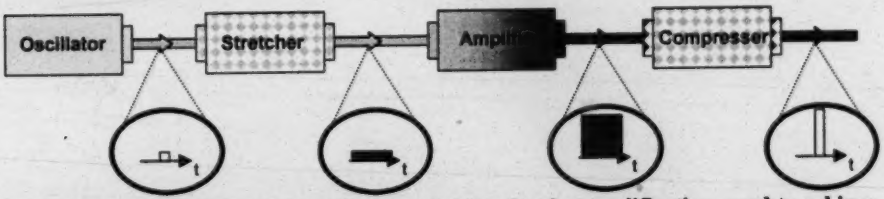

Figure 4-1. A schematic of the technique of chirped pulse amplification, used to achieve high laser intensities without causing damage to the laser amplifier. Due to the action of the pulse stretcher, the laser pulse is said to be "chirped."

The limiting factor in laser pulse amplification is the damage threshold of the amplifier components. CPA involves stretching the laser pulse in time, by a factor of up to 10^4, thus reducing the power and intensity by the same factor. The pulse energy can then be amplified by several orders of magnitude using traditional means (e.g. flashlamp-pumped Nd:glass slabs). The pulse is then compressed back nearly to its original duration. The stretching and compression are accomplished using a pair of diffraction gratings. The diffraction grating in the pulse stretcher forces the different frequency components of the original pulse to travel different path lengths, before being recombined spatially, such that the pulse has expanded in time, with lower frequency (i.e. more red) components at the leading edge of the pulse, and higher frequency (i.e. more blue) components at the trailing edge of the pulse. The correlation between frequency and temporal position in the pulse results in a "chirped" pulse, from which the technique derives its name. The compressor grating removes the chirp by reversing the operation of the first grating, restoring the pulse nearly to its original duration.

b) Applications of femtosecond Ion Emission

Based on the CPA technique, laser intensities of up to 10^{21} W/cm^2 have been achieved in a few laboratories in the world. These higher intensities have resulted in a variety of new phenomena. In particular, high-energy ions generated by the laser-plasma interaction are attracting attention for their exceptional properties: high energy, high degree of directionality, and high current density,

with a significant conversion efficiency. Researchers around the world are proposing exciting new applications for these fast ions. For example, fast ions may play an important role as part of a scheme to achieve inertial confinement fusion (ICF).

Controlled fusion promises to be the energy source of the future, with many advantages over traditional fossil fuel energy sources. There are two distinct efforts towards achieving controlled fusion. The first is magnetic confinement fusion, in which the fusion fuel is confined by magnetic fields while it is heated up to fusion temperatures. The second is inertial confinement fusion, in which the fusion fuel is rapidly compressed by powerful laser pulses, reaching sufficient density and temperature to ignite [Nak96]. The effort to achieve ICF has been hampered by various instabilities which arise due to the heating and acceleration of the imploding shell making it difficult to achieve the high densities and temperatures needed to achieve ignition of the pellet. In recent years, there has been interest in the fast ignitor (FI) concept, which is an advanced scheme for ICF which greatly relaxes the requirements on the compression-driving lasers [Tab94]. In the FI scheme, the compression-driving laser systems compress the pellet to a less extreme density; ignition is caused by a secondary energy source which injects energy directly into the partially compressed core. This secondary fast ignition source must deliver a relatively large amount of energy (tens of kJ) to a relatively small volume (less than 100 μm in radius) in a relatively short time (10 ps). The FI scheme is potentially more efficient than conventional ICF, but the various candidate secondary sources have their problems. One proposal for the fast ignitor source is to use a beam of high energy ions (Figure 4-2) [Rot01].

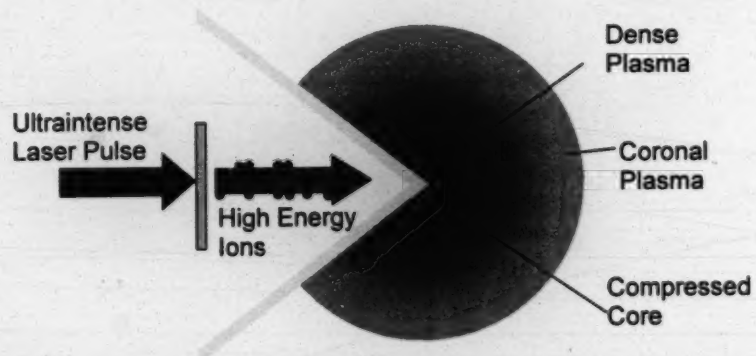

Figure 4-2. A schematic of one proposal for the fast ignitor scheme for inertial confinement fusion. A beam of high-energy protons is used to ignite the compressed pellet.

Reports of high energy ions produced at ultrahigh laser intensities (see below) appear promising for the FI scheme, but better control over the ion flux will be necessary to achieve the precise conditions to ignite a compressed ICF pellet. An enhanced understanding of the important laser-matter interaction mechanisms in

the ultrahigh intensity regime would enable such control. Since many of these mechanisms first appear in the femtosecond high intensity (10^{14}-10^{16} W/cm^2) regime, it is hoped that the present study of laser-matter interactions in this regime will contribute in some way to these efforts.

Another promising application of laser-produced plasmas lies in the field of medicine, where radiation therapy using high-energy ions has been explored. In radiation therapy, the chief objective is to maximize the amount of radiation delivered to the cancerous cells, while minimizing the damage to the surrounding healthy cells. Charged particles have attracted interest in the research community since the 1950s, since it was observed that the graph of energy loss as a charged particle travels through biological tissue displays a feature known as a Bragg peak, indicating that the bulk of the energy of the particle is lost just before the particle is stopped. Thus, using a beam of high-energy protons (or ions), a much higher degree of precision can be achieved (compared to conventional radiation therapy), since the heavier particle delivers most of its energy payload at the end of its journey, at the actual target cells. Also, the ions are not scattered significantly laterally, and can thus be confined to a small target spot. The chief obstacle to the clinical deployment of so-called proton therapy is the complexity and cost of present ion sources. An ideal ion source would provide a well-collimated ion beam with an energy tunable from 100 to 200 MeV, while maintaining a maximum flux of 10^{11} protons/s [Kho98]. While conventional particle accelerators can meet and exceed these specifications, they remain prohibitively expensive. For example, Japan has constructed the Heavy Ion Medical Accelerator, at a cost of $450 million. A compact radiation therapy ion source based on table top laser systems should be able to treat a patient at a fraction of the cost. It has been demonstrated that beams of fast ions with kinetic energies of up to 100 MeV are produced when firing ultraintense femtosecond laser pulses at thin foil targets [Hat00, Heg02, Rot02, Sna00]. However, it is clear that a large amount of research still needs to be done in this area. As with the proposed ion source for the FI scheme, an enhanced understanding of the interaction physics in this regime would enable better control of the ion flux. It is hoped that the present study can contribute to this understanding.

It has been proposed to use energetic ions emitted from laser-produced plasmas for ion implantation of various materials. Ion implantation is useful as a technique to change material properties in a controlled manner. Ion implantation based on laser-produced plasmas has already been demonstrated by Laska *et al.* [Las03, Wor00]. This group has demonstrated the implantation of a variety of ion species (Ag, Au, Pb, Sn, Ta ions) into various substrates (Al, Si, steel, plastic). The energetic ions were produced using an iodine laser system (τ_L~500 ps, E_L~45 J, I_L~1x10^{14} W/cm^2, 10-30 laser pulses). Using Rutherford backscattering spectroscopy, the doping profile was measured. For the case of Ag ions incident on an Al substrate, the group measured a maximum relative concentration of 7.6% at a depth of 40 nm, decreasing to 0.5% at 500 nm.

The aim of this chapter is to characterize the ion emission in the femtosecond regime in order to facilitate the use of the energetic ion flux for various applications. In particular, the feasibility of using the energetic particle

flux produced in the femtosecond regime for the technique of ion implantation will be investigated. Additionally, the particle flux could be used to test a high energy particle detection system.

Background

a) Laser-Matter Interaction Theory

The emission of fast ions is not a new phenomenon; from the early days of laser plasma research in the 1960s, the emission of fast ions has been observed. These ions originate from laser-plasma interactions at higher intensities ($>10^{13}$ W/cm^2).

The formation of a laser-produced plasma in the femtosecond regime is conceptually similar to plasma formation at low intensities (Chapter 2). There are, however, some important new issues which arise at the higher intensities achieved in the femtosecond regime. The first issue which arises is the presence of a prepulse. Many short-pulse laser systems unavoidably emit a lower energy pulse or series of pulses in advance of the main high-intensity laser pulse. This prepulse phenomenon can significantly alter the outcome of an experiment by altering the condition of the target before the arrival of the main pulse. For instance, if the prepulse is sufficiently intense, it can create a plasma on the target. If the main pulse arrives a short time later, it will interact with this plasma instead of interacting with a clean target surface. Of course, the physics of the laser absorption and other aspects of the laser-matter interaction will be drastically altered. Thus, the characteristics of the prepulse for a given laser system are an important consideration in this intensity regime. The prepulse is typically characterized by the contrast ratio, which is the ratio of the energy of the prepulse to the energy of the main pulse.

Assuming the presence of a significant prepulse, the main high-intensity laser pulse will interact with a plasma. The plasma will have an exponential density profile, characterized by a scale length L_{pre} (Figure 4-3).

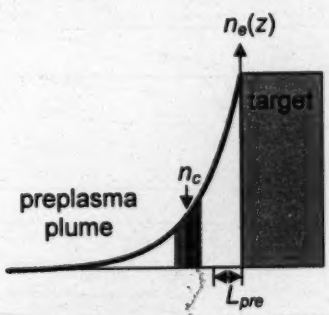

Figure 4-3. A schematic of the preplasma plume. The bulk of the laser energy absorption will occur near the critical surface.

The plasma scale length will vary depending on the precise characteristics of the prepulse. For smaller prepulse intensities, the plasma scale length is smaller. For

larger prepulse intensities, the plasma scale length can be larger, depending on the timing of the prepulse relative to the main pulse. The laser energy can be absorbed by the preplasma via a variety of mechanisms. The bulk of the laser energy absorption will occur near the critical surface, where the plasma electron density is equal to the critical density (n_c):

$$n_c = \frac{4\pi^2 m_e \varepsilon_0 c^2}{e^2 \lambda_L^2} \qquad \text{(4-1)}$$

where e is the elementary charge, ε_0 is the permittivity of free space, m_e is the electron mass, c is the speed of light, and λ_L is the laser wavelength [Che74].

Some of the energy absorption mechanisms will now be described. The common theme of these absorption models is that each gives rise to an unequal distribution of the laser energy among the electrons of the preplasma. Typically, a group of hot, non-thermalized electrons emerges from the interaction, carrying up to 20-40% of the absorbed laser energy [Gor02]. The hot electron temperature (T_h) scales with the laser intensity according to

$$T_h \propto B_h \left(I_L \lambda_L^2\right)^{a_h}, \qquad \text{(4-2)}$$

where I_L is the intensity of the laser pulse, λ_L is laser wavelength, and B_h and a_h are parameters which vary according to the mechanism. Some of the proposed mechanisms will now be described.

The resonance absorption model involves the excitation of longitudinal electron plasma waves by the p-polarized component of the electric field of the laser pulse at the critical surface [Che74, For77, Wil93]. When the waves reach sufficient amplitude and break, a relatively small number of electrons carry off the energy of the laser field. The hot electrons initially propagate in the backward (with respect to the laser propagation) direction, but some are reflected back into the forward direction by the ambipolar field which develops as a consequence of the separation of the electrons from the ions.

Another mechanism, described as vacuum heating, involves a small number of plasma electrons that are pulled away from the target and into the vacuum by the p-polarized component of the electric field of a laser pulse, and then reaccelerated back into the target by the electric field in the second half of the optical cycle [Bru87]. Because the quiver velocity of the electrons in the electric field of the laser radiation is so high, the electrons accelerated into the target can have energies greater than several tens of keV.

Another mechanism, described as direct laser acceleration, involves the ponderomotive force of the laser radiation [Yu00]. Essentially, the electrons of the preplasma are accelerated by the radiation pressure of the laser pulse [Bra04]. Normally, the acceleration caused by the rising half of the laser pulse would be counteracted by the deceleration caused by the falling half of the pulse. In the direct laser acceleration model, when the laser pulse reaches the critical surface, it will be reflected, so that electrons accelerated in the forward direction will maintain their energy. Furthermore, the forward acceleration of these electrons creates a charge imbalance in the preplasma, causing a return current of electrons to travel in the backward direction.

Another mechanism, termed *JxB* heating, arises from the *vxB* term in the Lorentz force equation [Kru85]. Preplasma electrons oscillate in the optical field with an energy (E_{osc}) given by [Puk03]

$$E_{osc} = \frac{eE_F \lambda_L^2}{16\pi^2 m_e c^2}, \quad \text{(4-3)}$$

where E_F is the electric field of the laser pulse, m_e is the electron mass, e is the elementary charge, and c is the speed of light. As the electron oscillatory velocity becomes significant, the *vxB* term in the Lorentz equation results in a force parallel with the direction of laser propagation. The electrons will oscillate longitudinally, and via collisions and other loss mechanisms, the laser field will lose its energy to these electrons.

The hot electrons generated by the above described mechanisms give rise to a variety of interesting phenomena. The electrons themselves have been observed to escape the target in highly collimated jets [Che01, Ser04]. If the atomic number of the target atoms is large enough, and a solid target is used, the hot electrons may interact with the target to produce hard x-rays [Ser04]. Most interesting, however, is the interaction of the hot electrons with the target resulting in the generation of high-energy ions. A variety of mechanisms have been proposed to explain the observed ion emission: target-normal sheath acceleration, interaction zone acceleration, *etc.*. These proposed mechanisms are essentially variations on a theme: the hot electrons escape the target (from the rear or from the front) and establish a strong electrostatic field which subsequently accelerates the ions [Cla00, Hat00, Rot02]. As early as 1986 [Git86], it was recognized that the identity of a number of the fastest ions observed in experiment was most likely to be protons. These protons would originate from hydrocarbon and water impurities on the target surface, due to the presence of oil in the vacuum systems used in experiments and water vapor from the air. Protons would be accelerated preferentially by the large electrostatic fields because of their favorable charge-to-mass ratio.

In addition to the above mechanisms, J. Badziak *et al.* [Bad04] have proposed a relatively unique mechanism which describes fast ion generation in the high intensity regime (10^{14}-10^{17} W/cm^2). In their model, referred to as the skin-layer ponderomotive acceleration model, the ponderomotive force of the laser pulse at the critical surface of the preplasma drives two macroscopic plasma blocks in opposite directions away from the critical surface. The high density of ions and electrons within these blocks results in a large current density. They estimate that the ion energy (E) scales approximately linearly with the incident laser irradiance $\left(I_L \lambda_L^2\right)$:

$$E \propto I_L \lambda_L^2. \quad \text{(4-4)}$$

b) Literature Survey

Experimentally, the determination of the exact scaling relationship between the ion energy and the incident laser intensity (or irradiance) has been the focus of much of the research in this field. In 1986, S. J. Gitomer *et al.* compiled available data on energetic ions produced by the interaction of long (typically a

few nanoseconds in duration) laser pulses with matter. This compilation consisted of data collected using a variety of detectors (Langmuir probes, Faraday cups, electrostatic analyzers, *etc.*) with a variety of laser systems (CO_2, Nd:glass, KrF, *etc.*) with a variety of targets (C, Al, Au, *etc.*). The result of this exhaustive compilation was the estimation of the approximate scaling of the fast ion energy with incident laser irradiation. Gitomer *et al.* found that the ion energy scales approximately as $(I\lambda^2)^{0.3}$ in the low irradiance regime (10^{10}-10^{15} $Wcm^{-2}\mu m^2$), as $(I\lambda^2)^{1.3}$ in the high irradiance regime (10^{14}-10^{17} $Wcm^{-2}\mu m^2$), and as $(I\lambda^2)^{0.4}$ in the relativistic irradiance regime (10^{17}-10^{19} $Wcm^{-2}\mu m^2$).

Since that time, many groups have performed similar scaling studies, attempting to study the fast ion emission in new intensity and pulse duration regimes which have only recently been made accessible (see above). In the short pulse regime at high intensities (10^{14}-10^{17} W/cm^2), a few groups have reported their findings.

V. M. Gordienko *et al.* used a femtosecond dye laser (τ_L=200 fs, λ_L=616 nm, contrast ratio of 10^{-5}) with a maximum intensity of $3x10^{16}$ W/cm^2 incident with p-polarization on a silicon target to determine the ion energy scaling parameter [Gor02]. They utilized a microchannel plate (MCP) detector [Dec02, Pan76, Str99] to measure the ion time-of-flight spectrum. Gordienko *et al.* found that the ion energy scaled approximately as $(I\lambda^2)^{0.8}$, in the range $2\text{-}8x10^{15}$ $Wcm^{-2}\mu m^2$.

J. Badziak *et al.* have performed several different studies of the ion energy scaling [Bad01, Bad03, Bad04]. In 2001, Badziak *et al.* reported that the ion energy scaled approximately as $(I\lambda^2)^{1.04}$ over the irradiance range $0.2\text{-}2.5x10^{16}$ $Wcm^{-2}\mu m^2$ [Bad01]. These results were obtained using a 1.05 μm Nd:glass laser, which generated 1 ps pulses of energy up to 1 J, with a contrast ratio of 10^{-4}. The s-polarized pulses were incident on a solid copper target, with an angle of incidence of 0° (measured with respect to the target normal). The determination of ion energy was made using a combination of time-of-flight analysis of ion collector signals and an electrostatic ion energy analyzer. In 2004, using the same laser system and detectors, but switching to a solid gold target, Badziak *et al.* reported that the ion energy scaled approximately as $(I\lambda^2)^{1.02}$ over the irradiance range $1\text{-}8x10^{16}$ $Wcm^{-2}\mu m^2$ [Bad04]. This value agreed (within error) with the scaling behavior predicted by two-fluid hydrodynamic simulations performed by the group. The simulations predicted that the ion energy scales approximately as $(I\lambda^2)^{0.88}$ over the irradiance range $0.1\text{-}2x10^{17}$ $Wcm^{-2}\mu m^2$.

P. A. VanRompay *et al.* did not investigate the scaling of ion energy with incident laser irradiance, but they did observe a fast proton signal using their MCP detector [Van98a]. They used a 780 nm Ti:Sapphire laser system producing 100 fs s-polarized pulses incident on a carbon target at an intensity of $1x10^{15}$ W/cm^2. At this intensity, they observed a fast proton velocity of $5.5x10^5$ m/s, corresponding to a proton energy of 1.58 keV.

A. Zhidkov *et al.* performed a study of the ion energy scaling using a particle-in-cell (PIC) simulation [Zhi00]. They used a subpicosecond pulse duration, with thin foil metal targets. They observed the emission of high-energy (MeV) ions over the irradiance range 10^{16}-10^{18} $Wcm^{-2}\mu m^2$.

The most energetic protons and electrons have been observed to emerge from laser-matter interactions in the ultrahigh intensity regime (10^{18}-10^{21} W/cm^2). Electrons with energies in excess of 100 MeV have been observed, and in addition, collimated (<5°) beams of nearly monoenergetic 75 MeV electrons [Man04] have also been reported. Collimated (<10°) beams of protons with energies in excess of 58 MeV have also been observed [Sna00]. Heavier ion species have also been produced, with energies up to 430 MeV [Cla00].

The above described data have been summarized in the figure below.

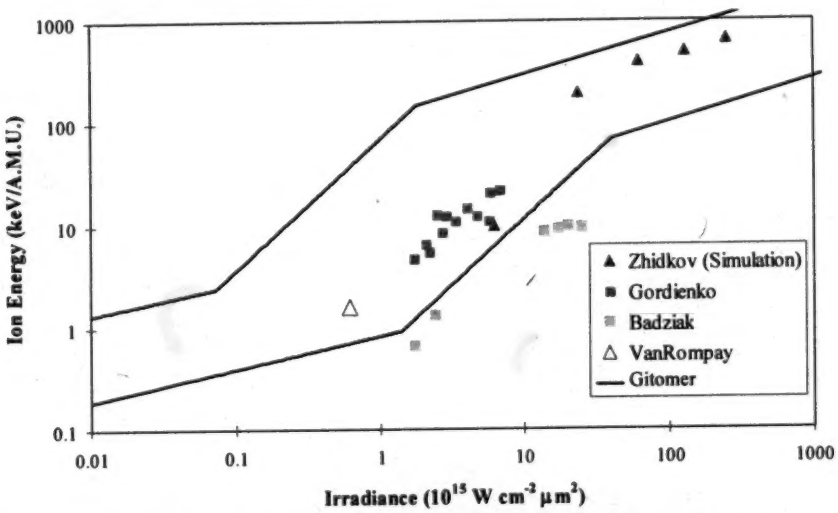

Figure 4-4. Summary of the currently available data for fast ion scaling with laser irradiance. This chapter involves irradiances ranging from 10^{14}-10^{16} Wcm^{-2}μm^2. The data has been compiled from the following sources: Zhidkov [Zhi00], Gordienko [Gor02], Badziak [Bad01], VanRompay [Van98a], and Gitomer [Git86].

Experiment

In the experiments of this chapter, a Spectra-Physics Hurricane laser system was used (see figure below). This laser system is an 800 nm Ti:Sapphire laser system based on the CPA principle described above.

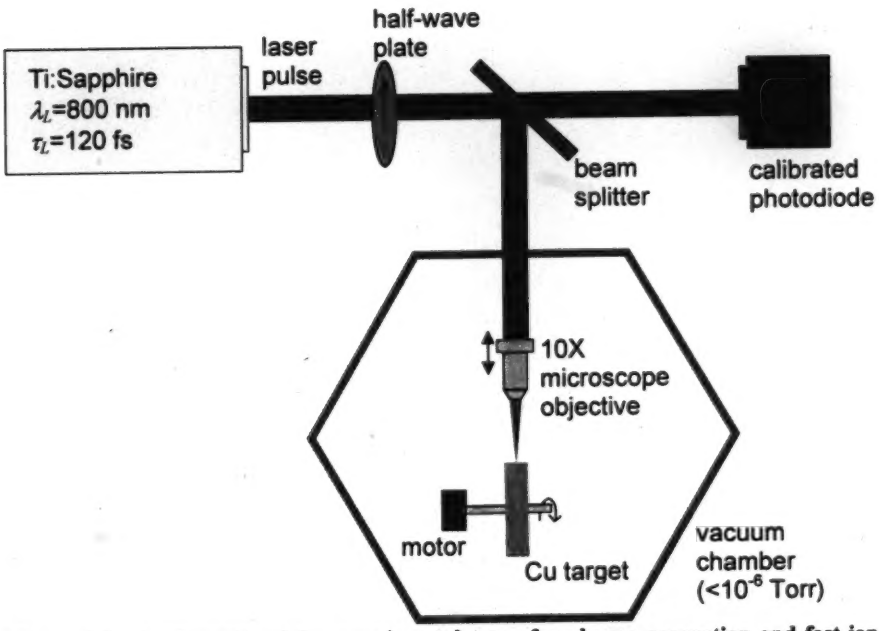

Figure 4-5. A schematic of the experimental setup for plasma generation and fast ion detection in the femtosecond regime.

The laser system is capable of producing 250 μJ pulses on target, as measured by a Gentec TPM-300 power meter. This power meter was used to calibrate an FND-100 photodiode, in order to monitor the laser energy for each individual shot. The pulse duration is approximately 120 fs full-width at half-maximum (FWHM), as measured by a single shot autocorrelator (Positive Light Model SSA). This is an approximate value, since the dispersion of the various optical elements in the figure above is not taken into account. The beam shape closely approximates the TEM_{00} mode according to beam profile measurements[1]. The laser polarization is controlled using a half-wave plate (CVI Laser, QWPO-800-06-2-R10). Either s- or p-polarized radiation can be employed.

As mentioned in the previous section, a series of low-energy prepulses precede the emission of the main pulse in the laser system. The prepulse train is caused by the finite leakage through the Pockels cell which switches the main pulse out of the laser cavity [Sal91]. The prepulse train was measured using an FND-100 photodiode with a fast capacitor as a charge source to limit the total signal which can be obtained, to cut off the main pulse which follows at much greater amplitude. An example of the photodiode signal due to the prepulse train is given in the figure below.

[1] These measurements were performed by S. E. Kirkwood, another graduate student in the laboratory.

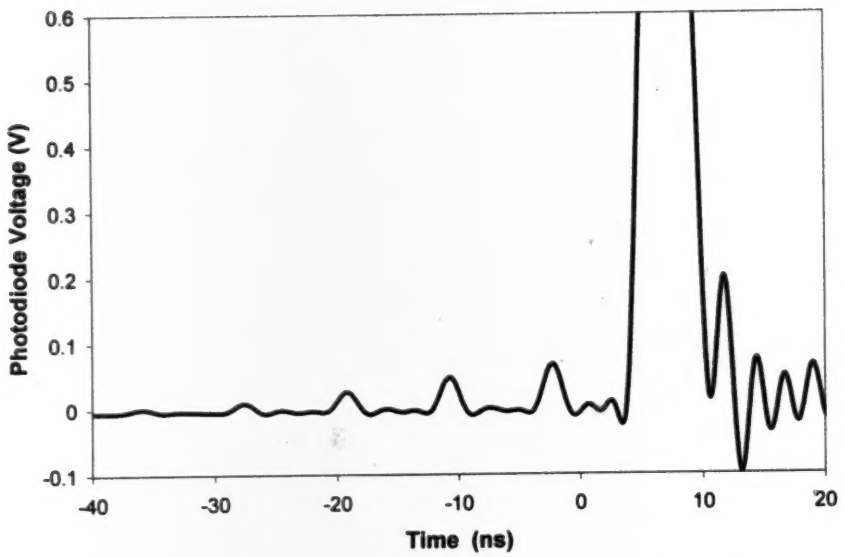

Figure 4-6. An image of the prepulse train which precedes the main pulse in the laser system. To detect the prepulse train, an FND-100 photodiode with a fast capacitor was used[1].

The main pulse, centered at 6.5 ns, is preceded by a train of increasingly energetic prepulses, spaced 8.4 ns apart. The oscillations trailing the main pulse in the above figure are due to ringing in the photodiode circuit. The contrast ratio of the largest prepulse was measured using the photodiode and a set of calibrated infrared filters (Schott NG 4 and NG 9 filters), and found to be $3\text{-}4 \times 10^{-4}$, varying from day-to-day depending on the laser operating parameters.

The laser pulses were focused onto the target using a large working distance microscope objective (M Plan Apo 10X Mitutoyo), located 6 m away from the laser output. The focal length of this microscope objective is 20 mm, the working distance is 33.5 mm, and the numerical aperture is 0.28. A blast shield, consisting of a microscope cover slip was used to shield the objective from the plasma deposition. The laser spot size on target was imaged with a 60X microscope objective onto an infrared CCD camera (Ultrak K-500), with Spiricon LBA-400PC software[1].

---

[1] These measurements were performed by C. Serbanescu, another graduate student in the laboratory.

Figure 4-7. The focused beam profile at low laser energy as measured using an infrared CCD camera (Ultrak K-500) with Spiricon LBA-400PC software[1].

The focal spot above is slightly asymmetric; the beam diameter measured along the x-coordinate is 1.8% larger than that measured along the y coordinate. The beam waist (ω, defined as the radius at which the beam intensity drops to exp(-2) of its peak value), averaged over the x and y coordinates was found to be 1.90 μm. Note that the beam energy was attenuated for this measurement; it is thus possible that some small fraction of the laser energy is scattered out of the focal region, decreasing the intensity on target.

The laser intensity on target was varied by changing the position of the microscope objective, thus changing the focal spot size on the target. The microscope objective was mounted on a Zaber Technologies TLA-60 motor, which has sub-micrometer resolution and excellent stability. The hysteresis of this motor was taken into account when moving the microscope objective. According to Gaussian beam theory [Sal91], the beam waist (ω) varies with the longitudinal distance (z) from the position of best focus according to

$$\omega^2 = \omega_0^2\left(1+\frac{z^2}{z_0^2}\right), \qquad \textbf{(4-5)}$$

where ω_0 is the beam waist at the position of best focus (1.90 μm), z_0 is the Rayleigh range given by

$$z_0 = \frac{\pi\omega_0^2}{\lambda_L}, \qquad \textbf{(4-6)}$$

and λ_L is the laser wavelength. Using ω_0=1.90 μm, and λ_L=800 nm, the Rayleigh range is calculated to be 14.2 μm. This calculation assumes that the measured beam waist corresponds to a diffraction limited TEM_{00} mode, which is unlikely.

[1] This measurement was performed by C. Serbanescu.

A more accurate calculation would incorporate the M^2 parameter of the beam, which was not measured. The various error contributions in the calculation of the intensity on target are discussed further below. Using the measured value of ω_0, the peak laser intensity (I_L) can be calculated for different microscope objective positions, with different laser energies (E_L), for a given Gaussian pulse duration (τ_L, defined as FWHM), according to the following equation:

$$I_L = \frac{4}{\pi\omega^2}\sqrt{\frac{\ln 2}{\pi}}\frac{E_L}{\tau_L}. \quad \textbf{(4-7)}$$

The determination of the position of best focus is described later in this section[1]. The estimated error in the calculation of intensity is discussed further later in this section.

The target was a polished solid copper disk, which was rotated briefly after each shot using a DC motor in order to provide a fresh target area for each pulse. No precautions were taken to ensure that the target surface is clean. This issue will be discussed further in the next section. Now, due to the small Rayleigh range (14.2 μm), the focal conditions were extremely demanding, such that a small longitudinal drift of the target (either towards or away from the microscope objective) could result in a significant change in the focal spot size on target. In order to overcome this difficulty, care was taken to ensure that the radius of the copper disk was extremely consistent from one sector of the disk to another, and the stability of the disk mount was verified, such that the consistency of the focal conditions from shot to shot was maintained. For the target used in the experiments, the variation in the disk radius was measured to be less than ± 6 μm for the entire disk, with significantly less variation within a given sector of the disk. In the experiments, typically less than 100-200 laser shots were taken, and the target rotation was only rotated very briefly after each shot, so that the total rotation of the disk over the course of an experiment was small (~20-30°). In this way, the target position (with respect to the microscope objective) would not drift appreciably[2].

The laser was incident on the copper target at an angle of 22° with respect to the target normal (see figure below).

---

[1] The focal system was developed by C. Serbanescu.

[2] The design of the target mount was performed by C. Serbanescu.

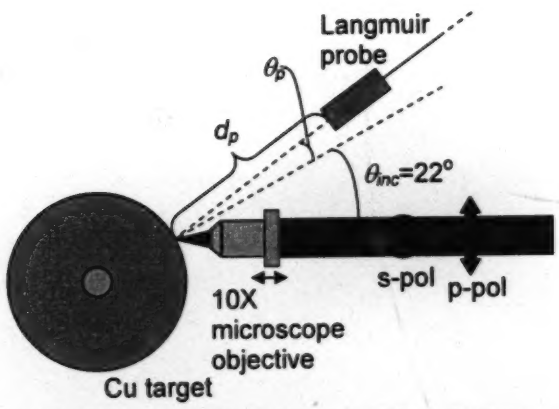

Figure 4-8. Side view of the experimental geometry. Note the laser angle of incidence (θ_{inc}) and the Langmuir probe position, defined by the probe distance (d_p) and the probe angle (θ_p) measured with respect to the target normal.

The target chamber was evacuated using a roughing pump and a diffusion pump, reaching a base pressure of $<7.5\times10^{-7}$ Torr (measured with an Edwards Active Pirani Gauge, model APG-L-NW16), such that the particle flux reached the detectors unimpeded by interactions with ambient gas particles.

To detect the ion flux, Langmuir probes were used, biased at -40 V, and terminated with 50 Ω resistors (see Figure 2-9). The detector signal was displayed using TDS 210/220/360/380 oscilloscopes and recorded using a laptop computer. The main probe used to detect the fast ion flux was positioned as close as possible to the target normal, with d_p=101 mm and θ_p=7°.

In addition to the Langmuir probe, a PIN diode detector (Quantrad silicon PIN diode detector, with an active layer thickness of 250 μm and a surface of 5 mm^2) fitted with a 25 μm aluminum filter was also used to detect x-rays and energetic electrons as part of the focusing procedure (see figure below).

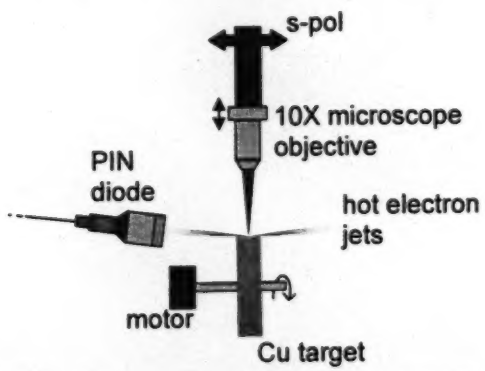

Figure 4-9. A schematic of the use of the PIN diode to capture the hot electron jet signal to ensure optimum focus of the laser beam on the target.

In work performed by C. Serbanescu, hot electrons were observed to be emitted from the laser-produced plasma in collimated jets [Ser04]. The direction of these jets was found to vary with the polarization of the incident radiation; for s-polarization, the jets are directed nearly parallel to the target surface, in the direction of the electric field vector. The PIN diode, normally used as an x-ray detector, was found to be sensitive to the hot electron jets. It was also observed that the hot electron signal was extremely sensitive to the focal conditions. It is assumed that the maximum hot electron signal corresponds to the maximum intensity on target. This assumption may be unfounded, and the intensity values reported in the next section should be viewed in this light. The PIN diode signal reaches a maximum of several volts at the position of best focus, and drops to a few tens of millivolts when the microscope objective moves 15-20 μm away (see figure below). An additional example of a focal scan is included in the Appendix.

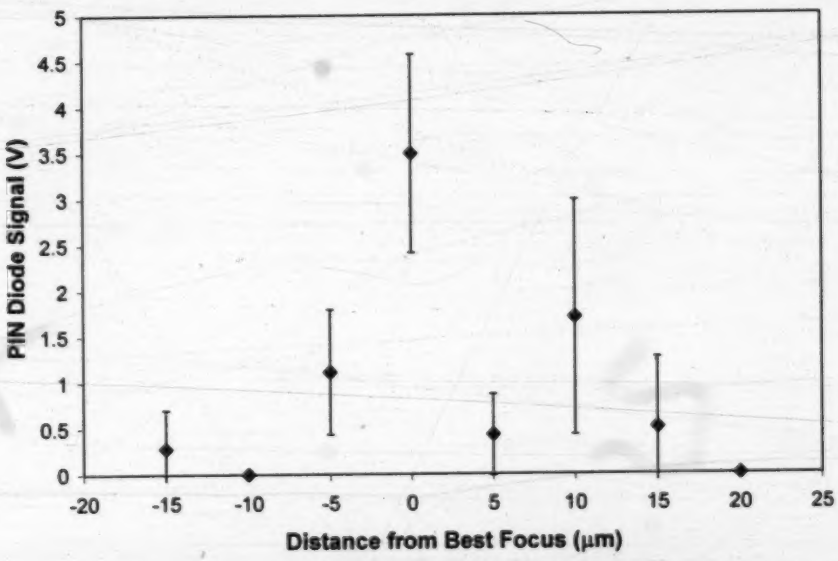

Figure 4-10. A typical focal scan using the PIN diode detector to monitor the hot electron signal. Each data point represents the average of three laser shots, with the error bars representing the difference between the maximum and minimum signal within the set of three shots.

The stochastic nature of the hot electron jet signal makes it difficult to accurately determine the position of best focus. It is estimated that the error in this measurement of the best focus position is ± 8 μm. Another important uncertainty is the estimated uncertainty in the target position (with respect to the microscope objective), which is taken to be ± 3 μm. Since the calculation of the intensity depends on the longitudinal distance from the position of best focus (via Equation 4-5), the combined uncertainties in the target position and the best focus position are the main consideration in the estimation of the error in the calculation of the

laser intensity on target. The estimated error in the intensity values ranges from ± 20-25% at the higher intensities (>$5x10^{15}$ W/cm^2) to ± 10-20% or less at the lowest intensities. In the future, the large uncertainty in the calculated intensity values could be reduced by characterizing the focal conditions more reliably, ensuring that the position of best focus is well-known and the stability of the target position is maintained.

Results and Discussion

a) Identification of Ion Species

Typical Langmuir probe signals are given in the figure below. Additional Langmuir probe data is included in the Appendix.

a)

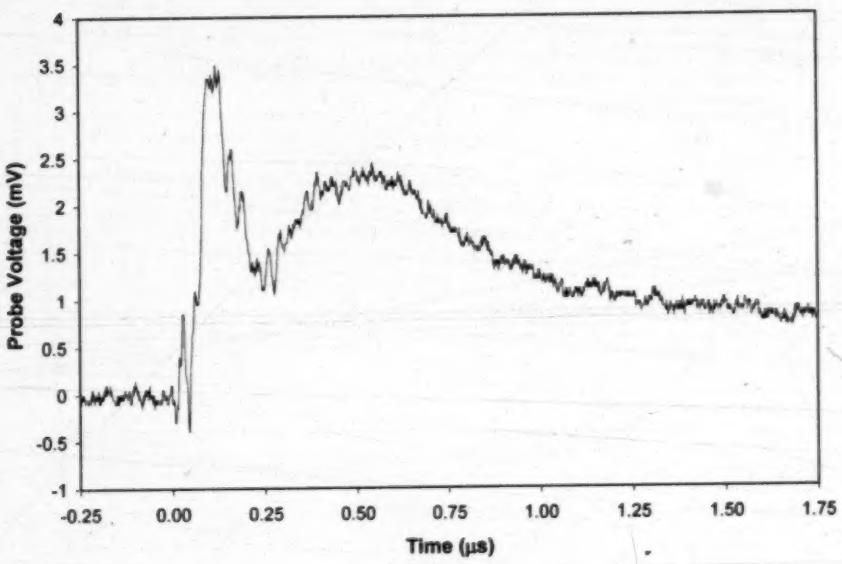

b)

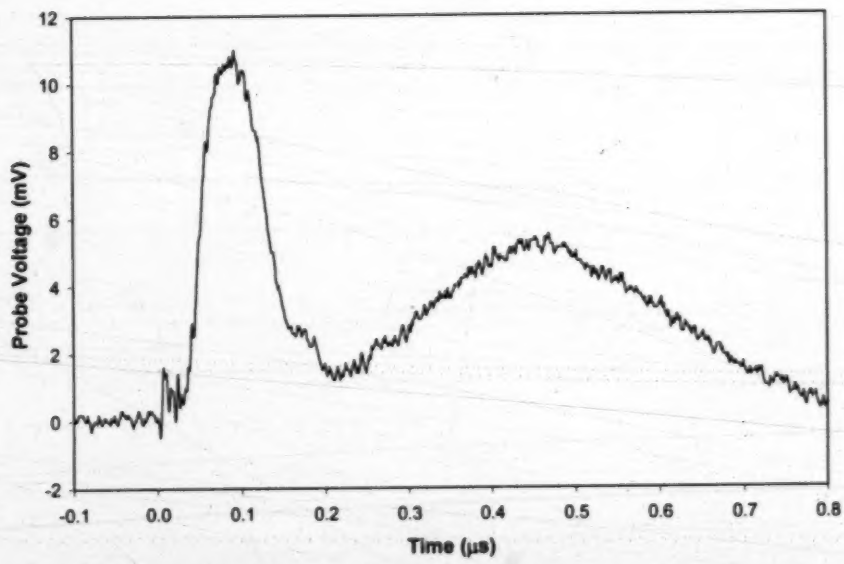

Figure 4-11. Example Langmuir probe signals. a) A typical Langmuir probe signal, recorded from a laser shot with an energy of 231 μJ and an intensity of 3.2×10^{16} W/cm^2, with s-polarization, for a probe distance of 101 mm. b) A typical Langmuir probe signal recorded from a laser shot with an energy of 214 μJ and an intensity of 2.9×10^{16} W/cm^2, with p-polarization. Time zero represents the instant when the laser pulse strikes the target.

For both signals, three distinct peaks can be observed. The first peak is significantly smaller in amplitude and significantly earlier in time compared to the other peaks. This early peak is probably hot electrons causing secondary electron emission from the detector (Equation 2-12). If $\gamma_{eff}(v)>1$ for the hot electrons, an electron incident on the detector would cause the emission of one or more secondary electrons, resulting in a net positive signal. This peak disappears when a ~0.2 T magnetic field is placed in front of the detector (see description of magnetic field experiment below). This confirms that the first peak is caused by energetic electrons, since electrons cannot pass through a 0.2 T magnetic field due to their small mass.

The second peak is the largest amplitude peak, and as discussed below appears to consist of fast protons arising from the hydrocarbon impurities on the copper target. This group of fast ions is the focus of this study. These faster particles are potentially useful (depending on their identity) for different applications; for instance, in ion implantation, the faster ions could penetrate a substrate and alter its physical properties. In order to ascertain the source of these fast ions, the surface of the copper target was pre-cleaned with a laser shot to vaporize the hydrocarbon impurity layer. After the surface was cleaned, another high-intensity laser shot was fired on the same spot on the target, and little to no fast ion signal was observed. The figures below demonstrate the effect of pre-cleaning.

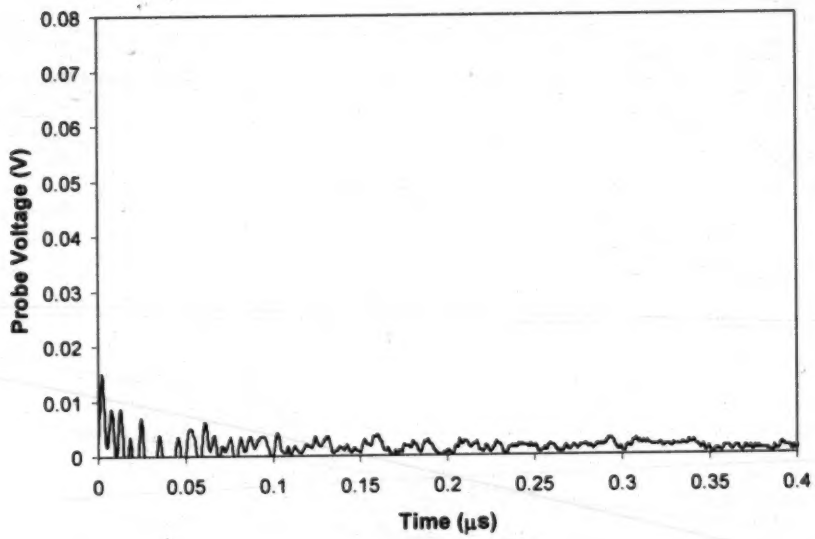

a)

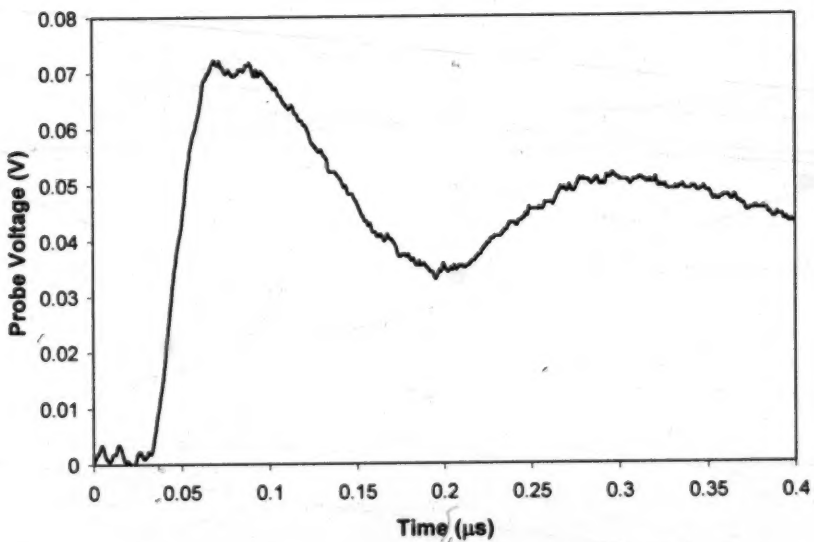

b)

Figure 4-12. Example Langmuir probe signals, with (a) and without (b) target pre-cleaning. The laser parameters were E_L=229 μJ, I_L=2.1x10^{16} W/cm^2 with p-polarized radiation, for both the above shots as well as the pre-cleaning shot.

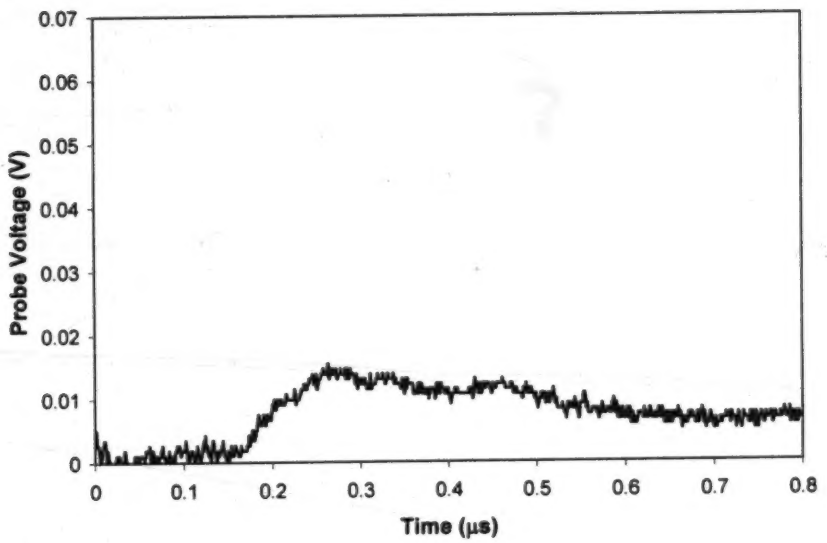

a)

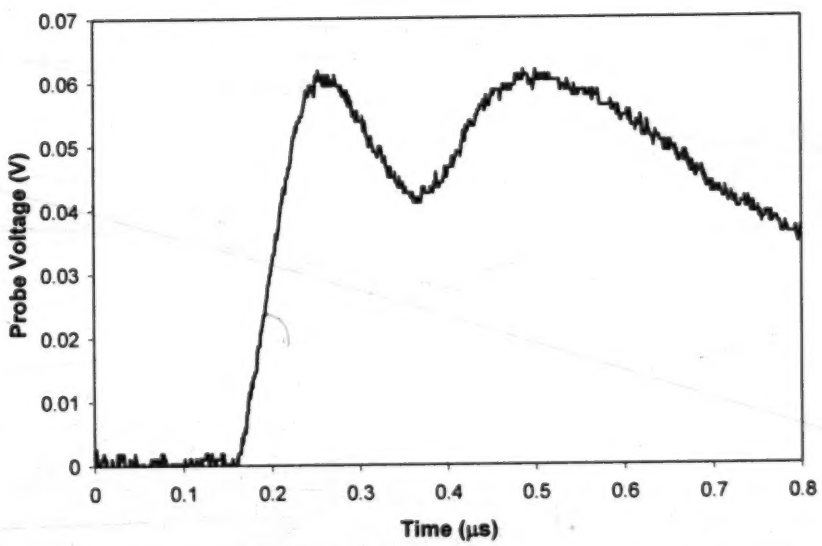

b)

Figure 4-13. Example Langmuir probe signals, with (a) and without (b) target pre-cleaning. The laser parameters were E_L=212 μJ, I_L=2.2x10^{15} W/cm^2 with s-polarized radiation, for both the above shots as well as the pre-cleaning shot.

These results suggest that the largest amplitude peak consists mainly of protons originating from hydrocarbon impurities on the surface of the target. However, since the intensity of the target pre-cleaning shot is fairly high, it may be possible that the diminished ion signal in Figures 4-12a and 4-13a is a consequence of the

presence of an ablation crater on the target surface due to the pre-cleaning shot. A more appropriate method of target pre-cleaning might involve the use of a series of low intensity laser pulses on target. Note also that in Figure 4-13a, some residual fast ion signal is observed, even after target pre-cleaning. This may indicate that some small impurity residue remained on the target after pre-cleaning, since the intensity for Figure 4-13 is an order of magnitude smaller than the intensity for Figure 4-12. Another possibility is that the small residual signal observed in Figure 4-13a actually consists of bulk target (i.e. copper) ions. In any case, it appears that the fast ion peak is dominated by ions originating from the impurity layer. As a further check on this hypothesis, the thickness of the impurity layer corresponding to the observed proton signal level is estimated below.

The third peak likely consists of oxygen ions and carbon ions from the hydrocarbon impurity layer, with some proportion of bulk target ions. In other studies [Bad01, Bad03, Bad04, Gor02], it was observed that the earliest and largest amplitude peak (here, the middle peak) generally consisted of fast protons. Subsequent peaks consisted of ions with smaller charge-to-mass ratios, such as carbon ions (from the hydrocarbon impurities) and bulk target ions. These observations are consistent with the above hypothesized identification of the peaks.

In order to gather more evidence regarding the identities of the ion species present in the fast ion flux, a magnetic field experiment was performed. Essentially, a crude ion spectrometer was constructed. A magnetic field was used to bend the fast ion flux, and three different Langmuir probes were positioned to detect the ions based on their trajectory (see figure below).

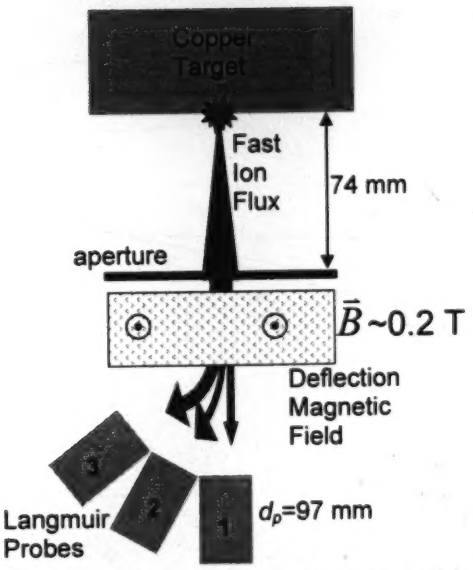

Figure 4-14. A schematic of the crude ion spectrometer used in the attempt to identify the various ion species present in the fast ion flux. The deflection magnetic field was directed out of the page. The laser pulse which produces the plasma is not shown. The aperture diameter was 6.35 mm.

The magnetic field was provided by a pair of simple bar magnets (dimensions 22 x 10 x 5 mm) separated by an 11 mm gap. The field between the two bar magnets was measured using a calibrated LakeShore 410 Digital Gaussmeter and found to have a maximum of 0.24 T (see figure below).

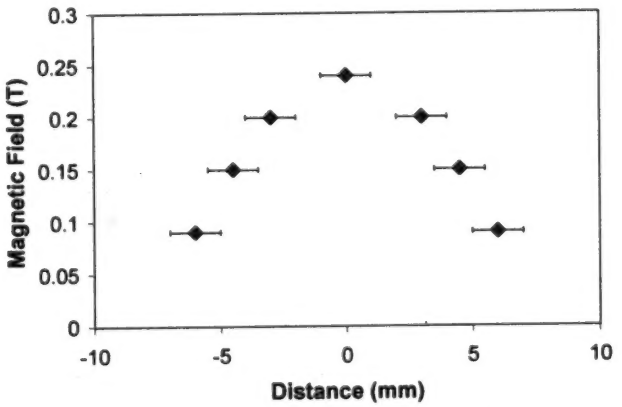

Figure 4-15. The magnetic field between the two bar magnets, measured along the undeflected ion trajectory. The distances are referenced to the position of maximum field.

The error in the distance measurements was ± 1 mm. The error in the field amplitude is ± 2%, according to the manufacturer's specification. The aperture diameter was 6.35 mm. The distance between the aperture and probe 1 was 23 mm, and the distance between probe 1 and the target was 97 mm (slightly closer to the target than for the other experiments of this chapter). The other two probes were roughly equidistant (~97 mm) from the target.

The three Langmuir probes were positioned so as to capture the deflected ions. The angular positioning of probe 1 with respect to the target normal is identical to the other experiments of this chapter; that is, the angle between probe 1 and the target normal is 7°. The other two probes were located in the same plane, with the probe faces directed towards the aperture as indicated in Figure 4-14. Probe 1 was positioned to capture the undeflected ions, although due to its diameter (6.35 mm), ions deflected through 0-9° (measured with respect to the undeflected ion trajectory) reached the probe. Probe 2 was positioned to capture ions deflected through 21-48°. Probe 3 was positioned to capture ions deflected through 50-56°.

Before continuing, it must be noted that this experiment was limited, in the sense that only partial information regarding the identity of the ion species present in the particle flux could be obtained. This was due to the fact that only three probes were used to detect the ions, and each of the probe signals captured ions from a fairly wide range of ion trajectories. Another factor was the large aperture diameter (6.35 mm). The aperture was comparable in size to the gap between the bar magnets (11 mm) and the probe diameter (6.35 mm). The large diameter of the aperture allowed ions passing through near one edge of the aperture to experience a different magnetic field than ions passing through near the opposite edge of the aperture. Additionally, ions passing through the aperture near opposite edges might be deflected by the same angle, but reach different probes due to the geometry and positioning of the probes. These issues make it difficult to draw definitive conclusions from the experimental results. However, the data do provide some evidence of the identity of the ion species.

In the analysis of the experimental results, it is helpful to estimate the ion trajectories due to the imposed magnetic field. Without doing detailed calculations of the ion trajectories, the angle of deflection of the various ion species can be estimated using the expression for the Lorentz force $\bar{F}$ on a particle of mass m_i and charge Ze traveling with velocity $\bar{v}$ through a magnetic field $\bar{B}$:

$$\bar{F} = Ze\bar{v} \times \bar{B}. \quad \textbf{(4-8)}$$

Then, the magnitude of the perpendicular velocity component $v_\perp$ generated by the Lorentz force can be estimated as

$$v_\perp = \frac{F}{m_i}\frac{d_B}{v} = \frac{Zed_BB}{m_i}, \quad \textbf{(4-9)}$$

where d_B is the length of the particle trajectory within the magnetic field. The angle of deflection θ_{def} can then be estimated as

$$\tan\theta_{def} = \frac{Zed_BB}{m_iv}. \quad \textbf{(4-10)}$$

Note that the preceding analysis assumes the ions behave as single particles. If the plasma flux incident on the detector was of sufficient density, the external magnetic field could be shielded out, and the bulk of the ion flux would be undeflected. However, the results below indicate that this is unlikely, since the ion flux is deflected substantially. Using these equations, the deflection angle for various species arriving at different times at the detectors can be estimated. The results are summarized in the table below.

Ion Species	Time of Flight (μs)	Deflection Angle (degrees)
H^+	0.1	11.2
	0.3	30.7
C^+	0.1	0.9
	0.3	2.8
C^{2+}	0.1	1.9
	0.3	5.6
C^{3+}	0.1	2.8
	0.3	8.4
Cu^+	0.1	0.2
	0.3	0.5
Cu^{5+}	0.1	0.9
	0.3	2.7
Cu^{10+}	0.1	1.8
	0.3	5.3

Table 4-1. Estimated deflection angles for various ion species with various velocities. These estimates may be used to interpret the experimental results, while keeping in mind the limitations of the estimates, and the uncertainty introduced by the large diameter of the aperture. Recall that the particle velocity is inversely related to its time-of-flight (Equation 2-5).

For the purposes of the estimate, the values B=0.2 T and d_B=1 cm were used. The estimates in the above table indicate that the protons within the fast ion peak will be deflected by the largest angle, and will likely reach the angled probes (probes 2 and 3). The carbon ions will be deflected appreciably, and may reach probe 2. The copper ions, due to their large mass, should not be bent to any significant degree. Also note that the velocity of the ions affects their trajectory. In this experiment, the intensity on target was varied, in order to produce a variation in the ion velocity (see Figure 4-18 below). Both s- and p-polarized radiation were used, in case the fast ion flux composition varied with the incident laser polarization.

The result of a typical laser shot is given in the figure below.

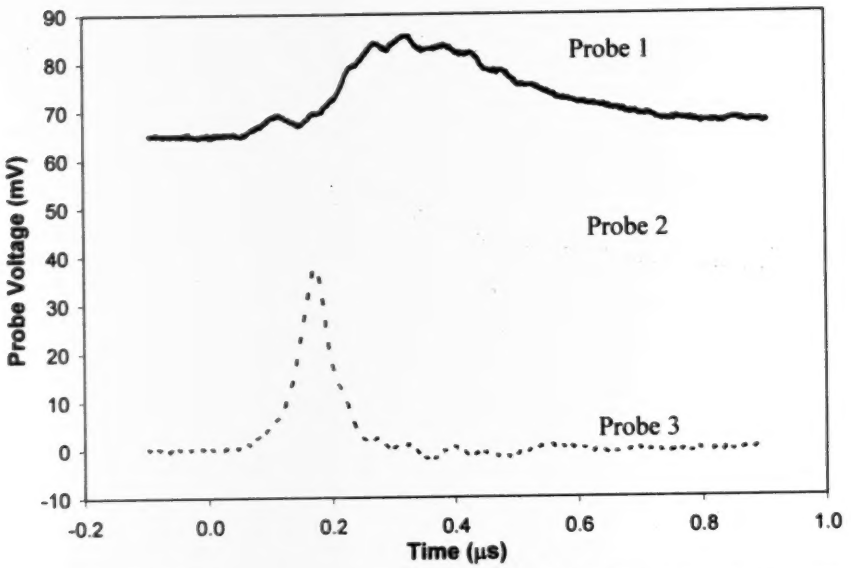

Figure 4-16. The Langmuir probe signals exhibiting the deflected ion signals. The radiation was s-polarized, the laser energy on target was E_L=214 μJ, corresponding to an intensity on target of I_L=2.0x10^{16} W/cm^2. The signals are offset vertically for the purposes of clarity.

The large amplitude signals observed for probes 2 and 3 indicate that the fast peak of ions is significantly bent by the magnetic field. This constitutes evidence that the fast ion peak is composed mainly of protons. Assuming the fast ion peak is composed entirely of protons, the above signals can be accounted for as follows. The fastest protons in the fast proton peak remain nearly undeflected, and arrive at probe 1. These protons are few in number, resulting only in a small peak in the probe 1 signal. Lower energy protons are deflected to probe 2, and the lowest energy protons within the fast ion peak arrive at probe 3. Of course, the small peak in the probe 1 signal may be attributed to carbon, oxygen, or copper ions. It might even be possible to attribute the probe 2 signal, and perhaps even the probe 3 signal, to high charge state copper, oxygen, or carbon ions. However, examining the estimates in the above table, this possibility appears remote. It is more appropriate to attribute the later peaks in the probe 1 and probe 2 signals to these ion species. As discussed earlier, such a conclusion is consistent with the literature.

Another example of a typical laser shot, at a lower laser intensity, is given in the figure below. Additional sample data is included in the Appendix.

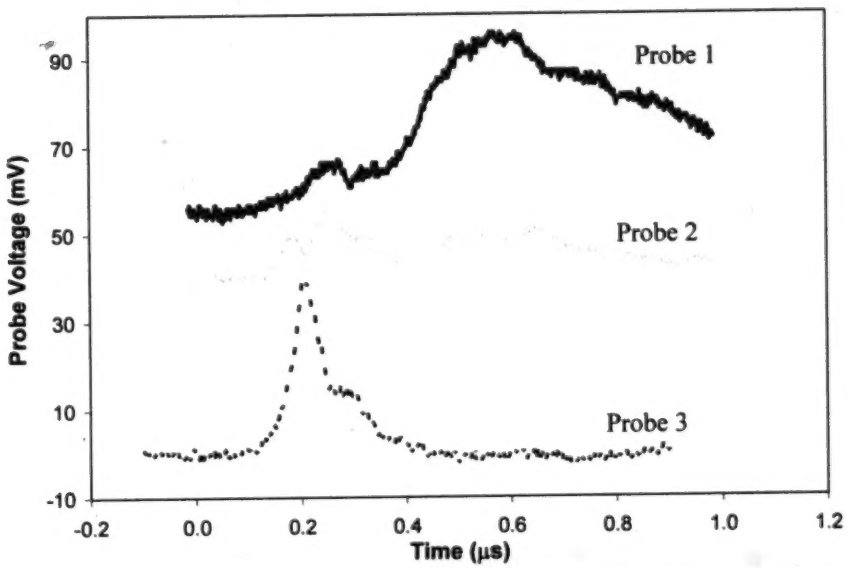

Figure 4-17. The Langmuir probe signals exhibiting the deflected ion signals. The radiation was s-polarized, the laser energy on target was E_L=220 μJ, corresponding to an intensity on target of I_L=1.2x10^{15} W/cm^2. The signals are offset vertically for the purposes of clarity.

The lower intensity produces slower ions, which are more readily deflected. This is the likely cause of the increase in the probe 3 signal relative to that of probe 2, compared to the previous figure. The peak in the probe 3 signal most likely consists of protons. The first peak in the probe 2 signal is likely to be protons which are slightly more energetic than those collected by probe 3. The second peak in the probe 2 signal is likely to be carbon ions. The peaks in the probe 1 signal could be due to copper, oxygen, or carbon ions.

Thus, from the results, it appears that the fast ion peak observed in the femtosecond experiments consists of protons, with subsequent peaks consisting of some combination of carbon, oxygen and copper ions. Such a multi-species ion flux is detrimental for certain applications, including ion implantation.

b) Ion Energy Scaling

The chief objective is to study the characteristics of the fast proton emission from the laser-matter interaction. To this end, the intensity scaling of the fast proton peak velocity was investigated. The laser intensity on target was varied by changing the distance between the microscope objective and the target, thus changing the focal spot area. The ion velocity is one of the most important parameters of the ion emission. For instance, in ion implantation, the chief determinant of the penetration depth of a given ion is its energy. Recall from Chapter 2 (Equation 2-5) that the ionic time-of-flight spectrum can be used to

calculate the velocity (v) of the ions. The equation is repeated here for the reader's convenience:

$$v(t) = \frac{d_p}{t} = \frac{v_{pk} t_{pk}}{t}, \quad \textbf{(4-11)}$$

where d_p is the probe distance, and v_{pk} represents the velocity of the ions arriving at the peak of signal. Note that the peak velocity is defined as the velocity corresponding to the time-of-flight of the peak of the signal, in accordance with the literature.

a)

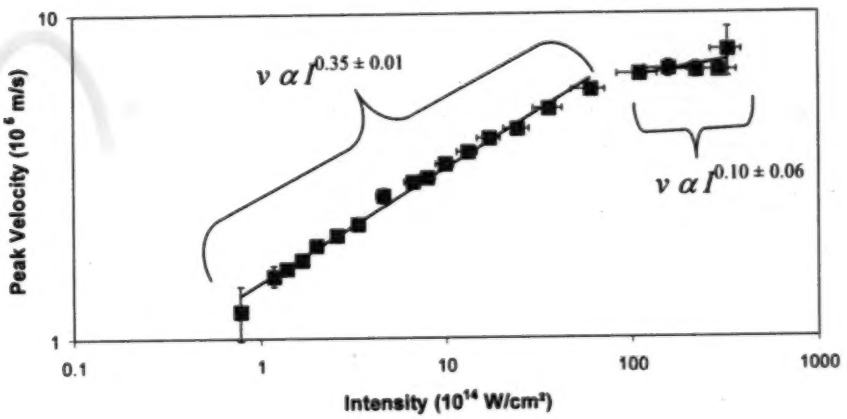

b)

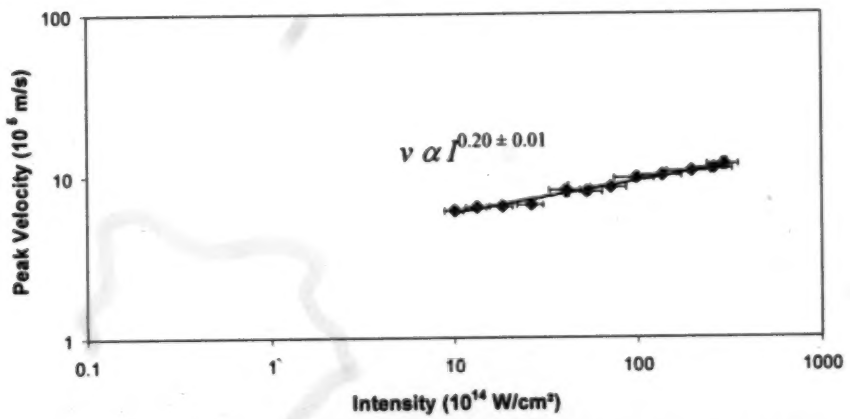

Figure 4-18. Intensity scaling of the velocity corresponding to the peak of the fast proton signal, for a) s-polarized radiation; b) p-polarized radiation. Each data point represents the average of at least 4 laser shots. The average laser energies were 238 μJ and 212 μJ, for the s- and p-polarized data, respectively.

The dominant source of error in the ion peak velocity measurement was the shot-to-shot variation in the ion signals. However, this shot-to-shot variation was not as large as in the nanosecond laser experiments. In most cases, the ion peak velocity varies by ± 3-4%. Each data point in the above figure represents the average of at least 4 laser shots. The error bars represent the difference between the maximum and minimum measured ion peak velocities within these 4 shot (or more) sequences. As discussed previously, the error in the intensity values ranges from 20-25% at the higher intensities (>$5x10^{15}$ W/cm^2) to 10-20% at the lower intensities.

It appears that there may be some kind of rolling off effect occurring at the higher intensities, for the s-polarized data. The s-polarized graph seems to exhibit a flattening trend at intensities above $1x10^{16}$ W/cm^2. This roll off effect appears to occur in other investigations (Figure 4-19). The error in ion energy is ± 6-8% based on the shot-to-shot variation in the ion peak velocity. Note that the error bars are not included in this figure, for the purposes of clarity.

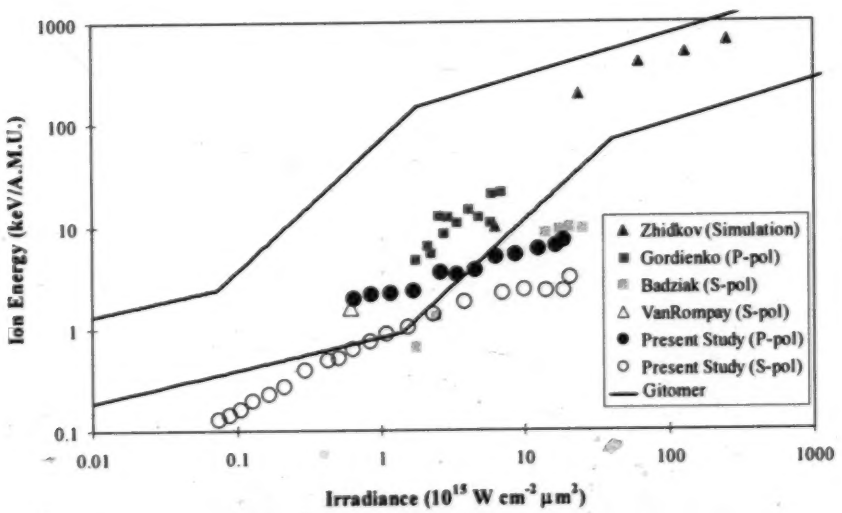

Figure 4-19. Intensity scaling results for the ion energy (Equation 2-6) corresponding to the fast proton peak, from several different investigations under varying conditions. The data has been compiled from the following sources: Zhidkov [Zhi00], Gordienko [Gor02], Badziak [Bad01], VanRompay [Van98a], and Gitomer [Git86].

The compilation of Gitomer *et al.* demonstrates a rolling off effect, as do the investigations of Badziak *et al.* and Zhidkov *et al.*. None of these groups offers a possible explanation for this apparent effect.

Another interesting feature of the scaling data in the present work is that the exponent values in the power law (Figure 4-18) are substantially smaller than those reported by other groups. As mentioned in a previous section, the reported values of the exponent have ranged from 0.4 to 0.65 (0.8 to 1.3 for the ion energy) in the high intensity regime (10^{14}-10^{17} W/cm^2). Additionally, the fast ions

observed in the present work appear to be less energetic than those observed by most other groups.

According to the model of fast ion generation, the energy characteristics of the hot electron flux determine the energy characteristics of the fast protons. The rolling off effect observed for the s-polarized data and the smaller ion energies and weaker intensity scaling may be an indication that some of the energy deposited in the hot electron flux is actually being siphoned off by some other absorption mechanism, which does not contribute to the acceleration of the fast protons. Another possibility is that at higher intensities, the hotter coronal preplasma extends further into the vacuum, increasing the distance over which the main pulse is absorbed. This would decrease the hot electron temperature, as the same amount of energy is distributed to a greater number of electrons, and thus decrease the ion velocity. Of course, this is highly speculative. In the future, it would be interesting to test these hypotheses by exerting control over the prepulse, and investigating the effect of the prepulse on the ion velocity scaling with intensity.

c) Ion Energy Spectrum

In order to extract further information from the data, the fast proton peak was investigated in detail. In particular, the proton signal profile was fitted with a two-piece modified Gaussian function. This function was described in Chapter 2; the equations are repeated here for the reader's convenience:

$$I(t) = I_{pk} \exp\left[-\left|\frac{t - t_{pk}}{\sigma}\right|^{p}\right], \quad \textbf{(4-12)}$$

where

$$\sigma = \begin{cases} \sigma_1 & t < t_{pk} \\ \sigma_2 & t \geq t_{pk} \end{cases} \text{ and } p = \begin{cases} p_1 & t < t_{pk} \\ p_2 & t \geq t_{pk} \end{cases}, \quad \textbf{(4-13)}$$

are temporal fitting parameters, t_{pk} is the temporal location of the signal peak, and I_{pk} is the amplitude of this peak. The fit is shown in Figure 4-20.

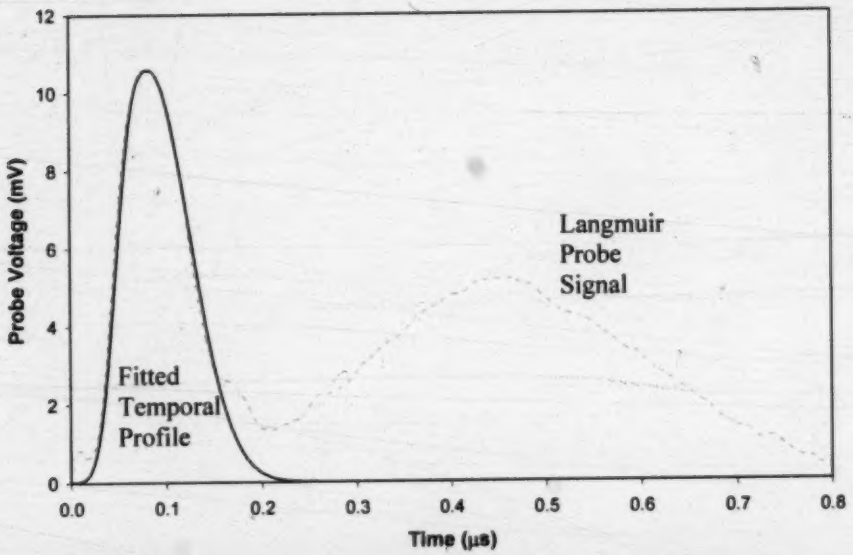

Figure 4-20. Fitting the peak profile described by Equations 2-10 and 2-11 to the proton signal from a single laser shot. This particular laser shot, the same laser shot as in Figure 4-11b, had an energy of 214 μJ and an intensity of 2.9×10^{16} W/cm^2, with p-polarized radiation. The parameters used to fit the fast proton peak were as follows: σ_1=40 ns, σ_2=60 ns, p_1=3, p_2=2, and t_{pk}=82.8 ns.

Clearly, the fitted profile is quite adequate to represent the fast proton peak. Near the tail end of the peak, the accuracy of the fit is uncertain, since the adjacent peak overlaps with the fast proton peak in this region. In any case, the fit represents a good approximation to the actual time-of-flight spectrum of the fast protons. Based on the fitted signal profile, the estimated total flux of fast protons arriving at the detector for this laser shot is approximately 3.9×10^{10} protons/sr. For the present experimental geometry, this corresponds to 1.2×10^{8} protons incident on the detector.

The error in the calculated value of the number of protons incident on the detector is dominated by the uncertainty in the secondary electron emission correction (Equation 2-12). Based on the uncertainty in R. R. Goforth's measurement of $\gamma_{eff}(v) \sim 3$, the estimated uncertainty in the number of protons arriving at the detector for that particular laser shot is ± 25%.

As a check on the observed number of protons, the corresponding impurity layer thickness on the surface of the target can be roughly calculated. Assuming the impurity layer consists mostly of diffusion pump oil (Santovac 5 polyphenyl ether oil), the corresponding proton density in the impurity layer is $\sim 7 \times 10^{28}$ m^{-3}. If the impurity layer consists mostly of water, the corresponding proton density in the impurity layer is, again, $\sim 7 \times 10^{28}$ m^{-3}. At the position of best focus ($\omega_0 \sim 2$ μm), the focal spot area is $\sim 1.3 \times 10^{-11}$ m^2. Integrating the observed proton number (1.2×10^{8}) over all angles, assuming a forward-directed angular distribution with a

full-width at half-maximum (FWHM) of 29.8°, the total number of protons emitted from the target is estimated to be 1.3×10^{10} (see below for further discussion on the proton angular distribution). If the angle is 11.2°, the corresponding proton number is 4.9×10^{9}. Based on these estimates, the calculated impurity layer thickness ranges from 5.7 nm (for 11.2° FWHM) to 15.7 nm (for 29.8° FWHM). These values seem reasonable, especially considering the fact that the target is not cleaned between experiments. These estimates support the contention that the fast ion peak consists mostly of protons.

Based on the fitted time-of-flight spectrum, the smooth energy spectrum of the fast protons can also be calculated. The calculation of the energy and the number of protons was discussed in Chapter 2 (Equations 2-6 and 2-7). The equations are repeated here for the reader's convenience. The energy is calculated using

$$E = \frac{1}{2} m_i v^2, \quad \textbf{(4-14)}$$

where m_i is the ion mass. Additionally, the probe voltage (V) is related to the ion current (I_i) incident on the probe,

$$I_i(t) = \frac{V(t)}{50\Omega}, \quad \textbf{(4-15)}$$

and integration of $I_i(t)$ yields the total charge collected by the detector, from which the number of protons (per unit solid angle) N_p is calculated (assuming Z=1). The energy spectrum is given in the figure below.

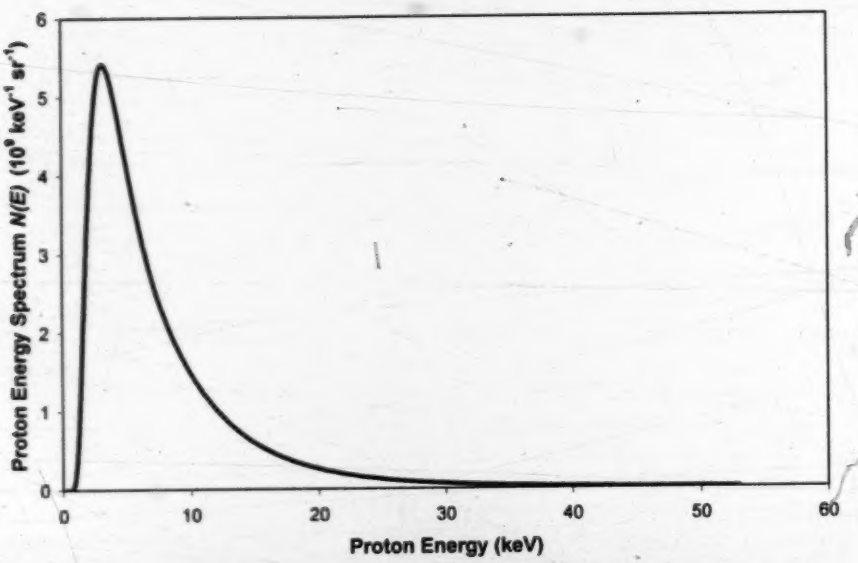

Figure 4-21. The energy spectrum *N(E)* corresponding to the fitted temporal profile of Figure 4-20, for the fast protons. Note that the vertical scale corresponds to the proton number per unit energy interval per unit solid angle, such that when this spectrum is integrated with respect to energy, the total number of protons per unit solid angle is obtained.

The spectrum $N(E)$ is defined such that the total number of protons (N_p, per unit solid angle) is given by

$$N_p = \int N(E)dE. \quad \textbf{(4-16)}$$

Then, to calculate the average energy $\overline{E}$ of the protons, the energy is integrated over this spectrum:

$$\overline{E} = \frac{\int EN(E)dE}{N_p}. \quad \textbf{(4-17)}$$

Again, the error in the total number of protons (and therefore, the error in the vertical scale of the above spectrum) is ± 25%.

The proton peak (in the Langmuir probe signal) corresponds to an energy of 6.9 keV. The average energy $\overline{E}$ of the protons is calculated to be 9.1 keV. The protons incident on the detector for this particular laser shot carry away an estimated 0.15 ± 0.05 μJ of the incident laser energy, where the error is calculated from the error in the number of protons and the error in the proton energies, both of which are described earlier. From the spectrum, approximately 10% of the protons have an energy greater than 15.5 keV and approximately 1% of the protons have an energy greater than 37.8 keV. Additional information regarding the higher energy ions is included in the table below.

Energy Range	Number of Protons (sr^{-1})	Absolute Number of Protons
10-11 keV	$1.4x10^9$	$4.3x10^6$
100-101 keV	$8.3x10^5$	2500
1-2 MeV	$1.8x10^5$	560
10-11 MeV	$3.1x10^3$	10

Table 4-2. The number of protons with energies in the given range, calculated from the energy spectrum in Figure 4-21. The third column provides the actual number of protons for the experimental configuration of the present work.

These estimates are subject to ± 25% uncertainty due to secondary electron emission. The extremely high energy ions would be useful to test high-energy particle detectors: they exist at low enough levels to test a proton telescope specifically designed for single-particle detection. This proton telescope is currently being designed in our laboratory as a means of investigating high energy ions interacting with the Earth's magnetic field in space. Before being sent into space, it is important that this detector be thoroughly tested, and the high energy particles emitted from the high intensity laser-matter interaction may provide a means of doing this testing. However, it must be noted that the presence of the high-energy particles is inferred from the fitted temporal profile, which may be inaccurate for these high energies.

Depending on its angular distribution, the total fast proton flux could carry away a significant fraction of the laser energy. In terms of characterizing the angular distribution of the fast proton flux, due to space considerations, the positioning of a second Langmuir probe to capture the fast proton signal was restricted. The primary detector was positioned at an angle of 7° with respect to the target normal, and, unfortunately, the second detector was placed at the relatively wide angle of 40° with respect to the target normal. Throughout the experiments, this detector did not register a fast proton signal, indicating that the proton flux was collimated to some unknown degree. However, some assumptions can be made regarding the angular distribution of the fast proton flux. It can be assumed that the flux (specifically, the total energy carried by the protons) is described by a cosine distribution $cos^n(\theta)$ (where θ is the angle measured with respect to the target normal) [Bad04]; this distribution can be further constrained by the requirements that the total energy of the flux on the detector be 0.15 μJ at θ=7°, and that the energy of the flux be negligible at θ=40° (see Figure 4-22).

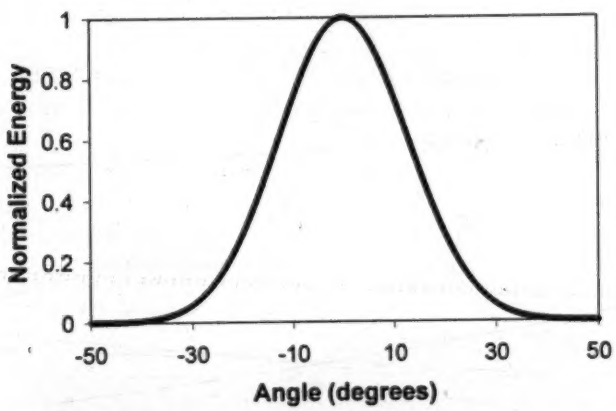

Figure 4-22. A hypothesized angular distribution of energy carried by the proton flux. This particular figure corresponds to a cosine distribution with power n=20, such that the full-width at half maximum (FWHM) is 29.8°, and the total energy carried by the fast proton flux is 16.8 μJ.

With these assumptions, the energy distribution can be integrated in three dimensions, using spherical coordinates, and the total energy carried by the fast protons is found to range from 6.1 μJ for a flux collimated to 11.2° at full-width half-maximum (FWHM) to 16.8 μJ for a flux collimated to 29.8° FWHM (Table 4-3).

n	FWHM (degrees)	Total Energy (μJ)	Conversion Efficiency (%)
20	29.8	16.8	7.9
50	19.0	8.7	4.1
80	15.0	6.8	3.2
110	12.8	6.2	2.9
140	11.2	6.1	2.9

Table 4-3. The estimated total energy carried by the fast proton flux, for different angular distribution characteristics.

Finally, the assumption that the proton flux follows a cosine distribution that is symmetric about the target normal is supported by experiments performed elsewhere. Badziak *et al.* reported that the peak current density of protons in their experiment had an angular divergence of ~10° FWHM, centered on the target normal [Bad04]. Regardless of the actual angular distribution of the proton flux, it is clear that the fast protons carry a significant fraction of the incident laser energy. In the ultrahigh intensity regime, R. A. Snavely *et al.* [Sna00] used a CPA laser system (τ_L=500 fs, E_L=400 J, I_L=3x10^{20} W/cm^2) to generate energetic protons (>10 MeV) which carried up to 12% of the incident laser energy. This value is comparable to the values estimated in Table 4-3 above. Unfortunately, comparison to conversion efficiencies observed in the high intensity regime (10^{14}-

10^{16} W/cm^2) is not possible, since neither total energies nor conversion efficiencies have been reported by any other group in this intensity regime.

If the same time-of-flight fitting procedure outlined above is performed on the entire s- and p-polarized data sets, the intensity dependence of the various characteristics of the fast protons can be observed. The figure below illustrates the intensity dependence of the estimated average energy $\overline{E}$ of the fast protons.

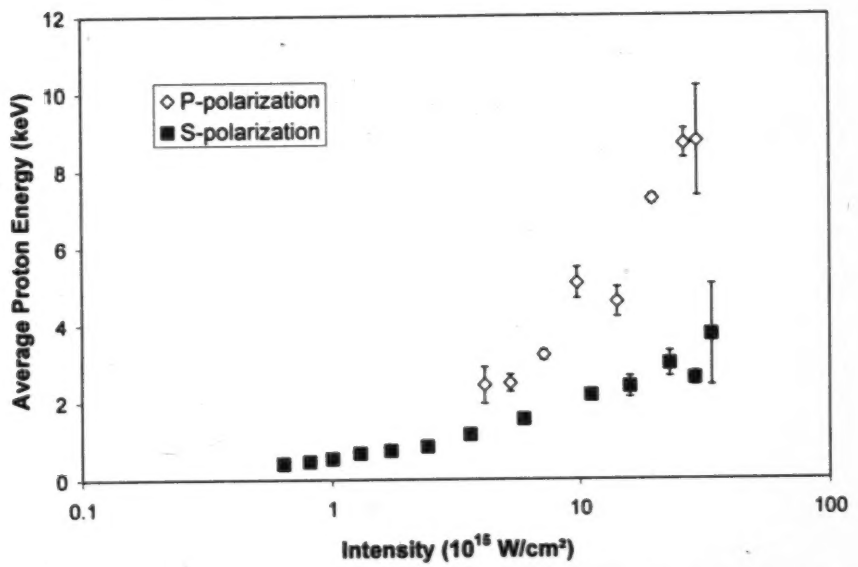

Figure 4-23. The estimated average proton energy as a function of intensity, for both s- and p-polarized radiation. The estimates were performed using the fitting procedure outlined above. The average laser energies were 239 μJ and 212 μJ, for the s- and p-polarized data, respectively.

Each data point in the above figure represents a single laser shot. The error bars were calculated based on the known shot-to-shot variation in the peak ion energy for both s- and p-polarized radiation. The intensity error bars are omitted in the interests of clarity.

Both the s- and p-polarized data sets exhibit the same trend: both increase with increasing intensity. This, of course, is as expected: at higher intensities, the laser focal spot size is smaller, so that the laser energy is deposited in a smaller number of hot electrons and fast ions, such that the average proton energy is larger. The average energy is larger for p-polarization, presumably indicating that the absorption of p-polarized radiation by the target is more efficient (compared to s-polarized radiation). This conclusion is supported by the fact that several absorption mechanisms (e.g. resonance absorption) are effective only for p-polarized radiation. This conclusion has also been borne out by experiment in this intensity regime, albeit at ultraviolet wavelengths [Fed90].

The figure below illustrates the intensity dependence of the estimated number of fast protons arriving at the detector.

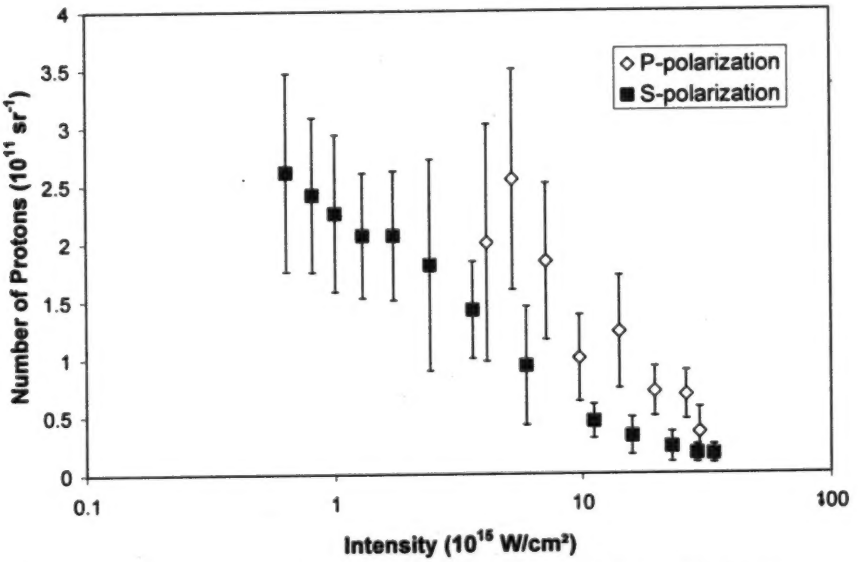

Figure 4-24. The estimated total number of protons (N_p) striking the detector, as a function of intensity, for both s- and p-polarized radiation. The estimates were performed using the fitting procedure outlined above. The average laser energies were 239 μJ and 212 μJ, for the s- and p-polarized data, respectively.

Each data point in the above figure represents the results of a single laser shot. The error bars are calculated based on the known shot-to-shot variation in the signal amplitude (typically ± 15-25%), as well as the uncertainty due to the correction of secondary electron emission (± 25%). The intensity error bars are omitted in the interests of clarity.

Again, both data sets exhibit the same trend: the number of protons decreases with increasing intensity. Again, at lower intensities, the laser focal spot size is larger, such that the laser energy is deposited into a larger number of fast particles, ejecting a larger volume of material from the impurity layer. Again, the number of protons is larger for p-polarized radiation, as a consequence of the more efficient absorption of p-polarized radiation. In terms of absolute numbers, Badziak *et al.* (Nd:YAG laser system, E_L=0.52 J, I_L=1x10^{17} W/cm^2, τ_L=1 ps, p-polarized radiation) [Bad04] calculated a larger value for N_p (~3x10^{14} sr^{-1}). However, they have used a different value of the secondary electron emission coefficient when correcting their ion signals (they use the value $\gamma_{eff}(v)$~1 from [Gof76]), so that their value (rescaled using the value $\gamma_{eff}(v)$~3) becomes ~1.5x10^{14} sr^{-1}. Additionally, their laser energy is substantially larger (by a factor of ~2200) than that used in the present work. It is expected that the ablated mass of the impurity layer (which would be proportional to the number of protons

incident on the detector) increases with increasing laser energy. This is the most likely reason for the discrepancy.

The figure below illustrates the intensity dependence of the total energy carried by the fast protons which reach the detector.

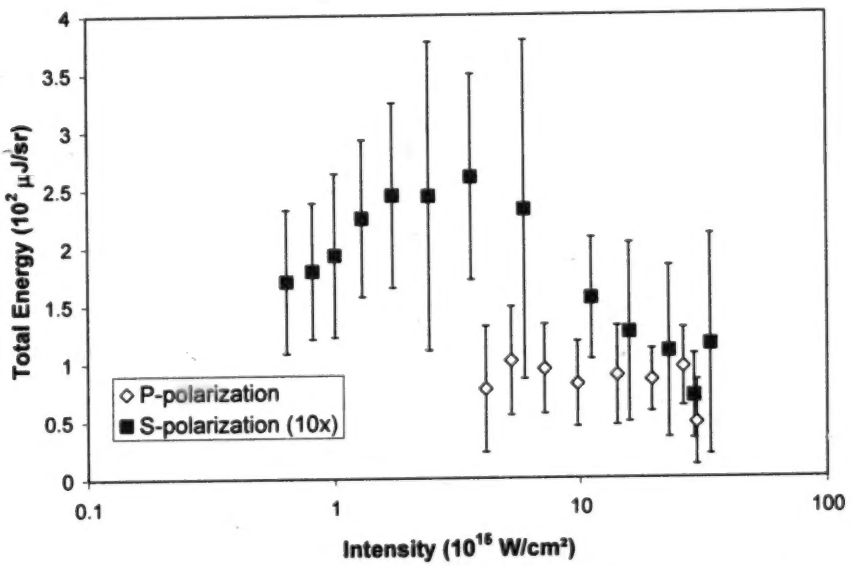

Figure 4-25. The estimated total energy carried by the fast protons striking the detector, as a function of the incident laser intensity, for both s- and p-polarized radiation. The estimates were performed using the fitting procedure outlined above. The average laser energies were 239 μJ and 212 μJ for the s- and p-polarized data, respectively. Note that the s-polarization total energy values were multiplied by a factor of 10 in the interests of clarity.

The calculated error bars represent the combined error due to the shot-to-shot variations in the signal amplitude, the peak ion velocity, and the secondary electron emission correction. The intensity error bars are omitted in the interests of clarity.

The s-polarized data set exhibits a peak, falling off at lower and higher intensities. Now, the proton number decreases with intensity, whereas the average proton energy increases with intensity. Since the total energy of the protons involves a combination of the proton number and the proton energy, it exhibits a maximum at an intermediate intensity. Interestingly, the p-polarized radiation does not exhibit such behavior. The total energy for the p-polarized data set seems to remain relatively constant. The reason for this behavior is not clear.

d) Ion Peak Current Density

The scaling of the peak proton current density with intensity is also examined. The current density is another important parameter of the ion flux. For instance, in ion implantation, the current density (in combination with the ion

energy) determines the density of ions implanted in the substrate. The peak current density was defined in Chapter 2 (Equation 2-8). The equation is repeated here for the reader's convenience:

$$J_i(t) = \frac{I_i(t)}{A_{det}}. \quad \textbf{(4-18)}$$

where $I_i(t)$ is the ion current, A_{det} is the probe area (3.17×10^{-5} m^2), and $J_i(t)$ is the current density. The scaling graphs are given in the figure below.

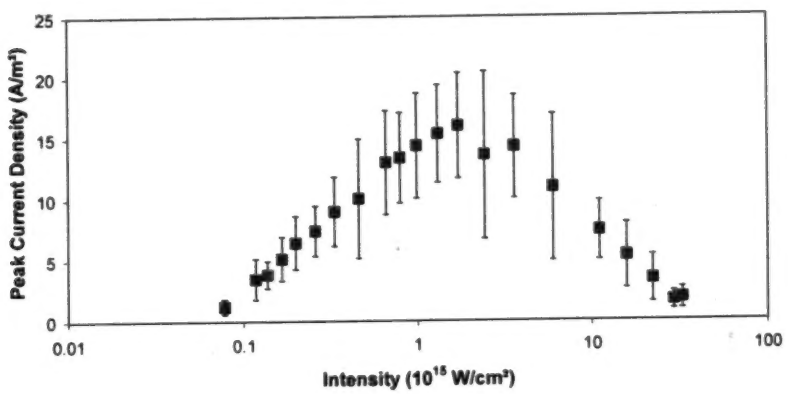

a)

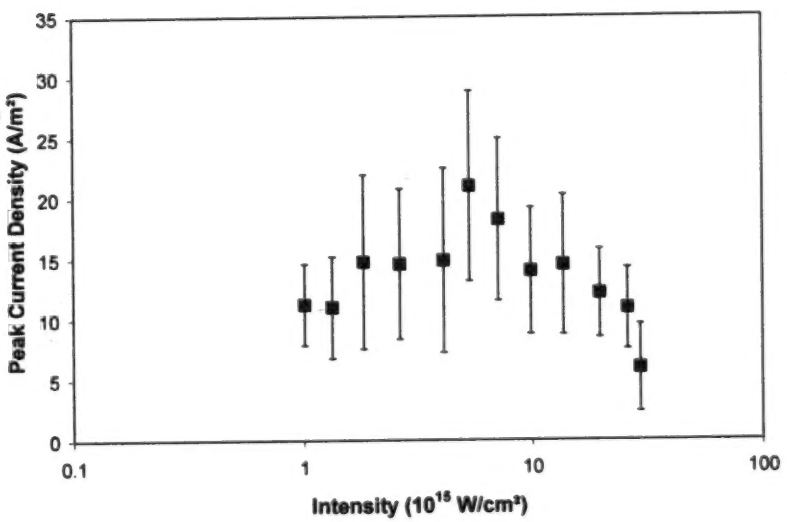

b)

Figure 4-26. The peak current density incident on the detector as a function of the laser intensity, for both a) s-polarized radiation; b) p-polarized radiation. Note that each data point represents the average of at least 4 laser shots. The average laser energies were 238 μJ and 212 μJ for the s- and p-polarized data, respectively.

The calculated error bars represent the combined error due to both the shot-to-shot variation in the signal amplitude and the uncertainty in the secondary electron emission correction. The intensity error bars are omitted in the interests of clarity.

The trend in Figure 4-26a is immediately apparent. In Figure 4-26b, the trend is much weaker, but may still be present. The reason for the peak in the graph is that the peak current density is a combination of the proton density and the velocity. As discussed earlier, the number of protons and the average proton energy follow opposing trends, giving rise to an intermediate intensity peak. It is not clear why the p-polarized data exhibits a weaker trend, or why the data seems to reach a maximum at a slightly higher intensity (~$6x10^{15}$ W/cm^2 instead of ~$2x10^{15}$ W/cm^2 for the s-polarized data). These differences may be attributable to the differences in absorption and hot electron generation mechanisms between the two polarizations. Elsewhere, much larger peak current densities have been reported. Badziak *et al.* [Bad04] report a peak current density of ~35 A/m^2 at a distance of 1 m from the target; this value corresponds to a peak current density of ~$3.5x10^4$ A/m^2 measured 10 cm from the target. However, as mentioned previously, the laser energy used in their experiment was a factor of 2200 greater than that used in the present experiment. It is expected that the discrepancy in the peak current density values is entirely attributable to this difference in laser energy.

e) Assessing the Feasibility of Ion Implantation

To ascertain the feasibility of performing ion implantation under the experimental conditions of the present work, a calculation of the depth profile of energetic boron ions originating from a laser-produced plasma and subsequently implanted into a silicon wafer was performed. Silicon is a commonly used substrate in electronics, and boron is widely used as a p-dopant in order to change the conductivity properties of silicon [Kit95]. An ionic energy spectrum which is based on a two-piece modified Gaussian time-of-flight spectrum, consisting of $3.9x10^{10}$ ions/sr with an average energy of 9.1 keV was assumed. This is precisely the energy spectrum which was obtained from experiment (see Figure 4-21), but with a different ionic species. As discussed previously, the presence of multiple ion species (protons, carbon ions, copper ions) is undesirable for ion implantation. Appropriate target cleaning methods (e.g. pre-cleaning with laser pulses) would be necessary to remove the impurity layer. It is unlikely that the observed energy spectrum in Figure 4-21 would remain unchanged for a different target material with no impurity layer. For this reason, a separate calculation, employing the ion energy spectrum calculated using the third (broadest) peak in Figure 4-11b was performed. Taken together, the two calculated doping profiles provide a better idea of the doping profile which may result from using a cleaned boron target. The information on boron ion penetration depth as a function of the incident energy (included in the Appendix) was calculated by C. W. Unick, a post-doctoral fellow in the laboratory, using the range and stopping-power tables published by L. C. Northcliffe and R. F. Schilling [Nor70]. The calculated doping profiles are given in the figure below.

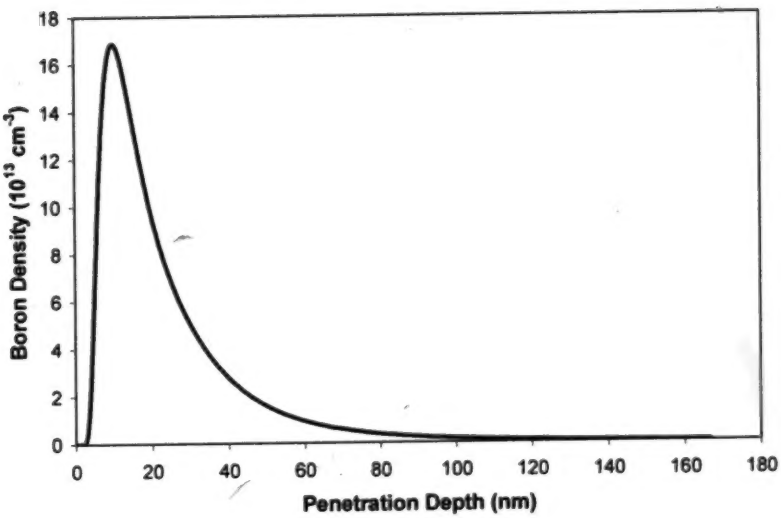

a)

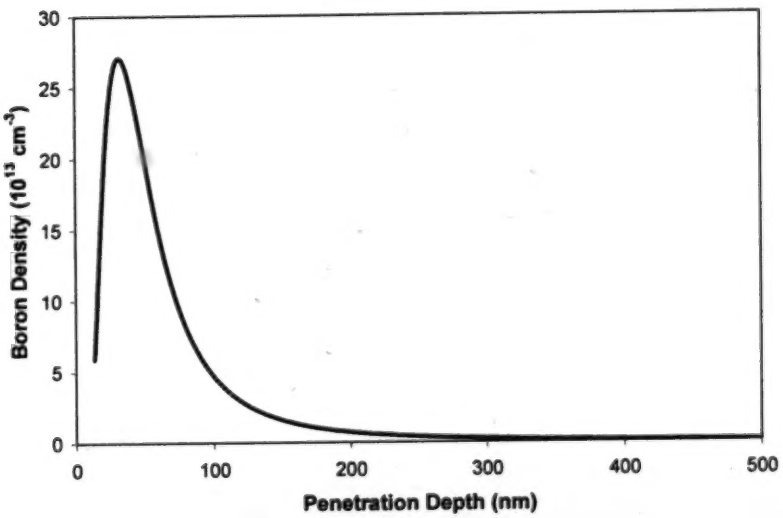

b)

Figure 4-27. The doping profile of energetic boron ions implanted into a silicon wafer. The boron ion energy spectrum was based on energy spectra obtained in the present work, assuming the substrate is located 101 mm from the target. In a), the proton energy spectrum in Figure 4-21 was used. In b), the ion energy spectrum used in the calculation was obtained from fitting the third (broadest) peak in Figure 4-11b with a two-piece modified Gaussian function (σ_1=200 ns, σ_2=220 ns, p_1=2, p_2=1.7, and t_{pk}=450 ns), assuming the ion species for this peak was Cu^+, and using the value $\gamma_{eff}(v)$=0.9 in correcting for secondary electron emission.

According to Figure 4-27a, in a single laser shot, a substantial density (1.68×10^{14} cm^{-3}) can be reached at a depth of 9.4 nm. For the profile in Figure 4-

27b, the density is slightly larger (2.69×10^{14} cm^{-3}), and the implanted ions penetrate the substrate more deeply, reaching their peak density at a depth of 30 nm. At a depth of 100 nm, the boron density is 1.65×10^{12} cm^{-3} for Figure 4-27a, and 4.67×10^{13} cm^{-3} for Figure 4-27b. The peak implanted ion density in Figure 4-27a corresponds to a relative concentration of 3.4×10^{-9}. At the kHz repetition rates common to many CPA laser systems (including the laser system used in the present work), the maximum relative concentration could reach ~0.7% after 30 minutes. This concentration is comparable to (although still smaller than) the maximum concentration (7.6%) achieved by Laska *et al.* [Las03, Wor00]. Of course, Laska *et al.* used a much higher laser energy (E_L~45 J), with far fewer laser pulses (10-30). Lastly, it is noted that the calculated doping profile can be tailored to suit the application by adjusting the incident laser intensity. According to Figures 4-11 and 4-19, a smaller intensity would result in a smaller penetration depth, but a higher dopant density. The doping profile could be further modified using a combination of electrostatic acceleration and deflecting magnetic fields. Thus, it is clear that the fast ions generated from laser-produced plasmas can be used for ion implantation.

Conclusion

In this investigation, the characterization of the fast ion emission from a laser-produced plasma in the femtosecond regime has been performed. Fast ions were observed and based on target pre-cleaning experiments as well as magnetic deflection experiments, these ions were tentatively identified as protons. Protons with peak velocities up to 1.17×10^{6}m/s (corresponding to a peak ion energy of 7 keV) have been observed, and the intensity dependence of the fast proton peak velocity, for both s- and p-polarizations, has been characterized. The energy spectrum of the fast protons has also been estimated. From this, the total number of fast protons incident on the detector was estimated, as was the total energy carried by these fast protons. It was estimated that at the highest laser intensity, the total fast proton flux at the detector was 3.9×10^{10} sr^{-1}, and that the total energy carried by the protons arriving at the detector was 0.15 μJ. One outstanding question that remains is the issue of the angular distribution of the fast proton flux. More investigation in this area will be required in order to fully characterize the fast proton emission. In particular, knowledge of the angular distribution would allow the accurate estimation of the total energy carried by the proton flux in all directions, and therefore allow the estimation of the conversion efficiency of the laser energy to fast protons. Another issue which remains unsettled is the question of the identity of the various ion groups observed in the Langmuir probe signals. Experiments using a crude magnetic spectrometer indicate that the fast ion peak is mostly composed of protons, with subsequent peaks consisting of carbon, oxygen, and copper ions. In the future, a more sophisticated detector such as an ion energy spectrometer could provide more detailed information on the relative proportions of the various ion species. Finally, in the future, the accuracy and reliability of the focal spot conditions should be improved. Such an

improvement could reduce the large uncertainties in the calculation of the laser intensity.

Furthermore, the feasibility of the application of the ion emission for the purposes of ion implantation has been evaluated. For boron ions incident on a silicon substrate, it was calculated that the bulk of the ions may penetrate to a depth of 30 nm, with an appreciable quantity of ions penetrating to a depth of 100 nm. Reasonable implanted ion densities could be achieved after ~1.8×10^6 laser pulses (~30 minutes at 1 kHz). Additionally, the doping profile could be tailored to suit the application.

Chapter 5
Conclusion

The central aim of this work is the characterization of the ion emission from laser-produced plasmas. As part of the ion emission characterization process, the non-ideal operation of Faraday cup detectors due to space charge effects has been investigated and characterized in detail. It was demonstrated that the analytical model used previously to describe the space charge distortion of the Faraday cup ion signal is inadequate, when compared to experiment. A two-particle simulation has been successfully used to reproduce the experimental results, and arrive at a better understanding of the phenomenon. Limited guidelines for the design of Faraday cup detectors have been provided, in order to avoid signal distortion due to this space charge effect. In the future, the development of a two-particle analytical model would provide investigators with the best means of evaluating their detector designs. Ultimately, due to space charge issues and other concerns, Langmuir probes were chosen to be the most effective detector to characterize the ion emission in the nanosecond and femtosecond regimes.

In the nanosecond regime, the ion emission from laser-produced plasmas for two different targets at several different laser intensities was investigated. Almost all of the relevant characteristics of the ion flux have been measured, including the emitted charge, the ion peak and average energies, and the angular distribution of each of these quantities. The predictions of the self-regulating model, as well as a simple gas expansion model, were tested, and found to be inadequate to describe the complex transition region between a vapor plume and a fully ionized plasma. One outstanding issue is the question of the average charge state of the ions present in the plasma plume. Some attempt to estimate this quantity has been made, but the exact value of the average charge state remains an open question. In the future, a more sophisticated detector, such as an ion energy spectrometer, could be used to settle this question. Another outstanding question is the issue of secondary electron emission. In the future, appropriate measurements should be made to address this issue. After characterizing the ion emission in this intensity regime, a more rigorous investigation of the properties of thin films deposited with these ion fluxes as a function of the laser intensity would be a natural extension of this work.

In the femtosecond regime, the intensity scaling of various characteristics of the fast ion emission has been investigated. In particular, the scaling of the ion peak velocity for both s- and p-polarized radiation was obtained. The scaling of the current density of the fast ions, for s- and p-polarized radiation was also obtained. Additionally, the energy spectrum of the fast ions was calculated, and the total energy carried by these ions was estimated. The variation of these quantities with intensity was also calculated. One outstanding question that remains is the issue of the angular distribution of the fast proton flux. More investigation in this area will be required in order to fully characterize the fast proton emission. Another issue which remains unsettled is the question of the identity of the various ion groups observed in the Langmuir probe signals.

Although this issue has been qualitatively addressed, a more sophisticated detector such as an ion energy spectrometer would provide more detailed information on the relative proportions of the various ion species. Finally, the feasibility of the application of the ion emission for the purposes of ion implantation was evaluated via a calculation based on the measured properties of the fast ion flux. In the future, this technique could be demonstrated experimentally, and the observed doping profile could be compared to the calculated profile. Tailoring of the doping profile could also be attempted, by adjusting the laser intensity on target, or by applying external electrostatic fields to the ion flux prior to impact on the substrate.

Thus, the ion emission in both the nanosecond and femtosecond regimes has been successfully characterized. Although a few outstanding issues remain, these results will enable researchers to understand the important issues in the use of this ion emission for a variety of applications.

Appendix

Chapter 2

The input file used to perform the two-particle simulations in OOPIC Pro is included below. As mentioned previously, in order to obtain a suitable ion (and electron) current profile, the signal was discretized into 200-400 individual pulses, each with a single amplitude and velocity. Combined, these individual pulses adequately represented the amplitude and velocity distribution of the desired ion (and electron) signal. Each individual pulse requires its own VarWeightBeamEmitter boundary condition. Due to space considerations, these conditions have been edited out of the code included below. The MATLAB code used to generate the text of the 400 VarWeightBeamEmitter boundary conditions is also included below.

```
faradaycup
{
This input file is intended to simulate a Faraday cup, to look for the
space charge effect. There is a beam of ions (with + charge) incident
on a biased conducting surface, in a cylindrical geometry
}
Variables
{
Jnum=100 //number of cells along z coordinate
Jmin=0.0 //min z coordinate, in metres
Jmax=1750e-6 //max z coordinate, in metres
Knum=6 //number of cells along r coordinate
Kmin=0.0 //min r coordinate (should be zero) in metres
Kmax=3/16*2.54*1e-2*0.5  //max r coordinate in metres
timestep=1e-11//timestep of simulation, in seconds
noisenp2c=1e5
elecnoisenp2c=2e4
ionamplitude=1
electronamplitude=1
iondensity=3.7e16
ionvelocity=7e4
mion=12*1.67e-27   //mass of ion, in kg
qion=1*1.6e-19  //charge of ion, in C
melectron=9.11e-31
qelectron=-1.6e-19
biasvoltage=-40 //probe is biased at -40 V
beamradius=2/3*Knum  //beam radius, in units of cells
beamcurrent=iondensity*ionvelocity*qion*PI*(beamradius/Knum*Kmax)^2
//typical current amplitude measured by an FC, in Amperes
//these are input parameters to define the current input to the FC
timepk=5.5e-6
```

```
power1=3
power2=1.2
sigma1=1.7e-6
sigma2=7.2e-6
}
Region
{
 Grid
 {
 J=Jnum
 K=Knum
 x1s=Jmin
 x1f=Jmax
 x2s=Kmin
 x2f=Kmax
 Geometry=0
 }
 Control
 {
 dt=timestep
 ElectrostaticFlag=1
 initPoissonSolve=1
 CurrentWeighting=0
 DivergenceCleanFlag=0
 }
 Species
 {
 name=ion //ions
 m=mion
 q=qion
 collisionModel=2
 particleLimit=1e16
 }
 Species
 {
 name=electron
 m=melectron
 q=qelectron
 collisionModel=1
 particleLimit=1e16
 }
 //Boundary conditions
 //this boundary represents the far end of the FC
 Equipotential
 {
 name= far end
```

```
j1=Jnum
j2=Jnum
k1=0
k2=Knum
C=biasvoltage //the conductor is biased at some voltage
normal=-1
IdiagFlag=1
Ihist_avg=4000
Ihist_len=64768
}
//this boundary represents the r=0 axis
CylindricalAxis
{
name=axis
j1=0
j2=Jnum
k1=0
k2=0
normal=1
}
//this boundary represents the outer radius of the region of interest,
//the outer conductor of the Faraday cup
Dielectric
{
name=outer radius
j1=0
j2=Jnum
k1=Knum
k2=Knum
normal=-1
er=1.0 //relative permittivity
}
Equipotential
{
name=near end
j1=0
j2=0
k1=0
k2=Knum
C=0 //the grid is fixed to 0 V (ground)
normal=1
}

VarWeightBeamEmitter
{
j1=0
```

```
j2=0
k1=0
k2=beamradius
normal=1
QuseFlag=0
np2c=noisenp2c
speciesName=ion
xtFlag=1
v1drift=ionvelocity*timepk/1.4362e-007
I=ionamplitude*beamcurrent*(step(timepk-1.4362e-007)*exp(-((step(timepk-
1.4362e-007)*(timepk-1.4362e-007)/sigma1)^power1))+step(1.4362e-007-
timepk)*exp(-(pow((step(1.4362e-007-timepk)*(1.4362e-007-
timepk)/sigma2),power2))))
F=step(t-1e-007)-step(t-1.8725e-007)
}
VarWeightBeamEmitter
{
j1=0
j2=0
k1=0
k2=beamradius
normal=1
QuseFlag=0
np2c=elecnoisenp2c
speciesName=electron
xtFlag=1
v1drift=ionvelocity*timepk/1.4362e-007
I=-electronamplitude*beamcurrent*(step(timepk-1.4362e-007)*exp(-
((step(timepk-1.4362e-007)*(timepk-1.4362e-
007)/sigma1)^power1))+step(1.4362e-007-timepk)*exp(-(pow((step(1.4362e-
007-timepk)*(1.4362e-007-timepk)/sigma2),power2))))
F=step(t-1e-007)-step(t-1.8725e-007)
}
.
.
.
.
.
.
.
.
.
.
.
.
.
```

```
VarWeightBeamEmitter
{
j1=0
j2=0
k1=0
k2=beamradius
normal=1
QuseFlag=0
np2c=noisenp2c
speciesName=ion
xtFlag=1
v1drift=ionvelocity*timepk/3.4956e-005
I=ionamplitude*beamcurrent*(step(timepk-3.4956e-005)*exp(-((step(timepk-
3.4956e-005)*(timepk-3.4956e-005)/sigma1)^power1))+step(3.4956e-005-
timepk)*exp(-(pow((step(3.4956e-005-timepk)*(3.4956e-005-
timepk)/sigma2),power2))))
F=step(t-3.4913e-005)-step(t-3.5e-005)
}
VarWeightBeamEmitter
{
j1=0
j2=0
k1=0
k2=beamradius
normal=1
QuseFlag=0
np2c=elecnoisenp2c
speciesName=electron
xtFlag=1
v1drift=ionvelocity*timepk/3.4956e-005
I=-electronamplitude*beamcurrent*(step(timepk-3.4956e-005)*exp(-
((step(timepk-3.4956e-005)*(timepk-3.4956e-
005)/sigma1)^power1))+step(3.4956e-005-timepk)*exp(-(pow((step(3.4956e-
005-timepk)*(3.4956e-005-timepk)/sigma2),power2))))
F=step(t-3.4913e-005)-step(t-3.5e-005)
}

}
```

The following is the MATLAB code used to generate the text of the 400 VarWeightBeamEmitter boundary conditions.

```
%this will generate text which can then be inserted into OOPIC
%the text will define many (say 100) VarWeightBeamEmitter boundaries
%which launch ions into the faradaycup OOPIC simulation
```

```
%this is the brute force method of creating a velocity profile
%the temporal current profile is broken up into 100 (or so)
%pieces, each of which has a different velocity and different current
%amplitude

clear all;
n=400;  %number of steps in current profile
%the variables we are working with are
%timepk
%iondensity
%ionvelocity
%beamcurrent


tstart=0.1e-6;   %start time for current pulse
tstop=35e-6;   %stop time for current pulse
deltat=(tstop-tstart)/n;

outputstring='';    %initialize outputstring, will which contain the final product-a
huge text string
%this for loop will create n VarWeightBeamEmitters
for i=1:n
  time=tstart+(i-1/2)*deltat; %we shift by 1/2 so that the sampling of the true
curve occurs in the middle of the interval
  %v1drift=ionvelocity*timepk/time   this is the formula
  v1driftstring=strcat('v1drift=ionvelocity*timepk/', num2str(time));
  %formula for I--basically, everywhere you see t, put in num2str(time)
  %OOPIC will evaluate everything else for us
  Istring=strcat('I=ionamplitude*beamcurrent*(step(timepk-
',num2str(time),')*exp(-((step(timepk-',num2str(time),')*(timepk-
',num2str(time),')/sigma1)^power1))+step(',num2str(time),'-timepk)*exp(-
(pow((step(',num2str(time),'-timepk)*(',num2str(time),'-
timepk)/sigma2),power2)))))');
  %in this string, we rely on the defaults units=MKS, nEmit=0
  %this F is a square wave function, to ensure that the ions from this particular
  %VarWeightBeamEmitter turn on only at the appropriate time
  Fstring=strcat('F=step(t-',num2str(time-0.5*deltat),')-step(t-
',num2str(time+0.5*deltat),')');

  newstring1=strvcat('VarWeightBeamEmitter','{','j1=0','j2=0',
'k1=0','k2=beamradius','normal=1');
  newstring2=strvcat('QuseFlag=0','np2c=noisenp2c','speciesName=ion',
'xtFlag=1');
  additionalstring=strvcat(newstring1, newstring2, v1driftstring, Istring, Fstring,
'}');
  if 0   %if including electrons
```

```
    Inegstring=strcat('I=-electronamplitude*beamcurrent*(step(timepk-
',num2str(time),')*exp(-((step(timepk-',num2str(time),')*(timepk-
',num2str(time),')/sigma1)^power1))+step(',num2str(time),'-timepk)*exp(-
(pow((step(',num2str(time),'-timepk)*(',num2str(time),'-
timepk)/sigma2),power2))))');

newstring3=strvcat('QuseFlag=0','np2c=elecnoisenp2c','speciesName=electron',
'xtFlag=1');
    additionalstring2=strvcat(newstring1, newstring3, v1driftstring, Inegstring,
Fstring, '}');
    additionalstring=strvcat(additionalstring, additionalstring2);
  end %end if which can add electrons
  outputstring=strvcat(outputstring, additionalstring);
end %end for

%now we want to print the very long string into a file, so that the string
%can be manually copied into the OOPIC input file

%the fopen/fclose commands should delete the old diary file, otherwise it
%just keeps appending to it
fid=fopen('C:\Program                                          Files\OOPIC
Pro\input\faradaycup\OOPICtextgenoutput.txt', 'w');
fclose(fid);
diary('C:\Program Files\OOPIC Pro\input\faradaycup\OOPICtextgenoutput.txt');
outputstring
diary off;
```

Below are example current waveforms from the one-particle simulations, two-particle simulations, and experiment.

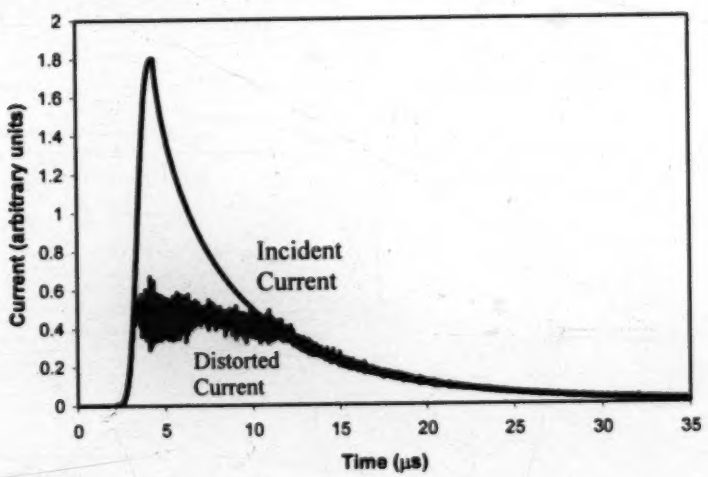

Figure A-1. An output waveform from the one-particle OOPIC simulations. This particular simulation was performed using z_f=150 μm, v_{pk}=1x10^3 m/s, ϕ_f=-30 V, and n_{pk}=3.5x10^{18} m^{-3}, with σ_1=1.1 μs, σ_2=4 μs, p_1=3, p_2=0.75, and t_{pk}=4.4 μs resulting in F=0.63.

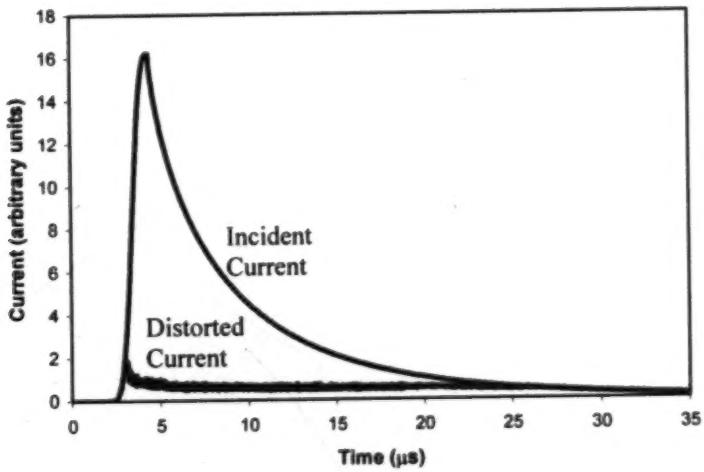

Figure A-2. An output waveform from the one-particle OOPIC simulations. This particular simulation was performed using z_f=150 μm, v_{pk}=9x10^3 m/s, ϕ_f=-30 V, and n_{pk}=3.5x10^{18} m^{-3}, with σ_1=1.1 μs, σ_2=4 μs, p_1=3, p_2=0.75, and t_{pk}=4.4 μs resulting in F=0.18.

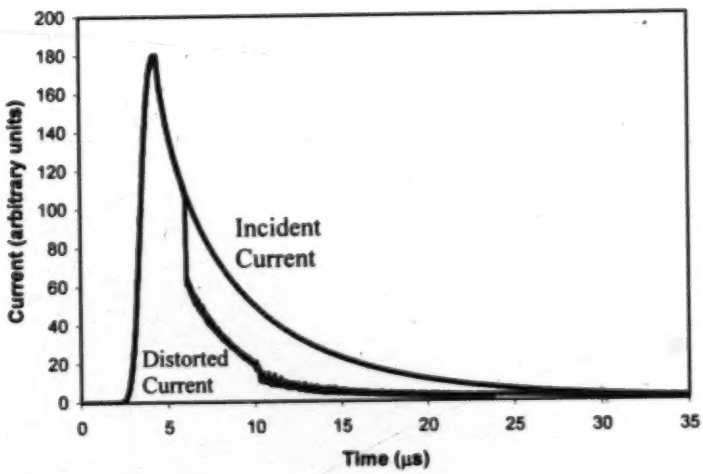

Figure A-3. An output waveform from the one-particle OOPIC simulations. This particular simulation was performed using z_f=150 μm, v_{pk}=1x10^5 m/s, ϕ_f=-30 V, and

n_{pk}=3.5x10^{18} m^{-3}, with σ_1=1.1 μs, σ_2=4 μs, p_1=3, p_2=0.75, and t_{pk}=4.4 μs resulting in F=0.63.

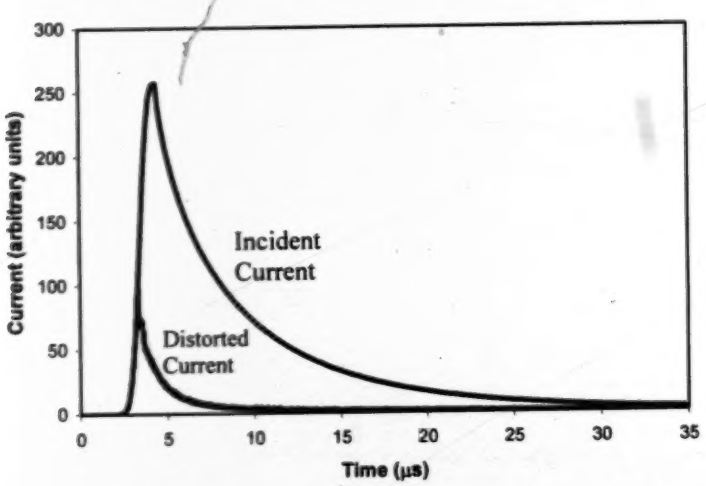

Figure A-4. An output waveform from the one-particle OOPIC simulations. This particular simulation was performed using z_f=125 μm, v_{pk}=5x10^4 m/s, ϕ_f=-30 V, and n_{pk}=1x10^{19} m^{-3}, with σ_1=1.1 μs, σ_2=4 μs, p_1=3, p_2=0.75, and t_{pk}=4.4 μs resulting in F=0.12.

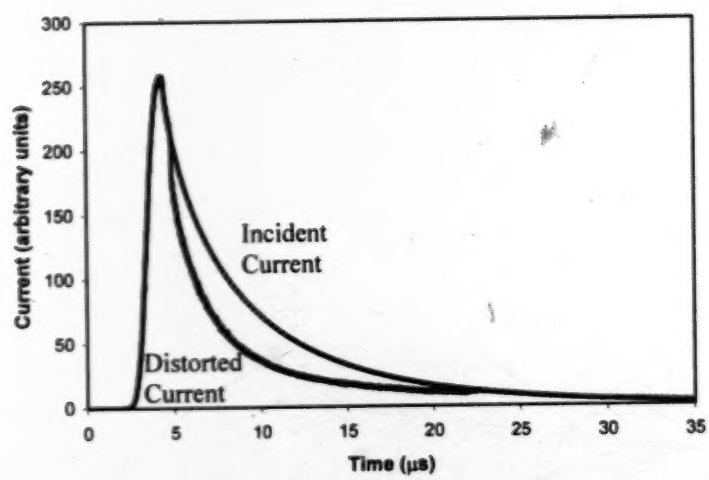

Figure A-5. An output waveform from the one-particle OOPIC simulations. This particular simulation was performed using z_f=50 μm, v_{pk}=5x10^4 m/s, ϕ_f=-30 V, and n_{pk}=1x10^{19} m^{-3}, with σ_1=1.1 μs, σ_2=4 μs, p_1=3, p_2=0.75, and t_{pk}=4.4 μs resulting in F=0.72.

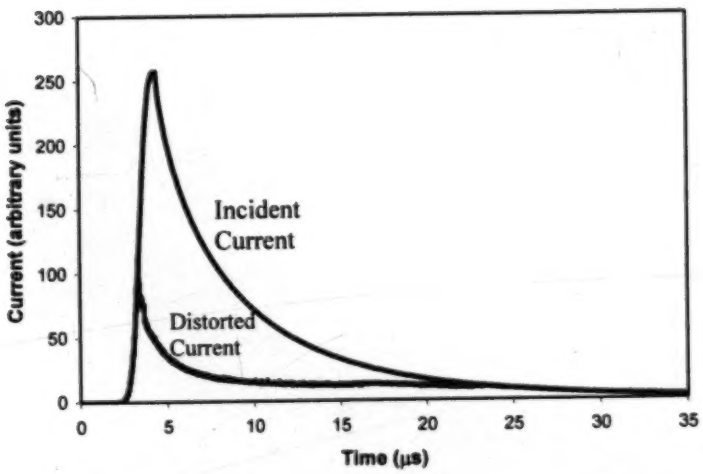

Figure A-6. An output waveform from the one-particle OOPIC simulations. This particular simulation was performed using z_f=150 μm, v_{pk}=5x10^4 m/s, ϕ_f=-200 V, and n_{pk}=1x10^{19} m^{-3}, with σ_1=1.1 μs, σ_2=4 μs, p_1=3, p_2=0.75, and t_{pk}=4.4 μs resulting in F=0.31.

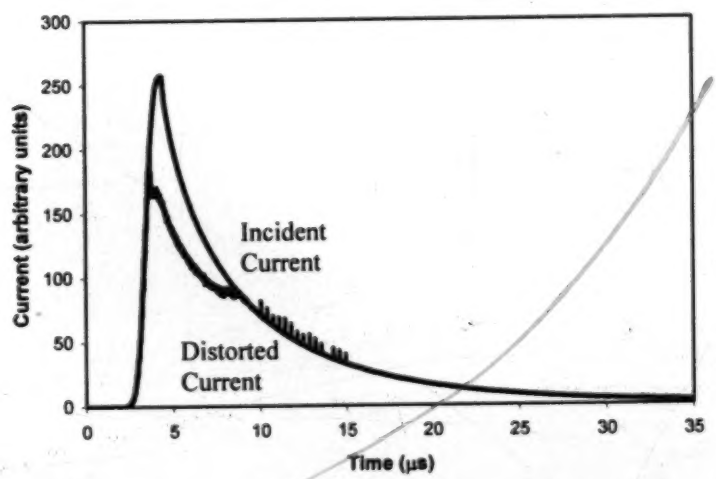

Figure A-7. An output waveform from the one-particle OOPIC simulations. This particular simulation was performed using z_f=150 μm, v_{pk}=5x10^4 m/s, ϕ_f=-800 V, and n_{pk}=1x10^{19} m^{-3}, with σ_1=1.1 μs, σ_2=4 μs, p_1=3, p_2=0.75, and t_{pk}=4.4 μs resulting in F=0.85.

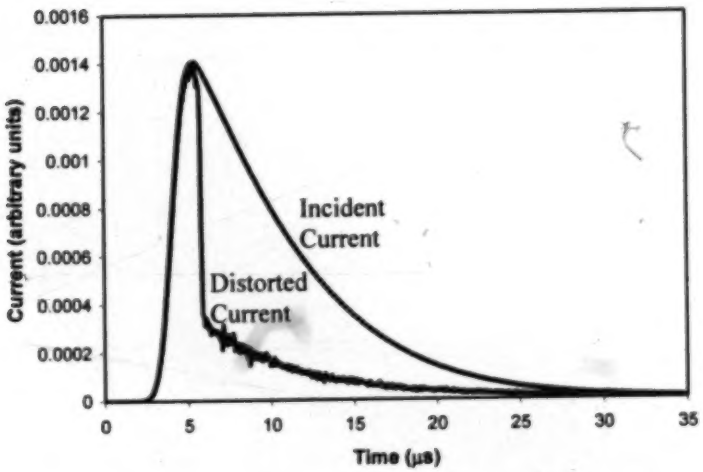

Figure A-8. A typical output waveform from the two-particle OOPIC simulations. This particular simulation was performed using z_f=1.75 mm, v_{p4}=3x10^4 m/s, ϕ_f=-40 V, and n_{p4}=3.7x10^{16} m^{-3}, with σ_1=1.7 μs, σ_2=7.2 μs, p_1=3, p_2=1.2, and t_{p4}=5.5 μs, corresponding to F=0.39.

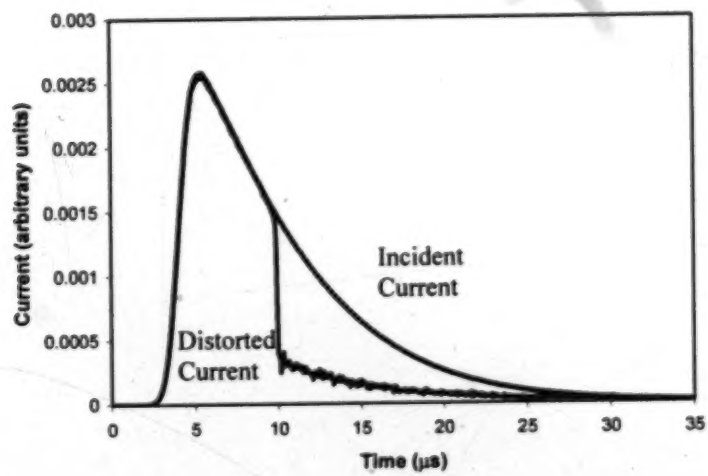

Figure A-9. A typical output waveform from the two-particle OOPIC simulations. This particular simulation was performed using z_f=1.75 mm, v_{p4}=5.5x10^4 m/s, ϕ_f=-40 V, and n_{p4}=3.7x10^{16} m^{-3}, with σ_1=1.7 μs, σ_2=7.2 μs, p_1=3, p_2=1.2, and t_{p4}=5.5 μs, corresponding to F=0.71.

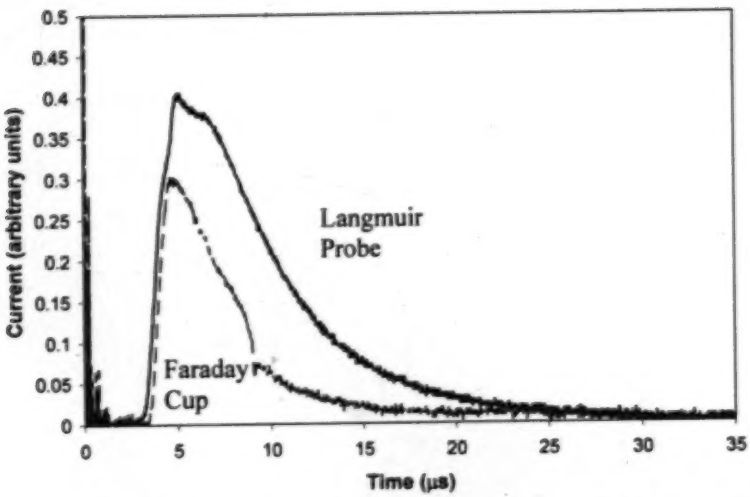

Figure A-10. A signal recorded from an individual laser shot. The laser parameters were: I_L=1.7x10^{10} W/cm^2, E_L=73.7 mJ, d_L=51.3 cm, with F=0.50. The signals were corrected for factors such as the grid transmission and the detector aperture diameters.

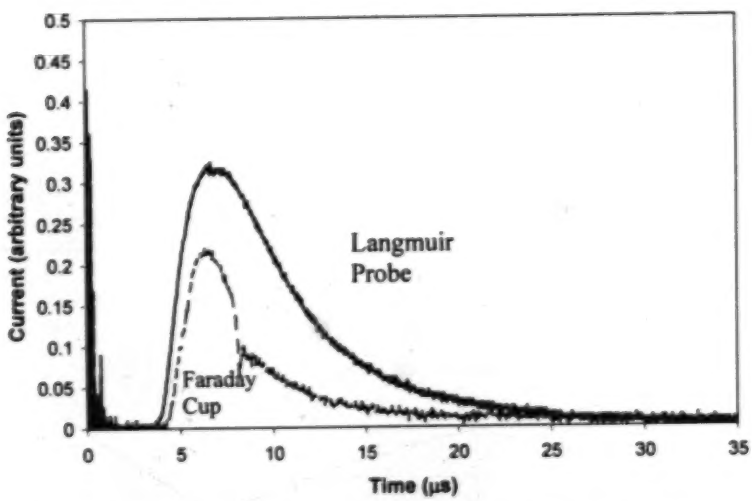

Figure A-11. A signal recorded from an individual laser shot. The laser parameters were: I_L=1.1x10^{10} W/cm^2, E_L=71.6 mJ, d_L=50.8 cm, with F=0.44. The signals were corrected for factors such as the grid transmission and the detector aperture diameters.

Chapter 3

The following graphs are images of the focal spot for different lens-to-target distances.

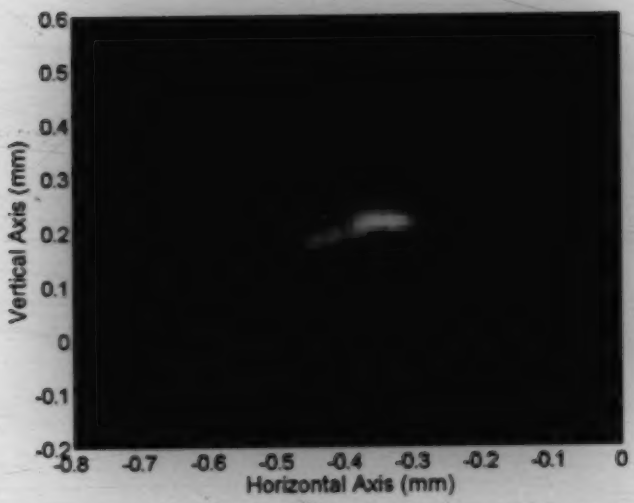

Figure A-12. An example digitized image of the laser spot on target, obtained using a filtered CCD camera. This particular image was taken at a lens-to-target distance of 50.8 cm.

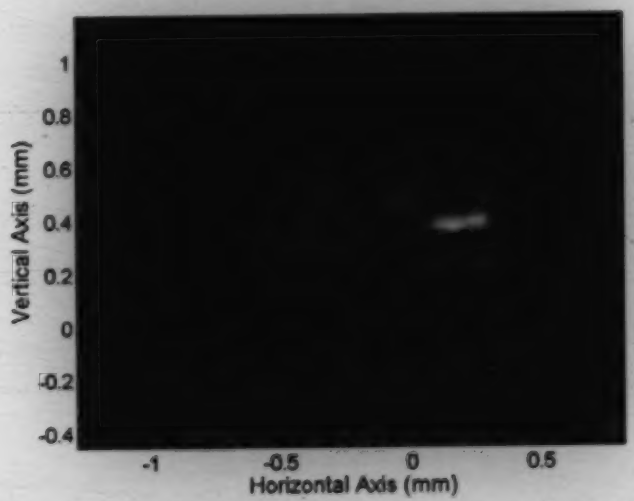

Figure A-13. An example digitized image of the laser spot on target, obtained using a filtered CCD camera. This particular image was taken at a lens-to-target distance of 45.8 cm.

The following figures are sample Langmuir probe ion signals.

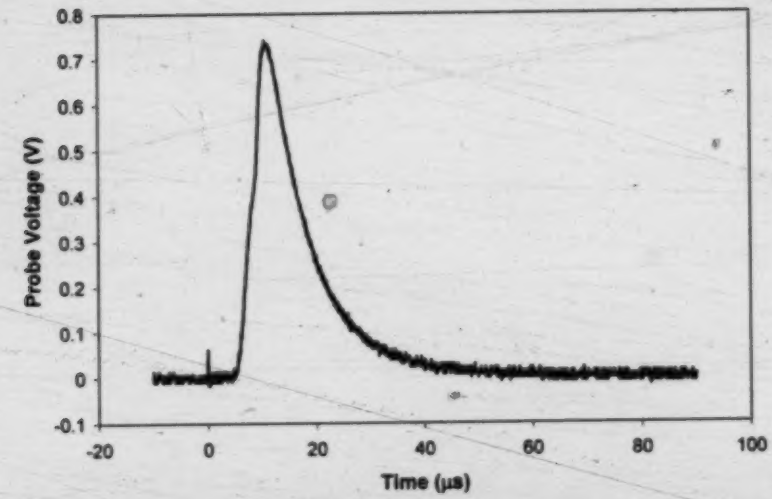

Figure A-14. An example ion signal collected by a Langmuir probe. This particular signal was produced at a laser intensity of 3.7×10^9 W/cm^2 (E_L=59.5 mJ, d_L=59.9 cm) incident on a zinc oxide target, for a probe positioned 16.5 cm from the target, at an angle of 7°, biased at -40 V. Time zero represents the instant when the laser pulse strikes the target.

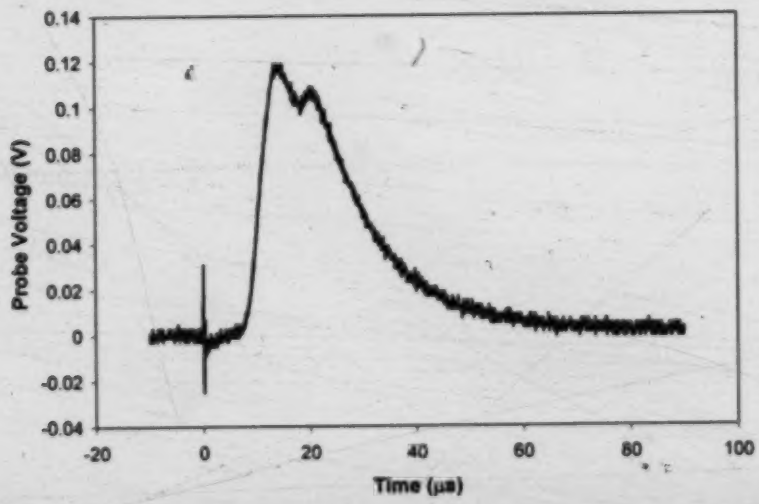

Figure A-15. An example ion signal collected by a Langmuir probe. This particular signal was produced at a laser intensity of 3.7×10^9 W/cm^2 (E_L=59.5 mJ, d_L=59.9 cm) incident on a zinc oxide target, for a probe positioned 17.7 cm from the target, at an angle of 21°, biased at -40 V. Time zero represents the instant when the laser pulse strikes the target.

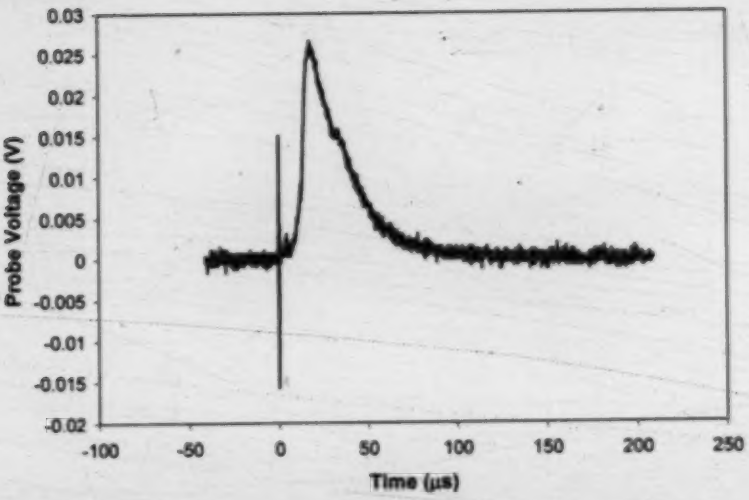

Figure A-16. An example ion signal collected by a Langmuir probe. This particular signal was produced at a laser intensity of 3.7×10^9 W/cm^2 (E_L=59.5 mJ, d_L=59.9 cm) incident on a zinc oxide target, for a probe positioned 16.4 cm from the target, at an angle of 30°, biased at -40 V. Time zero represents the instant when the laser pulse strikes the target.

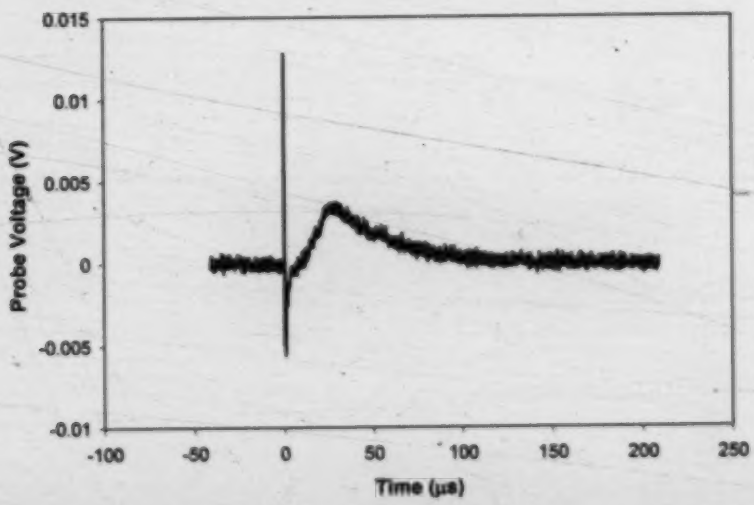

Figure A-17. An example ion signal collected by a Langmuir probe. This particular signal was produced at a laser intensity of 3.7×10^9 W/cm^2 (E_L=59.5 mJ, d_L=59.9 cm) incident on a zinc oxide target, for a probe positioned 16.5 cm from the target, at an angle of 40°, biased at -40 V. Time zero represents the instant when the laser pulse strikes the target.

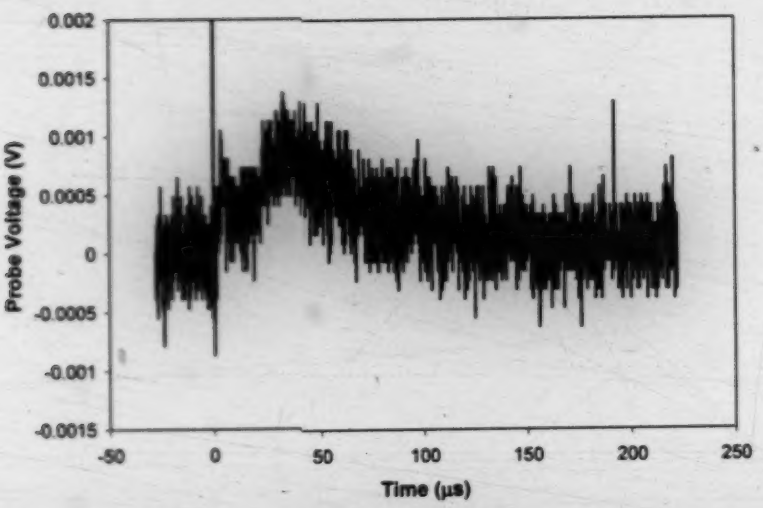

Figure A-18. An example ion signal collected by a Langmuir probe. This particular signal was produced at a laser intensity of 3.7×10^9 W/cm^2 (E_L=59.5 mJ, d_L=59.9 cm) incident on a zinc oxide target, for a probe positioned 16.3 cm from the target, at an angle of 54°, biased at -40 V. Time zero represents the instant when the laser pulse strikes the target.

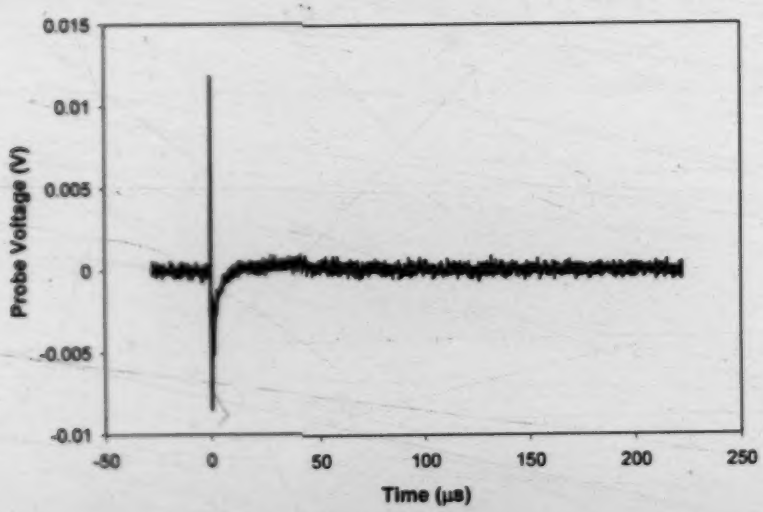

Figure A-19. An example ion signal collected by a Langmuir probe. This particular signal was produced at a laser intensity of 3.7×10^9 W/cm^2 (E_L=59.5 mJ, d_L=59.9 cm) incident on a zinc oxide target, for a probe positioned 16.7 cm from the target, at an angle of 69°, biased at -40 V. Time zero represents the instant when the laser pulse strikes the target.

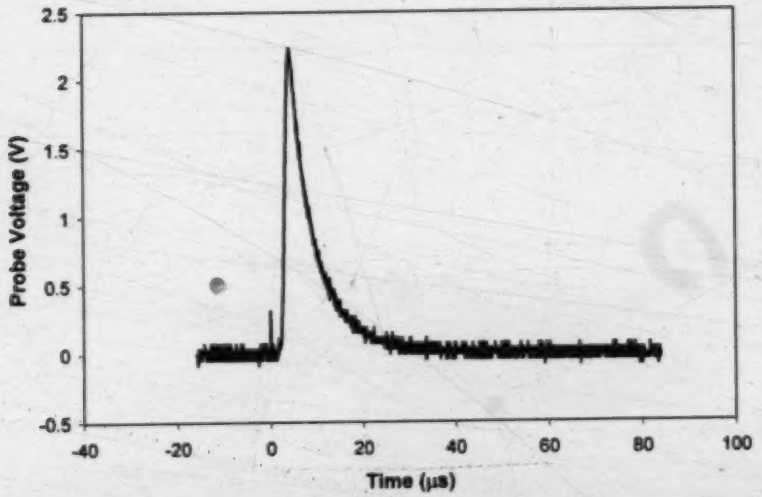

Figure A-20. An example ion signal collected by a Langmuir probe. This particular signal was produced at a laser intensity of 8.6×10^9 W/cm^2 (E_L=73.5 mJ, d_L=53.4 cm) incident on a zinc oxide target, for a probe positioned 16.5 cm from the target, at an angle of 7°, biased at -40 V. Time zero represents the instant when the laser pulse strikes the target.

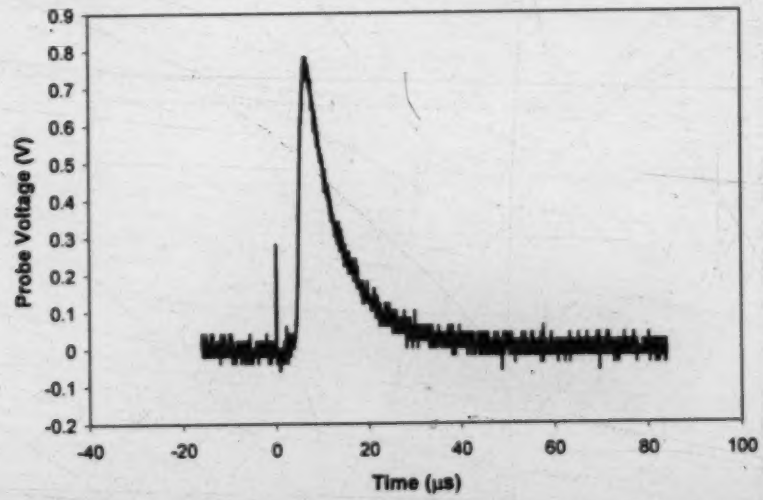

Figure A-21. An example ion signal collected by a Langmuir probe. This particular signal was produced at a laser intensity of 8.6×10^9 W/cm^2 (E_L=73.5 mJ, d_L=53.4 cm) incident on a zinc oxide target, for a probe positioned 17.7 cm from the target, at an angle of 21°, biased at -40 V. Time zero represents the instant when the laser pulse strikes the target.

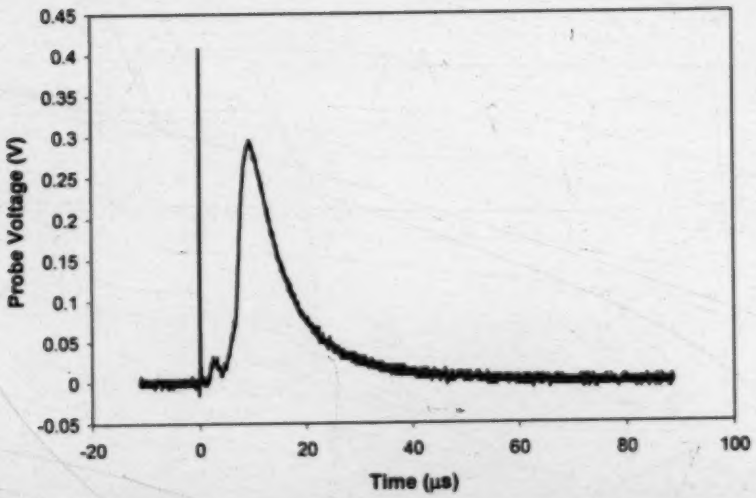

Figure A-22. An example ion signal collected by a Langmuir probe. This particular signal was produced at a laser intensity of 8.6×10^9 W/cm^2 (E_L=73.5 mJ, d_L=53.4 cm) incident on a zinc oxide target, for a probe positioned 16.4 cm from the target, at an angle of 30°, biased at -40 V. Time zero represents the instant when the laser pulse strikes the target.

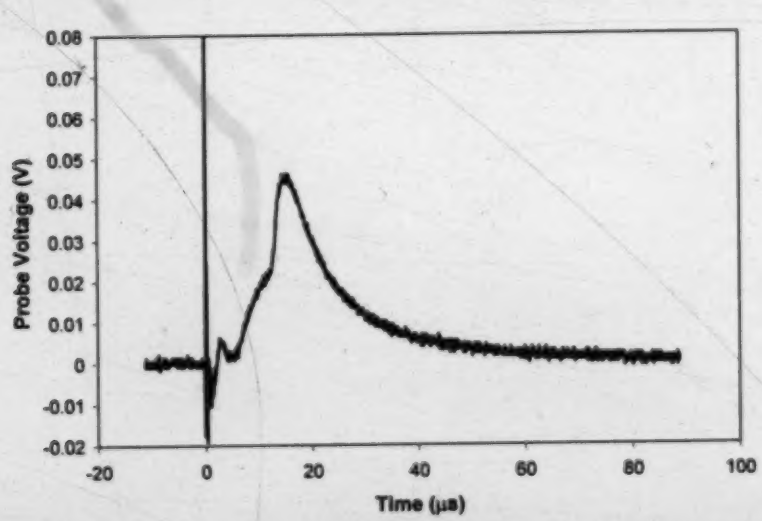

Figure A-23. An example ion signal collected by a Langmuir probe. This particular signal was produced at a laser intensity of 8.6×10^9 W/cm^2 (E_L=73.5 mJ, d_L=53.4 cm) incident on a zinc oxide target, for a probe positioned 16.5 cm from the target, at an angle of 40°, biased at -40 V. Time zero represents the instant when the laser pulse strikes the target.

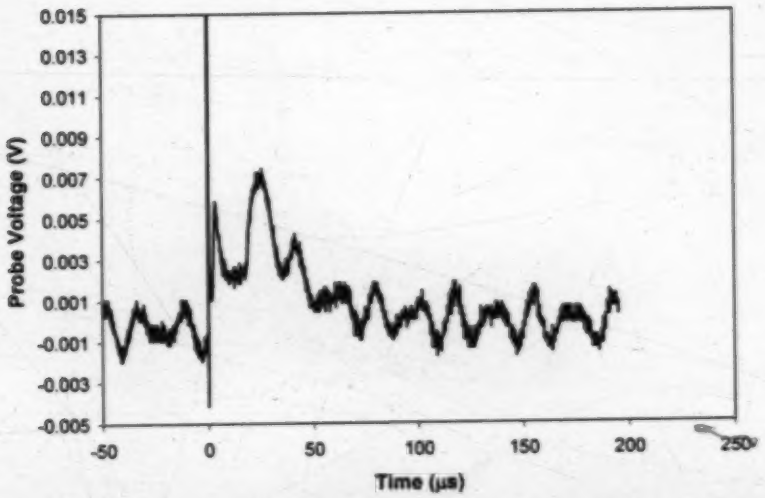

Figure A-24. An example ion signal collected by a Langmuir probe. This particular signal was produced at a laser intensity of 8.6×10^9 W/cm^2 (E_L=73.5 mJ, d_L=53.4 cm) incident on a zinc oxide target, for a probe positioned 16.3 cm from the target, at an angle of 54°, biased at -40 V. Time zero represents the instant when the laser pulse strikes the target. The oscillations are attributed to noise in the biasing circuit.

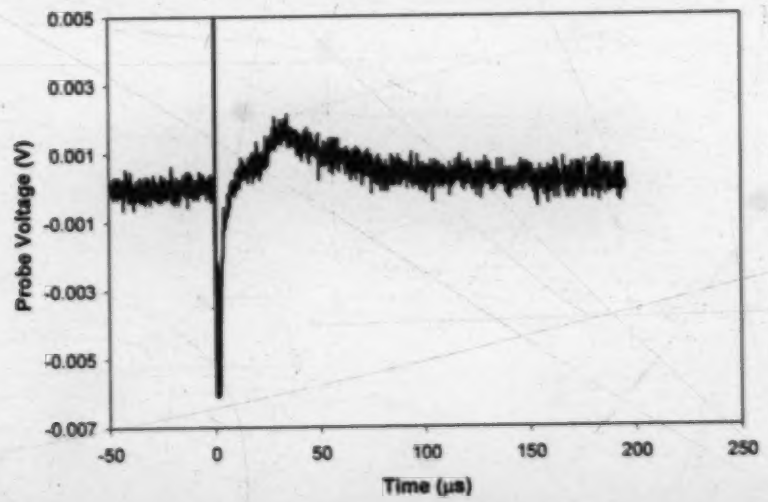

Figure A-25. An example ion signal collected by a Langmuir probe. This particular signal was produced at a laser intensity of 8.6×10^9 W/cm^2 (E_L=73.5 mJ, d_L=53.4 cm) incident on a zinc oxide target, for a probe positioned 16.7 cm from the target, at an angle of 69°, biased at -40 V. Time zero represents the instant when the laser pulse strikes the target.

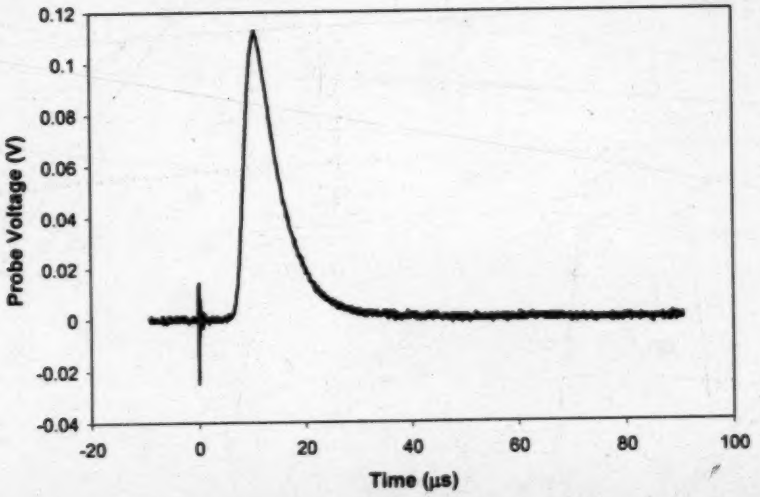

Figure A-26. An example ion signal collected by a Langmuir probe. This particular signal was produced at a laser intensity of 1.2×10^9 W/cm^2 (E_L=119.3 mJ, d_L=45.8 cm) incident on a carbon target, for a probe positioned 18.0 cm from the target, at an angle of 6°, biased at -30 V. Time zero represents the instant when the laser pulse strikes the target.

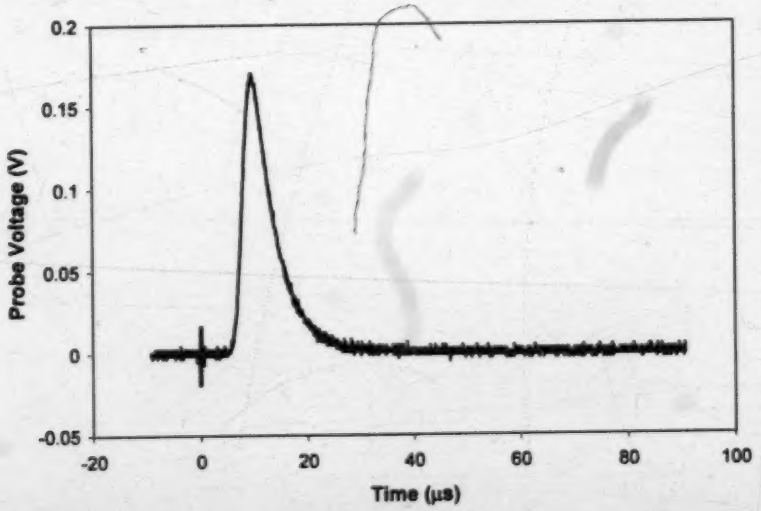

Figure A-27. An example ion signal collected by a Langmuir probe. This particular signal was produced at a laser intensity of 1.3×10^9 W/cm^2 (E_L=126.4 mJ, d_L=45.8 cm) incident on a carbon target, for a probe positioned 18.0 cm from the target, at an angle of 6°, biased at -70 V. Time zero represents the instant when the laser pulse strikes the target.

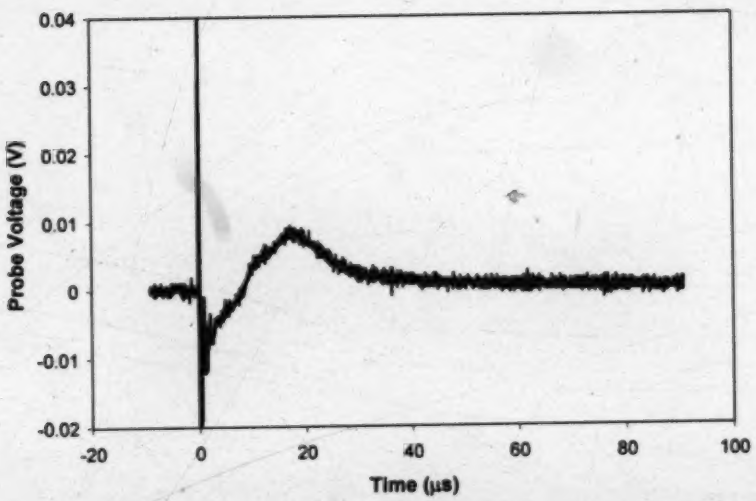

Figure A-28. An example ion signal collected by a Langmuir probe. This particular signal was produced at a laser intensity of 1.2×10^9 W/cm^2 (E_L=119.3 mJ, d_L=45.8 cm) incident on a carbon target, for a probe positioned 17.9 cm from the target, at an angle of 17°, biased at -30 V. Time zero represents the instant when the laser pulse strikes the target.

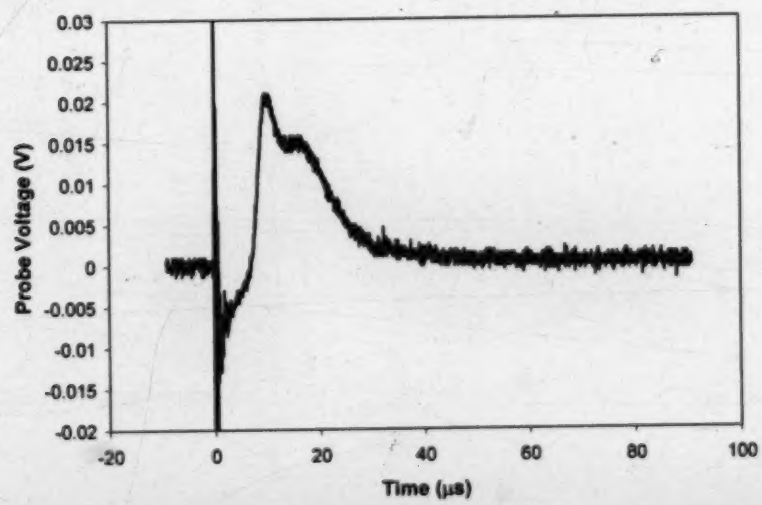

Figure A-29. An example ion signal collected by a Langmuir probe. This particular signal was produced at a laser intensity of 1.3×10^9 W/cm^2 (E_L=126.4 mJ, d_L=45.8 cm) incident on a carbon target, for a probe positioned 17.9 cm from the target, at an angle of 17°, biased at -70 V. Time zero represents the instant when the laser pulse strikes the target.

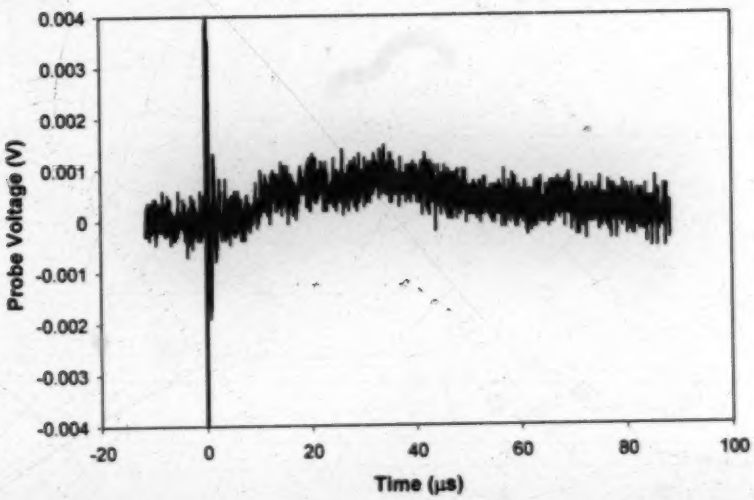

Figure A-30. An example ion signal collected by a Langmuir probe. This particular signal was produced at a laser intensity of 1.2×10^9 W/cm^2 (E_L=119.3 mJ, d_L=45.8 cm) incident on a carbon target, for a probe positioned 17.6 cm from the target, at an angle of 28°, biased at -30 V. Time zero represents the instant when the laser pulse strikes the target.

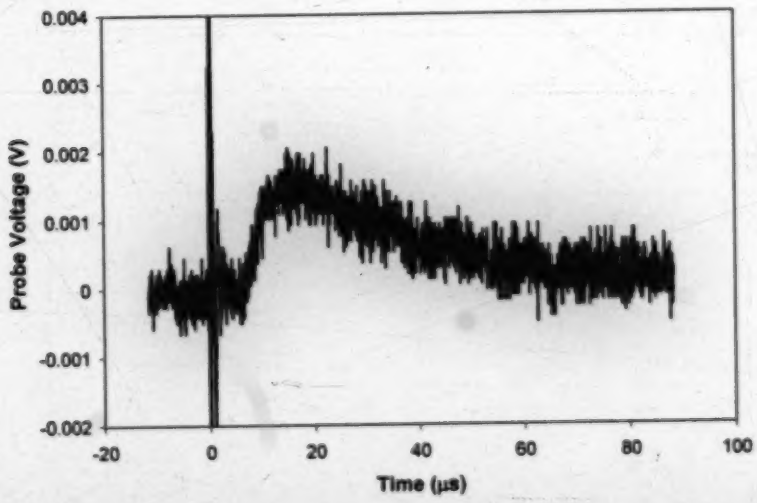

Figure A-31. An example ion signal collected by a Langmuir probe. This particular signal was produced at a laser intensity of 1.3×10^9 W/cm^2 (E_L=126.4 mJ, d_L=45.8 cm) incident on a carbon target, for a probe positioned 17.6 cm from the target, at an angle of 28°, biased at -70 V. Time zero represents the instant when the laser pulse strikes the target.

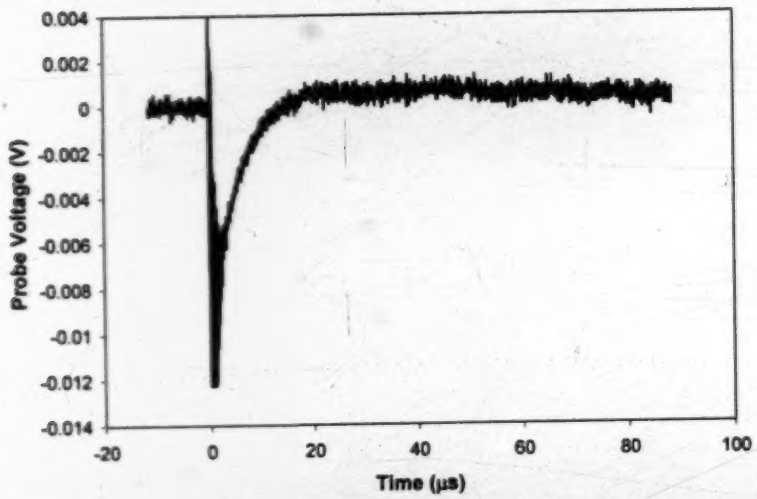

Figure A-32. An example ion signal collected by a Langmuir probe. This particular signal was produced at a laser intensity of 1.2×10^9 W/cm^2 (E_L=119.3 mJ, d_L=45.8 cm) incident on a carbon target, for a probe positioned 17.4 cm from the target, at an angle of 40°, biased at -30 V. Time zero represents the instant when the laser pulse strikes the target.

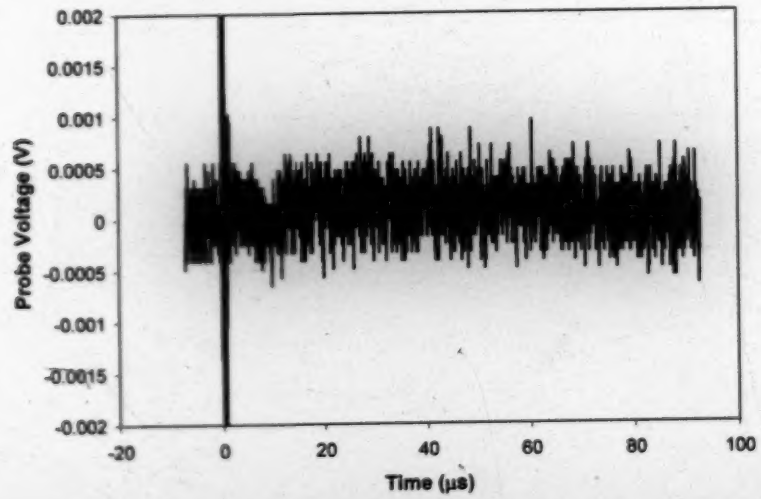

Figure A-33. An example ion signal collected by a Langmuir probe. This particular signal was produced at a laser intensity of 1.2×10^9 W/cm^2 (E_L=119.3 mJ, d_L=45.8 cm) incident on a carbon target, for a probe positioned 17.0 cm from the target, at an angle of 52°, biased at -30 V. Time zero represents the instant when the laser pulse strikes the target.

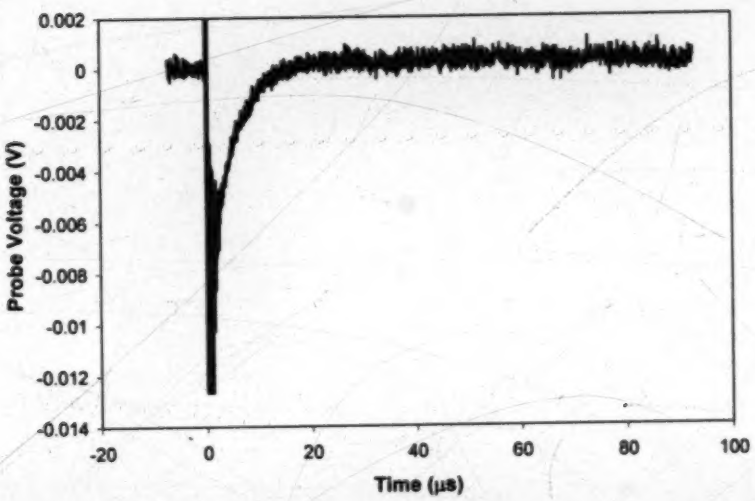

Figure A-34. An example ion signal collected by a Langmuir probe. This particular signal was produced at a laser intensity of 1.2×10^9 W/cm^2 (E_L=119.3 mJ, d_L=45.8 cm) incident on a carbon target, for a probe positioned 17.1 cm from the target, at an angle of 60°, biased at -30 V. Time zero represents the instant when the laser pulse strikes the target.

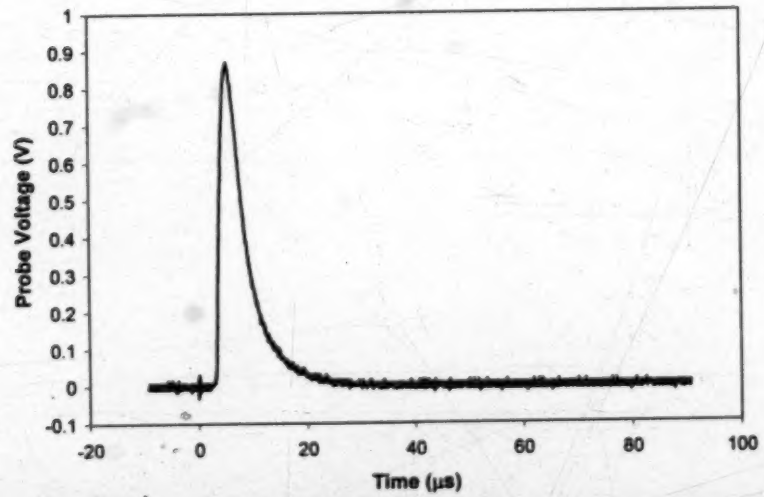

Figure A-35. An example ion signal collected by a Langmuir probe. This particular signal was produced at a laser intensity of 6.9×10^9 W/cm^2 (E_L=44.8 mJ, d_L=50.8 cm) incident on a carbon target, for a probe positioned 18.0 cm from the target, at an angle of 6°, biased at -40 V. Time zero represents the instant when the laser pulse strikes the target.

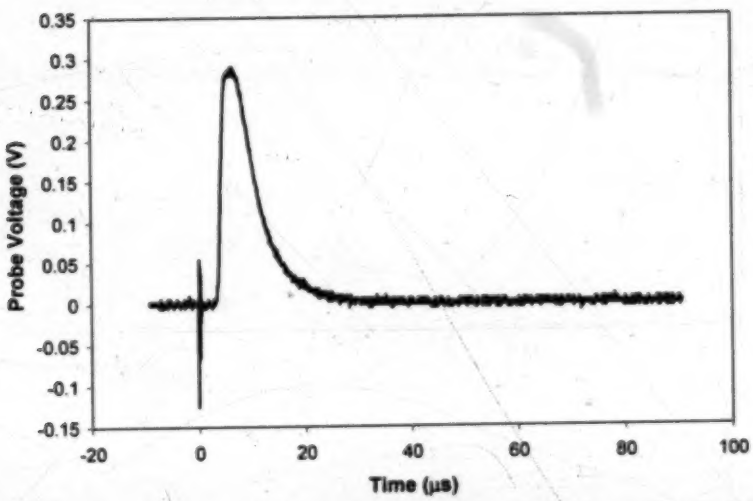

Figure A-36. An example ion signal collected by a Langmuir probe. This particular signal was produced at a laser intensity of 6.9×10^9 W/cm^2 (E_L=44.8 mJ, d_L=50.8 cm) incident on a carbon target, for a probe positioned 17.9 cm from the target, at an angle of 17°, biased at -40 V. Time zero represents the instant when the laser pulse strikes the target.

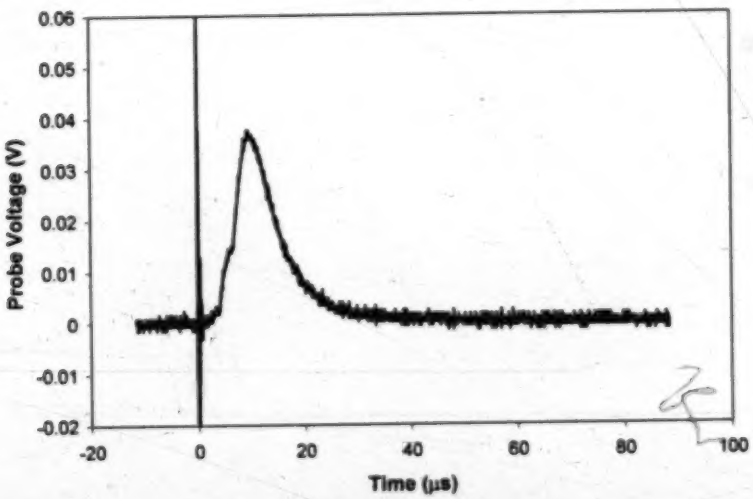

Figure A-37. An example ion signal collected by a Langmuir probe. This particular signal was produced at a laser intensity of 6.9×10^9 W/cm^2 (E_L=44.8 mJ, d_L=50.8 cm) incident on a carbon target, for a probe positioned 17.6 cm from the target, at an angle of 28°, biased at -40 V. Time zero represents the instant when the laser pulse strikes the target.

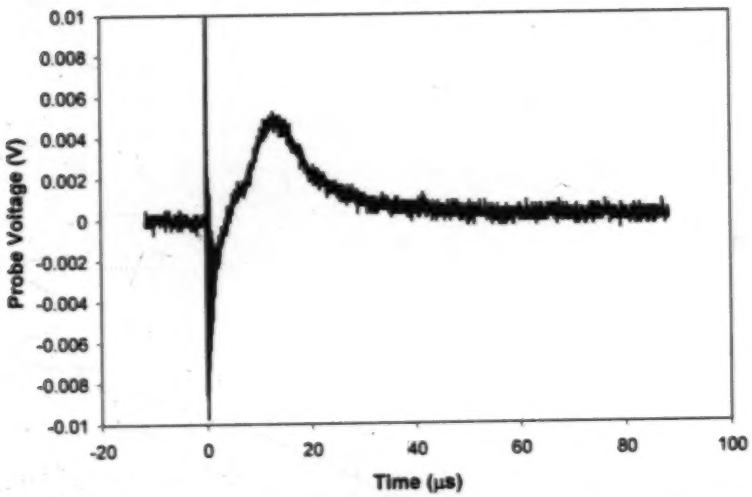

Figure A-38. An example ion signal collected by a Langmuir probe. This particular signal was produced at a laser intensity of 6.9×10^9 W/cm^2 (E_L=44.8 mJ, d_L=50.8 cm) incident on a carbon target, for a probe positioned 17.4 cm from the target, at an angle of 40°, biased at -40 V. Time zero represents the instant when the laser pulse strikes the target.

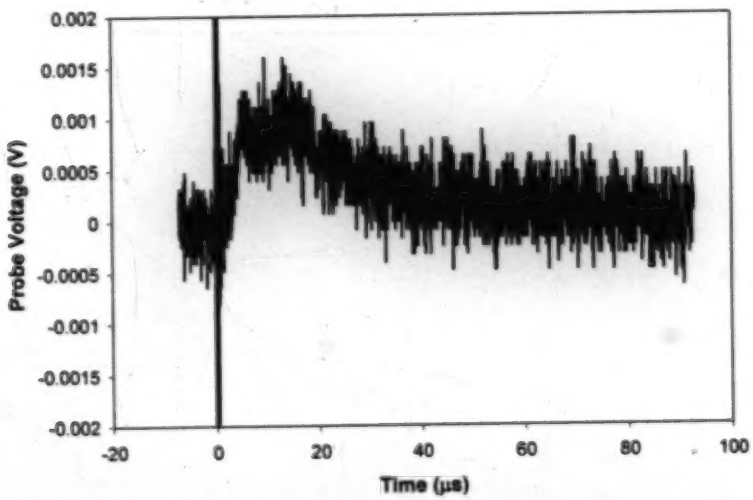

Figure A-39. An example ion signal collected by a Langmuir probe. This particular signal was produced at a laser intensity of 6.9×10^9 W/cm^2 (E_L=44.8 mJ, d_L=50.8 cm) incident on a carbon target, for a probe positioned 17.0 cm from the target, at an angle of 52°, biased at -40 V. Time zero represents the instant when the laser pulse strikes the target.

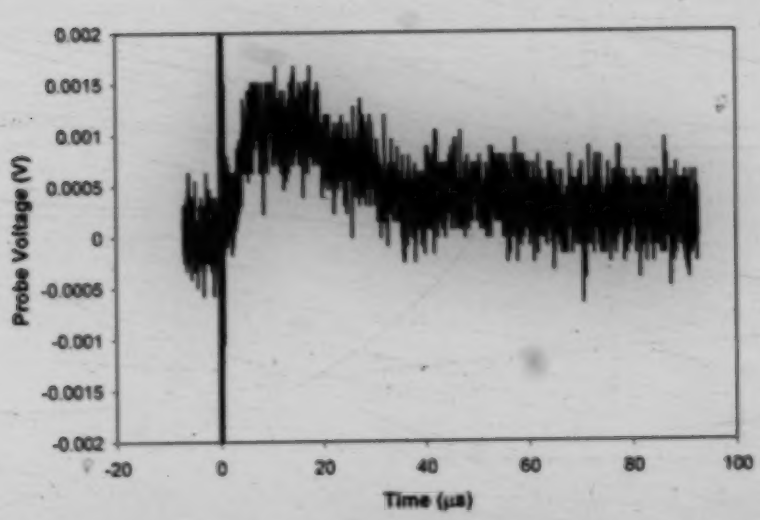

Figure A-40. An example ion signal collected by a Langmuir probe. This particular signal was produced at a laser intensity of 7.2×10^9 W/cm^2 (E_L=46.3 mJ, d_L=50.8 cm) incident on a carbon target, for a probe positioned 17.0 cm from the target, at an angle of 52°, biased at -60 V. Time zero represents the instant when the laser pulse strikes the target.

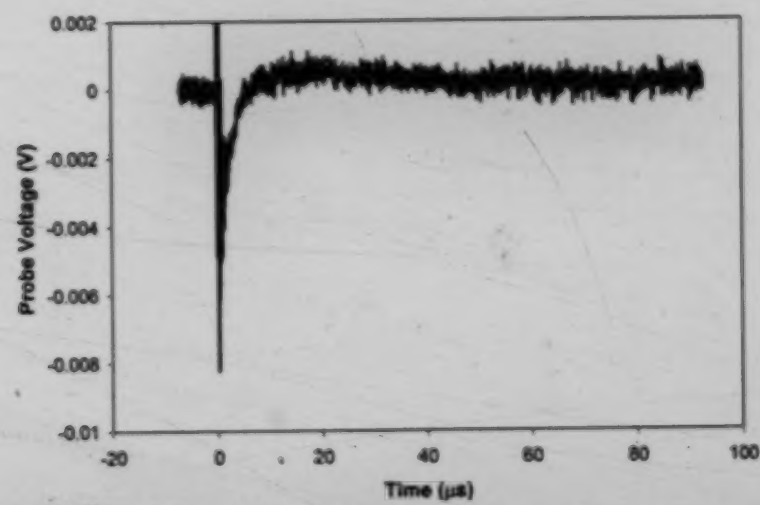

Figure A-41. An example ion signal collected by a Langmuir probe. This particular signal was produced at a laser intensity of 6.9×10^9 W/cm^2 (E_L=44.8 mJ, d_L=50.8 cm) incident on a carbon target, for a probe positioned 17.1 cm from the target, at an angle of 60°, biased at -40 V. Time zero represents the instant when the laser pulse strikes the target.

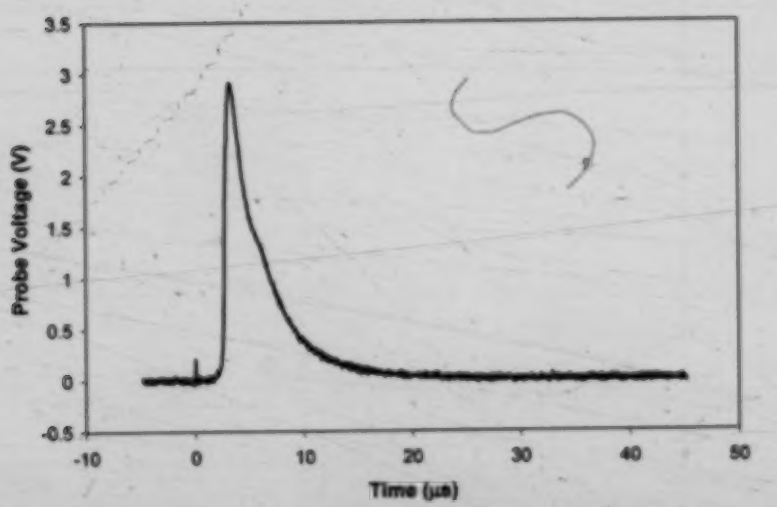

Figure A-42. An example ion signal collected by a Langmuir probe. This particular signal was produced at a laser intensity of 2.1×10^{10} W/cm^2 (E_L=79.3 mJ, d_L=52.8 cm) incident on a carbon target, for a probe positioned 18.0 cm from the target, at an angle of 6°, biased at -40 V. Time zero represents the instant when the laser pulse strikes the target.

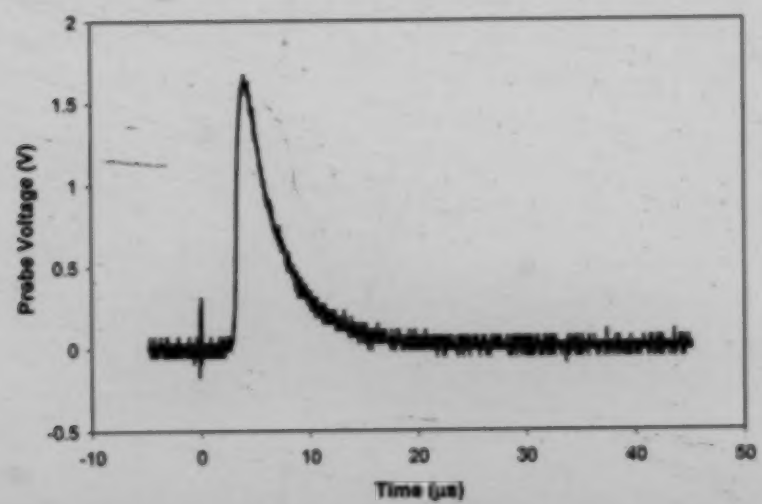

Figure A-43. An example ion signal collected by a Langmuir probe. This particular signal was produced at a laser intensity of 2.1×10^{10} W/cm^2 (E_L=79.3 mJ, d_L=52.8 cm) incident on a carbon target, for a probe positioned 17.9 cm from the target, at an angle of 17°, biased at -40 V. Time zero represents the instant when the laser pulse strikes the target.

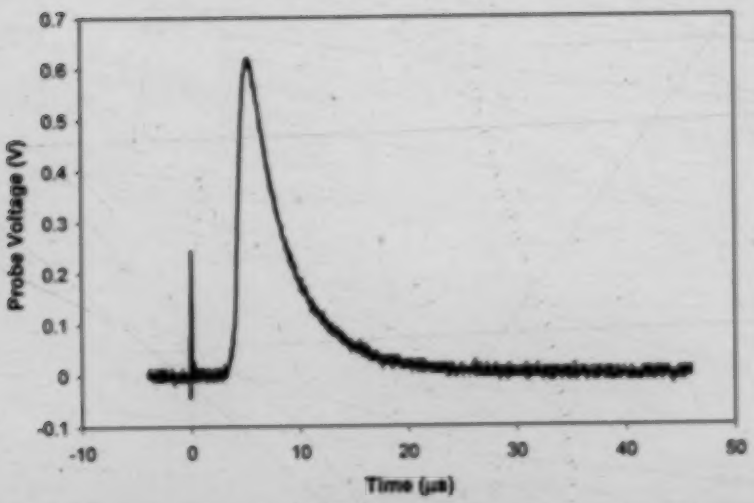

Figure A-44. An example ion signal collected by a Langmuir probe. This particular signal was produced at a laser intensity of 2.1×10^{10} W/cm^2 (E_L=79.3 mJ, d_L=52.8 cm) incident on a carbon target, for a probe positioned 17.6 cm from the target, at an angle of 28°, biased at -40 V. Time zero represents the instant when the laser pulse strikes the target.

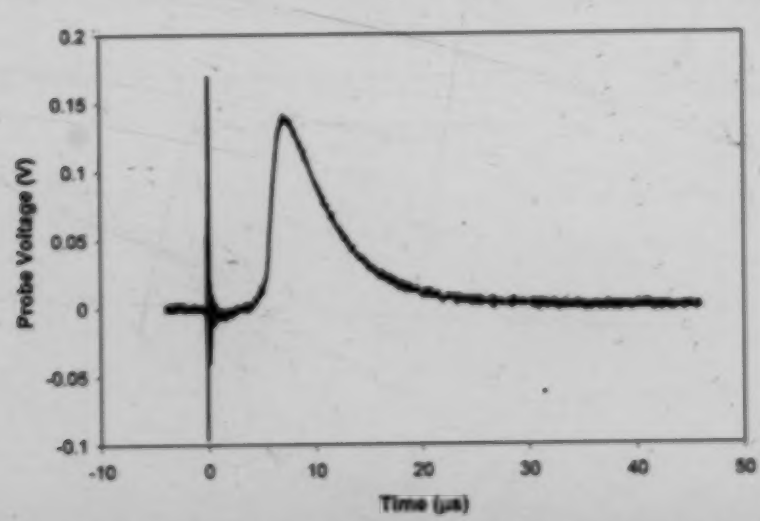

Figure A-45. An example ion signal collected by a Langmuir probe. This particular signal was produced at a laser intensity of 2.1×10^{10} W/cm^2 (E_L=79.3 mJ, d_L=52.8 cm) incident on a carbon target, for a probe positioned 17.4 cm from the target, at an angle of 40°, biased at -40 V. Time zero represents the instant when the laser pulse strikes the target.

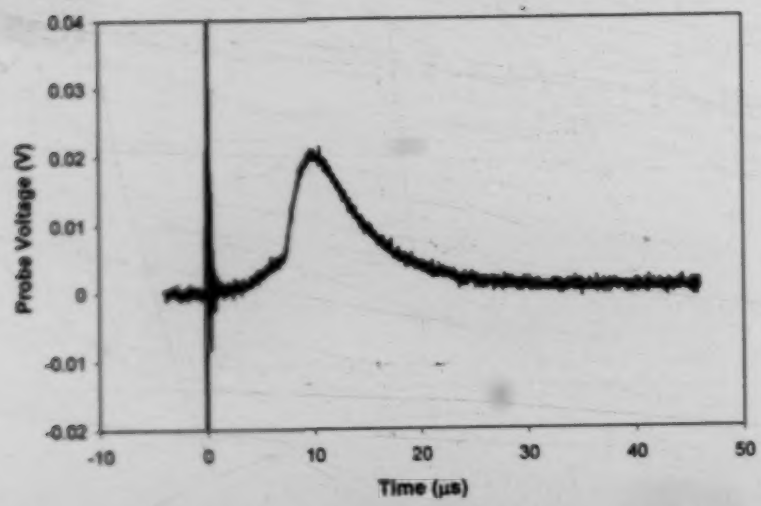

Figure A-46. An example ion signal collected by a Langmuir probe. This particular signal was produced at a laser intensity of 2.1×10^{10} W/cm^2 (E_L=79.3 mJ, d_L=52.8 cm) incident on a carbon target, for a probe positioned 17.0 cm from the target, at an angle of 52°, biased at -40 V. Time zero represents the instant when the laser pulse strikes the target.

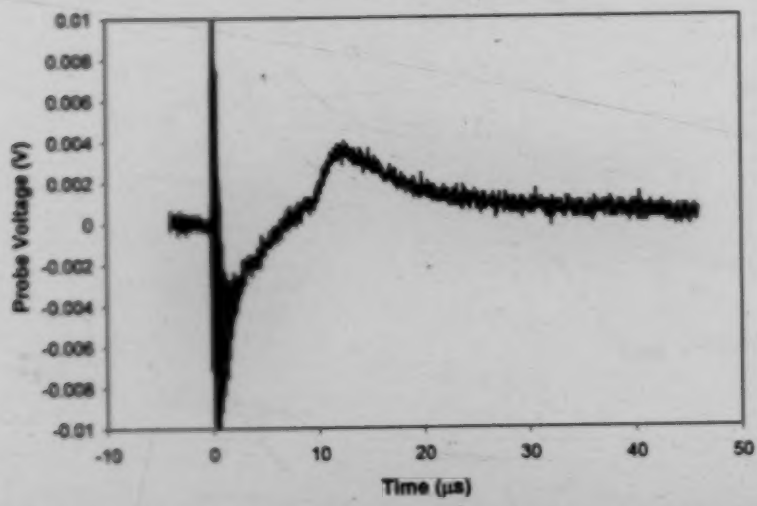

Figure A-47. An example ion signal collected by a Langmuir probe. This particular signal was produced at a laser intensity of 2.1×10^{10} W/cm^2 (E_L=79.3 mJ, d_L=52.8 cm) incident on a carbon target, for a probe positioned 17.1 cm from the target, at an angle of 60°, biased at -40 V. Time zero represents the instant when the laser pulse strikes the target.

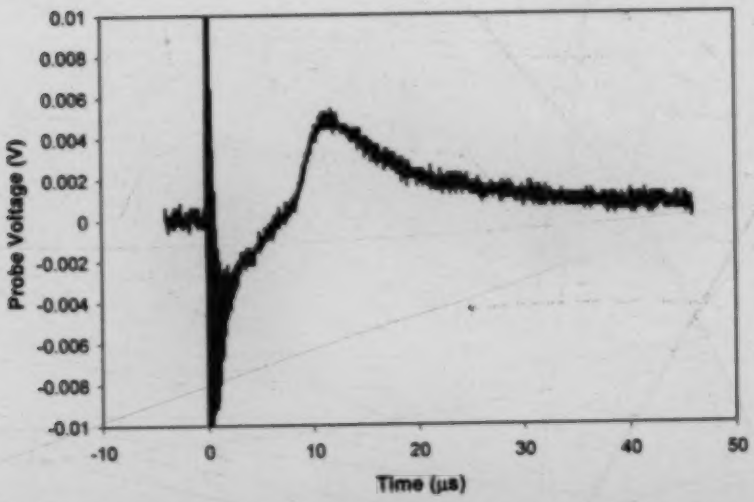

Figure A-48. An example ion signal collected by a Langmuir probe. This particular signal was produced at a laser intensity of 2.1×10^{10} W/cm^2 (E_L=79.9 mJ, d_L=52.8 cm) incident on a carbon target, for a probe positioned 17.1 cm from the target, at an angle of 60°, biased at -50 V. Time zero represents the instant when the laser pulse strikes the target.

The following figures are sample biasing curves used to calculate the electron temperature for different targets, different intensities, and different detector angles for the nanosecond laser-produced plasma (Chapter 3). The calculation of the electron temperature depends on the selected portion of the curve to fit. The electron temperature values provided by the graphs reflect the particular choice of fit, whereas the values in Tables 3-7 and 3-8 reflect the average over a range of chosen fits. The error estimate represents the standard error of the fit, for each particular graph.

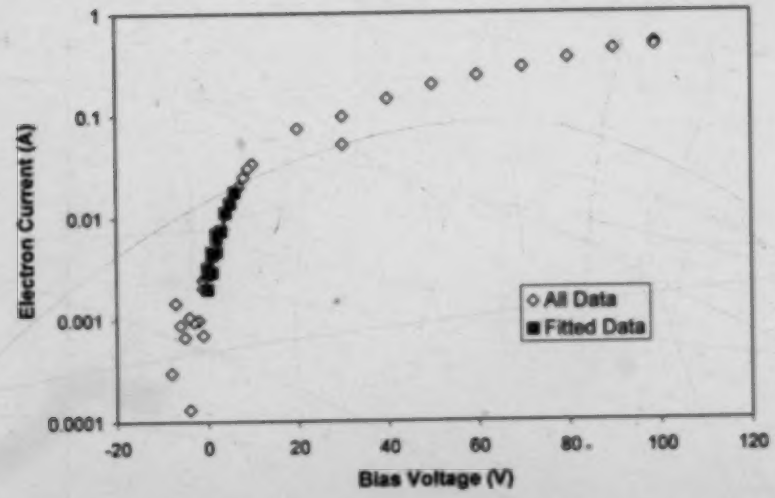

Figure A-49. An example of the bias curve from a Langmuir probe used to extract T_e for a carbon plasma. This particular probe was located a distance 17.9 cm away from the target, at an angle of 17° with respect to the target normal. The average laser parameters were: I_L=7.9x10^9 W/cm^2, E_L=50.8 mJ, d_L=50.8 cm. The slope of the fit allows the calculation of T_e=3 ± 0.3 eV, using Equation 2-4.

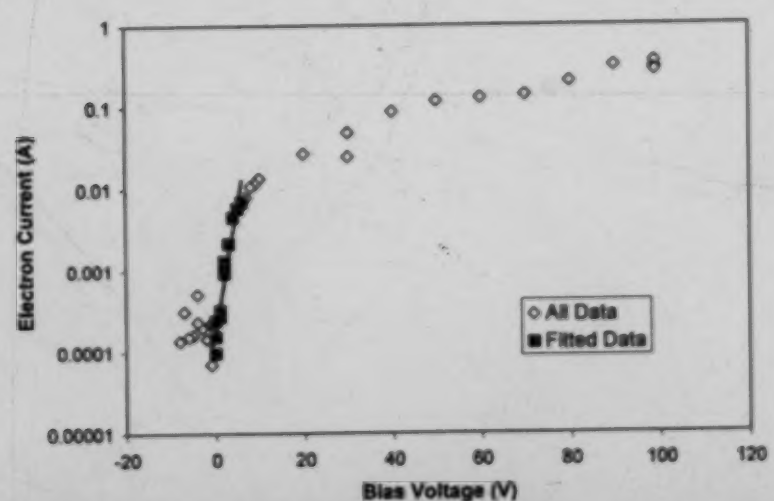

Figure A-50. An example of the bias curve from a Langmuir probe used to extract T_e for a carbon plasma. This particular probe was located a distance 17.6 cm away from the target, at an angle of 28° with respect to the target normal. The average laser parameters were: I_L=7.9x10^9 W/cm^2, E_L=50.8 mJ, d_L=50.8 cm. The slope of the fit allows the calculation of T_e=3 ± 0.3 eV, using Equation 2-4.

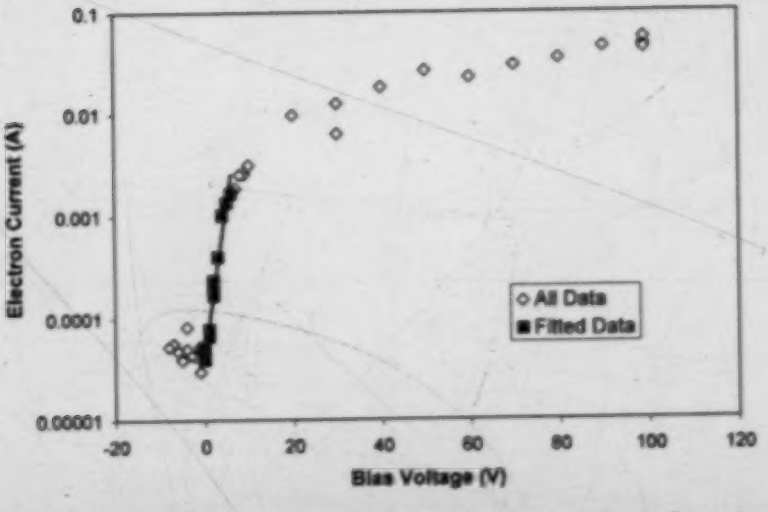

Figure A-51. An example of the bias curve from a Langmuir probe used to extract T_e for a carbon plasma. This particular probe was located a distance 17.4 cm away from the target, at an angle of 40° with respect to the target normal. The average laser parameters were: I_L=7.9x10^9 W/cm^2, E_L=50.8 mJ, d_L=50.8 cm. The slope of the fit allows the calculation of T_e=3 ± 0.3 eV, using Equation 2-4.

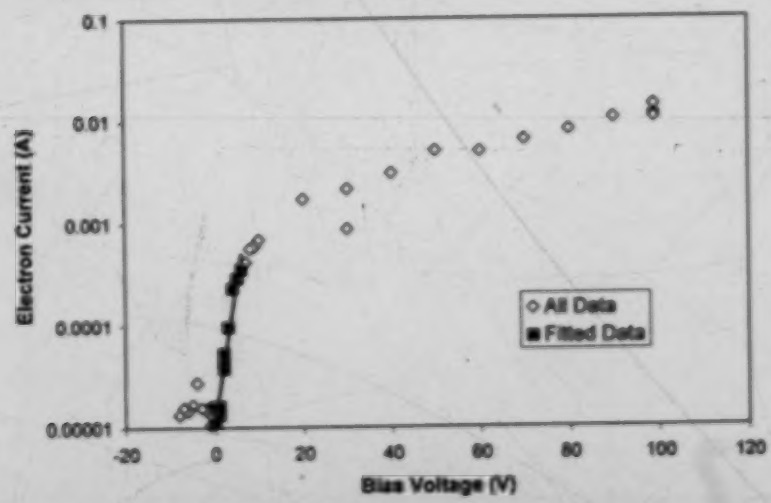

Figure A-52. An example of the bias curve from a Langmuir probe used to extract T_e for a carbon plasma. This particular probe was located a distance 17.0 cm away from the target, at an angle of 52° with respect to the target normal. The average laser parameters were: I_L=7.9x10^9 W/cm^2, E_L=50.8 mJ, d_L=50.8 cm. The slope of the fit allows the calculation of T_e=3 ± 0.3 eV, using Equation 2-4.

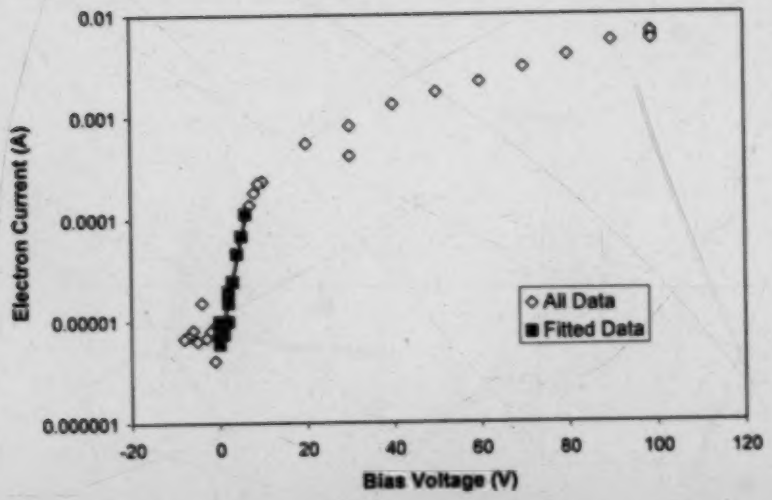

Figure A-53. An example of the bias curve from a Langmuir probe used to extract T_e for a carbon plasma. This particular probe was located a distance 17.1 cm away from the target, at an angle of 60° with respect to the target normal. The average laser parameters were: I_L=7.9x10^9 W/cm^2, E_L=50.8 mJ, d_L=50.8 cm. The slope of the fit allows the calculation of T_e=3 ± 0.3 eV, using Equation 2-4.

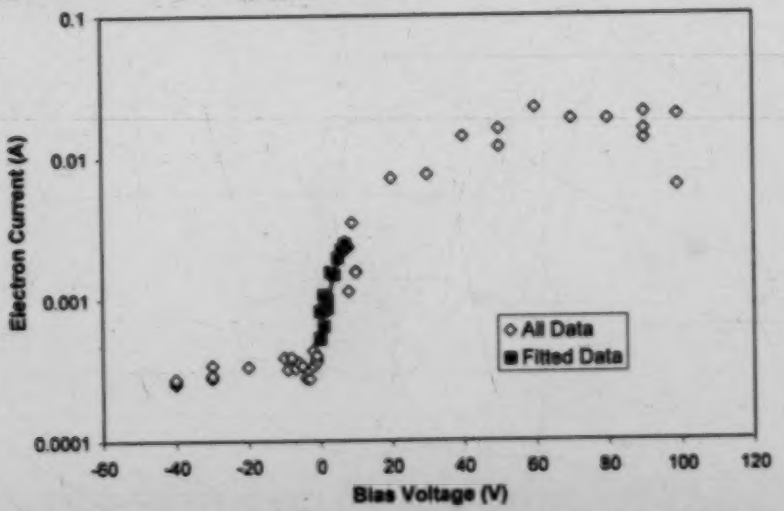

Figure A-54. An example of the bias curve from a Langmuir probe used to extract T_e for a carbon plasma. This particular probe was located a distance 17.9 cm away from the target, at an angle of 17° with respect to the target normal. The average laser parameters were: I_L=1.1x10^9 W/cm^2, E_L=108.1 mJ, d_L=45.8 cm. The slope of the fit allows the calculation of T_e=4.8 ± 0.5 eV, using Equation 2-4.

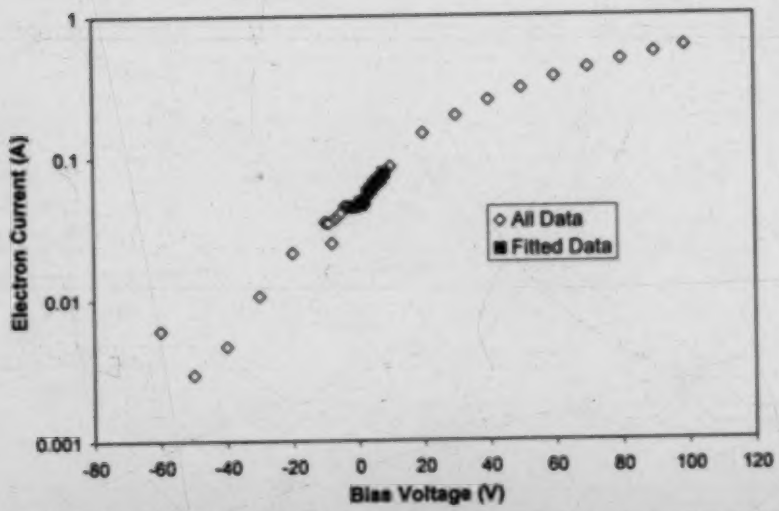

Figure A-55. An example of the bias curve from a Langmuir probe used to extract T_e for a zinc oxide plasma. This particular probe was located a distance 16.5 cm away from the target, at an angle of 7° with respect to the target normal. The average laser parameters were: I_L=7.7x10^9 W/cm^2, E_L=65.3 mJ, d_L=53.4 cm. The slope of the fit allows the calculation of T_e=14 ± 0.6 eV, using Equation 2-4.

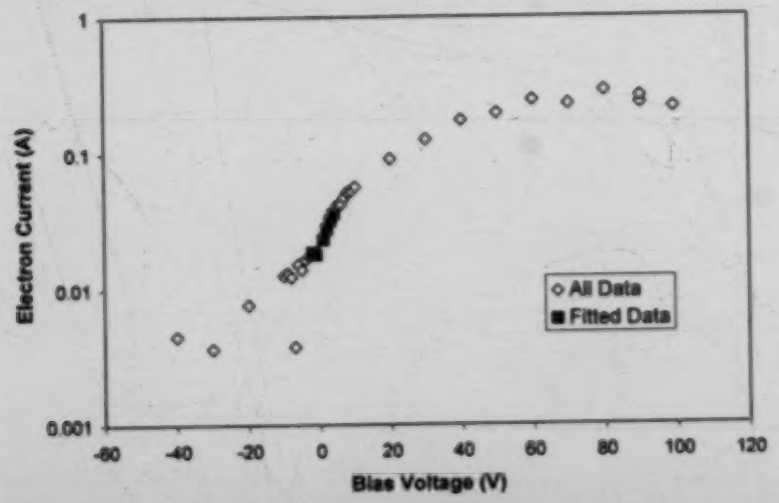

Figure A-56. An example of the bias curve from a Langmuir probe used to extract T_e for a zinc oxide plasma. This particular probe was located a distance 16.5 cm away from the target, at an angle of 7° with respect to the target normal. The average laser parameters were: I_L=2.7x10^9 W/cm^2, E_L=44.0 mJ, d_L=59.9 cm. The slope of the fit allows the calculation of T_e=9.7 ± 0.6 eV, using Equation 2-4.

The following graph is an additional example of a focal scan.

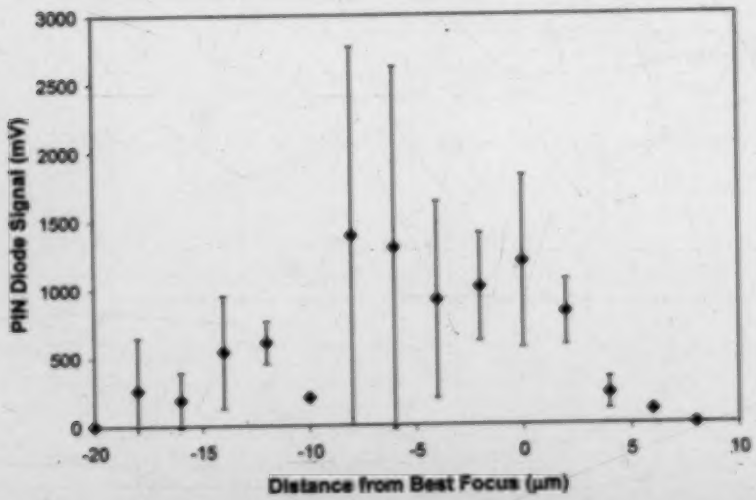

Figure A-57. A typical focal scan using the PIN diode detector to monitor the hot electron signal. Each data point represents the average of three laser shots, with the error bars representing the difference between the maximum and minimum signal within the set of three shots.

The following graphs are additional examples of Langmuir probe data.

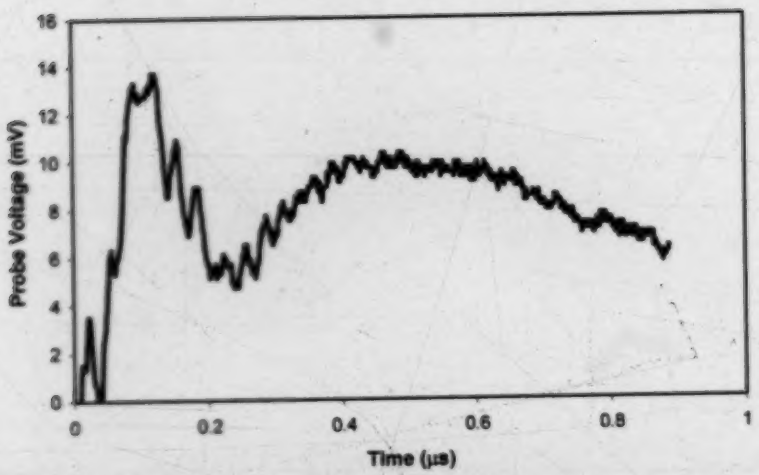

Figure A-58. Example Langmuir probe signal. The laser parameters were: E_L=243 μJ, I_L=3.4x10^{16} W/cm^2, with s-polarization, for a probe distance of 101 mm. Time zero represents the instant when the laser pulse strikes the target.

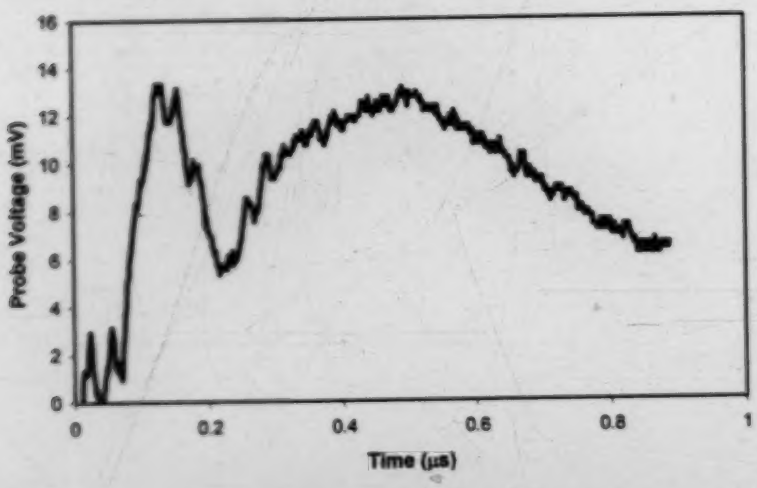

Figure A-59. Example Langmuir probe signal. The laser parameters were: E_L=235 μJ, I_L=2.9x10^{16} W/cm^2, with s-polarization, for a probe distance of 101 mm. Time zero represents the instant when the laser pulse strikes the target.

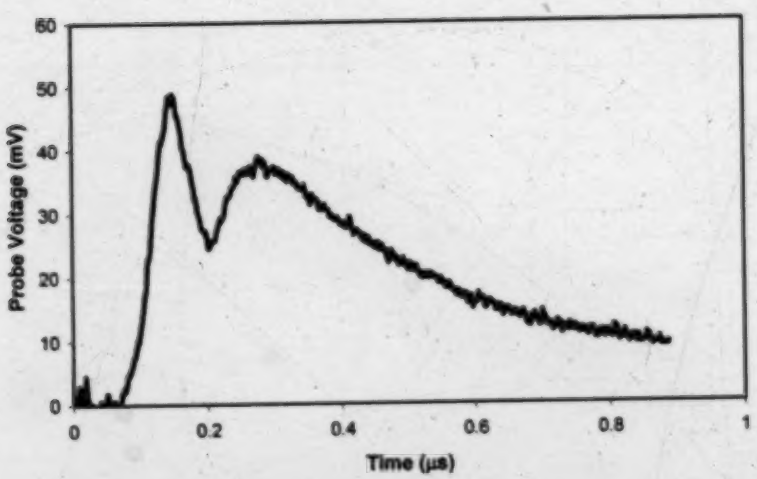

Figure A-60. Example Langmuir probe signal. The laser parameters were: E_L=241 μJ, I_L=1.1x10^{16} W/cm^2, with s-polarization, for a probe distance of 101 mm. Time zero represents the instant when the laser pulse strikes the target.

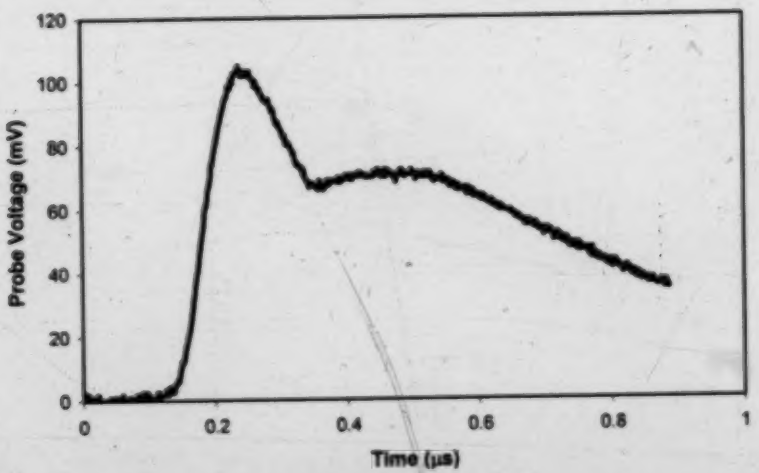

Figure A-61. Example Langmuir probe signal. The laser parameters were: E_L=237 μJ, I_L=1.7x10^{15} W/cm^2, with s-polarization, for a probe distance of 101 mm. Time zero represents the instant when the laser pulse strikes the target.

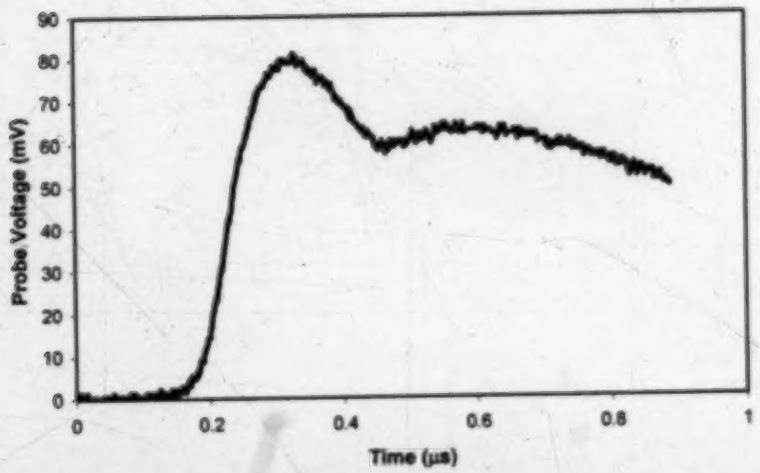

Figure A-62. Example Langmuir probe signal. The laser parameters were: E_L=235 μJ, I_L=6.4x10^{14} W/cm^2, with s-polarization, for a probe distance of 101 mm. Time zero represents the instant when the laser pulse strikes the target.

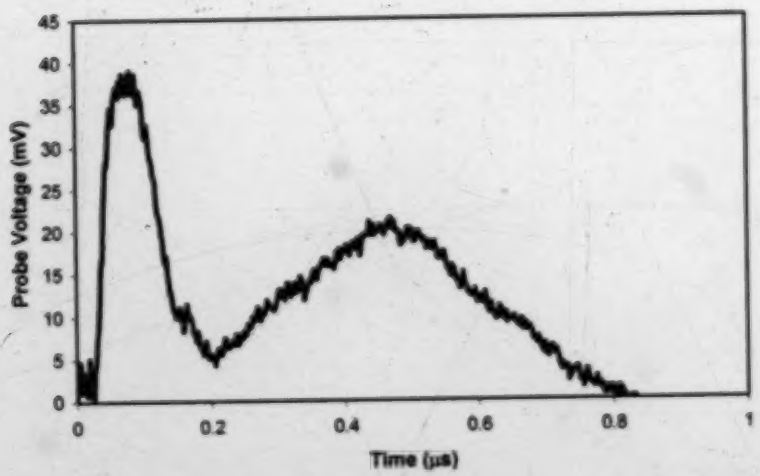

Figure A-63. Example Langmuir probe signal. The laser parameters were: E_L=214 μJ, I_L=2.9x10^{16} W/cm^2, with p-polarization, for a probe distance of 101 mm. Time zero represents the instant when the laser pulse strikes the target.

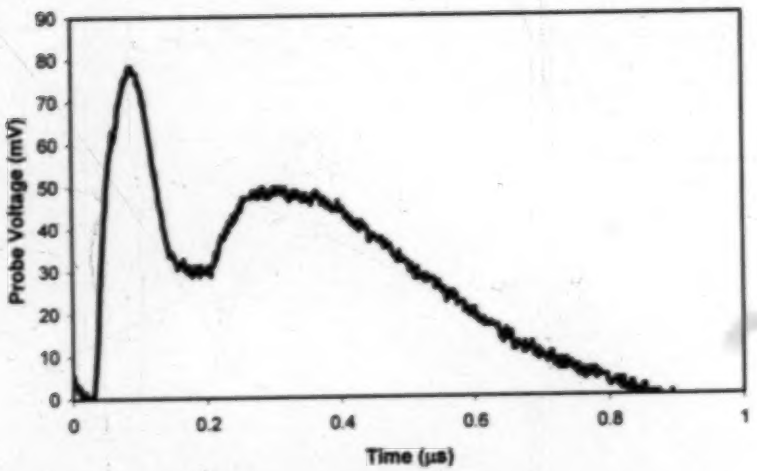

Figure A-64. Example Langmuir probe signal. The laser parameters were: E_L=211 μJ, I_L=1.9x10^{16} W/cm^2, with p-polarization, for a probe distance of 101 mm. Time zero represents the instant when the laser pulse strikes the target.

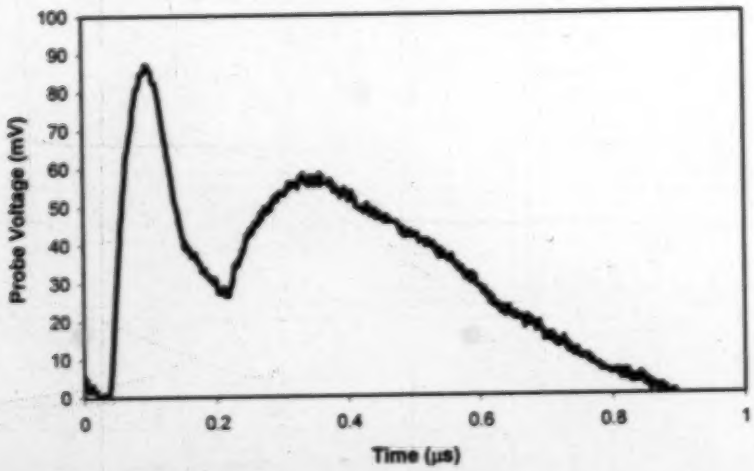

Figure A-65. Example Langmuir probe signal. The laser parameters were: E_L=211 μJ, I_L=9.8x10^{15} W/cm^2, with p-polarization, for a probe distance of 101 mm. Time zero represents the instant when the laser pulse strikes the target.

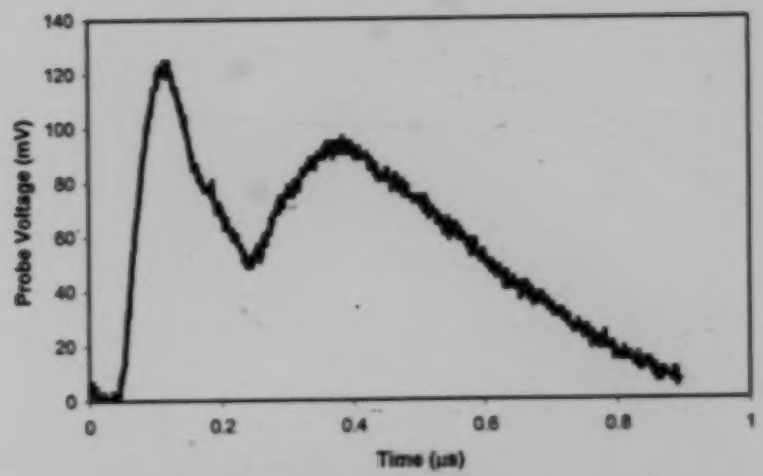

Figure A-66. Example Langmuir probe signal. The laser parameters were: E_L=214 μJ, I_L=7.2x10^{15} W/cm^2, with p-polarization, for a probe distance of 101 mm. Time zero represents the instant when the laser pulse strikes the target.

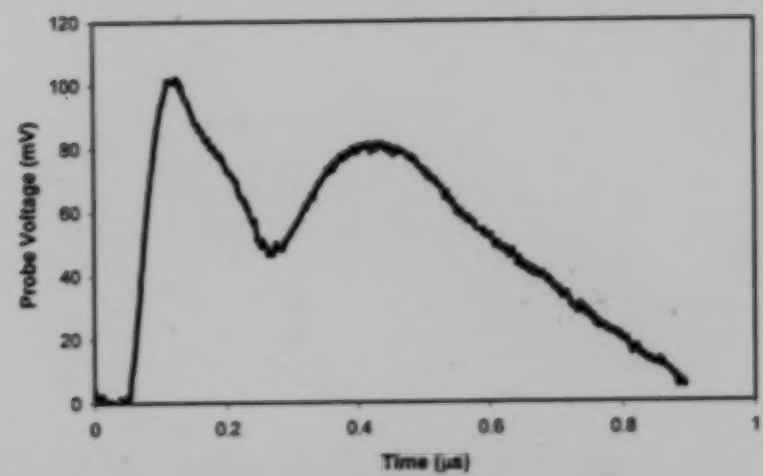

Figure A-67. Example Langmuir probe signal. The laser parameters were: E_L=212 μJ, I_L=4.1x10^{15} W/cm^2, with p-polarization, for a probe distance of 101 mm. Time zero represents the instant when the laser pulse strikes the target.

Below are additional figures containing data obtained from the three Langmuir probes used in the experiment to identify the ion species present in the fast ion flux.

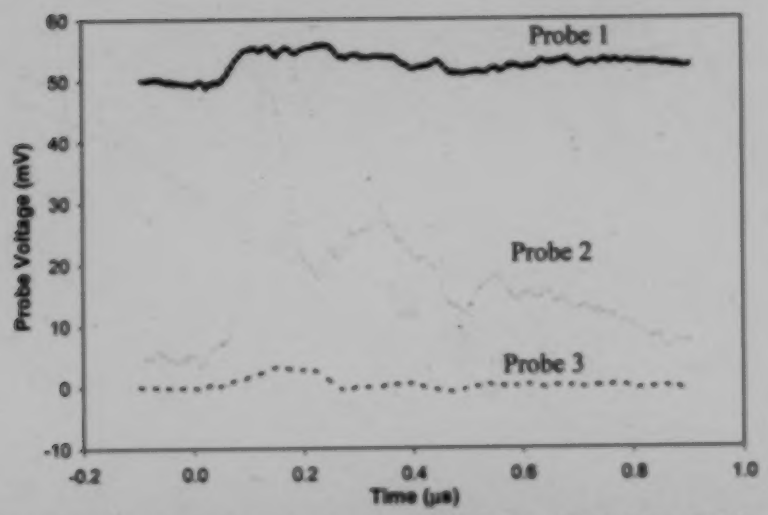

Figure A-68. The Langmuir probe signals exhibiting the deflected ion signals. The radiation was s-polarized, the laser energy on target was E_L=212 μJ, corresponding to an intensity on target of I_L=2.9x10^{14} W/cm^2. The signals are offset vertically for the purposes of clarity.

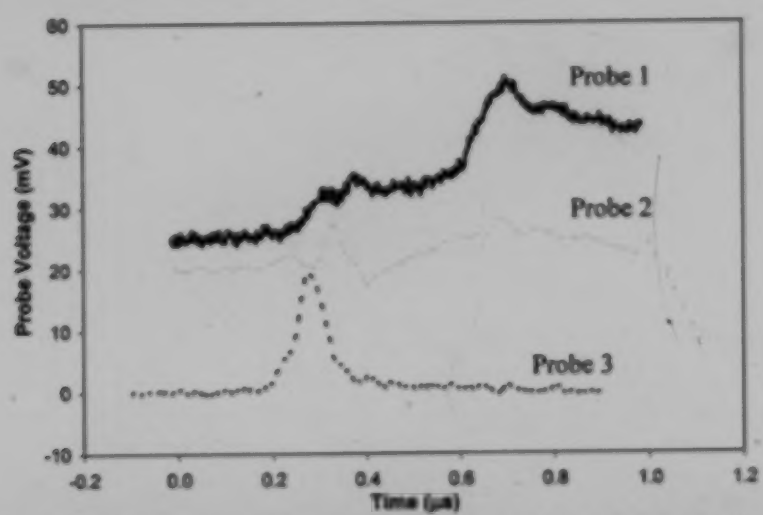

Figure A-69. The Langmuir probe signals exhibiting the deflected ion signals. The radiation was s-polarized, the laser energy on target was E_L=219 μJ, corresponding to an intensity on target of I_L=4.9x10^{14} W/cm^2. The signals are offset vertically for the purposes of clarity.

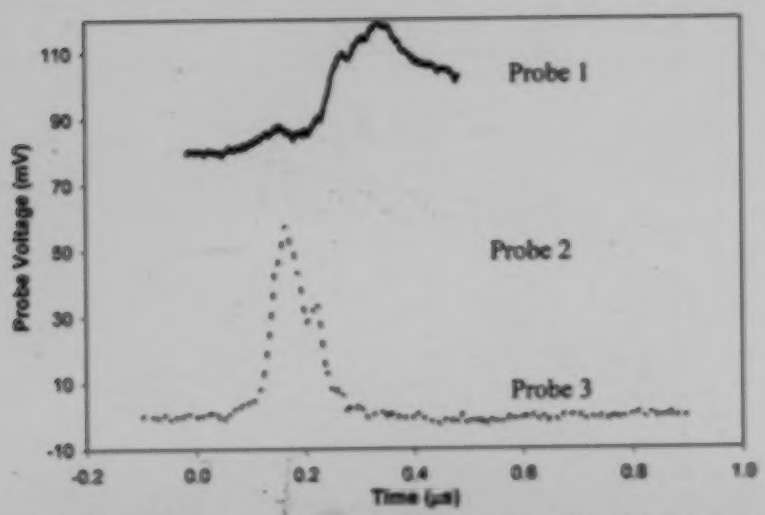

Figure A-70. The Langmuir probe signals exhibiting the deflected ion signals. The radiation was s-polarized, the laser energy on target was E_L=214 μJ, corresponding to an intensity on target of I_L=9.9x10^{14} W/cm^2. The signals are offset vertically for the purposes of clarity.

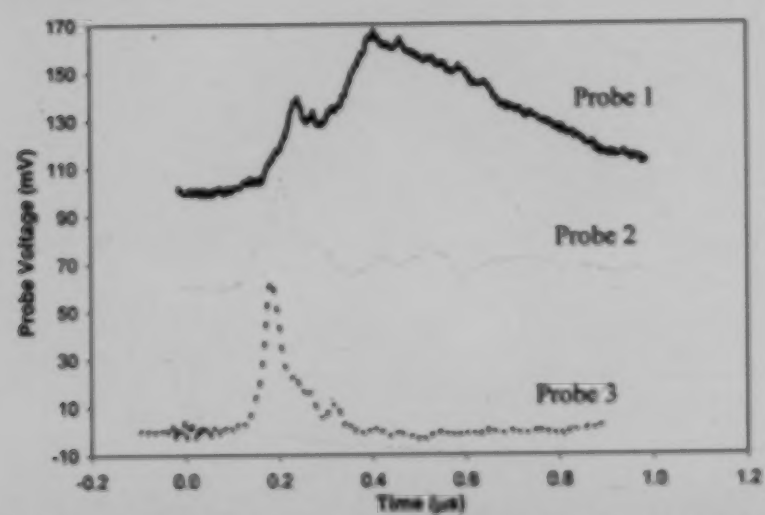

Figure A-71. The Langmuir probe signals exhibiting the deflected ion signals. The radiation was s-polarized, the laser energy on target was E_L=220 μJ, corresponding to an intensity on target of I_L=2.2x10^{15} W/cm^2. The signals are offset vertically for the purposes of clarity.

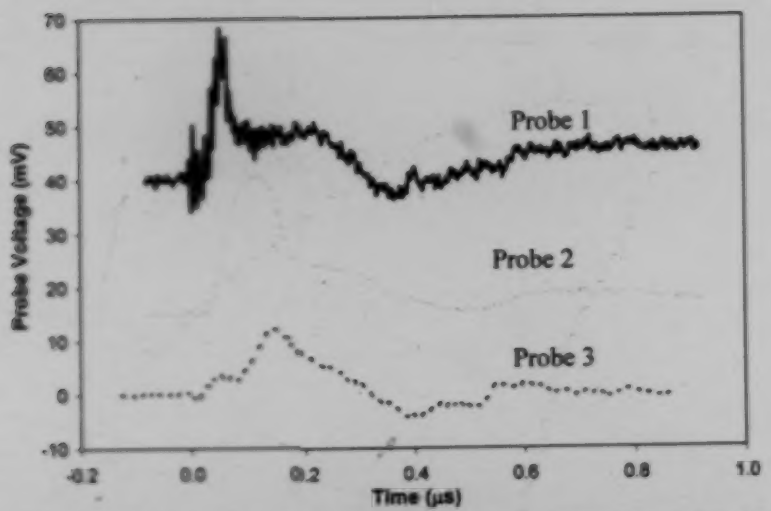

Figure A-72. The Langmuir probe signals exhibiting the deflected ion signals. The radiation was p-polarized, the laser energy on target was E_L=223 μJ, corresponding to an intensity on target of I_L=3.1x10^{16} W/cm^2. The signals are offset vertically for the purposes of clarity.

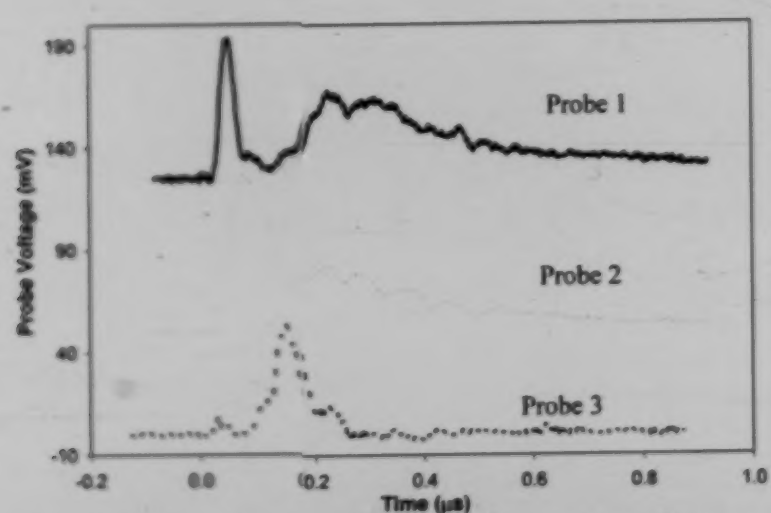

Figure A-73. The Langmuir probe signals exhibiting the deflected ion signals. The radiation was p-polarized, the laser energy on target was E_L=225 μJ, corresponding to an intensity on target of I_L=1.0x10^{16} W/cm^2. The signals are offset vertically for the purposes of clarity.

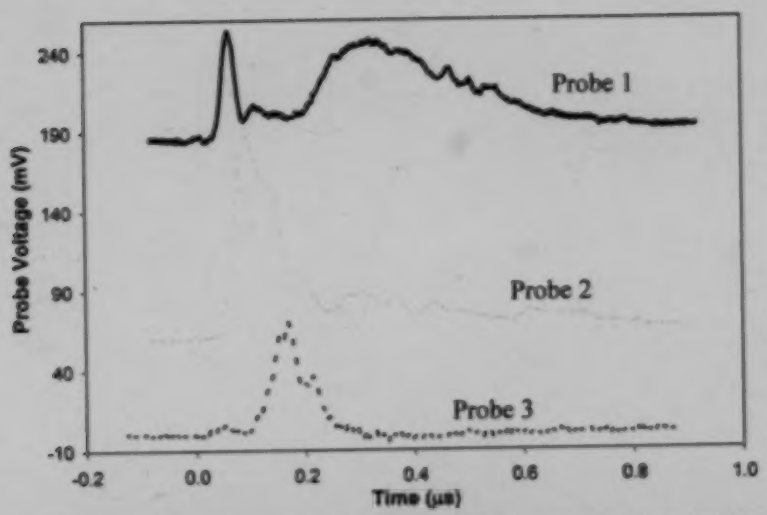

Figure A-74. The Langmuir probe signals exhibiting the deflected ion signals. The radiation was p-polarized, the laser energy on target was E_L=225 μJ, corresponding to an intensity on target of I_L=5.6x10^{15} W/cm^2. The signals are offset vertically for the purposes of clarity.

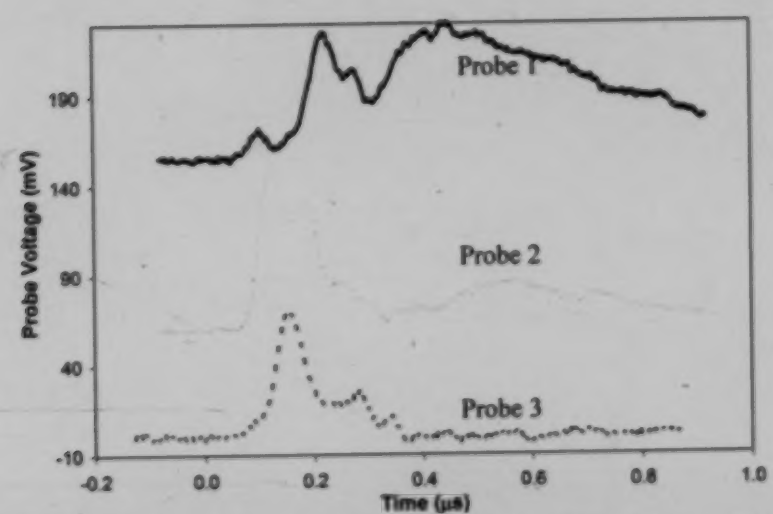

Figure A-75. The Langmuir probe signals exhibiting the deflected ion signals. The radiation was p-polarized, the laser energy on target was E_L=220 μJ, corresponding to an intensity on target of I_L=1.2x10^{15} W/cm^2. The signals are offset vertically for the purposes of clarity.

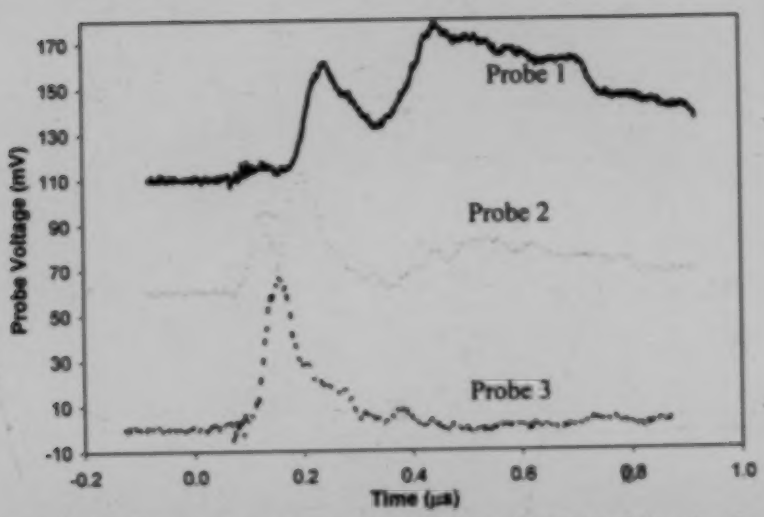

Figure A-76. The Langmuir probe signals exhibiting the deflected ion signals. The radiation was p-polarized, the laser energy on target was E_L=230 μJ, corresponding to an intensity on target of I_L=7.7x10^{14} W/cm^2. The signals are offset vertically for the purposes of clarity.

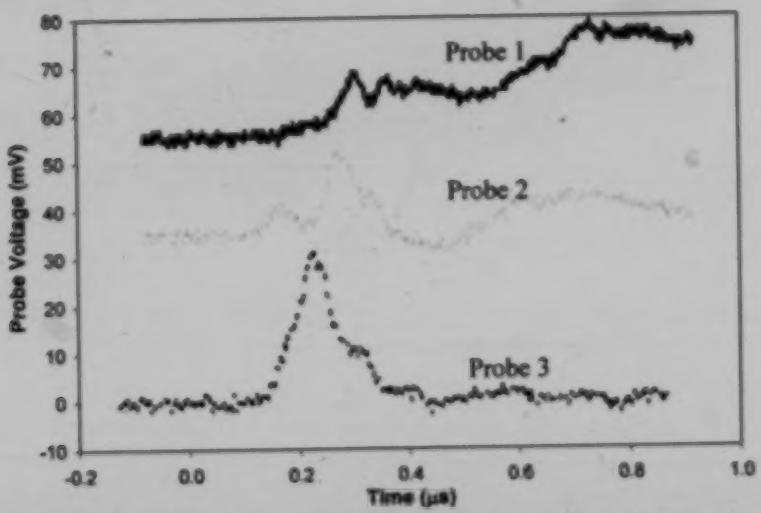

Figure A-77. The Langmuir probe signals exhibiting the deflected ion signals. The radiation was p-polarized, the laser energy on target was E_L=220 μJ, corresponding to an intensity on target of I_L=2.7x10^{14} W/cm^2. The signals are offset vertically for the purposes of clarity.

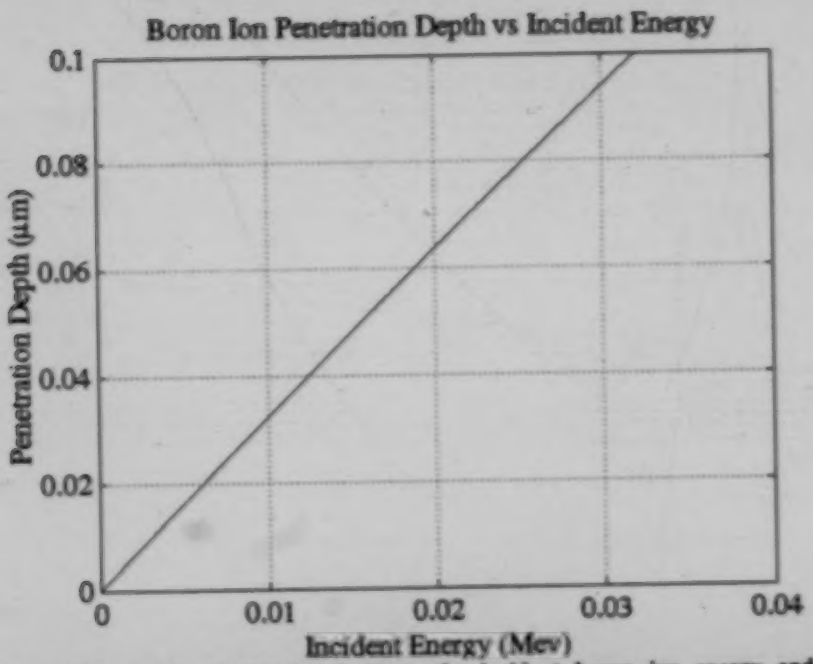

Figure A-78. The relationship between the incident boron ion energy and the penetration depth of the ion into a silicon substrate. This calculation was performed by C. W. Unick, using the range and stopping-power tables published by L. C. Northcliffe and R. F. Schilling [Nor70].

Bibliography

[Amo97] S. Amoruso *et al.*, *Appl. Phys. A* **65** 265 (1997).

[Bad01] J. Badziak *et al.*, *J. Phys. D: Appl. Phys* **34** 1885 (2001).

[Bad03] J. Badziak *et al.*, *Nucl. Instrum. Methods A* **498** 503 (2003).

[Bad04] J. Badziak *et al.*, *Plasma Phys. Control. Fusion* **46** B541 (2004).

[Bau00] D. Bauerle, *Laser Processing and Chemistry* (Berlin, Springer, 2000).

[Ben95] O. Benka *et. al.*, *Phys. Rev. A* **52** 3959 (1995).

[Bra04] C. A. Brau, *Modern Problems in Classical Electrodynamics* (New York, Oxford University Press, 2004).

[Bru87] F. Brunel, *Phys. Rev. Lett.* **59** 52 (1987).

[Bru01] D. L. Bruhwiler *et. al., Phys. Rev. ST Accel. Beams* **4** 101302 (2001).

[Che65] F. F. Chen in Plasma Diagnostic Techniques. R. H. Huddlestone and S. L. Leonard eds. New York: Academic (1965).

[Che74] F. F. Chen, *Introduction to Plasma Physics* (New York, Plenum Press, 1974).

[Che01] L.M. Chen *et al.*, *Phys. Rev. Lett.* **87** 225001-1 (2001).

[Cla00] E. L. Clark *et al.*, *Phys. Rev. Lett.* **85** 1654 (2000).

[Cla01] F. Claeyssens *et al.*, *J. Appl. Phys.* **89** 697 (2001).

[Cla02] F. Claeyssens *et al.*, *J. Appl. Phys.* **92** 6886 (2002).

[Col92] C. B. Collins *et al.*, *Diamond Films and Technology* **2** 25 (1992).

[Dec02] B. Deconihout *et. al., Rev. Sci. Instrum.* **73** 1734 (2002).

[Din80] R. Dinger *et al.*, *J. Phys. D: Appl. Phys.* **13** 2301 (1980).

[Fed90] R. Fedosejevs *et al.*, *Phys. Rev. Lett.* **64** 1250 (1990).

[For77] D. W. Forslund *et al.*, *Phys. Rev. Lett.* **39** 284 (1977).

[Git86] S. J. Gitomer *et al.*, *Phys. Fluids* **29** 2679 (1986).

[Gof76] R. R. Goforth, *Rev. Sci. Instrum.* **47** 548 (1976).

[Gor02] V. M. Gordienko *et al.*, *Plasma Phys. Control. Fusion* **44** 2555 (2002).

[Gre70] T. S. Green, *Plasma Physics* **12** 877 (1970).

[Gup86] P. D. Gupta *et al.*, *Appl. Phys. Lett.* **48** 103 (1986).

[Gup87] P. D. Gupta *et al.*, *Phys. Fluids* **30** 179 (1987).

[Har97] S. S. Harilal *et al.*, *J. Appl. Phys.* **82** 2140 (1997).

[Hat00] S. Hatchett et al, *Phys. Plasmas* **7** 2076 (2000).

[Hav03] J. Haverkamp *et al.*, *J. Appl. Phys.* **93** 3627 (2003).

[Heg02] M. Hegelich et al, *Phys. Rev. Lett.* **89** 085002 (2002).

[Hut02] I. H. Hutchinson, *Principles of Plasma Diagnostics, 2nd ed.* (Cambridge, Cambridge University Press, 2002).

[Ike05] N. Ikenaga *et al.*, *Surf. Coat. Tech.* **196** 226 (2005).

[Kes04] A. M. Keszler and L. Nemes, *J. Molecular Structure* **695-696** 211 (2004).

[Kho98] V.S. Khoroshkov and E.I. Minakova, *Eur. J. Phys.* **19** 523 (1998).

[Kit95] C. Kittel, *Introduction to Solid State Physics* (New York, Wiley, 1995).

[Koi99] K. J. Koivusaari *et al.*, *J. Appl. Phys.* **85** 2915 (1999).

[Koo71] D. W. Koopman, *Phys. Fluids* **14** 1707 (1971).

[Koo92] J. C. S. Kools *et al.*, *J. Appl. Phys.* **71** 4547 (1992).

[Kru85] W. L. Kruer and K. Estabrook, *Phys Fluids* **28** 430 (1985).

[Las03] L. Laska *et al.*, *Plasma Phys. Control. Fusion* **45** 585 (2003).
[Man04] S. P. D. Mangles *et al.*, *Nature* **431** 535 (2004).
[Mis99] A. Misra *et al.*, *Int. J. Modern Phys.* **13** 1503 (1999).
[Mor82] P. Mora, *Phys. Fluids* **25** 1051 (1982).
[Nak96] S. Nakai and H Takabe, *Rep. Prog. Phys.* 59 1071 (1996).
[Ng84] A. Ng *et al.*, *Appl. Phys. Lett.* **45** 1046 (1984).
[Nov00] O. A. Novodvorsky *et al.*, *Opt. Lasers Eng.* **32** 449 (2000).
[Nor70] L. C. Northcliffe and R. F. Schilling, *Nuclear Data Tables* **A7** 233 (1970).
[Pan76] J.A. Panitz and J.A. Foesch, *Rev. Sci. Instrum.* **47** 44 (1976).
[Pap92] D. L. Pappas *et al.*, *J. Appl. Phys.* **71** 5675 (1992).
[Pea77] J. S. Pearlman, *Rev. Sci. Instrum.* **48** 1064 (1977).
[Pel76] I. Pelah, *Phys. Lett.* **59A** 348 (1976).
[Puk03] A. Pukhov, *Rep. Prog. Phys.* **66** 47 (2003).
[Qia95] F. Qian *et al.*, *Appl. Phys. Lett.* **67** 6120 (1995).
[Red02] D. G. Redman *et al.*, "Space Charge Saturation of Faraday Cup Detectors Used in Laser-Produced Plasmas Studies," poster presentation at the International Conference on Plasma Science, May 26-30, Banff (2002).
[Rob94] J. Robertson, *Pure and Appl. Chem.* **66** 1789 (1994).
[Rob02] J. Robertson, *Mat. Sci. Eng. R* **37** 129 (2002).
[Rot01] M. Roth et al, *Phys. Rev. Lett.* **86** 436 (2001).
[Rot02] M. Roth et al, *Plasma Phys. Control. Fusion* **44** B99 (2002).
[Rup91] A. Rupp and K. Rohr, *J. Phys. D: Appl. Phys.* **24** 2229 (1991).
[Rup95] A. Rupp and K. Rohr, *J. Phys. D: Appl. Phys.* **28** 468 (1995).
[Sal91] B. E. A. Saleh and M. C. Teich, *Fundamentals of Photonics* (New York, John Wiley & Sons, 1991).
[Sch80] J. Schou, *Phys. Rev. B* **22** 2141 (1980).
[Ser04] C. Serbanescu et al., "Hot electrons, keV X-rays and Fast Ions from Femtosecond Laser Produced Micro Plasma," oral presentation at the 31st IEEE International Conference on Plasma Science, June 28-July 1, Baltimore (2004).
[Sna00] R. Snavely et al, *Phys. Rev. Lett.* **85** 2945 (2000).
[Spi62] L. Spitzer, *Physics of Fully Ionized Gases* (New York, Interscience Publishers, 1962).
[Str85] D. Strickland, G. Mourou, *Opt. Commun.* **56** 219 (1985).
[Str99] H.C. Straub *et. al.*, *Rev. Sci. Instrum.* **70** 4238 (1999).
[Tab94] M. Tabak et al, *Phys. Plasmas* **1** 1626 (1994).
[Tof00] B. Toftmann *et al.*, *Phys. Rev. Lett.* **84** 3998 (2000).
[Thu00a] A. Thum-Jaeger *et al.*, *Phys. Rev. E* **61** 3063 (2000).
[Thu00b] A. Thum-Jaeger *et al.*, *Phys. Rev. E* **63** 016405 (2000).
[Tsu92] Y. Y. Tsui, *Hydrodynamics of UV laser-produced plasma*, Thesis (Ph.D.), University of Alberta (1992).
[Tsu93] Y. Y. Tsui *et al.*, *Phys. Fluids B.* **5** 3357 (1993).
[Van98a] P. A. VanRompay *et al.*, *Appl. Surf. Science* **127-129** 1023 (1998).
[Van98b] P. A. VanRompay *et al.*, *Surf. Coat. Tech.* **100-101** 496 (1998).
[Ver95] J. P. Verboncouer *et. al.*, *Comp. Phys. Comm.* **87** 199 (1995).

[Vic99] D. Vick *et al.*, *Thin Solid Films* **350** 49 (1999).
[Wei04] S. Weissmantel *et al.*, *Surf. Coat. Tech.* **188-189** 268 (2004).
[Wil93] S. C. Wilks, *Phys. Fluids B* **5** 2603 (1993).
[Wor00] E. Woryna *et al.*, *Rev. Sci. Instrum.* **71** 949 (2000).
[Yan03] H. Yan *et al.*, *J. Am. Chem. Soc.* **125** 4728 (2003).
[Yu00] W. Yu *et al.*, *Phys. Rev. Lett.* **85** 570 (2000).
[Zha02] Z. Zhang *et al.*, *J. Appl. Phys.* **92** 2867 (2002).
[Zhi00] A. Zhidkov *et al.*, *Phys. Rev. E* **61** R2224 (2000).